

Thesis by

William H. Amidon

In Partial Fulfillment of the Requirements for the

Degree of

Doctor of Philosophy

CALIFORNIA INSTITUTE OF TECHNOLOGY

Pasadena, California

2010

(Defended May 17, 2010)

© 2010

William Amidon

All Rights Reserved

ACKNOWLEDGEMENTS

I would like to sincerely thank my advisor Ken Farley for his intellectual and financial support throughout my time at Caltech. He has given me the flexibility to pursue a wide range of projects, many unrelated to the topics presented in this thesis. He has trained me to be a critical thinker and to always make the back of the envelope calculation first. For these things I am truly grateful. I would also like to thank my fiancé Susan Parsons for never making me feel guilty when I was not home in time for Jeopardy and for understanding why I love being in the field so much. Thanks are also due to Jean-Philippe Avouac, Jason Saleeby, and Kerry Sieh. Time spent in the field with these incredible people has made me into a capable geologist and better person. Thanks to Don Burnett and George Rossman for always having their doors open to talk about mineralogy and nuclear chemistry, two subjects I have learned a lot about during the course of my thesis. Finally, I give thanks to Caltech as an institution, a truly wonderful place that has given me five years that I would not trade for anything.

ABSTRACT

The development of terrestrial cosmogenic nuclide dating has led to applications as varied as the dating of glacial moraines, establishing slip-rates on faults, measuring the erosion rates of basins, and measuring rates of soil formation. Studies in many of these fields could greatly benefit from analysis of far more samples than can be easily dated using ^{10}Be , ^{26}Al , and ^{36}Cl . The rapid preparation and analysis of samples for cosmogenic ^3He often allows a greater number of samples to be analyzed, but has so far been applied primarily to olivine and pyroxene in mafic rocks. Because ^3He is produced in all mineral phases, it can potentially be applied in almost any lithology. The goals of this thesis is to expand the range of target lithologies suitable for cosmogenic ^3He dating by calibrating production rates of cosmogenic ^3He in accessory mineral phases such as apatite, zircon, and garnet. Results are presented from three calibration studies: glacial moraine boulders in the Nepal Himalaya, young rhyolite surfaces from California's Coso volcanic field, and rhyolite surfaces scoured by the Bonneville flood near Twin Falls, Idaho. Both the Nepal and Coso studies compare ^3He in zircon, apatite, and garnet against ^{10}Be in quartz, finding that higher than expected ^3He concentrations are likely due to anomalous elevation scaling in the Himalaya, and to production of ^3He via neutron capture on ^6Li at Coso. The Idaho calibration study is unique in that it is calibrated against the age of the Bonneville outburst flood (known by ^{14}C dating), and uses a shielded sample to definitively document Li-produced ^3He components in the deep sub surface. Collectively, these studies highlight several challenges associated with cosmogenic ^3He dating of accessory phases: the difficulty in measuring small amounts of cosmogenic ^3He in the presence of large amounts of radiogenic ^4He , the importance of production of ^3He via neutron capture on ^6Li , and the redistribution of energetic ^3He and ^3H between adjacent mineral phases. Despite these challenges, adopting a ^{10}Be production rate of $4.51 \text{ at g}^{-1} \text{ a}^{-1}$ in quartz (Balco et al., 2008), brings three independent ^3He production rate estimates into good agreement with grand means of 103 ± 3 , 133 ± 6 , and about $134 \pm 13 \text{ at g}^{-1} \text{ a}^{-1}$ in zircon, apatite, and spessartine garnet respectively. Such agreement suggests that these phases are suitable for cosmogenic dating. ^3He in accessory phases may enable a range of unique applications including the study of ancient sediments, paleo-altimetry, and rates of chemical weathering in soils.

TABLE OF CONTENTS

Acknowledgements	iii
Abstract	iv
Table of Contents.....	v
List of Figures and Tables	vi
Chapter I: The utility of cosmogenic ^3He dating	1
Chapter II: Anomalous cosmogenic ^3He production and elevation scaling in the high Himalaya	10
Chapter III: Cosmogenic ^3He and ^{21}Ne production rates calibrated against ^{10}Be in minerals from the Coso volcanic field	40
Chapter IV: Cosmogenic ^3He production rates in apatite, zircon, and pyroxene inferred from Bonneville flood erosional surfaces	70
Chapter V: Mass spectrometric ^3He measurement in ^4He -rich phases: techniques and limitations for cosmogenic ^3He dating in zircon, apatite, and titanite.....	102
Chapter VI: Conclusions and directions for future research.....	118
Bibliography.....	128
Appendix A: Matlab scripts used in calculation of ^3He production	144
Appendix B: Matlab scripts used in uncertainty calculations	171

LIST OF FIGURES AND TABLES

Chapter 2: Anomalous cosmogenic ^3He production and elevation scaling in the high Himalaya

<i>Figure Number</i>	<i>Page</i>
2.1 Map of Nepal study area.....	12
2.2 Zircon ^3He data.....	19
2.3 Apatite ^3He data.....	19
2.4 Garnet ^3He data.....	20
2.5 Li-produced ^3He components.....	26
2.6 Results of grain size analyses.....	30
2.7 Predicted ^3He from elevation scaling model.....	33
2.8 Actual sample elevations vs. predicted elevations.....	33
2.9 Neutron energy spectrums and $^3\text{He}/^{10}\text{Be}$ excitation functions.....	36

<i>Table Number</i>	<i>Page</i>
2.1 Zircon helium data.....	14
2.2 Apatite helium data.....	14
2.3 Garnet and kyanite ^3He data.....	15
2.4 Garnet compositional data.....	15
2.5 Selected neutron flux parameters.....	22
2.6 Bulk rock composition.....	23

Chapter 3: Cosmogenic ^3He and ^{21}Ne production rates calibrated against ^{10}Be in minerals from the Coso volcanic field

<i>Figure Number</i>	<i>Page</i>
3.1 Measured and corrected ^3He	51
3.2 Grain size vs. ^3He	51
3.3 Neon results.....	54
3.4 Corrected ^3He results.....	60

<i>Table Number</i>	<i>Page</i>
3.1 ^{10}Be data.....	47
3.2 Helium crushing data.....	48
3.3 Helium fusion data.....	49
3.4 ^3He production rate estimates.....	50
3.5 Neon data.....	53
3.6 Host mineral Li calculations.....	55
3.7 Mineral compositions.....	55
3.8 Selected parameters from neutron flux calculations.....	63
3.9 Bulk rock compositions.....	69

Chapter 4: Cosmogenic ^3He production rates in apatite, zircon, and pyroxene inferred from Bonneville flood erosional surfaces

<i>Figure Number</i>	<i>Page</i>
----------------------	-------------

4.1	Map of sample locations.....	73
4.2	Helium data from shielded samples.....	84
4.3	Pyroxene helium data.....	84
4.4	Pyroxene vs. zircon and apatite helium data.....	84
4.5	Predicted fractions of spallation produced ^3He	98
4.6	Predicted analytical uncertainties.....	99

<i>Table Number</i>		<i>Page</i>
4.1	Sample locations and elevations.....	74
4.2	Zircon helium data.....	80
4.3	Apatite helium data.....	81
4.4	Pyroxene helium data.....	81
4.5	Crushing results.....	82
4.6	Li, U, and Th results.....	82
4.7	Mineral compositions.....	82
4.8	Bulk rock compositions.....	83
4.9	Selected parameters from neutron flux calculations.....	87
4.10	Bulk rock composition and nuclear constants.....	88
4.11	Comparison of production rate studies.....	94

Chapter 5: Mass spectrometric ^3He measurement in ^4He -rich phases: techniques and limitations for cosmogenic ^3He dating of zircon, apatite, and titanite

<i>Figure Number</i>		<i>Page</i>
5.1	Sensitivity determined by Air standards and MM spiking.....	106
5.2	Sensitivity as a function of ^4He	107
5.3	Mass scans across ^3He and HD peaks.....	108
5.4	Results from thorianite helium analyses.....	110
5.5	Slopes of time vs. ^3He array as a function of ^4He	111
5.6	Uncertainty as a function of ^3He cps and slope.....	112
5.7	Predicted $^3\text{He}/^4\text{He}$ ratios and associated uncertainties.....	116

<i>Table Number</i>		<i>Page</i>
5.1	Results from thorianite helium analyses.....	110

Chapter 6: Conclusions and future research

<i>Figure Number</i>		<i>Page</i>
6.1	Depth profile of neutron stopping rate.....	123
6.2	Depth profile of ^3He production rate.....	123
6.3	Time evolution of $^3\text{He}_{\text{hbl}}/^{21}\text{Ne}_{\text{qtz}}$ ratio with time.....	123
6.4	Energy spectrum of spallation produced ^3H and ^3He	125
6.5	Retention of ^3H and ^3He as a function of grain radius.....	125

Chapter 1

THE UTILITY OF COSMOGENIC ^3He DATING

1.1 Why Cosmogenic ^3He and ^{21}Ne Are Useful

Cosmogenic dating is a widely used tool for establishing the exposure age or erosion rate of terrestrial surfaces. Cosmogenic dating involves collecting rock samples that have been exposed on the surface of the Earth and measuring the concentration of rare isotopes (e.g. ^3He , ^{10}Be , ^{21}Ne , ^{26}Al , and ^{36}Cl) that are produced when high-energy atmospheric nucleons interact with target nuclei inside the rock. If the production rate of these isotopes is known, their concentration can be used to infer the amount of time the rock has been exposed to cosmic rays, or its “surface exposure age.” Alternatively, because high-energy neutrons penetrate an average of several meters into rock, the surface concentration of a cosmogenic nuclide can also be modeled as a time-integrated erosion rate (Bierman, 1994; Lal, 1991).

The ability to quantify the exposure history of surfaces in the landscape has led to major advancements in a wide range of disciplines. For example, cosmogenic dating of glacial moraine boulders has contributed to a quantitative chronology of terrestrial climate change and largely replaced the relative dating criteria previously used by glaciologists (Brown et al., 1991; IvyOchs et al., 1996; Zreda and Phillips, 1995). Cosmogenic dating of offset and deformed geomorphic surfaces has provided a widely applicable dating method which has greatly improved our understanding of geologic slip rates on faults in a variety of tectonic settings (Bierman et al., 1995; Hetzel et al., 2002; Klinger et al., 2000; Matmon et al., 2005; Siame et al., 1997). Perhaps most importantly, cosmogenic dating has allowed geomorphologists to directly measure rates of physical and chemical weathering for the first time. For example, analysis of cosmogenic nuclides on river sands provides an integrated erosion rate over entire drainage basins, allowing comparison of such rates across a range of climatic and tectonic regimes (Bierman and Steig, 1996; Granger et al., 1996; Kirchner et al., 2001; Schaller et al., 2001). Likewise, it has been

shown that measurement of cosmogenic nuclides in soil profiles can yield rates of soil formation and chemical weathering, addressing some of the longest standing questions in soil geomorphology (Heimsath et al., 1997; 1999; Riebe et al., 2001b).

Although cosmogenic dating has proven to be an invaluable technique, many important questions remain unanswered due to the high costs associated with analyzing ^{10}Be , ^{26}Al , and ^{36}Cl , which often limit the number of samples analyzed in a given study. Thus, the relatively high analytical precision on a given sample is often dwarfed by the geomorphic uncertainties associated with the study site. For example, older glacial moraines typically contain boulders that yield a large spread of exposure ages – some appear younger than the true moraine age due to prior burial whereas other boulders appear older due to prior exposure in other parts of the landscape (Brown et al., 2005; Chevalier et al., 2005a; b). A reliable estimate of the true moraine age is best obtained by dating a large number of boulders and analyzing the statistical distribution of ages (Putkonen and Swanson, 2003). In other cases, the only way to reliably test the relationship between two geomorphic variables- such as hill slope angle and erosion rate is to analyze a large number of samples, from which the random geomorphic variability of the landscape can be filtered (Burke et al., 2009; Carretier et al., 2009; Dixon et al., 2009). Cosmogenic ^3He dating shows great promise for achieving rapid sample throughput because it does not require chemical extraction processes and ^3He is measured on noble gas mass spectrometers which are less expensive to maintain and operate than the accelerator mass spectrometer required for the analysis of ^{10}Be , ^{26}Al , and ^{36}Cl .

In addition to offering the potential for high sample throughput, cosmogenic ^3He occupies a unique niche in the family of cosmogenic isotopes for several reasons. Because it is stable, ^3He is potentially useful for estimating erosion rates on extremely old surfaces, such as those found in various hyper-arid landscapes of Australia, Africa, and Antarctica (Bierman and Caffee, 2002; Bruno et al., 1997b; Cockburn et al., 1999; Schafer et al., 1999). It also provides an ideal nuclide to be paired with ^{10}Be ($T_{1/2} = 1.3 \text{ Ma}$) for burial dating, a technique that uses the ratio of two

isotopes with different decay constants to solve for the length of time that a sample has been shielded from cosmic rays (Balco and Shuster, 2009; Balco et al., 2005a). Cosmogenic ^3He can also be used to determine exposure ages of buried paleo-surfaces and for estimating basin-scale erosion rates from ancient sediments (Balco et al., 2005b; Schaller et al., 2004). Most importantly, ^3He is produced at a high production rate from most common rock forming elements and can be applied to many different mineral phases (Farley et al., 2006; Leya et al., 1998b). A large fraction of cosmogenic ^3He originates as ^3H , which decays to ^3He with a half life of ~ 12.3 years (Andrews and Kay, 1982). This stands in contrast to ^{10}Be , ^{26}Al and ^{36}Cl which are only produced in measurable quantities from parent elements within several AMU of their own mass. Recognizing the potential benefits of cosmogenic ^3He dating in diverse mineral phases, the goal of this thesis is to calibrate the production rate of ^3He in common accessory mineral phases.

1.2 Production of Cosmogenic Isotopes on Earth

On Earth, the production of cosmogenic isotopes is driven primarily by high energy neutrons which are part of the nuclear cascade of atmospheric secondaries (Cocconi, 1947; Cocconi et al., 1950). This cascade is initiated by high energy galactic particles ($\sim 92\%$ protons, $\sim 8\%$ He nuclei) which enter Earth's atmosphere, collide with atoms of N and O and induce a downward-directed shower of secondary particles. Due to their longer stopping range, neutrons dominate the atmospheric cascade at Earth's surface with typical neutron fluxes $\sim 4-7$ times higher than protons (Brunstein, 1964). As nucleons lose energy by electronic slowing and nuclear collisions, the energy spectrum of the nuclear cascade becomes somewhat less energetic at lower depths in the atmosphere (Sato and Niita, 2006). Because Earth's surface occupies only the very lowest parts of the atmosphere, the energy spectrum of the neutron flux changes only slightly as a function of elevation.

Cosmogenic nuclides in rock are produced by the same type of reactions that sustain the nuclear cascade in air. At energies above ~ 50 MeV direct reactions, often described as spallation

reactions, are the most important (Dahanayake et al., 1955; Nir et al., 1966; Yasin, 1964). One type of direct reaction, a knock-on reaction, occurs when a high energy nucleon enters the nucleus of a target element and directly collides with one or more nucleons, directly ejecting them from the nucleus (Friedlander et al., 1981). At energies between ~10-50 MeV indirect reactions such as compound-nucleus and pick-up reactions become more important. In a compound nucleus reaction, the incident nucleon enters a nucleus and disseminates its energy to other nucleons creating an excited “compound nucleus.” De-excitation occurs when one or more nucleons are “evaporated” from the nuclei. Pick-up reactions occur when a passing nucleon strips away one or more nucleons from the nucleus they are passing, often creating deuterium, tritium, or helium (Ahmad et al., 1979; Zatzick and Maxson, 1963). A third type of reaction is neutron capture in which very low energy neutrons (~ 1 keV) are captured and become part of the target nuclei, with their excess binding energy often leading to nuclear instability and subsequent decay of the target nucleus (Andrews and Kay, 1982; Friedlander et al., 1981).

The variety of nuclear reactions described above lead to a critical difference between ^3He and its higher-mass cosmogenic counterparts such as ^{10}Be , ^{21}Ne , ^{26}Al and ^{36}Cl . Whereas larger nuclei are most commonly formed as the residual of some nuclear reaction (i.e. ^{36}Cl produced from ^{39}K), ^3H and ^3He are often formed as the ion that is actually spalled, stripped, or evaporated from the residual nuclei. As a result ^3He is produced from virtually all parent elements and is produced at higher rates via low energy reactions than heavier isotopes (Leya et al., 2004; Leya et al., 2000a). Because of these differences the production rate of ^3He may change in a different manner than larger isotopes as a function of the nucleon energy spectrum at different locations on Earth’s surface (Gayer et al., 2004). Another important difference between ^3He and heavier cosmogenic isotopes is that the small charge of newly produced ^3H or ^3He ions (+1 or +2), allows them to travel longer distances before being slowed and stopped by electronic interactions (Ziegler, 2003).

Traditionally, the production rate of cosmogenic isotopes has been assumed to

scale directly with the flux of high energy neutrons at Earth's surface (Lal and Peters, 1967; Simpson and Uretz, 1953). To the first order, the neutron flux at Earth's surface scales exponentially with elevation with a mean free path of $\sim 140\text{-}160 \text{ g/cm}^2$ (Carmichael et al., 1968; Simpson, 1951). A second order control on production rate comes from the Earth's magnetic field, which deflects charged galactic particles and prevents them from entering the atmosphere. The effect of the Earth's magnetic field is described by the rigidity cutoff, or the minimum energy required for a vertically incident galactic proton to penetrate Earth's magnetic field (Lal and Peters, 1967). Changes in the strength and orientation of Earth's magnetic field have occurred throughout geologic time in response to changes in Earth's dynamo as well as changes in the intensity of the solar wind (Lifton et al., 2005; Lifton et al., 2008; Simpson et al., 1953). These changes are one of the largest sources of uncertainty in extrapolating production rates backwards through time, although it is often argued that variations in the magnetic field average out for time scales $> \sim 20 \text{ ka}$ (Gosse and Phillips, 2001).

Because changes in production rate through time and space are significant and are still the topic of active research, the convention in the cosmogenic isotope community is to state production rates at sea level high-latitude 'SLHL' locations ($>60^\circ$ latitude). Importantly, these sites are not susceptible to the effects of Earth's magnetic field, because the rigidity cutoff is zero. To extrapolate SLHL production rates to sites elsewhere on Earth, scaling models are used that consider changes in elevation, air pressure, and changes in the rigidity cutoff at that site through time. As more calibration studies have been completed in recent years, several authors have suggested that existing scaling models do not accurately predict regional production rates, thereby limiting the accuracy of cosmogenic dating (Balco et al., 2009; Putnam et al., 2010). A detailed review and comparison of five different scaling models has recently been published by Balco et al. (2008).

Despite the inherent uncertainty in scaling models, most production rates have been determined by measuring cosmogenic isotopes in uneroded surfaces of a known age and

extrapolating these rates to sea level high latitude. These field based production rate calibrations are useful because of the huge uncertainties associated with estimating production rates from nuclear properties alone (Masarik and Reedy, 1995). Such “first principles” predictions require knowledge of the excitation functions (the production cross section as a function of incident neutron energy) for a huge range of target elements. Because it is difficult and expensive to generate high energy neutron beams (>50 MeV) in the lab, well documented neutron excitation functions have traditionally been scarce, but are slowly becoming more widely available (Chadwick et al., 2006; Nakagawa et al., 2002). Such data are important, because the shape of the excitation functions for different nuclides (e.g. ^3He and ^{10}Be) can differ significantly. Furthermore, accurate calculations require knowledge of the neutron energy spectrum just below the rock surface at different points on Earth’s surface. Measuring the complete neutron energy distribution at Earth’s surface as a function of elevation has proven difficult (Armstrong et al., 1973; Goldhagen et al., 2002; Hendrick and Edge, 1966; Powell et al., 1959; Yamashita et al., 1966). However, several coupled production-transport numerical codes have been recently developed and employed to predict the nucleon flux and energy spectra throughout Earth’s atmosphere and near Earth’s surface (Lei et al., 2004; Masarik, 2008; Masarik and Beer, 2009; Sato and Niita, 2006; Webber et al., 2007).

1.3 Previous Production Rate Estimates for ^3He and ^{21}Ne

As explained above, most SLHL production rates have been calculated experimentally by measuring cosmogenic isotopes in surfaces of known age. Many previous studies using ^3He have targeted olivine and pyroxene phenocrysts in volcanic rocks, providing a strong foundation for the study of new mineral phases. For example, numerous production rate determinations for olivine and pyroxene have been made on basalt flows of known age, yielding SLHL production rates between ~ 115 and 136 at $\text{g}^{-1} \text{yr}^{-1}$ (Ackert et al., 2003; Blard et al., 2006; Cerling and Craig, 1994; Dunai and Wijbrans, 2000; Kurz et al., 1990; Licciardi et al., 1999; Licciardi et al., 2006).

Because these studies have been performed at a range of elevations and latitudes, their mean production rate is dependent upon the scaling scheme that is used to convert local measurements to SLHL production rates. Although different scaling models give different mean SLHL production rates, the production rate studies for olivine and pyroxene agree to ~7-12% when any particular scaling model is applied to all of them (Balco et al., 2008; Goehring et al., 2010).

Although the He retentivity of many mineral phases is well established (Dunai and Roselieb, 1996; Farley, 2000; Reiners and Farley, 1999; Reiners et al., 2002; Shuster and Farley, 2005), only a handful of previous studies have explored the production rate of cosmogenic ^3He in new mineral phases. Production rates of ^3He in apatite, zircon, titanite and Fe-Ti oxides were determined by cross calibration against cosmogenic ^{21}Ne in Andean tuffs (Farley et al., 2006; Kober et al., 2005). The production rate in garnet was calibrated against ^{10}Be in glacial moraine boulders from the Nepal Himalaya (Gayer et al., 2004). In addition, Kober et al. (2005) provide estimates of element-specific ^3He production rates based on a combination of field calibration and neutron bombardment experiments. These estimates are useful for predicting production rates in minerals that have not been directly calibrated.

1.4 New Problems Addressed in This Thesis

The goal of this thesis is to calibrate the production rate of cosmogenic ^3He in a variety of mineral phases in an effort to broaden the range of suitable target lithologies. Collectively, the three calibration studies presented here (chapters 2-5) highlight the potential benefits and several complications to cosmogenic ^3He dating. The most significant complication discussed in chapters 2-4 is ^3He production via low-energy neutron capture on ^6Li in the reaction: $^6\text{Li}(n,\alpha)^3\text{H} \rightarrow ^3\text{He}$ (Andrews and Kay, 1982; Dunai et al., 2007; Lal, 1987; Mamyrin and Tolstikhin, 1984). The low energy neutrons that drive ^3He production from ^6Li are derived from three primary sources: 1) radiogenic neutrons produced by decay

of U and Th whose alpha particles are involved in (α ,n) reactions on light elements (Andrews and Kay, 1982; Chmiel et al., 2003), 2) low energy cosmogenic neutrons produced by excitation of target nuclei in rock by high-energy atmospheric neutrons (Dunai et al., 2007; Phillips et al., 2001), and 3) muogenic neutrons produced by slowing and stopping of muons by target nuclei in rock (Heisinger et al., 2002a; Heisinger et al., 2002b).

A common theme in the Coso (chapter 3) and Idaho (chapter 4) calibration studies is that large fractions of the measured ^3He can be attributed to Li-produced ^3He due to the high Li contents that are apparently typical of intra-continental rhyolites. Detailed analyses of different grain sizes from both studies confirm that newly created ^3H nuclei experience redistribution into adjacent mineral phases due to their small size and high energy (Farley et al., 2006). Cosmic-ray shielded samples from the Idaho site demonstrate that Li-produced components can be accurately calculated and directly subtracted from exposure samples without greatly increasing the uncertainty. A major conclusion of this thesis is that ^3He dating of accessory phases in continental igneous rocks requires grain size sieving and Li measurements in both exposed and shielded samples.

Another question addressed in this thesis is whether the production rate of ^3He should scale in the same manner as other cosmogenic isotopes. For example, the Nepal calibration study in chapter 2 discusses whether anomalously high production rates can be attributed to a lower threshold energy for production of ^3He relative to heavier isotopes such as ^{10}Be and ^{21}Ne (Gayer et al., 2004). This implies that changes in the energy distribution of the incident neutron flux, either through space, through time, or with depth in rock, could change the ratio of the ^3He production rate relative to other isotopes. This is of particular relevance to the Nepal study because Nepal sits at high elevation near the peak in rigidity cutoff, implying that the neutron flux is slightly more energetic than most other places on Earth. Although such a scenario would present a challenge to existing scaling models, it could also potentially

be exploited as a new form of paleo-altimetry or be used in conjunction with depth profiles to gain more detailed information about erosion rates over time.

Other new problems addressed by this thesis are the analytical challenges associated with precisely measuring small amounts of cosmogenic ^3He in U or Th rich accessory phases. Data drawn from all three calibration studies are synthesized in chapter 5 to explore the effect of high ^4He pressures on the analytical characteristics of the MAP 215-50 noble gas mass spectrometer. Due to a number of factors, samples with $^3\text{He}/^4\text{He}$ ratios less than $\sim 2 \times 10^{-10}$ cannot be measured reliably under typical operating conditions. This implies that ^3He dating in zircon and apatite can be subject to large errors when applied to samples from young surfaces (< 10 ka), surfaces that are very near sea level (< 500 m), rocks with old (U-Th)/He closure ages (> 50 Ma), or some combination thereof.

Chapter 2

ANOMALOUS COSMOGENIC ^3He PRODUCTION AND ELEVATION SCALING IN THE HIGH HIMALAYA

2.1 Introduction

Due to its role in determining ages and erosion rates of surfaces in the landscape, cosmogenic dating has grown rapidly in the last several decades (Bierman, 1994; Gosse and Phillips, 2001; Lal and Peters, 1967). Although cosmogenic dating using ^3He is not as widely applied as that using ^{10}Be or ^{26}Al , ^3He occupies a unique niche in the family of cosmogenic isotopes for several reasons. It has a higher production rate relative to its detection limit than other cosmogenic isotopes, and can thus be used to date very small samples or young surfaces. It is produced by spallation from nearly all target elements, so can potentially be applied to many different mineral phases. Because it is stable, ^3He is potentially useful for estimating erosion rates on extremely old surfaces, for determining exposure ages of paleo-surfaces, and for estimating catchment-scale erosion rates from ancient sediments. In addition, cosmogenic ^3He dating potentially provides a faster and simpler alternative to cosmogenic radionuclide dating because it does not involve intensive preparation chemistry and measurement on an accelerator mass spectrometer.

Most previous studies using ^3He have targeted olivine and pyroxene phenocrysts in volcanic rocks because these phases retain helium under Earth surface conditions and usually have acceptably small non-cosmogenic ^3He concentrations. Numerous production rate determinations for olivine have been made on basalt flows of known age, yielding sea-level high latitude (SLHL) rates between ~ 100 and $150 \text{ at g}^{-1} \text{ yr}^{-1}$ (Ackert et al., 2003; Cerling and Craig, 1994; Dunai and Wijbrans, 2000; Kurz et al., 1990; Licciardi et al., 1999; Licciardi et al., 2006). Recent efforts have explored extending ^3He dating by establishing production rates and the non-cosmogenic background in additional mineral phases found in more diverse lithologies. For example, production rates of ^3He in apatite, zircon, titanite and Fe-Ti oxides were determined by

cross calibration against cosmogenic ^{21}Ne in Andean tuffs (Farley et al., 2006; Kober et al., 2005). Similarly, the production rate in garnet was calibrated against ^{10}Be in glacial moraine boulders from the Nepalese Himalaya (Gayer et al., 2004). In addition, Kober et al. (2005) provide estimates of element-specific ^3He production rates based on a combination of field calibration and neutron bombardment experiments. These estimates are useful for predicting production rates in minerals that have not been directly calibrated. However, due to complicating variables such as Li content, grain size, elevation, and lithology, further calibration studies are needed before robust and widely applicable production rates are established.

Here we calibrate the production rate of spallogenic ^3He in zircon, apatite, kyanite, and garnet against ^{10}Be in quartz in a suite of glacial moraine boulders spanning a range of elevations, exposure ages, and lithologies in the Nepalese Himalaya. Our approach and sampling locality are similar to the study of cosmogenic ^3He in garnet performed by Gayer et al. (2004). Our sample suite also allows us to assess Gayer et al's (2004) observations of anomalous production rates and altitude scaling of cosmogenic ^3He in Himalayan garnets, and a recently proposed explanation that these anomalies arise from nuclear reactions on lithium (Dunai et al., 2007).

Natural samples have multiple sources of ^3He in addition to the sought-after cosmogenic spallation component. With knowledge of the Li concentration of the analyzed phases, the composition of the whole rock, and appropriate models, we can isolate the spallation ^3He from these other components. After correcting for non-spallogenic ^3He , SLHL production rates are estimated by multiplying the corrected $^3\text{He}/^{10}\text{Be}$ ratio by the known SLHL ^{10}Be production rate. This approach eliminates the need to assume negligible surface erosion or burial, but requires that cosmogenic isotope production rates scale identically with elevation and latitude. Unless otherwise stated, ^3He production in this paper refers to both direct production, and production via ^3H , which decays to ^3He with a half life of ~ 12.3 yrs (Lal, 1987).

2.2 Geologic Setting and Samples

The geology of central Nepal can be simplified as three major tectonic packages separated by two major shear zones (Fig. 1). The Main Central Thrust is a diffuse shear zone defining the boundary between the upper amphibolite grade Greater Himalayan Series gneisses to the north, and the meta-sedimentary rocks of the Lesser Himalayan Series to the south (Colchen et al., 1986). The South Tibetan Detachment (STD) is a dominantly normal sense shear zone separating the gneisses below it from the meta-sedimentary rocks of the Tibetan Sedimentary Series above it (Colchen et al., 1986). Intruding the gneisses, but commonly truncated by the STD is the 18-25 My old Manaslu granite (Deniel et al., 1987).

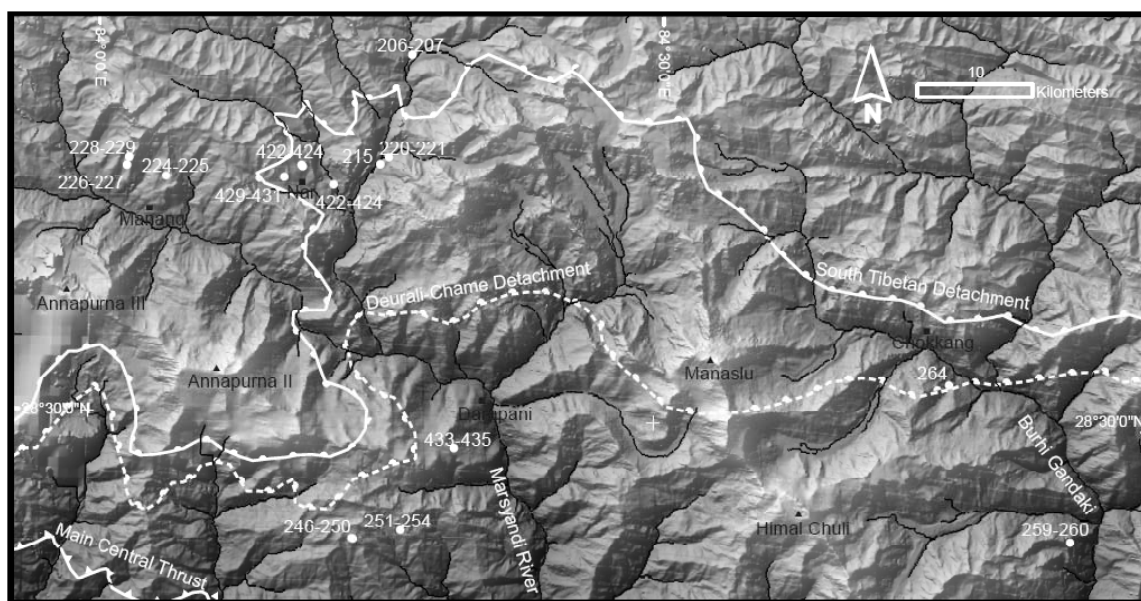


Figure 1.1

Map of field area showing sample sites (white circles), towns (black squares), and major summits (black triangles). Major structural features are shown following (Searle and Godin, 2003), and delineate the Tethyan Sedimentary Series (north of the South Tibetan Detachment), from the Greater Himalayan Series (south of the Deurali-Chame detachment). The shaded relief map is derived from SRTM 90 m data.

Field sampling and ^{10}Be analysis of glacial moraine boulders was performed by Pratt-Sitaula (2004). She sampled three types of glacial moraine boulders: quartzite, gneiss, and granite. Quartzitic moraine boulders were sampled entirely above 4000 m and are thought to be derived

primarily from the Thini-Chu group, which is a Carboniferous aged section of the Tethyan Sedimentary Series (Garzanti et al., 1994b). They contain low but variable concentrations of illite, sericite, and other clay minerals, as well as trace amounts of rutile, pyrite, and zircon. The gneissic moraine boulders were sampled from between 3215 and 3960 meters, and are derived from Formation I of the Greater Himalayan Series (Fig. 1). These gneisses typically contain varying amounts of quartz, K-feldspar, plagioclase (albite to labradorite), muscovite and biotite. The Manaslu granite is a generally medium grained leucocratic granite, which typically contains ~32% quartz, ~37% plagioclase (An 2-21), ~21% K-feldspar, ~7% muscovite, and ~3% biotite (Deniel et al., 1987).

Useable quantities of zircon were recovered only from the quartzitic and gneissic boulders after they were processed for quartz. Zircons from the quartzites are typically well rounded, dark pink in color, and are often frosted, whereas zircons from the gneisses are typically euhedral, translucent, and colorless to pink. There is no systematic variation in grain size between lithologies, with average dimensions of analyzed zircon aliquots ranging from 76-190 μm in length and 52-140 μm in prism cross-section (Table 2.1). Apatites were recovered from all lithologies, ranging in mean grain size from 114-300 μm in length, and 84-225 μm in cross section (Table 2.2). These are assumed to be primarily metamorphic apatites because it is unlikely that such pristine apatite crystals would survive the detrital cycle. Kyanites and garnet occurred only in a subset of the gneisses, and were hand-picked from the 250 < 500 μm size fraction (Table 2.3). Garnets show a narrow compositional range, averaging about 70% almandine, and 18% pyrope (Table 2.4). Although the retentivity of ^3He in kyanite has never been demonstrated, it is a member of the nesosilicate family and is structurally similar to other retentive nesosilicates such as olivine, zircon and garnet.

Table 2.1: Zircon data

		Measured ^3He	Corrected ^3He	^{10}Be (10^5 at/g)	3/10 Ratio	Excess ^3He (Mat/g)	^{10}Be age ^a (Kyr)	Elevation (m)	U/Th-He age (Ma)	^4He (10^{15} at/g)	3/4 Ratio	Li (ppm)	Avg. Length (μm)	Avg. Width (μm)
	n	(Mat/g)	(Mat/g)	(10^5 at/g)		(Mat/g)	(Kyr)	(m)	(Ma)	(10^{15} at/g)		(ppm)	(μm)	(μm)
<i>Granite</i>														
	206	3 49.1	43.7	9.3	47.1	28.7	13.7	4300		4.40	1.1E-08	12.5	275	207
	207	2 48.1	42.7	9.1	46.9	28.1	5.2	4300		3.73	1.3E-08	13.9	282	206
	215	2 26.0	22.8	6.0	37.7	12.7	12.5	3720		3.75	6.9E-09	4.3	291	212
	220	3 24.3	17.9	4.7	38.4	14.1	9.1	3815	8	5.80	4.2E-09	20.3	299	225
	221	3 25.2	16.7	5.0	33.5	14.3	9.7	3815	6	4.58	5.5E-09	33.4	137	90
<i>Gneiss</i>														
	253	2 27.9	27.5	5.8	47.2	15.1	12.2	3631		0.88	3.2E-08	1.5	269	200
	259	5 13.1	12.4	3.6	34.1	5.1	11.8	3215	0.8	0.33	3.9E-08	1.1	116	87
	260	1 13.6	12.9	3.3	39.1	6.4	11.0	3215	1.5	0.33	4.1E-08	1.7	114	84
	264	6 13.6	12.7	3.4	37.0	6.1	16.3	3450	1.5	0.21	6.5E-08	3.7	244	180
<i>Quartzite</i>														
	433	2 17.7	17.5	3.7	46.8	9.5	6.9	4010		0.25	7.1E-08	2.0	262	200
	435	2 17.4	17.2	4.0	42.9	8.6	6.9	4070		0.20	8.6E-08	1.5	263	199

Table 2.2: Apatite data

		Measured ^3He	Corrected ^3He	^{10}Be (10^5 at/g)	3/10 Ratio	Excess ^3He (Mat/g)	^{10}Be age ^a (Kyr)	Elevation (m)	U/Th-He age (Ma)	^4He (10^{15} at/g)	3/4 Ratio	Li (ppm)	Avg. Length (μm)	Avg. Width (μm)
	n	(Mat/g)	(Mat/g)	(10^5 at/g)		(Mat/g)	(Kyr)	(m)	(Ma)	(10^{15} at/g)		(ppm)	(μm)	(μm)
<i>Quartzite</i>														
	222	1 40.7	39.9	10.1	39.3	23.4	11.7	4614	11.5	11.5	3.1E-09	1.10	115	78
	224	2 45.5	44.7	11.0	40.6	26.7	12.3	4660	13.1	11.1	3.6E-09	0.98	129	90
	226	2 18.6	17.6	5.2	33.6	9.7	6.9	4500	17	3.1	5.0E-09	3.70	95	52
	227	1 23.9	22.9	6.1	37.5	13.5	8	4500	16.5	14.1	1.5E-09	1.60	99	64
	228	2 22.4	21.5	5.9	36.6	12.4	6.8	4744	14.9	21.1	1.1E-09	3.80	105	68
	229	2 23.9	22.7	5.4	41.9	14.7	6.4	4744	20.5	10.5	1.9E-09	3.50	76	52
	420	2 25.2	24.0	6.1	39.4	14.8	6.6	4821	19.6	13.6	1.9E-09	7.80	118	74
	423	1 27.6	26.6	5.5	48.1	18.2	6.5	4700	14.6	10.5	2.6E-09	5.40	127	78
	424	1 24.6	23.8	5.2	45.8	15.7	6.1	4700	9	14.8	1.5E-09	5.10	114	74
	429	1 48.5	46.8	13.1	35.6	26.1	15.1	4600	12.7	2.4	2.0E-08	7.10	122	77
	431	2 38.1	35.7	9.4	37.9	22.0	11.2	4580	41.3	17.1	2.0E-09	8.90	190	139
	434	2 20.8	20.2	3.8	53.2	14.3	6.6	4057		29.1	1.6E-09	3.40	186	100
<i>Gneiss</i>														
	246	5 22.8	22.4	6.6	34.0	11.6	11.8	3960	1.5	2.2	8.6E-09	0.20	136	86
	251	2 19.7	19.0	6.0	31.4	9.4	12.8	3610	1.5	3.8	7.4E-09	0.22	168	101
	259	10 10.8	10.0	3.6	27.5	4.6	11.8	3215	2	2.0	5.0E-09	0.28	133	76

Table 2.3: Kyanite and garnet data

		Measured ^3He	Corrected ^3He	^{10}Be	3/10	^{10}Be age ^a	Elevation	^4He	3/4	Li	Width	Length
	n	(Mat/g)	(Mat/g)	(10^5 at/g)	Ratio	(Kyr)	(m)	(10^{12} a/g)	Ratio	(ppm)	(μm)	(μm)
<i>Kyanite</i>												
246	2	22.7	NA	6.6	34.4	11.8	3960	87	2.6E-07	0.175	>500	>1000
249	2	22.3	NA	6.2	36.1	11.4	3910	79	2.8E-07	0.085	>500	>1000
251	2	20.4	NA	6.3	32.6	12.8	3610	114	1.8E-07	0.065	>500	>1000
252	1	23.6	NA	6.0	39.1	13	3625	122	1.9E-07	0.030	>500	>1000
253	2	22.6	NA	5.7	39.9	12.5	3652	166	1.4E-07	0.096	>500	>1000
254	2	19.4	NA	5.9	32.7	12.4	3640	87	2.2E-07	0.025	>500	>1000
<i>Garnet</i>												
247	2	25.1	19.7	6.7	29.5	12	3960	36	6.9E-07	61.6	>300 ^b	>300 ^b
249	2	24.4	21.6	6.2	35.0	11.4	3910	11	2.3E-06	31.3	>300 ^b	>300 ^b
250	2	19.6	16.2	6.3	25.6	11.7	3910	31	6.4E-07	37.9	>300 ^b	>300 ^b
251	4	20.5	18.3	6.0	30.3	12.8	3610	31	6.7E-07	25.2	>300 ^b	>300 ^b
253	2	21.7	19.5	5.8	33.4	12.5	3630	80	2.7E-07	27.6	>300 ^b	>300 ^b

Table 2.4: Garnet compositional data

Sample #	Al_2O_3	FeO	MgO	CaO	SiO_2	MnO	Totals
247	21.36	29.80	1.93	4.68	37.53	6.55	101.86
249	21.16	32.42	2.70	0.48	36.89	7.71	101.38
250	21.66	27.58	6.70	0.44	38.09	6.60	101.07
251	22.12	30.09	8.93	0.74	38.81	0.49	101.17
253	21.80	28.37	8.55	0.79	38.28	3.34	101.13

Beryllium concentrations in quartz range from 0.32 to 1.3 Mat/g, interpreted as moraine ages from 5.2 to 16.3 ky (Pratt-Sitaula, 2004). The wide range of ^{10}Be concentrations, moraine ages, and elevations makes this an ideal sample suite with which to assess factors controlling the cosmogenic ^3He production rate. Interestingly, some moraines from similar elevations in nearly adjacent valleys yielded very different ^{10}Be ages, allowing separation of age from elevation effects. Our approach for calibration of ^3He production rates assumes that these ^{10}Be concentrations are accurate, purely cosmogenic in origin, and that the proportion of muogenic production is the same for both isotopes. We have no independent way to assess the validity of the ^{10}Be ages other than to note that they can be rationalized (Pratt-Sitaula, 2004) and other studies in central Nepal and elsewhere in the Himalaya report moraine boulders with comparable ages (Gayer et al., 2006; Owen et al., 2005).

2.3 Methods

Apatite and zircon were extracted from the <250 μm sieve fraction produced during original preparation for ^{10}Be analysis (Pratt-Sitaula, 2004). Standard heavy liquid and magnetic separation procedures were used, followed by negative picking of contaminant mineral phases. Zircon separates were purified by dissolution of remaining phases in a room temperature solution of 2:1 HF to HNO_3 . Purity of apatite was verified by recovery of the sample following helium extraction, and dissolution in 10% HNO_3 . After dissolution only quartz remained, and never exceeded 1% of the analyzed mass. Typically, 3-30 mg of apatite or zircon was analyzed to generate a measurable amount of ^3He (usually 10^{-4} to 10^{-3} fmol), which typically corresponded to ~ 4 to 250 pmol of ^4He . Samples were degassed using either a Nd-YAG laser (House et al., 2000) or a double-walled resistance furnace, purified by diffusion through a liquid nitrogen-chilled charcoal trap and hot and cold SAES getters, then cryogenically focused and analyzed on a MAP 215-50 noble gas mass spectrometer.

The most challenging aspect of measuring cosmogenic ^3He in zircon and apatite is the measurement of small amounts of ^3He in the presence of large quantities of radiogenic ^4He . Issues such as variable ionization efficiency, pressure broadening of the ^4He and HD peaks, and scrubbing of ^3He off the walls of the vacuum line and mass spectrometer are all potential concerns. Although the mass spectrometer is continually calibrated using external gas standards, in-run sensitivity is determined using a “spike” of ^3He gas introduced mid-way through each sample analysis. To test for tailing and other effects of high helium pressure, we did experiments using a virtually pure ^4He gas derived from a sample of cosmic-ray shielded thorianite. A full description of these experiments and the analytical technique can be found in chapter 6.

Lithium measurements were made on a Thermo-Finnegan Element 1 single-collector ICPMS, using isotope dilution with a ^6Li spike calibrated with a commercial Li normal solution.

Measurements were made on ~1 mg of handpicked zircon or apatite, but not the same aliquots used for ^3He analysis. Apatites were directly dissolved in nitric acid, whereas zircons, kyanites, and garnets were dissolved first in HF in a Parr bomb at 220° C, then dried down and redissolved in 6N HCl at 180°, then dried down again before final dissolution in concentrated HNO_3 . Reproducibility of Li measurements was established by performing at least two replicate measurements on all samples. External precision was determined by analyzing replicates of ~15 Durango apatite samples (Young et al., 1969), which were found to have a mean Li concentration of 1.31 +/- 0.15 ppm. Lithium blanks typically totaled less than 0.1% of measured lithium, with a maximum of ~5%.

A critical aspect of this method is ensuring that Li contamination from heavy liquids can be removed from the samples prior to analysis. This was verified by taking samples of Durango apatite which had never been exposed to heavy liquids, and immersing them for 30 minutes in either lithium metatungstate, methylene iodide, or acetylene tetrabromide. The samples were subsequently washed with acetone, then washed in distilled water in an ultrasonic bath for three 15 minute cycles with the water decanted and refilled between each cycle. Samples of Durango apatite exposed to heavy liquids were found to yield Li concentrations within error of the unimmersed samples. We used this cleaning procedure prior to all Li measurements.

Knowledge of the (U-Th)/He age of the phases we are working with is useful for assessing the duration over which nucleogenic ingrowth has occurred (Farley et al., 2006). Therefore (U-Th)/He ages were measured on hand-picked, inclusion free single apatite and zircon crystals following the method of House et al. (House et al., 2000). Most of the quartzites have zircon helium ages from ~13-20 Ma, whereas zircons from the gneisses have ages from 1.5 to 2 Ma (Table 2.1). Apatite (U-Th)/He ages range from 6 to 8 Ma in the granitic samples, and from 0.8 to 1.5 Ma in the gneisses (Table 2.2). The correlation of age with lithology arises from the fact that lithology varies with structural position and elevation.

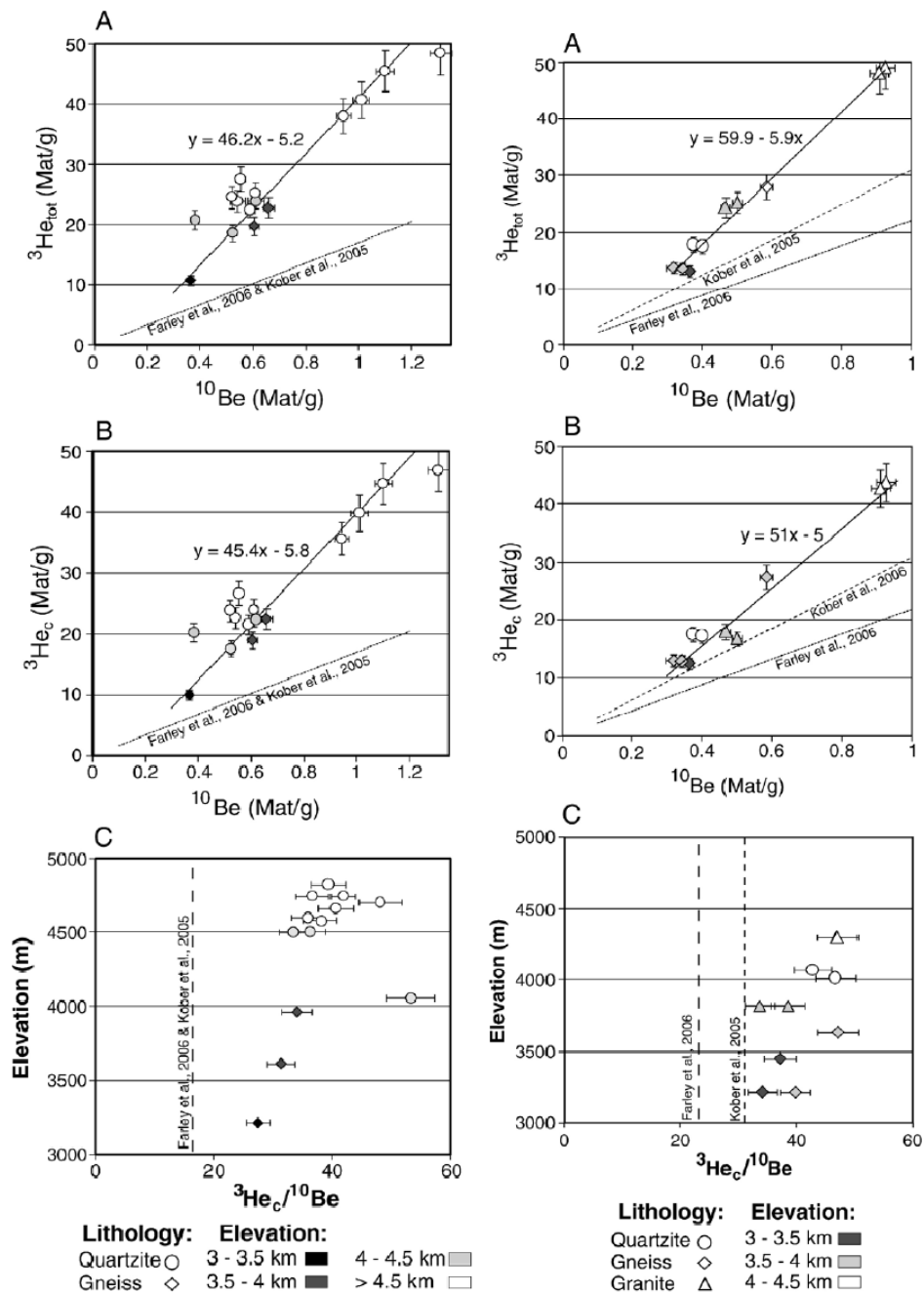
2.4 Results

2.4.1 ^3He Concentrations

Helium concentrations are summarized in Tables 2.1-2.3 and Figures 2.2-2.4.

Concentrations of ^3He measured in apatite and zircon range from ~ 10 to 50 Mat/g, whereas ^3He concentrations in kyanite and garnet range from ~ 19 to 25 Mat/g. ^4He concentrations range from $2-40 \times 10^{15}$ atoms/g in zircon, $0.2-6 \times 10^{15}$ in apatite, and $11-166 \times 10^{12}$ in kyanite and garnet. These values yield $^3\text{He}/^4\text{He}$ ratios ranging from $0.8-2 \times 10^{-8}$ in zircon, $0.7-1 \times 10^{-8}$ in apatite, and $0.69-2.5 \times 10^{-6}$ in kyanite and garnet. The external precision of the measurements was determined by replicate analyses of 10 different aliquots of zircon from sample 259 (Table 2.1), as well as 10 replicate analyses of a gas standard which gave a ^3He signal comparable to a typical sample (2-3 counts per second). The standard deviation was $\sim 8\%$ in both cases, a value that we take as the uncertainty on a single analysis. The standard error of the sample mean for each sample is then determined by dividing this uncertainty by the square root of the number of replicate analyses for that sample. Full process blanks were measured before most analyses, resulting in blank corrections from 1 to 5%.

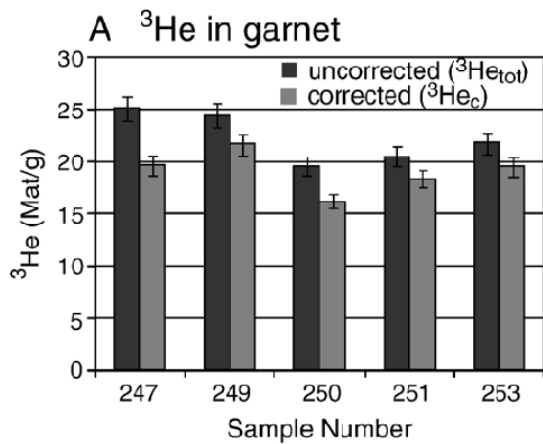
As shown in Figures 2.2a and 2.3a, ^3He concentrations in the apatites and zircons are strongly correlated with ^{10}Be , providing unequivocal evidence that at least a large fraction of the ^3He in these samples is cosmogenic in origin. There is insufficient variability in the ^{10}Be measurements to make the same statement for the garnet and kyanite samples, but $^3\text{He}/^4\text{He}$ ratios near or in excess of the atmospheric ratio leave little doubt that cosmogenic He is present in these minerals as well.

**Figure 2.2**

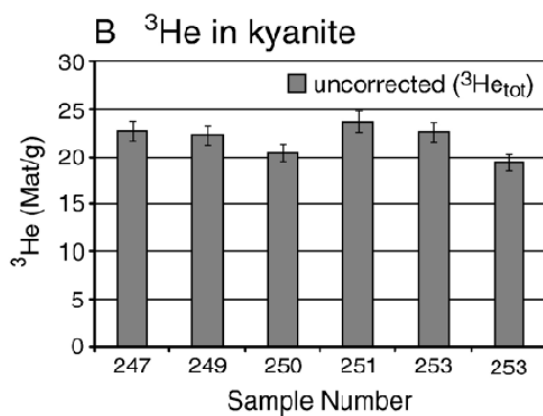
A) Plot of total ${}^3\text{He}$ in zircon against measured ${}^{10}\text{Be}$ in quartz, with the best-fit line through the data, and the relationship predicted by (Farley et al., 2006; Kober et al., 2005) (dotted line). B) Plot of spallation ${}^3\text{He}$ in zircon obtained by subtraction of the estimated amount of ${}^3\text{He}$ produced by thermal neutron capture by ${}^6\text{Li}$ (i.e. the ${}^3\text{He}_{cn}$ and ${}^3\text{He}_{nuc}$ components). The slope of 45.4 coupled with the known ${}^{10}\text{Be}$ production rate gives an apparent SLHL ${}^3\text{He}$ production rate of 226 at/g*yr in zircon. C) Corrected ${}^3\text{He}/{}^{10}\text{Be}$ ratios for zircon plotted against elevation, showing an increase with elevation.

Figure 2.3

A) Plot of uncorrected ${}^3\text{He}$ in apatite against measured ${}^{10}\text{Be}$ in quartz, with the best-fit line through the data, and the relationships predicted by (Farley et al., 2006; Kober et al., 2005) (dotted lines). B) Plot of spallation ${}^3\text{He}$ in apatite obtained by subtraction of the estimated amount of ${}^3\text{He}$ produced by thermal neutron capture by ${}^6\text{Li}$ (i.e. the ${}^3\text{He}_{cn}$ and ${}^3\text{He}_{nuc}$ components). The slope of 51 gives an apparent SLHL production rate of 254 at/g*yr in apatite. C) A plot of the corrected ${}^3\text{He}/{}^{10}\text{Be}$ ratios for apatite against elevation, showing an increase with elevation.

**Figure 2.4**

A) Bar graph showing ^3He concentration before and after subtraction of the estimated amount of ^6Li produced ^3He in garnet with 1-sigma error bars. B) Bar graph showing measured ^3He concentrations in kyanite with 1-sigma error bars. No correction was made to kyanite, because of its large grain size and extremely low Li content.



2.4.2 Lithium Contents

Li contents in zircon and apatite correlate strongly with host lithology. Zircons from the gneisses have Li contents of 0.17-0.30 ppm, whereas zircons from the quartzites range from ~1.6-9 ppm. The reason for this difference is unknown. Apatites from the gneisses have ~0.8-4 ppm of Li, whereas apatites from the Manaslu granite range from 4-33 ppm. In general, these are extremely high Li contents for apatite, based on analyses of unrelated apatite samples from 8 other locations, which showed concentrations of 0.5 to 1.5 ppm (Amidon and Farley, unpublished data). In contrast, kyanites have extremely low Li concentrations, ranging from 0.03 to 0.18 ppm. Lithium concentrations in garnet range from ~25 to 62 ppm.

2.5 Discussion

2.5.1 Sources of ^3He in Minerals

As shown in equation (1), the ^3He we measured ($^3\text{He}_{tot}$) is derived from several different sources:

$$^3\text{He}_{tot} = ^3\text{He}_c + ^3\text{He}_{cn} + ^3\text{He}_{nuc} + ^3\text{He}_{in} \quad (2.1)$$

We are interested in determining the production rate of spallogenic ^3He ($^3\text{He}_c$), which also includes a small component of direct muogenic production. Production can also occur via capture of cosmogenically derived low-energy neutrons ($^3\text{He}_{cn}$), which includes thermalized atmospheric neutrons, evaporation neutrons, and neutrons produced by stopping of slow and fast muons (Dunai et al., 2007). A third term is nucleogenic ($^3\text{He}_{nuc}$) production, which refers to ^3He produced by capture of radiogenic neutrons and by ^{238}U fission. Finally, some minerals may contain inherited ^3He ($^3\text{He}_{in}$) in inclusions or from prior exposure. In this section, we will estimate $^3\text{He}_{cn}$, $^3\text{He}_{nuc}$, and $^3\text{He}_{in}$ and subtract them from the measured $^3\text{He}_{tot}$ to determine $^3\text{He}_c$ in our samples.

The $^3\text{He}_{cn}$ component is derived from capture of cosmogenically derived low-energy (<1 KeV) neutrons (CNs): $^6\text{Li}(n,\alpha)^3\text{H} \rightarrow ^3\text{He}$ (Lal, 1987; Mamyrin and Tolstikhin, 1984).

Estimating the $^3\text{He}_{cn}$ component requires the Li content in the mineral, and the CN stopping rate in the rock. To calculate the CN stopping rate, we used the equations of Phillips et al. (Phillips et al., 2001). Both the absolute CN stopping rate and its profile with depth in rock depend heavily on the composition of the rock, particularly on highly neutron-absorbing elements such as B, Li, Cl, Mn, Sr, Cd, and rare Earth elements. Hydrogen is also important because it is a good neutron moderator (Friedlander et al., 1981; Phillips et al., 2001). The neutron flux near the rock surface is particularly sensitive to composition because neutrons diffuse out of the rock surface into the air, creating a peak in flux at about 50 g/cm² below the surface, as discussed in section 2.7.

Typical neutron fluxes and other calculated parameters for rocks in this study are included in Table 2.5.

Table 2.5: Selected outputs from neutron flux calculations

	Quartzite	Gneiss	Granite
RTN flux (n/g*yr*ppm U)	0.76	1.27	1.51
RTN flux (n/g*yr*ppm Th)	0.17	0.39	0.51
CTN flux (n/g*yr)*	8884	5278	5303
FMTN flux (n/g*yr)*	3.37	3.77	3.76
SMTN flux (n/g*yr)*	24.6	38.6	38.5
Direct muon produced ³ He (3He/g*yr)*	28.6	28.6	28.6
3He P.R. from CTNs (³ He/g*yr*ppm Li) **	30	29.9	53.7
3He P.R. from CTNs (³ He/g*yr*ppm Li)***	49.1	53	99.8
3He P.R. from RTNs (³ He/g*yr*ppm Li) **	0.015	0.071	0.335
3He P.R. from RTNs (³ He/g*yr*ppm Li)***	0.0094	0.04	0.18
ppm Li in bulk rock	11	20	40
Fractional XS of Li	0.012	0.022	0.042
Resonance escape probability	0.81	0.91	0.9
Effective resonance integral (cm ² /g)	0.0063	0.005	0.0052
Macroscopic scattering XS (cm ² /g)	0.116	0.136	0.135
Macroscopic absorption XS (cm ² /g)	0.0055	0.0057	0.0059

RTN=radiogenic thermal neutrons, CTN=cosmogenic produced thermal neutrons

FMTN=fast muon produced thermal neutrons, SMTN=slow muon produced thermal neutrons

* Average in upper 4 cm of rock at 4000 m for a 10 Ky exposure age

** Average in upper 4 cm at 4000 m for a 10 Ky exposure age and 200 um grain diameter

*** Average in upper 4 cm at 4000 m for a 10 Ky exposure age and 100 um grain diameter

Table 2.6: Selected outputs from neutron flux calculations

15

	Gneiss (ppm)	Granite (ppm)	Quartzite (ppm)	Atomic Mass (g/mol)	Avg. Log. Energy Loss per Collision	Scattering Cross Section (cm ² /at)	Absorption Cross Section (cm ² /at)	Resonance Integral (cm ² /at)	Neutron Yield per ppm U (n g ⁻¹ yr ⁻¹ ppm ⁻¹)	Neutron Yield per ppm Th (n g ⁻¹ yr ⁻¹ ppm ⁻¹)
H	700	1000	1109	1.00	1.0000	2.05E-23	3.30E-25	0.00E+00	0	0
Li	20	40	10	6.94	0.2623	9.50E-25	7.10E-23	0.00E+00	23.8	10.4
Be	3	3	0.97	9.01	0.2063	6.15E-24	7.60E-27	4.00E-27	265	91.2
B	30	30	34	10.80	0.1742	4.27E-24	7.67E-22	1.72E-21	62.4	19.7
C	191	191	491	12.00	0.1578	4.74E-24	3.40E-27	1.60E-27	0.453	0.177
N	59	59	0	14.00	0.1363	1.00E-23	1.90E-24	6.35E-24	0	0
O	511616	515048	520431	16.00	0.1199	3.76E-24	2.00E-28	4.00E-28	0.235	0.0831
F	440	1000	183	19.00	0.1017	3.64E-24	9.60E-27	2.10E-26	0	0
Na	13471	23825	452	23.00	0.0845	3.03E-24	5.30E-25	3.11E-25	12.5	5.89
Mg	9647	783	494	24.30	0.0801	3.42E-24	6.30E-26	3.80E-26	5.81	2.54
Al	44841	78617	18635	27.00	0.0723	1.41E-24	2.30E-25	1.70E-25	5.09	2.55
Si	386573	343886	422481	28.10	0.0695	2.01E-24	1.70E-25	1.27E-25	0.684	0.335
P	480	523	960	31.00	0.0632	5.00E-24	2.00E-25	0.00E+00	0.86	0.572
S	140	140	860	32.06	0.0611	9.79E-25	5.20E-25	7.00E-23	0.174	0.103
Cl	40	40	42	35.50	0.0553	1.58E-23	3.35E-23	1.37E-23	1.31	0.793
K	7369	24746	5395	39.10	0.0503	2.04E-24	2.15E-24	1.00E-24	0.116	0.0798
Ca	3645	4002	2144	40.10	0.0491	2.53E-24	4.30E-25	2.35E-25	0.0379	0.0262
Ti	2877	599	1558	47.90	0.0412	4.09E-24	6.10E-24	3.10E-24	0	0
V	18	18	33	50.94	0.0388	4.80E-24	5.08E-24	2.80E-24	0	0
Cr	20	20	20	52.00	0.0380	3.38E-24	3.07E-24	1.60E-24	0	0
Mn	155	07.3	154	54.90	0.0360	2.20E-24	1.33E-23	1.40E-23	0	0
Fe	15452	6696	23618	55.80	0.0354	1.14E-23	2.56E-24	1.39E-24	0.184	0.203
Co	2.3	2.3	6.4	58.93	0.0336	6.00E-24	3.70E-23	5.50E-23	0	0
Ni	0	0	16.6	58.71	0.0337	1.78E-23	4.49E-24	1.76E-24	0	0
Cu	12	12	19	63.55	0.0311	7.78E-24	3.78E-24	4.10E-24	0	0
Zn	45	45	20	65.37	0.0303	4.08E-24	1.11E-24	2.81E-24	0	0
Rb	63	123	29	85.47	0.0232	6.40E-24	3.80E-25	4.64E-24	0	0
Sr	54	78	58	87.62	0.0227	1.00E-23	1.28E-24	1.10E-23	0	0
Y	14.23	13.33	21.5	88.91	0.0223	7.67E-24	1.28E-24	1.00E-24	0	0
Zr	139	200	214	91.22	0.0218	6.40E-24	1.85E-25	9.50E-25	0	0
La	25.27	13.37	21	138.90	0.0143	1.01E-23	8.97E-24	1.21E-23	0	0
Pr	17	17	5.4	140.90	0.0141	2.54E-24	1.15E-23	1.74E-23	0	0
Nd	21.81	9.16	21	144.24	0.0138	1.60E-23	5.05E-23	4.50E-23	0	0
Sm	4.73	2.88	4.7	150.40	0.0132	3.80E-23	5.82E-21	1.40E-21	0	0
Gd	3.68	2.77	4.5	157.30	0.0127	1.72E-22	4.90E-20	3.90E-22	0	0
Dy	2.61	2.46	4.1	162.50	0.0123	1.06E-22	9.40E-22	1.48E-21	0	0
Er	1.03	0.92	2	167.26	0.0119	9.00E-24	1.59E-22	7.30E-22	0	0
Yb	0.73	0.82	1.92	173.04	0.0115	2.34E-23	3.55E-23	1.55E-22	0	0
Lu	0.08	0.13	0.3	174.97	0.0114	6.80E-24	7.64E-23	6.22E-22	0	0
Hf	5.7	5.7	6.6	178.49	0.0112	1.03E-23	1.04E-22	1.99E-21	0	0
Ta	1.4	1.4	0.42	180.95	0.0110	6.12E-24	2.05E-23	6.60E-22	0	0
W	0.43	0.43	1.16	183.85	0.0108	4.77E-24	1.84E-23	3.52E-22	0	0
Pb	46	46	7.6	207.19	0.0096	1.13E-23	1.71E-25	1.38E-25	0	0
Th	10.02	5	7	232.04	0.0086	1.30E-23	7.37E-24	8.50E-23	0	0
U	2.5	10	2.1	238.03	0.0084	9.38E-24	2.68E-24	2.77E-22	0	0

We used the composition of the IGGE sandstone GSR-4 (Potts et al., 1992) as the bulk rock composition of quartzite, and used published compositions measured from nearby locations in the Himalaya for granite and gneiss (Barbey et al., 1996; Brouand et al., 1990; Colchen et al., 1986; Guillot and Le Fort, 1995; Le Fort, 1981). Bulk compositions used in our calculations are given in table 2.6. Li contents of 11 ppm for quartzite (measured in quartz), 20 ppm for gneiss

(Brouand et al., 1990), and 60 ppm for granite (Barbey et al., 1996) were adopted. The concentration of Li in the mineral of interest was measured (Tables 2.1-2.3). To calculate ${}^3\text{He}_{cn}$ we convert the total neutron stopping rate (R_{cn}) into a neutron stopping rate on Li (Andrews and Kay, 1982) by multiplying by the fractional absorption cross section of Li in the rock (F_{σ}). This quantity is then multiplied by the ratio of the Li concentration in the mineral to that in the bulk rock to yield the production rate from Li in the mineral (P_{cn}).

$$P_{cn} = R_{cn} * F_{\sigma} * \left(\frac{C_{min}}{C_{rock}} \right) \quad (2.2)$$

After an identical calculation is made to determine the production rate in the whole rock, the effect of implantation and export of ${}^3\text{H}$ produced in-situ and in the neighboring minerals is considered. This is done by calculating the apparent production rate in the mineral, following Farley et al. (2006):

$$P_a = P_i \left[1 - 0.75 \left(\frac{S}{R} \right) + 0.0625 \left(\frac{S}{R} \right)^3 \right] + P_h \left[0.75 \left(\frac{S}{R} \right) - 0.0625 \left(\frac{S}{R} \right)^3 \right] \quad (2.3)$$

This equation assumes a spherical geometry to calculate the apparent production rate of nucleogenic ${}^3\text{He}$ in the crystal (P_a), by considering the in-situ production rate in the crystal of interest (P_i), the in-situ production rate in the adjacent neighbors (P_h), the stopping distance of the particle (S), and the radius of the crystal (R) (Dunai and Wijbrans, 2000; Farley et al., 2006). The stopping distance of tritium emitted by ${}^6\text{Li}$ is ~ 30 μm in common minerals (Farley et al., 2006; Ziegler, 2003). We assume that the neighbors have, on average, the Li concentration of the whole rock. The apparent ${}^3\text{He}$ production rate (P_a) is then multiplied by the exposure age of the surface (from ${}^{10}\text{Be}$) to determine ${}^3\text{He}_{cn}$.

Calculating the nucleogenic ${}^3\text{He}$ production (${}^3\text{He}_{nuc}$) follows an identical process, except that estimates of the radiogenic neutron (RN) flux and the (U-Th)/He closure age are used (Farley et al., 2006). Radiogenic neutrons come primarily from (α, n) reactions on light elements such as Al and Mg. The RN flux was calculated following (Andrews and Kay, 1982; Chmiel et al., 2003) and is likely an overestimate due to the assumption of compositional homogeneity, when in

reality, much of the α flux from U and Th rich minerals is stopped before it enters minerals rich in light elements (Farley et al., 2006). Based on published values (Barbey et al., 1996; Brouand et al., 1990; Potts et al., 1992), U contents of 2.1, 2.5, and 10 ppm were used for the quartzites, gneisses and granites respectively, and Th contents of 7, 10, and 5 ppm respectively.

Nucleogenic ^3He can also be produced by ternary fission of ^{238}U , but this is negligible (Farley et al., 2006).

We assume that the inherited ^3He component ($^3\text{He}_m$) is negligible for several reasons. First, inheritance from “recent” prior exposure (e.g. reworked moraine material) is unlikely, and should be irrelevant due to the long half life of ^{10}Be relative to the rapid rate of landscape change in the High Himalaya (Burbank et al., 2003). Inheritance from “ancient” prior exposure (e.g. prior to deposition of the now meta-sedimentary rock) is unlikely because apatite, kyanite and garnet are not detrital in origin, and the gneisses and quartzites have been heated to temperatures sufficient for complete diffusive loss of helium from zircon. Peak metamorphic temperatures of 340-400° C for the quartzites are well known from a combination of index minerals, illite crystallinity, and vitrinite reflectance, as well as from carbonate-solvus thermometry (Garzanti et al., 1994a; Schneider and Masch, 1993). Complete diffusive helium loss is also confirmed by the young (U-Th)/He ages of zircons in this study, relative to their Paleozoic and Proterozoic U-Pb ages (Gehrels et al., 2003). Excess ^3He in fluid inclusions is unlikely because the minerals used in this study are not rich in fluid inclusions and are not derived from a mantle source rich in ^3He .

2.5.2 Calculating Cosmogenic ^3He Production Rates

Results of the above calculations are summarized in figure 2.5. We estimate that CN production from ^6Li ranges from 0.15 to 2.4 Mat/g of ^3He in apatite, 0.23 to 1.2 Mat/g in zircon, 0.75 to 4.6 Mat/g in garnet, and 0.13 to 0.16 Mat/g in kyanite. Likewise, we estimate that ^3He production from RNs ranges between 0.03 and 6.1 Mat/g in apatite, 0.12 to 1.5 Mat/g in zircon,

0.35 to 0.80 Mat/g in garnet, and ~ 0.026 Mat/g in kyanite. ${}^3\text{He}_{\text{cn}}$ and ${}^3\text{He}_{\text{nuc}}$ combined typically represent only about 2 to 7% of total ${}^3\text{He}$ in zircon, 1 to 25% in apatite, 10 to 21% in garnet, and $\sim 0.6\%$ in kyanite (Fig. 5). Production of ${}^3\text{He}$ from muon derived neutrons was calculated following (Heisinger et al., 2002b; Lal, 1987) and found to be negligible.

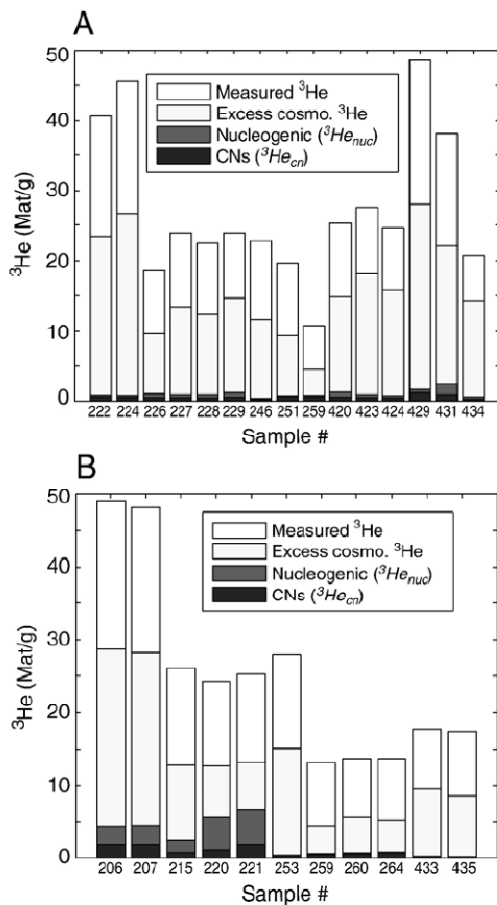


Figure 2.5

Bar graph showing the estimated concentrations of ${}^3\text{He}$ in zircon (A) and apatite (B) from capture of low-energy cosmogenic neutrons (${}^3\text{He}_{\text{cn}}$) and radiogenic neutrons (${}^3\text{He}_{\text{nuc}}$) overlain on the excess cosmogenic ${}^3\text{He}$ (relative to Farley et al. 2006) and the total observed ${}^3\text{He}$. Note that the measured ${}^3\text{He}$, excess cosmogenic ${}^3\text{He}$, and ${}^3\text{He}_{\text{cn}}$ bars are plotted from zero, whereas the ${}^3\text{He}_{\text{nuc}}$ bar is stacked on top of the ${}^3\text{He}_{\text{cn}}$ bar because they are both produced from Li. Detailed discussion of these calculations can be found in section 5.1.

As an initial attempt to calculate the production rate of cosmogenic ${}^3\text{He}$, we subtracted the ${}^3\text{He}_{\text{cn}}$ and ${}^3\text{He}_{\text{nuc}}$ components from the measured ${}^3\text{He}_{\text{tot}}$, and then performed an error-weighted total least-squares regression of ${}^{10}\text{Be}$ vs. ${}^3\text{He}_{\text{c}}$, taking the slope of the resulting line as the average ${}^3\text{He}_{\text{c}}/{}^{10}\text{Be}$ ratio for all samples (Figures 2.2 and 2.3). This ratio is then multiplied by a time-averaged ${}^{10}\text{Be}$ SLHL production rate of 4.98 ± 0.34 at $\text{g}^{-1} \text{yr}^{-1}$ (Balco et al., 2008) to get the SLHL ${}^3\text{He}_{\text{c}}$ production rate. Importantly, this implicitly assumes that ${}^3\text{He}_{\text{c}}$ and ${}^{10}\text{Be}$ are produced by spallation in a constant ratio through time and over a range of elevations, as in most scaling models (Lal, 1991; Pigati and Lifton, 2004). As we discuss below, this assumption is not met, so

these initial production rate estimates must be treated with skepticism. The 2-sigma errors on the $^3\text{He}_c$ production rates reported below are taken only from the error on the slope of the linear fit, propagated in quadrature with the uncertainty on the SLHL ^{10}Be production rate. As discussed by Farley et al. (2006) long stopping distances can lead to net import of spallation ^3He into phases with small grain sizes. Following that work, the approach used here leads to “apparent” production rates (i.e., including both in-situ produced and net injected ^3He).

A linear fit to the zircon data (Fig. 2b) yields a slope of $\sim 45.4 \pm 7.8$ with an intercept of -5.8 ± 4.1 corresponding to a SLHL ^3He production rate of $\sim 226 \pm 39$ at $\text{g}^{-1} \text{yr}^{-1}$. This production rate is ~ 3 times higher than the 76 at $\text{g}^{-1} \text{yr}^{-1}$ estimate of Farley et al. (2006), and ~ 2 times higher than the 112 at $\text{g}^{-1} \text{yr}^{-1}$ predicted by the element specific production rates of Kober et al. (2005). For apatite (Fig. 3b), the corrected data give a slope of ~ 51.0 and an intercept of -5.0 ± 5.2 , which corresponds to a SLHL $^3\text{He}_c$ production rate of $\sim 254 \pm 60$ at $\text{g}^{-1} \text{yr}^{-1}$ (Fig 3c). This production rate is ~ 2.3 times higher than the 112 at $\text{g}^{-1} \text{yr}^{-1}$ observed by Farley et al. (2006), and ~ 1.7 times higher than the 148 at $\text{g}^{-1} \text{yr}^{-1}$ predicted from Kober et al. (2005).

Because the range of ^{10}Be concentrations for garnet and kyanite is limited, we use the error weighted mean $^3\text{He}/^{10}\text{Be}$ ratios rather than fitting a line to the points. Due to the large grain size and low Li content in kyanite, no correction for non-cosmogenic ^3He is made, giving a SLHL production rate of 177 ± 24 at $\text{g}^{-1} \text{yr}^{-1}$. Correction for the non-cosmogenic ^3He component in garnet gives a $^3\text{He}/^{10}\text{Be}$ ratio of $\sim 30.8 \pm 7.2$, corresponding to a production rate of 153 ± 35 at $\text{g}^{-1} \text{yr}^{-1}$. This number is within error of the 154 at $\text{g}^{-1} \text{yr}^{-1}$ that we recalculate from the data of Gayer et al. (2004) in section 2.6.2.

2.5.3 Limited Importance of Non-Cosmogenic ^3He

Because production rates in this study are higher than previously observed (Farley et al., 2006), we must consider whether we have somehow underestimated non-spallogenic sources of

^3He . The strong linear relationship between uncorrected $^3\text{He}_{\text{tot}}$ in zircon and apatite and ^{10}Be in quartz, and the near-zero intercepts of the fitted lines demonstrate that ^3He in these samples is primarily produced by spallation (Figures 2.2b and 2.3b). This conclusion is supported by the absence of a correlation between Li content and uncorrected $^3\text{He}_{\text{tot}}/^{10}\text{Be}$ ratio, either within mineral groups or between them. Likewise, no correlation was discovered when a step-wise multiple linear regression model was constructed in which Li content, exposure age, (U-Th)/He closure age, lithology, and grain size were sequentially added as predictor variables and regressed against $^3\text{He}_{\text{tot}}/^{10}\text{Be}$ ratio. The lack of correlation between Li content and uncorrected $^3\text{He}_{\text{tot}}/^{10}\text{Be}$ ratio is particularly important for garnet, because its large grain size and high Li content make its corrected ^3He concentration insensitive to the assumed Li concentration of the host mineral. Likewise, the lack of correlation between Li content and $^3\text{He}_{\text{tot}}/^{10}\text{Be}$ ratio for zircons in quartzite is important because the homogenous quartzitic lithology leads to roughly constant implanted $^3\text{He}_{\text{en}}$ and $^3\text{He}_{\text{nuc}}$ components among our samples (Figure 2.5).

Another piece of evidence supporting a limited contribution of non-cosmogenic ^3He is the relatively similar uncorrected $^3\text{He}_{\text{tot}}/^{10}\text{Be}$ ratios of kyanite and garnet, despite the fact that garnet has three orders of magnitude higher Li contents. Because grain size and composition are similar between the two mineral phases, and they are cohosted in three different moraine boulders, their spallogenic $^3\text{He}_c$ production rates should be similar. Because the non-spallation ^3He component in kyanite is negligible due its low Li content, the production rate in kyanite can also be used to validate the corrected production rate calculated in garnet. For example, the element-specific production rates of both Masarik (2002) and Kober et al. (2005) predict that the production rate in the Fe-rich garnets used in this study should be ~14% lower than in kyanite. Using this value and the observed production rate in kyanite, we expect a production rate in our garnet of $\sim 152 \text{ at g}^{-1} \text{ yr}^{-1}$. This agrees well with our corrected production rate of $153 \text{ at g}^{-1} \text{ yr}^{-1}$, which reflects the average 14% correction calculated for Li produced ^3He . Taken together, these

observations suggest that our estimates of Li produced ^3He are correct and strongly support the conclusion that the ^3He production rates we infer are in fact cosmogenic.

A puzzling observation of our study is that production rates in kyanite and garnet are significantly lower than in apatite and zircon, despite predictions based on element-specific production rates that suggest they should be higher. The difference between kyanite and zircon is particularly compelling, because both minerals have very small non-cosmogenic components. We can use our observed production rate in kyanite to calculate element-specific production rates for Al, Si, and O if it is assumed that the ratio of production rates between these elements matches those predicted by Kober et al. (2005) and Masarik (2002). This is an appropriate assumption because the two models agree well, predicting that 14-16% of production derives from Si, 29-31% from Al, and 55% from O. Using these values, we predict 153, 159, and 197 at $\text{g}^{-1} \text{yr}^{-1}$ for Si, Al, and O.

If estimates for Si and O are combined with the observed production rate in zircon, an element-specific production rate of ~ 270 at $\text{g}^{-1} \text{yr}^{-1}$ is calculated for Zr. The production rate from this element has not been established, but our value is far higher than other elements which have been tabulated (Kober et al., 2005; Masarik, 2002) and seems implausible. One possible explanation is implantation of spallation produced ^3He from adjacent minerals, which would affect smaller grain sizes (e.g. apatite and zircon) more severely. However, this explanation is unlikely for three reasons. First, grain-size experiments run on samples 259 and 431 show no grain-size dependence, except for very small grains. No significant difference in $^3\text{He}_{\text{tot}}$ concentration was detected between samples with average grain sizes of ~ 65 and $168 \mu\text{m}$ for sample 431, and only a $\sim 15\%$ difference was observed between average grain sizes of ~ 36 and $98 \mu\text{m}$ for sample 259 (Figure 2.6). Second, Farley et al. (2006) did not see elevated ^3He production in apatite or zircon of only slightly larger size than used in this experiment, and observed only $\sim 10\%$ increase in ^3He concentration over a two-fold range in grain size. Most importantly, even

if *all* of the ^3He in our zircon and apatite samples were implanted by spallation in adjacent crystals, the observed production rate is still much higher than the ~ 177 at $\text{g}^{-1} \text{yr}^{-1}$ we would expect for quartz using our estimates for Si and O given above. Production rates in other rock-forming minerals would not be expected to differ from quartz by more than $\sim 5\%$ (Farley et al., 2006). As discussed below, the higher production rate in zircon than in garnet is most likely a result of an unexpected correlation of $^3\text{He}_c/^{10}\text{Be}$ ratio with elevation coupled with the fact that on average the garnets were sampled at a lower elevation than the zircons.

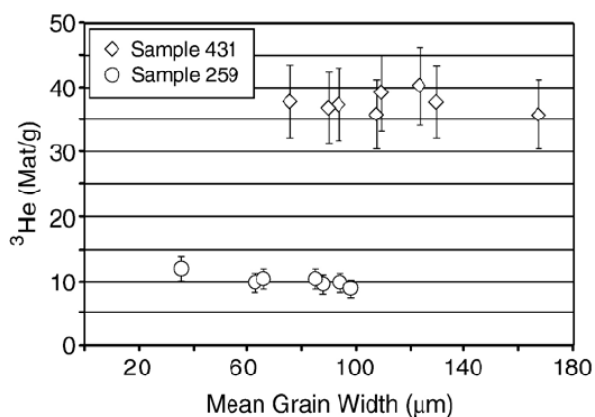


Figure 2.6

Results of ^3He measurements made on different grain size aliquots of zircon from sample numbers 259 and 431. Error bars show the 2-sigma external error discussed in the text. No relationship is observed between ^3He concentration and grain size for sample 431, and only the smallest grain size aliquot for sample 259 (~ 36 μm width) shows a moderately higher concentration.

2.5.4 Increasing ^3He Production Rate With Elevation

Because both ^3He and ^{10}Be are produced primarily by neutron-induced spallation, both production rates are commonly assumed to scale with the atmospheric neutron flux, and the $^3\text{He}_c/^{10}\text{Be}$ should be invariant with elevation (Gayer et al., 2004). However, our results show that the corrected $^3\text{He}_c/^{10}\text{Be}$ increases with elevation in both zircon and apatite (Figures 2.2c and 2.3c). This trend is particularly striking because it agrees very well with similar observations by Gayer et al. (2004) on Himalayan garnets. Likewise, although our garnet samples span a limited elevation, their $^3\text{He}_{\text{tot}}/^{10}\text{Be}$ ratios plot exactly on the predicted relationship between $^3\text{He}/^{10}\text{Be}$ and elevation shown in figure 8 of Gayer et al. (2004). The average $^3\text{He}_{\text{tot}}/^{10}\text{Be}$ ratio of ~ 36.9 , and the average elevation of ~ 3800 m for our five garnet samples matches the ratio of 37.4 predicted at 3800 m when using an SLHL production rate of 112 at $\text{g}^{-1} \text{yr}^{-1}$ and an attenuation length of 121

g/cm^2 as done by Gayer et al. (2004). If this elevation trend reflects variations in cosmogenic production, it would require that ^3He production rate scales differently with elevation than ^{10}Be , a hypothesis discussed in Section 6. While both we and Gayer have suggested that ^3He production scales anomalously with elevation, it is also possible that production of ^{10}Be increases more slowly with elevation than expected (i.e. a longer effective attenuation length).

Regardless of the origin of the elevation correlation, its existence has implications for estimation of SLHL production rates. Because samples from higher elevations often have higher ^{10}Be concentrations, the correlation tends to rotate the $^3\text{He}_c$ vs ^{10}Be correlation line counterclockwise. This may account for the negative y-intercepts in figures 2.2b and 2.3b. More importantly it calls into question our approach to estimating ^3He production rates, and may account at least partially for the anomalously high SLHL ^3He production rates.

We can accommodate this effect in determining SLHL production rates by performing a least-squares regression that allows the $^3\text{He}_c/^{10}\text{Be}$ ratio to vary with elevation:

$$^3\text{He}_c/^{10}\text{Be} = R_o * \exp\left(\frac{Z}{Z^*}\right) \quad (2.4)$$

where Z is sample elevation (km), Z^* is the characteristic lengthscale (km) of the difference in production rate of the two nuclides, and R_o is the $^3\text{He}_c/^{10}\text{Be}$ production ratio at sea level. The justification for this formulation is that cosmogenic production rates scale exponentially with elevation (Lal and Peters, 1967); if two isotopes scale differently with elevation, then their ratio is also likely to scale exponentially. Note that if Z^* is infinite, the two isotopes scale identically with elevation and equation (4) reduces to the simple approach for determining production rates described in section 5.2.

For zircon, fitting of the data in figures 2.2b and 2.3b to equation 2.4 are shown in results in $R_o=13.0$ at $^3\text{He}/^{10}\text{Be}$ at sea level, and $Z^*=4.2$ km. For apatite, $R_o= 16.6$ at $^3\text{He}/^{10}\text{Be}$ and $Z^*=4.2$ km. As shown in figure 2.7, the resulting correlations between $^3\text{He}_c$ measured and modeled are excellent for both phases, providing further justification for the form of equation 2.4.

The fact that two mineral phases yield almost identical values for Z^* suggests the elevation correlation is not an artifact of inadequate correction for non-cosmogenic ^3He . Using these values for R_0 , we obtain SLHL production rates of 65 at $\text{g}^{-1} \text{yr}^{-1}$ for zircon and 83 at $\text{g}^{-1} \text{yr}^{-1}$ for apatite. If kyanite and garnet follow the same elevation dependence, then their SLHL production rates are 73 and 72 at $\text{g}^{-1} \text{yr}^{-1}$ respectively. These SLHL production rates are far lower than obtained without attempting to accommodate the elevation correlation. In addition, this approach at least partially explains the observation that the production rate in zircon exceeded that in garnet when ignoring the elevation correlation: because on average the zircons come from higher elevations than the garnets, the elevation effect was greater on the zircons than on the garnets. These SLHL production rates and $Z^*=4.2$ km provide an approach for estimating ^3He production rates at any elevation. Gayer et al. (Gayer et al., 2006) provided a similar approach based on their more limited garnet data.

Equation 2.4 can be rearranged to estimate elevations based solely on measured $^3\text{He}/^{10}\text{Be}$ ratios. Figure 2.8 shows a strong linear correlation ($R^2=0.68$) between the elevation implied by the $^3\text{He}/^{10}\text{Be}$ ratio and the known elevation of each sample in the combined apatite and zircon data set. The standard error of the elevation estimate is ~ 0.4 km. If the robustness of this relationship, especially its validity through time and space, can be established, it may provide a new method for reasonably precise paleoelevation estimates.

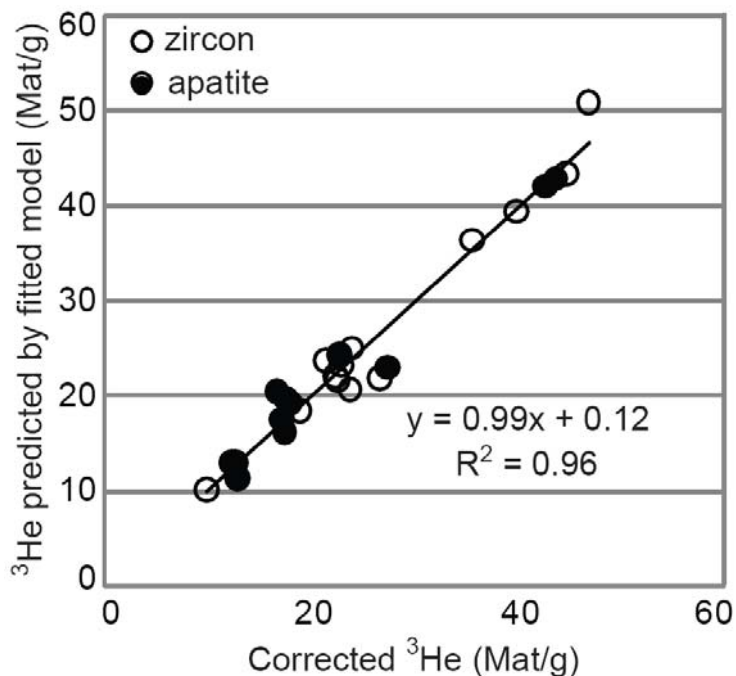


Figure 2.7
Plot of the corrected ^3He concentrations against ^3He concentrations predicted by the exponential fitted model described in the text.

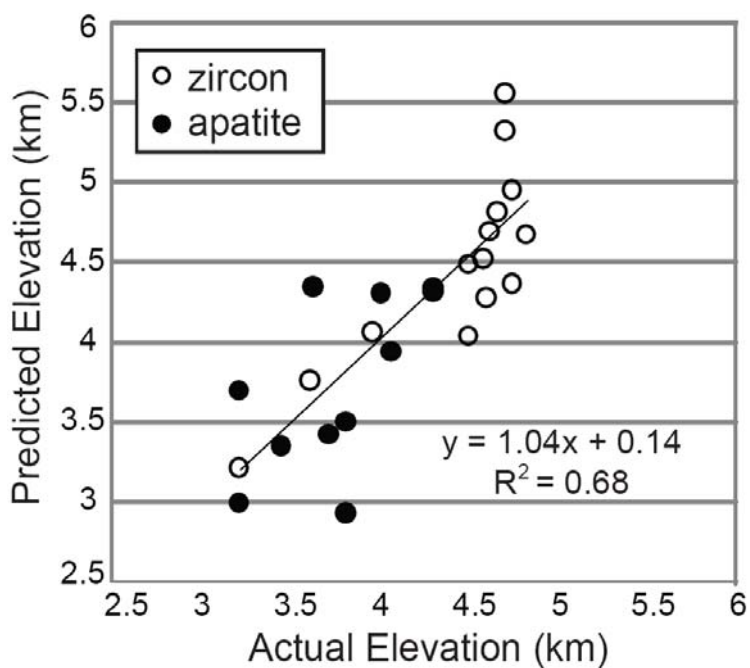


Figure 2.8
Plot of actual sample elevation against the elevation predicted by rearranging Eq. 5.4 and solving for elevation using the measured $^3\text{He}/^{10}\text{Be}$ ratio.

2.6 Possible Causes of Anomalous Production Rates

2.6.1 Altitudinal Variations in the Neutron Energy Spectrum

One hypothesis to explain elevated ^3He production at high elevations is that the neutron energy spectrum becomes increasingly energetic with altitude, somehow favoring increased

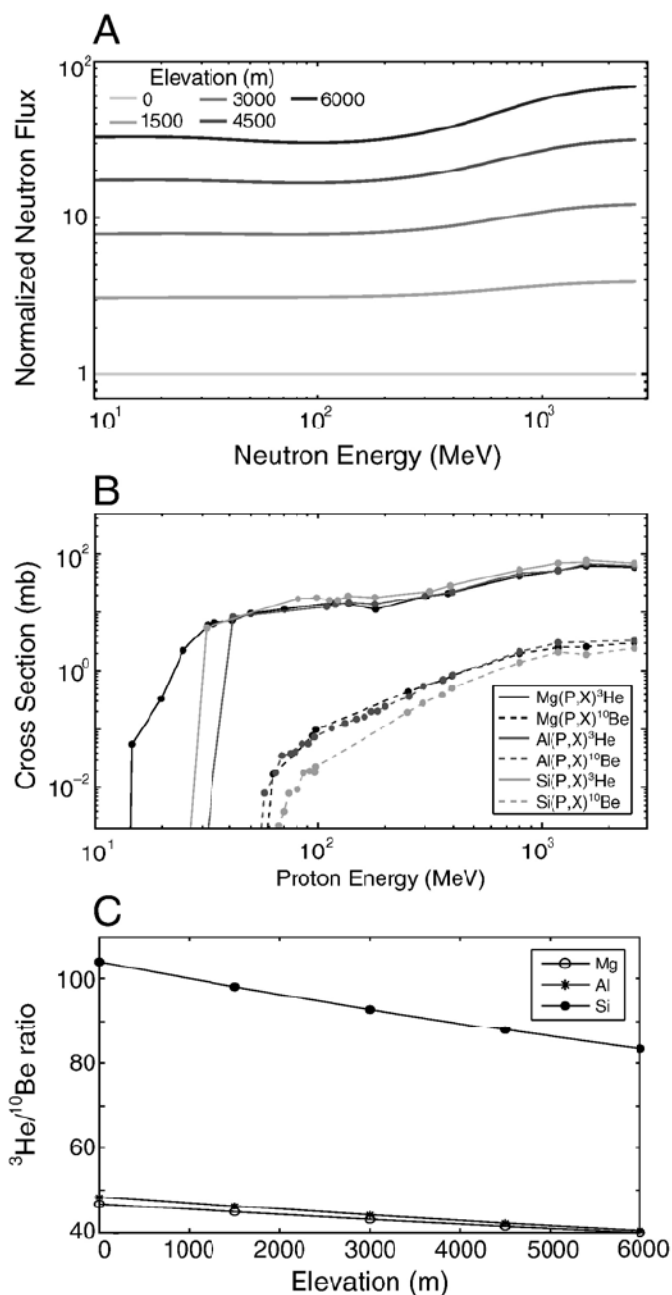
production of ^3He over ^{10}Be (Gayer et al., 2004). This could happen because ^{10}Be and ^3He have different excitation functions, causing their production rates to respond differently to changes in the neutron energy spectrum. It is important to note that this hypothesis does not require changes in scaling of the overall neutron flux, only that the flux of high-energy neutrons increases with elevation relative to flux in other parts of the energy spectrum. Although atmospheric energy spectra do show an increasing high-energy “tail” between 100 and 10^4 MeV, where flux increases 2-3 times more rapidly with elevation than other parts of the spectrum (Goldhagen et al., 2002), earlier studies do not report greatly increased ^3He production at high elevation. For example, ^3He studies have been done at several high elevation locations worldwide (~4000 m), including Bolivia (Farley et al., 2006), and Hawaii (Blard et al., 2006), and have shown no evidence of elevated ^3He production rates. However the study of Kober et al. (Kober et al., 2005) (>4000 m) observes production rates in Fe-Ti oxides that are higher than expected relative to the accepted values for olivine and pyroxene.

Another way to test this hypothesis is to estimate ^3He and ^{10}Be production rates at different elevations using the neutron energy spectrum and excitation functions for production of ^3He and ^{10}Be . In general, excitation functions for neutron-induced reactions are poorly known for ^3He , necessitating the use of excitation functions for proton interactions. However, the lack of cross section data for proton-induced ^3He production from oxygen is a critical limitation in making mineral-specific calculations (Leya et al., 2000b). Additionally, although it is often assumed that neutron and proton excitation functions are similar for a given reaction, this is not necessarily the case (Leya et al., 2000a).

As an alternative to mineral-specific calculations, we estimate ^3He and ^{10}Be production rates for pure magnesium, aluminum, and silicon as a function of elevation to see if the $^3\text{He}/^{10}\text{Be}$ production ratio in these common rock-forming elements increases with elevation. The proton excitation functions for these reactions are compiled from (Bodemann et al., 1993; Leya et al., 1998a; Leya et al., 2000a; Leya et al., 2000b; Michel et al., 1995; Schielke et al., 1996), and are

shown in figure 2.9b. To predict the neutron flux and energy spectrum at each elevation, we use the analytical equations of Sato et al. (Sato and Niita, 2006), calculated with a rigidity cutoff of 14 GeV, zero water content, and a moderate solar modulation of 1000 MV (Fig. 2.9a). We use linear interpolation of the experimentally observed cross sections to create a discretized excitation function between 10 and 2600 MeV. Next, the discretized excitation function is multiplied by the discretized energy spectrum for each elevation, and the resulting functions are numerically integrated to obtain elemental production rates at various elevations. We did not include the portion of the neutron flux above 2600 MeV in our calculation due to unknown cross-sections in this region. However, because such a small portion of the total neutron flux occurs above 2600 MeV, calculations using a linear extrapolation to approximate the excitation function between 2600 and 10^4 MeV do not yield significantly different results. Our calculations show that the $^3\text{He}/^{10}\text{Be}$ production ratio actually decreases with elevation in all three elements because the shape of the ^{10}Be excitation function dictates that relatively more of the ^{10}Be production occurs in the high-energy part of the spectrum than for ^3He (Fig. 2.9c). If this relationship holds true for other elements, most importantly for oxygen, it would suggest that an increase in the high-energy neutron component with elevation would actually lead to lower $^3\text{He}/^{10}\text{Be}$ ratios. Indeed if the energy spectrum varies in time or space, it is hard to imagine that the $^3\text{He}/^{10}\text{Be}$ ratio will remain constant.

An alternative hypothesis presented by Gayer et al. (Gayer et al., 2004) suggests that increased ^3He production with elevation could occur if high-energy neutrons induce an initial spallation event in the rock, from which the resultant tertiary neutrons retain enough energy to induce additional spallation of ^3He , but not of ^{10}Be (Gayer et al., 2004). Because the experimental cross sections used in this calculation are measured in foils, and not in real rock, our calculation does not explicitly test this hypothesis, although it seems reasonable given that ^3He production cross sections in the 10-100 MeV range are significantly larger than for ^{10}Be (Fig. 2.9b).

**Figure 2.9**

Results of calculations performed to test the hypothesis that an increase in the high-energy neutron flux relative to other parts of the energy spectrum could cause the cosmogenic $^3\text{He}/^{10}\text{Be}$ ratio to vary with elevation. A) Neutron energy spectra at different elevations (see section 6.1) normalized to the sea level spectrum, as predicted by the equations of Sato and Niita, 2006. B) Excitation functions for production of ^3He by proton interactions with Mg, Al and Si (Bodemann et al., 1993; Heimsath et al., 2002; Heimsath et al., 1997; Leya et al., 1998a; Leya et al., 2000b; Michel et al., 1997; Schickel et al., 1996). Dots represent actual measurements taken from the literature, lines are the interpolations used in our calculations.

2.6.2 The Effect of Snow Cover

An alternate hypothesis for elevated ^3He production rates is an elevated low-energy neutron flux at the rock surface due to snow cover. This occurs because covering the surface reduces the diffusive loss of thermal neutrons from the rock into the air, a process that normally reduces the

low-energy neutron flux in the upper ~20 cm of unshielded rock. This hypothesis is attractive because it could explain why production rates are higher in our study area than at calibration sites where snow cover is less significant. Increasing mean annual snow cover with elevation might also explain the observed increase in $^3\text{He}/^{10}\text{Be}$ ratios with elevation. However, because increased low-energy neutron flux can only drive ^3He production by thermal neutron capture on ^6Li , this hypothesis would also predict that ^3He production in rocks with similar exposure histories should correlate with Li content in the minerals, which it does not. Similarly, in most of our kyanite and zircon samples, the concentration of Li is too low for an increased thermal neutron flux to be important.

However, snow cover is part of the reasoning used by Dunai et al. (2007) to recalculate the ^3He production rate observed in Himalayan garnet by Gayer et al. (2004): they attribute a substantial amount of ^3He production to neutron capture on ^6Li and thereby reduce the high spallation production rate. We suspect the calculations of Dunai et al. (2007) overestimate the magnitude of the effect, and for this reason, along with the absence of a correlation between $^3\text{He}/^{10}\text{Be}$ and Li in our samples, we suggest it does not account for our high production rates and lower atmospheric attenuation length.

Neither the commonly used CHLOE model (Phillips and Plummer, 1996), nor the model of Phillips et al. (2001) can accurately predict the effect of overlying snow or ice on the low-energy neutron flux, so Dunai et al. (2007) estimate the effect by converting snow cover to an equivalent thickness of rock and assuming that the snow has the same composition as the rock. The result of this assumption is that the dated surface occurs at a deeper effective depth closer to the peak in neutron flux, thereby driving increased production from capture on ^6Li . This simplification ignores the fact that snow is rich in nitrogen, giving it a much larger macroscopic absorption cross section than rock, potentially reducing the low-energy neutron flux at the surface of the rock.

Another reason the low-energy neutron flux estimated by Dunai et al. (2007) is probably too high is the assumption of 3% water by mass (3300 ppm H) in the gneisses. This value is high compared with published values for Himalayan gneisses (400 to 1400 ppm), and increases the maximum low-energy neutron flux by 30-40% in a gneissic sample at an elevation of 4000 m (Brouand et al., 1990; Phillips et al., 2001). Thus, although it is important to correct the results of Gayer et al. (2004) for the production of ^3He by low-energy cosmogenic neutrons, if the $^3\text{He}_{cn}$ component is computed following Dunai et al. (2007), but using the surface neutron flux and assuming a more appropriate ~650 ppm of H in the rock, the average corrected $^3\text{He}/^{10}\text{Be}$ ratio is ~31.3 giving a SLHL production rate of about 156 at $\text{g}^{-1} \text{yr}^{-1}$ for garnet. This result agrees well with our estimate of 153 at $\text{g}^{-1} \text{yr}^{-1}$ in garnet.

2.7 Conclusions

This study further demonstrates the feasibility of using apatite, zircon, and kyanite for cosmogenic ^3He dating. In particular, we have shown that small amounts of cosmogenic ^3He can be reliably measured in the presence of large amounts of radiogenic ^4He . Use of these mineral phases, as well as garnet (Gayer et al., 2004), and Fe-Ti oxides (Kober et al., 2005), can expand the variety of target lithologies suitable for cosmogenic ^3He dating.

Based on $^3\text{He}/^{10}\text{Be}$ systematics in Himalayan moraine boulders from 3-5 km elevation, we obtained apparent production rates of 226 at $\text{g}^{-1} \text{yr}^{-1}$ in zircon, 254 at $\text{g}^{-1} \text{yr}^{-1}$ in apatite, 177 at $\text{g}^{-1} \text{yr}^{-1}$ in kyanite, and 153 at $\text{g}^{-1} \text{yr}^{-1}$ in garnet. These results are surprising because they are significantly higher than production rates estimated by Farley et al. (2006) for apatite and zircon from comparable elevation in Bolivia. The production rates determined for kyanite and garnet are significantly lower than in apatite and zircon, but are still much higher than would be expected based on extrapolation from observed production rates in olivine elsewhere in the world.

However, apparent production rates in kyanite and garnet match the production rate observed in Himalayan garnet by Gayer et al. (2004), and are consistent with the recently published element-specific production rates of Kober et al. (2005).

The elevated production rates in our study area are not the result of cosmogenic thermal neutron capture as suggested by Dunai et al. (2007) for Himalayan garnets. Instead it seems that something unique to the geographic location of the study area may be causing elevated production rates of ^3He . The unusually high production rate is also associated with increasing production rate with elevation. Both observations can be explained by an exponential increase in the $^3\text{He}/^{10}\text{Be}$ ratio with elevation, with a characteristic length scale of 4.2 km. Our observations thus call into question the currently employed latitude-altitude scaling laws, at least for cosmogenic ^3He production. If our key result and that of Gayer et al. (2004) that different cosmogenic isotopes scale differently with altitude are general, then this may provide a new approach to paleoaltimetry. Further work is required to establish whether the same effect is seen outside the Himalayan region and over longer exposure intervals. Samples from a single ~ 100 kyr surface at 4 km in Bolivia (Farley et al., 2006) do not show the same effect, suggesting a geographically or temporally complex behavior. It will also be important to compare ^3He production rates with those of cosmogenic isotopes other than ^{10}Be .

Chapter 3

COSMOGENIC ^3He AND ^{21}Ne PRODUCTION RATES CALIBRATED AGAINST ^{10}Be MINERALS FROM THE COSO VOLCANIC FIELD

3.1 Introduction

Dating of geologic surfaces using cosmogenic ^3He or ^{21}Ne offers a fast and relatively simple alternative to cosmogenic dating using radioisotopes such as ^{10}Be and ^{26}Al (Gosse and Phillips, 2001). Although cosmogenic dating using ^3He has most often been performed on olivine and pyroxene, all major elements produce spallogenic ^3He as well as ^3H , which quickly decays to ^3He ($t_{1/2}=12.3$ a). Therefore, cosmogenic ^3He dating can be applied to any mineral phase that is retentive to helium and for which the production rate of cosmogenic ^3He is known. The He retentivity of many mineral phases is well established (Copeland et al., 2007; Dunai and Roselieb, 1996; Farley, 2002; Shuster and Farley, 2005), but ^3He production rates remain uncertain.

Previous studies provide several ^3He production rate estimates for olivine and pyroxene (Ackert et al., 2003; Blard et al., 2006; Cerling and Craig, 1994; Dunai and Wijbrans, 2000; Kurz et al., 1990; Licciardi et al., 1999; Licciardi et al., 2006), a few estimates in garnet, zircon, apatite, titanite and kyanite (Amidon et al., 2008a; Farley et al., 2006; Gayer et al., 2006; Gayer et al., 2004) and some results on Fe-Ti oxides and calcite (Amidon et al., 2008b; Bryce and Farley, 2002; Kober et al., 2005). ^3He production rates in pyroxene and olivine range from ~ 100 to ~ 150 at $\text{g}^{-1} \text{a}^{-1}$ at sea level and high latitude (SLHL), a wider range than for comparable calibration studies of ^{10}Be or ^{26}Al and outside of the stated analytical uncertainties. This large scatter may arise from incomplete or inaccurate consideration of one or more of the following factors: 1) significant amounts of ^3He can be produced by capture of radiogenic or cosmogenic slow neutrons by ^6Li (Andrews and Kay, 1982; Dunai et al., 2007), 2) newly created ^3He (and ^3H) nuclei experience redistribution into adjacent mineral phases due to their small size and high

energy (Farley et al., 2006); 3) cosmogenic ^3He must be deconvolved from mantle-derived ^3He in common mafic phases (Blard and Pik, 2008; Kurz, 1986b); 4) ^3He spallation production rates may not follow accepted elevation scaling laws (Gayer et al. 2004; Farley et al. 2006; Gayer et al. 2006; Amidon et al. 2008a).

Here we attempt to eliminate some of these sources of uncertainty and expand the utility of cosmogenic ^3He dating by cross-calibrating its production rate in pyroxene, olivine, garnet, zircon, and apatite against the known production rate of ^{10}Be in co-existing quartz. The rhyolite domes of the Coso volcanic field were chosen for this study because they are well studied petrographically and geochemically, and the Devil's Kitchen dome contains abundant coarse-grained crystals of all of the above mineral phases in a single rock (Manley and Bacon, 2000). In addition, the high U, Th and Li of this rock presents an opportunity to develop and validate an approach to quantifying Li-produced ^3He in these phases.

3.2 Geologic Overview

The Coso volcanic field is located in the southern Owens Valley, east of the Sierra Nevada Mountains. The focus of this study, the Devil's Kitchen rhyolite dome, has an $^{40}\text{Ar}/^{39}\text{Ar}$ isochron age of 0.613 ± 0.003 Ma (Simon et al., 2008). It contains an unusual assemblage of 0.1-1 mm sized phenocrysts including quartz, sanidine, plagioclase, magnetite, ilmenite, pyroxene, hornblende, biotite, olivine, and trace amounts of zircon and apatite (Bacon et al., 1981; Manley and Bacon, 2000). The rock typically exhibits a fine-grained ($< 10 \mu\text{m}$) quartz-feldspar matrix. Of particular importance to this study is that the rhyolite is unusually rich in U, Th and Li, with concentrations of 14, 42, and 156 ppm respectively (Bacon et al., 1981). Zircons contain up to 2.5 weight percent of U, and up to 1.5 weight percent of Th (Miller and Wooden, 2004). The Devil's Kitchen rhyolite also contains dm-sized inclusions of a porphyritic andesite (Bacon and Metz, 1984). The andesitic inclusions contain 0.5 to 4 mm phenocrysts of plagioclase, as well as

smaller (< few mm) phenocrysts of quartz, clinopyroxene, olivine, and Fe-Ti oxides. In addition to andesitic inclusions, one of our rhyolite samples (co-5) also contains small plagioclase-garnet xenoliths.

3.3 Methods

3.3.1 Sampling

Two closely-spaced localities were sampled on a low ridge on Dome 28, at ~1333 m elevation (Bacon et al., 1980). Locality co-5 (N 36.03014, W 117.79654) was a flat bedrock surface about 40 cm above the alluvial surface of the ridge. A sample of the rhyolite (denoted co-5) was collected from the surface, along with an andesitic inclusion (sample co-5x). The inclusion measured approximately 10 x 8 x 5 cm and was sampled from an average depth of 8 cm directly below co-5. Locality co-6 (N 36.0299, W 117.79658), about 25 meters away from co-5, was a bedrock knob rising about 80 cm above the surface of the ridge on the west side and about 2 m above the steeply sloping edge of the ridge on the east side. Again a rhyolite sample (co-6) was collected from the surface and an andesitic inclusion (sample co-6x, from an average depth of 5 cm) directly below this surface. The inclusion measured approximately 12 x 7 x 7 cm in dimension.

We thus have four rock samples for analysis: one rhyolite and one andesitic inclusion from each of two localities. The two lithologies from each location will have the same cosmic ray exposure history after correction for the sub-surface depth at which the inclusion was located. Similarly, we assume that the chemical composition of each lithology is the same at the two localities (Table 3.9). As we show below, the two localities have very different exposure histories, providing us the opportunity to see how ^3He concentrations vary with the total cosmic ray exposure derived from ^{10}Be .

No topographic shielding corrections are necessary at either locality, nor do we attempt to correct for shielding by snow or ice. Ignoring these corrections is further justified by the fact that we are comparing ^3He and ^{21}Ne directly to ^{10}Be , so shielding effects should cancel when production rates are calculated.

Mineral separations were done following standard heavy liquid procedures followed by HF leaching of quartz for ^{10}Be and ^{21}Ne analysis. All samples were handpicked of contaminant phases prior to analysis.

3.3.2 ^{10}Be Analyses and ^{10}Be Production Rate

Analysis of ^{10}Be concentrations in quartz was performed at Lawrence Livermore National Laboratory (LLNL). Quartz samples were purified by HF leaching following Kohl and Nishiizumi (1992), and Be was extracted and analyzed following standard LLNL procedures. Measured $^{10}\text{Be}/^9\text{Be}$ ratios are normalized to the 07KNSTD3110 with a $^{10}\text{Be}/^9\text{Be}$ ratio of 2.85×10^{-12} , based on a ^{10}Be half life of 1.36 million years (Nishiizumi et al., 2007). To calculate ^3He and ^{21}Ne production rates we adopt a SLHL ^{10}Be production rate of $4.87 \text{ at g}^{-1} \text{ a}^{-1}$. This is based on the average production rate published in Balco et al. (2008) scaled following Lifton et al. (2005), and reduced by a factor of 0.904 to reflect the newly adopted ^{10}Be half life mentioned above. This ignores muogenic production of ^{10}Be , which should be ~2-3% of spallogenic production (Heisinger et al., 2002a; Heisinger et al., 2002b).

3.3.3 Helium Analyses

Samples were analyzed for ^3He either directly as obtained from mineral separation or after crushing, either in vacuum or in air. Crushing is required in some mineral phases to release and/or measure magmatic helium contained in inclusions. Samples crushed under vacuum were crushed for 3 minutes in a steel tube following published procedures (Patterson et al., 1997).

After crushing either on-line or in air sample material was wet-sieved through a 24 μm sieve and recrushed as necessary until all material was smaller than 24 μm . Three samples were re-crushed for a second 3 minute cycle and analyzed to verify that all ^3He is removed during the initial crushing phase. None of the zircon or apatite samples were crushed prior to analysis, under the assumption that the magmatic ^3He component is negligible in these very fine grained phases.

Only grains from the $>150 \mu\text{m}$ size fraction were used during analysis of pyroxene, olivine and garnet, making the effect of implanted ^3He from adjacent mineral phases negligible. To document the effect of implanted ^3He on fine-grained phases, zircons were sieved into grain size fractions if enough sample material was available. The average dimensions of mineral grains are expressed in terms of the equivalent radius of a sphere with the same surface area to volume ratio (Farley et al., 1996).

Extraction of matrix-sited ^3He was performed by diffusing helium gas out of the sample either by heating to $\sim 1300^\circ \text{C}$ in a double-walled resistance furnace, or to similar temperatures by heating with a Nd-YAG laser in a Pt capsule. Complete helium extraction from each sample was verified by re-extracts under identical heating conditions. In both cases, helium was purified by exposure to hot and cold SAES getters, and was cryogenically focused on charcoal at 12°K before release of He at 32°K into a MAP 215-50 mass spectrometer. Sensitivity of the mass spectrometer was determined by analysis of gas standards at similar helium pressures and $^3\text{He}/^4\text{He}$ ratios to the samples being analyzed. The precision of our measurements can be estimated from five replicate analyses of sample co-5x (pyroxene), which gave a 1σ standard deviation of $\sim 5.5\%$ for ^3He counting rates of 5-10 cps. Zircon and apatite were typically measured at lower counting rates of 1-3 cps, a range in which replicate standards yield a 1σ standard deviation of $\sim 8\%$ on ^3He .

3.3.4 ^{21}Ne Analyses

Uncrushed quartz samples were either heated in a single step to 1300° C or step-heated at 250, 800, and 1300° C to preferentially release matrix-sited neon from adsorbed or inclusion-held neon (Niedermann, 2002). None of the 250 or 1300° C steps contained excess ^{21}Ne , although the 1300° step contained large air components. Pyroxene was either heated in a single temperature step at ~1500° C, or fused by rastering a Nd-YAG laser over bare grains. Neon was purified over hot and cold SAES getters and then cryogenically focused at 32 K on charcoal before release at 75 K into a GV Helix-SFT split tube mass spectrometer operating in peak-jumping mode on the electron multiplier spur. Because the $^{40}\text{Ar}^{++}$ peak is resolved from the $^{20}\text{Ne}^+$ peak, no correction for the ^{40}Ar isobar was applied. Corrections for the $^{44}\text{CO}_2$ isobar were <2% and were made by determining a $^{44}\text{CO}_2^{++}/^{44}\text{CO}_2^+$ ratio of 0.0153 ± 0.0003 for CO_2 signals which were constant to $\pm 10\%$ for all samples, standards and blanks. Mass fractionation corrections of 1.1% per AMU based on air standards were applied. The precision on Ne concentrations is estimated to be ~7% (1σ standard deviation) based on five replicate analyses of sample co-6 (quartz).

3.3.5 Li Analysis

Lithium measurements were made on a Thermo-Finnagan Element 1 single-collector ICPMS, using isotope dilution with a ^6Li spike calibrated with a commercial Li normal solution. Measurements were made on ~1 mg of handpicked material, but not the same aliquots used for ^3He analysis. Most samples were dissolved on a hot plate in a 2:1 HF:HNO₃ cocktail except for zircons, which were Parr bombed in HF, redissolved in HCl, and finally in HNO₃. Reproducibility of Li measurements was established by performing at least two replicate measurements on separately picked aliquots of each sample. If agreement within 15% was not achieved, additional aliquots were analyzed. Lithium blanks typically total less than 0.1% of measured lithium, with a maximum of ~2%. The sample cleaning procedure, and a 2σ external precision of ~12% are established and discussed by Amidon et al. (2008a).

3.3.6 Determining Average Host Mineral Li Contents

The capture of low energy neutrons on ${}^6\text{Li}$ produces ${}^3\text{He}$ via the reaction ${}^6\text{Li}(n,\alpha){}^3\text{H}(\beta^-){}^3\text{He}$ (Andrews and Kay, 1982). These tritium nuclei have an average energy of ~ 2.7 MeV and a stopping range of ~ 30 μm in apatite and zircon (Farley et al., 2006; Ziegler, 2003). Although apatite and zircon are low in Li, their small grain size makes them vulnerable to implantation of Li-produced ${}^3\text{He}$ from adjacent Li-rich phases, e.g., biotite. As a result, calculation of the total Li-derived ${}^3\text{He}$ in apatite and zircon requires knowledge of the average Li content of the immediately adjacent minerals. To establish this quantity, individual zircon and apatite crystals were identified in polished sections of rock and their minimum and maximum dimensions as well as the relative proportion of their surface area in contact with each adjacent mineral were documented. One dataset was generated for the andesitic inclusions (co 5x/6x) and another for the host rhyolite samples (co-5/6) for grains of minimum dimension of 20 μm . Multiplying the fractional contact area of each adjacent mineral phase by its measured Li content and summing over all mineral phases gives the average Li content surrounding the mineral of interest.

3.4 Results

3.4.1 ${}^{10}\text{Be}$ Results

The quartz in sample co-5 has a ${}^{10}\text{Be}$ concentration of 0.637 ± 0.015 Mat/g, compared to 1.202 ± 0.019 Mat/g for sample co-6 (Table 3.1). These quite different concentrations are factors of ~ 11.6 and ~ 6.1 lower than expected for a 0.613 Ma uneroded/unburied surface and give a ${}^{10}\text{Be}_{\text{co5}}/{}^{10}\text{Be}_{\text{co6}}$ ratio of 0.53. As discussed below, the simplest interpretations of these ${}^{10}\text{Be}$ concentrations are either as apparent exposure ages of ~ 49 and 93 ka, or as steady-state erosion rates of ~ 0.070 and 0.036 mm/yr respectively (Bierman, 1994).

Table 3.1: ^{10}Be analyses

Sample	$(^{10}\text{Be}/^9\text{Be})_{\text{blank}}$	$^{10}\text{Be}_{\text{blank}}$ (atoms)	$(^{10}\text{Be}/^9\text{Be})_{\text{samp}}$	$^{10}\text{Be}_{\text{samp}}$ (Mat/g)	1σ SD (Mat/g)
CO-5	1.41E-15	18473	2.97E-13	0.637	0.015
CO-6	1.41E-15	18538	8.22E-13	1.201	0.019
C3_C4	1.40E-15	23085	9.77E-13	2.918	0.078

Results reported relative to the 07KNSTD3110 standard. C3_C4 from Farley et al. (2006).

3.4.2 Helium results

Results of helium extracted by crushing are presented in Table 3.2. Pyroxenes and olivines from the andesitic inclusions (samples co-5x/6x) give much higher concentrations of ^3He during crushing than those from the host rhyolite, with pyroxene giving about an order of magnitude more ^3He than olivine in both cases. The pyroxenes from co-5x/6x yield $^3\text{He}/^4\text{He}$ ratios near 8 Ra, suggesting they contain a significant mantle-derived component, whereas most other mineral phases give intermediate to radiogenic $^3\text{He}/^4\text{He}$ ratios (0.01-4 Ra). Results of degassing of matrix sited helium in pyroxene, olivine, and garnet are presented in Table 3.3 and Figure 3.1. Samples co-5/5x and co-6/6x are found to have ~ 23 and ~ 41 Mat/g of ^3He respectively, for a $^3\text{He}_{\text{co5/5x}}/^3\text{He}_{\text{co6/6x}}$ ratio of about 0.56, quite similar to the ratio of 0.53 observed in the ^{10}Be data. Results of ^3He released by laser heating of uncrushed zircon and apatite are presented in Table 3.4 and Figure 3.2. A strong correlation is observed between grain size (equivalent radii 33-78 μm) and total measured ^3He concentration in zircon. This grain size range is correlated with a range of ^3He concentrations between 23 and 37 Mat/g in co-5/5x and ~ 39 to 62 Mat/g in co-6/6x. Analyses of apatite aliquots with equivalent radii of ~ 100 μm from samples co-5x and co-6x yield 23.8 and 44.6 Mat/g respectively, giving a $^3\text{He}_{\text{co5x}}/^3\text{He}_{\text{co6x}}$ ratio of 0.53.

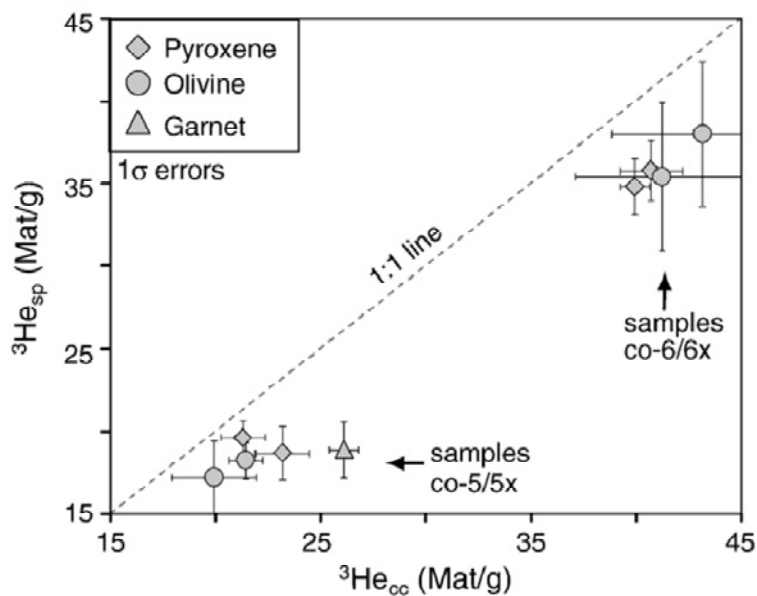
Table 3.2: ^3He crushing analyses

Sample	Mass (mg)	^3He (Mat/g)	1 σ SD (Mat/g)	^4He (ncc STP/g)	1 σ SD (ncc STP/g)	$^3\text{He}/^4\text{He}$ (Ra)	1 σ SD (Ra)
<i>Pyroxene</i>							
co5-p-1	6.21	1.4	0.1	80.3	2.2	0.5	0.05
co5x-p-1	85.70	6.3	0.4	19.5	0.8	8.7	0.6
co5x-p-2	21.20	6.3	0.5	20.5	0.9	8.3	0.7
co5x-p-3	43.40	6.6	0.5	20.7	0.8	8.5	0.7
Mean co5x		6.4		20.2		8.5	
co6-p-1	8.84	2.2	0.2	64.4	2.3	0.9	0.1
co6-p-2	13.70	3.2	0.3	18.9	0.7	4.5	0.4
Mean co6		2.7	0.3	41.6		2.7	
co6x-p-1	99.00	7.5	0.4	22.5	0.6	8.9	0.5
co6x-p-2	18.90	7.1	0.4	23.1	0.7	8.2	0.6
co6x-p-3	29.78	7.2	0.5	22.7	0.6	8.5	0.6
Mean co6x		7.3		22.8		8.6	
<i>Olivine</i>							
co5-o-1	7.90	0.01	0.00	11.9	0.5	0.01	0.01
co6-o-1	8.42	0.02	0.01	74.5	2.0	0.01	0.004
co5x-o-1	23.31	0.8	0.1	5.1	0.3	4.0	0.7
co6x-o-1	11.51	0.6	0.1	5.1	0.3	3.4	0.6
<i>Garnet</i>							
co5-g-1	10.63	0.8	0.1	1580.3	39.5	0.01	0.002
<i>Hornblende</i>							
co5-h-1	10.00	0.4	0.1	9.1	0.2	1.2	0.3
<i>Re-crush data</i>							
co5x-p1-RC	85.7	0.15	–	0.01	–	–	–
co6-p1-RC	8.8	0.02	–	0.02	–	–	–
co5x-o1-RC	23.3	0.00	–	0.00	–	–	–

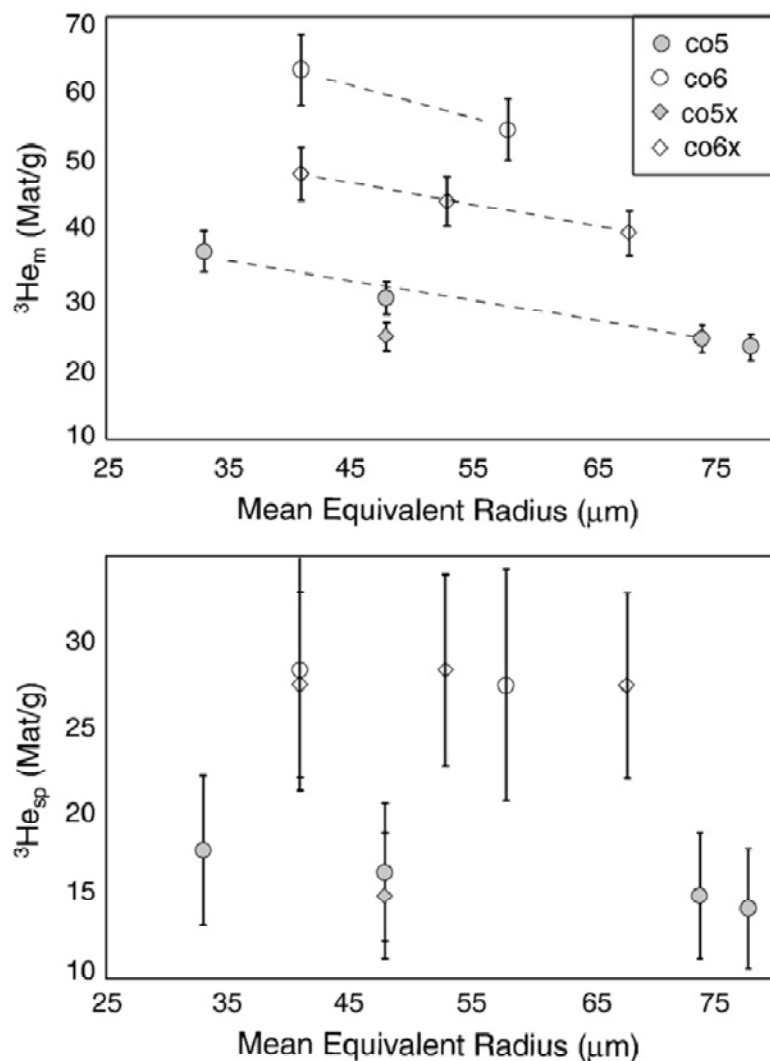
Table 3.4: Data summary and production rates

Sample	Mass (mg)	$^3\text{He}_m$ (Mat/g)	$1\sigma\text{SD}$ (Mat/g)	$^3\text{He}_{\text{cp}+\text{nuc}+\text{mu}}$ (Mat/g)	$1\sigma\text{SD}$ (Mat/g)	$^3\text{He}_{\text{sp}}$ (Mat/g)	$^3\text{He}_{\text{sp}}(z=0)$ (Mat/g)	$1\sigma\text{SE}$ (Mat/g)	$^4\text{He}_m$ (ncc-STP/g)	$^3\text{He}_m/^4\text{He}_m$ (Ra)	Eq. Rad. (μm)	^{10}Be (Mat/g)	$1\sigma\text{SD}$ (Mat/g)	$\frac{^3\text{He}_{\text{sp}}}{^{10}\text{Be}}$	$1\sigma\text{SE}$	PR ($\text{at}\cdot\text{g}^{-1}\cdot\text{a}^{-1}$)	$1\sigma\text{SE}$ ($\text{at}\cdot\text{g}^{-1}\cdot\text{a}^{-1}$)	
Zircon																		
co5-z-1	6.32	23.2	1.9	9.0	2.2	14.2	14.2	0.7	274	0.002	78							
co5-z-2	1.39	24.3	1.9	9.4	2.3	14.9	14.9		222	0.003	74							
co5-z-3	1.24	30.2	2.4	13.8	3.5	16.4	16.4		302	0.003	49							
co5-z-4	1.29	30.2	2.4	13.8	3.5	16.4	16.4		292	0.003	48							
co5-z-5	1.33	36.8	2.9	19.1	4.8	17.7	17.7		423	0.002	33	0.637	0.015	25.0	1.2	121.5	8.2	
Mean		28.9		25.8	6.5	28.2	28.2	0.7	302	0.005	58							
co5-z-1	4.33	54.0	4.3	25.8	8.9	27.0	27.0		357	0.005	41	1.201	0.019	23.0	0.8	112.0	6.5	
co5-z-2	3.32	62.5	5.0	35.5	8.9	27.0	27.0		357	0.005	41	0.637	0.015	23.5	5.4	114.3	27.6	
Mean		58.3		11.3	2.8	13.3	13.3	0.8	76	0.009	48							
co5x-z-1	4.78	24.6	2.0	11.3	2.8	15.0	15.0	3.4	38	0.027	68							
co5x-z-1	4.04	39.3	3.1	13.8	3.5	25.5	27.4		71	0.017	53							
co5x-z-2	5.73	43.9	3.5	17.5	4.4	26.4	28.4		75	0.017	41							
co5x-z-3	5.06	47.8	3.8	22.2	5.6	25.6	27.5		75	0.017	41							
Mean		43.7		22.2	5.6	25.6	27.8	0.4				1.201	0.019	23.1	0.5	112.6	5.7	
													Weighted mean for zircon		23.3	0.4	114.3	
Apatite																		
co5x-a-1	4.56	23.8	1.9	6.4	1.6	17.4	19.5	2.5	1.8	0.346	100	0.637	0.015	30.6	4.0	149.0	20.9	
co5x-a-1	3.06	44.6	3.6	10.5	2.6	34.1	36.6	4.4	11.5	0.104	101	1.201	0.019	30.5	3.7	148.6	19.8	
													Weighted mean for apatite		30.6	2.7	148.8	14.4

All samples uncrushed; $^3\text{He}_m$ = measured during heating; $^3\text{He}_{\text{cp}+\text{nuc}+\text{mu}}$ = calculated concentration of all Li-produced ^3He components; $^3\text{He}_{\text{sp}}$ = after subtraction of Li-produced components. $^3\text{He}_{\text{sp}}(z=0)$, after correction for sampling depth (if necessary); $^4\text{He}_m$ = measured during heating; Eq. Rad. = mean equivalent spherical radius calculated following Farley et al. (1996).

**Figure 3.1**

Spallogenic ^3He ($^3\text{He}_{\text{sp}}$) vs. crush-corrected ^3He ($^3\text{He}_{\text{cc}}$) in pyroxene, olivine, and garnet. Samples plot to the left of the 1:1 line owing to the presence of Li-produced ^3He . Each of the four data points for pyroxene and olivine represents the mean for a given sample (i.e. co5, co6, co5x and co6x). Garnet was only found in sample co5.

**Figure 3.2**

Relationship between grain-size and measured ^3He ($^3\text{He}_m$) in zircon (upper panel), and the same relationship after correction for Li-produced ^3He ($^3\text{He}_{\text{sp}}$, lower panel). The grain-size relationship is due to the implantation of Li-produced and spallation produced ^3He from neighboring mineral phases.

3.4.3 Neon Results

Results of neon analyses are presented in Table 3.5 and Figure 3.3. Measured $^{21}\text{Ne}/^{20}\text{Ne}$ and $^{22}\text{Ne}/^{20}\text{Ne}$ ratios in hand-picked quartz samples plot within error of the air-cosmogenic mixing line for quartz on a three-isotope diagram (Niedermann et al., 1993). In addition, two analyses were made of inclusion bearing quartz extracted from the samples; these plot well away from the air-cosmogenic mixing line. Four samples of pyroxene degassed at 1500°C also plot within error of the air-cosmogenic mixing line for quartz, and are statistically indistinguishable from the mixing line of lower slope proposed for pyroxene (Schafer et al., 1999). Two additional pyroxene samples degassed by complete fusion of the grains using a laser give $^{21}\text{Ne}/^{20}\text{Ne}$ and $^{22}\text{Ne}/^{20}\text{Ne}$ ratios that plot away from the mixing line, and closer to the MORB line (Staudacher and Allegre, 1993).

Table 3.5: ^{21}Ne analyses

Sample	Mass (g)	$^{20}\text{Ne}_m$ (Mat/g)	$1\sigma\text{SD}$ (Mat/g)	$^{21}\text{Ne}_m$ (Mat/g)	$1\sigma\text{SD}$ (Mat/g)	$^{22}\text{Ne}_m$ (Mat/g)	$1\sigma\text{SD}$ (Mat/g)	$\frac{^{21}\text{Ne}}{^{20}\text{Ne}}$	$\frac{^{22}\text{Ne}}{^{20}\text{Ne}}$	$^{21}\text{Ne}_{\text{air}}$ (Mat/g)	$^{21}\text{Ne}_{\text{nuc}}$ (Mat/g)	$^{21}\text{Ne}_c$ (Mat/g)	$^{21}\text{Ne}_{c(z=0)}$ (Mat/g)	$1\sigma\text{SE}$ (Mat/g)	^{10}Be (Mat/g)	$1\sigma\text{SD}$ (Mat/g)	$\frac{^{21}\text{Ne}_c}{^{10}\text{Be}}$	$^{21}\text{Ne PR}$ (at g $^{-1}$ a $^{-1}$)	$1\sigma\text{SE}$ (at g $^{-1}$ a $^{-1}$)
co5-Q1	0.5124	6371	85.5	21.4	1.0	649	13.0	0.0034	0.1019	18.85	0.00	2.52	2.52						
co5-Q2	0.4802	6271	87.0	20.7	0.9	642	12.8	0.0033	0.1023	18.56	0.00	2.19	2.19						
co5-Q3	0.3306	6339	84.0	21.0	1.0	652	13.0	0.0033	0.1028	18.76	0.00	2.29	2.29						
co5-Q4	0.2565	1292	25.8	5.9	0.4	134	5.4	0.0046	0.1040	3.82	0.00	2.09	2.09						
Mean														0.11	0.637	0.015	3.57	17.4	1.2
co6-Q1	0.5053	3864	75.3	15.3	0.6	402	8.0	0.0042	0.1040	11.43	0.00	4.83	4.83						
co6-Q2	0.3278	6526	117.5	23.9	1.1	674	13.5	0.0037	0.1033	19.31	0.00	4.63	4.63						
co6-Q3	0.2563	1265	38.0	7.9	0.3	133	4.7	0.0062	0.1053	3.74	0.00	4.15	4.15						
co6-Q4	0.2559	5850	114.1	21.4	0.9	602	12.0	0.0037	0.1029	17.31	0.00	4.14	4.14						
co6-Q5	0.2542	1728	51.8	3.6	0.5	179	6.3	0.0055	0.1034	5.11	0.00	4.46	4.46						
Mean												4.44	4.44	0.15	1.201	0.019	3.70	18.0	1.1
Weighted mean quartz																			
Co5x-P1	0.4053	4733	52.3	13.0	0.8	484	9.7	0.0038	0.1023	14.01	0.07	3.88	4.36						
Co6x-P1	0.2433	2158	48.6	14.1	0.8	227	4.5	0.0066	0.1053	6.39	0.14	7.61	8.18						
Co6x-P2	0.2443	7881	130.0	30.6	1.3	814	16.3	0.0039	0.1033	23.32	0.14	7.12	7.65						
Co6x-P3	0.1070	3282	73.8	17.0	0.9	341	6.8	0.0052	0.1039	9.71	0.14	7.15	7.69						
Mean												7.29	8.42	0.21	1.201	0.019	7.01	34.2	1.7
Weighted mean pyroxene																			
Co5-Qincl.	0.0071	286757	4302	735.2	35.2	26434	528.6	0.0026	0.0922										
Co6-Qincl.	0.0508	44538	667.5	133.4	6.4	4445	88.8	0.003	0.0998										
co5x-Plaser	0.1776	1285	38	5.2	0.5	114	3.85	0.0041	0.0885										
co6x-Plaser	0.1025	3582	81	27.9	1.2	254	7.5	0.0078	0.0709										

$^{21}\text{Ne}_{\text{air}}$ = concentration of ^{21}Ne derived from air contamination of sample; $^{21}\text{Ne}_{\text{nuc}}$ = concentration of ^{21}Ne calculated from reactions $^{18}\text{O}(\alpha,n)^{21}\text{Ne}$ and $^{24}\text{Mg}(n,\alpha)^{21}\text{Ne}$.

$^{21}\text{Ne}_c$ = concentration of cosmogenic ^{21}Ne remaining after subtraction of $^{21}\text{Ne}_{\text{air}}$ and $^{21}\text{Ne}_{\text{nuc}}$ components from measured component ($^{21}\text{Ne}_m$).

"Qincl" denotes inclusion-bearing quartz samples; "Plaser" denotes pyroxene samples fused with a Nd-YAG laser.

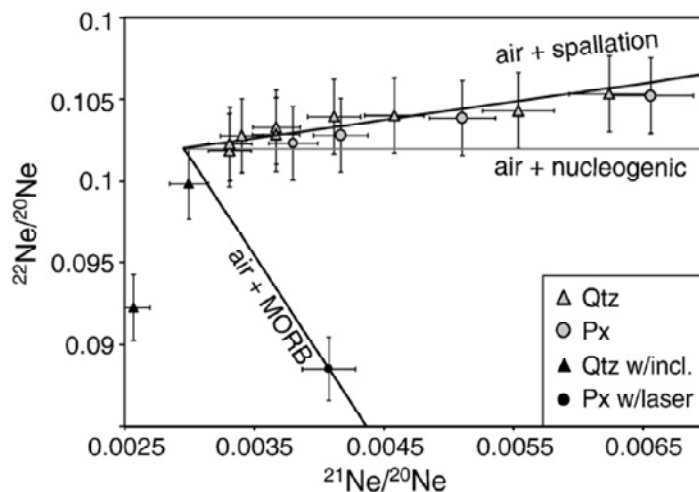


Figure 3.3

Neon three-isotope diagram showing that most Coso samples plot along an air-spallation mixing line. Grey symbols represent data used to calculate the ^{21}Ne production rate. Black symbols show analyses of inclusion bearing quartz (triangles) and pyroxene fused with laser (circles), which contain significant non-cosmogenic neon components and thus plot away from the air-spallation mixing line for quartz, with slope of 1.12 (Niedermann, 2002).

3.4.4 Li Concentrations

Results of Li analyses are summarized in Table 3.6. Concentrations of Li are high in most minerals, ranging from a minimum of ~1.4 ppm in some zircons to >5000 ppm in biotite. Zircon and apatite cluster from 1-15 ppm, olivine and pyroxene from 25-50 ppm, quartz and garnet near 100 ppm, and feldspars around 150 ppm.

The distributions of minerals adjacent to apatite and zircon (section 3.6) and their associated Li content are presented in online Table 3.4. These differ significantly between the rhyolite (co-5/6) and the andesitic inclusions (co-5x/6x). Zircons in the rhyolite are primarily in contact with matrix material, which in combination with a small amount of high-Li biotite gives an average Li content of 430-668 ppm. In the andesitic inclusions, zircons and apatites are in contact primarily with feldspar and matrix material, with average Li contents of 360-400 ppm. In both cases, average Li contents of adjacent mineral assemblages are extremely high, and are most sensitive to small amounts of contact area with biotite, a high Li phase.

Table 3.6: Host mineral Li calculations

Sample:	co5-zr (n=53)			co6-zr (n=53)			co5x-zr (n=40)			co6x-zr (n=40)			co5x-ap (n=63)			co6x-ap (n=63)		
	Fr	Li (ppm)	W. Li (ppm)	Fr	Li (ppm)	W. Li (ppm)	Fr	Li (ppm)	W. Li (ppm)	Fr	Li (ppm)	W. Li (ppm)	Fr	Li (ppm)	W. Li (ppm)	Fr	Li (ppm)	W. Li (ppm)
Matrix	0.79	153	121	0.79	159	126	0.31	423	129	0.31	683	208	0.46	423	194	0.46	513	235
Feldspar	0.05	140	7	0.05	140	7	0.37	27	10	0.37	19	7	0.37	27	10	0.37	19	7
Quartz	0.07	108	7	0.07	115	8	0.00	20	0	0.00	15	0	0.00	20	0	0.00	15	0
Pyroxene	0.02	53	1	0.02	41	1	0.17	20	3	0.17	12	2	0.06	20	1	0.06	12	1
Biotite	0.06	5070	294	0.06	8576	497	0.09	2490	216	0.09	2100	182	0.06	2490	155	0.06	2100	130
Avg. Li of adj. phases:	430			638			358			399			360			373		

"Fr" = fraction of zircon or apatite surface area in contact with mineral; "Li" = Li content of mineral (ppm), "W. Li" = Li content weighted by contact area

"n" = the number of zircon or apatite grains documented with minimum dimension > 20µm

Summing over the "W. Li" column gives the average Li content of the adjacent mineral phases for that sample

3.4.5 Compositional Analysis

Mineral compositions were determined using the JEOL JXA-8200 electron microprobe at Caltech, and are summarized in online Table 3.1. Pyroxenes have an augitic composition averaging $(\text{Ca}_{0.83}, \text{Na}_{0.02})(\text{Mg}_{0.76}, \text{Fe}_{0.23}, \text{Al}_{0.28})(\text{Si}_{1.8}, \text{Al}_{0.28})\text{O}_6$. Olivines average Fo₇₆, with very little compositional variation. Garnets have a spessartine/almandine composition averaging $(\text{Mn}_{1.57}, \text{Ca}_{0.17}, \text{Mg}_{0.12}, \text{Fe}_{1.33})\text{Al}_{1.8}\text{Si}_3\text{O}_{12}$.

Table 3.7: Mineral compositions determined by electron microprobe analysis

Mineral	SiO ₂	TiO ₂	Al ₂ O ₃	Cr ₂ O ₃	FeO	MnO	MgO	CaO	Na ₂ O	Totals
Olivine										
co5	38.5	0.0	0.0	0.0	21.9	0.3	40.3	0.3	0.0	101.3
co5x	39.4	0.0	0.0	0.0	20.6	0.3	40.9	0.2	0.0	101.6
co6	38.9	0.0	0.0	0.0	21.6	0.3	40.0	0.3	0.0	101.2
co6x	38.4	0.0	0.0	0.0	24.6	0.4	37.7	0.2	0.0	101.3
Pyroxene										
co5	50.2	1.2	6.3	0.1	7.0	0.1	14.8	20.9	0.5	101.1
co5x	48.3	1.9	6.9	0.1	7.9	0.2	13.5	21.2	0.6	100.4
co6	49.2	1.5	6.4	0.2	7.4	0.2	14.0	21.1	0.6	100.5
co6x	49.0	1.8	6.2	0.0	8.3	0.2	13.6	21.2	0.6	100.8
Garnet										
co5	37.0	0.3	19.3	0.0	18.8	22.5	1.1	1.7	0.0	100.8

3.5 Data Interpretation

3.5.1 Interpretation of Measured ³He

Several lines of evidence suggest that the ^3He in all five minerals is dominantly cosmogenic. First, measured $^3\text{He}_{\text{co5/5x}}/^3\text{He}_{\text{co6/6x}}$ ratios for each phase range between 0.48 and 0.59, similar to the value of 0.53 obtained for ^{10}Be in quartz. If a large non-cosmogenic component were present in *subequal concentrations* in the two different samples, it would skew the observed $^3\text{He}_{\text{co5/5x}}/^3\text{He}_{\text{co6/6x}}$ ratio. Likewise, the concentrations of ^3He in different phases within each sample are roughly equal, implying that the different phases do not contain a large non-cosmogenic component of *variable concentration*.

Nevertheless the Li contents in each of the mineral phases and in their host phases are high enough that a correction for Li-produced ^3He is required before estimating a production rate. In addition, we observe a strong correlation between measured ^3He and grain size in zircon (Figure 3.2), implying that there is a significant implanted ^3He component, either Li or spallation-produced, that needs to be accounted for.

The amount of spallation-produced ^3He in each sample can be expressed as:

$$^3\text{He}_{\text{sp}} = ^3\text{He}_{\text{m}} - ^3\text{He}_{\text{in}} - ^3\text{He}_{\text{nuc}} - ^3\text{He}_{\text{cn}} - ^3\text{He}_{\text{mu}} \quad (3.1)$$

where $^3\text{He}_{\text{sp}}$ is the ^3He produced via cosmic ray spallation, $^3\text{He}_{\text{m}}$ is the total ^3He measured in the sample, $^3\text{He}_{\text{in}}$ is inherited from inclusions or prior exposure, $^3\text{He}_{\text{nuc}}$ is the nucleogenic component produced by capture of neutrons produced from (α, n) reactions on light elements, $^3\text{He}_{\text{cn}}$ is the ^3He produced by capture of slow neutrons derived from interactions with “secondary” cosmogenic neutrons, and $^3\text{He}_{\text{mu}}$ is produced directly from stopping of slow muons and from capture of slow neutrons derived from muon interactions.

3.5.2 The Magmatic He Component

Assuming our samples did not experience prior exposure, the inherited ^3He component ($^3\text{He}_{\text{in}}$) is only magmatic. For uncrushed mineral phases (other than apatite and zircon), the magmatic component is taken as the concentration of ^3He released during crushing of other

aliquots of the same mineral separate, and is subtracted from the measured ^3He ($^3\text{He}_m$) in uncrushed samples to give the crush-corrected ($^3\text{He}_{cc}$) value (Table 3.3). For samples that were crushed prior to fusion, it is assumed that the entire magmatic component was released during crushing, and no correction is made. This differs from the typical approach used to calculate the magmatic component, which is to calculate $^3\text{He}_{in} = ^4\text{He}_{fusion} * (^3\text{He}/^4\text{He})_{crush}$ implicitly assuming that all ^4He in the fused sample is magmatic (Blard and Farley, 2008; Blard and Pik, 2008; Kurz, 1986b). This approach is not appropriate here because the measured ^4He concentrations in our pyroxene and olivine samples are high and variable, leading to erroneous corrections. Variability in ^4He concentration may be attributed to the presence of mineral inclusions or to implanted ^4He from high U and/or Th phases that were intergrown with pyroxene and olivine. The approach used in this study is a reasonable alternative based on the fact that replicate crushings of pyroxenes from sample co-5x and co-6x released comparable amounts of ^3He , and because correction of uncrushed samples by this approach brings the resultant ^3He concentrations into good agreement with crushed samples (Table 3.3). For apatite and zircon, the $^3\text{He}_{in}$ component is assumed to be negligible because the grain size is too small for significant fluid inclusion retention.

3.5.3 Quantifying Li-Produced ^3He Components

To calculate each Li-produced component, we follow the procedure described in Amidon et al. (2008a), which is described and applied in the online appendix to this paper. These calculations reveal that the total Li-produced ^3He ($^3\text{He}_{cn}$, $^3\text{He}_{mu}$, and $^3\text{He}_{nuc}$) for pyroxene and olivine varies, but is ~ 4 and ~ 6.5 Mat/g for co-5/5x and co-6/6x respectively (Table 3.3), or about 12-20% of the matrix-sited ^3He ($^3\text{He}_{cc}$). For garnet, this number is ~ 7.2 Mat/g, or $\sim 27\%$ of the measured ^3He . The difference between samples co-5/5x and co-6/6x is due to the different $^3\text{He}_{cn}$ components which result from using the different steady-state erosion rates inferred from

the ^{10}Be results. Because the Coso samples have a young eruptive age and a long exposure duration, the $^3\text{He}_{\text{nuc}}$ component is about 1/3 the size of the $^3\text{He}_{\text{cn}}$ component. Neutrons produced from fast muon stopping and direct production of ^3He from fast muons are found to be negligible, whereas neutrons derived from stopping of slow muons account for ~20% of the total Li-derived ^3He .

In zircon the total Li-produced ^3He concentrations are grain size dependent, and reach maxima of ~19 and ~35 Mat/g for samples co-5/5x and co-6/6x respectively (Table 3.4). For apatite, values of 6.4 and 10.5 Mat/g are estimated for co-5x and co-6x respectively. Because the magnitude of the Li-produced ^3He component is grain size dependent, subtraction of this component reduces the slope of the correlation between grain size and ^3He for zircon (Figure 3.2). This grain size effect is not important for larger grain sizes (i.e., olivine, pyroxene and garnet), and is not observable in apatite because only one grain size fraction was analyzed.

Uncertainties on the Li-produced ^3He estimates were calculated using a Monte Carlo simulation in which 11 variables were allowed to vary with a 1σ standard deviation of 15% over 1000 trials. These variables include internal Li content of the mineral, average Li content of adjacent minerals, bulk rock concentrations of the trace elements that strongly modulate neutron production or absorption (H, Li, B, Gd, Sm, U and Th), grain radius, and erosion rate. Although the major elements Si, K, Na and Al account for ~50% of neutron absorption, their published concentrations in the Devil's Kitchen rhyolite are unlikely to be wrong by more than a few relative percent and they are not included in the error analysis. For the coarser mineral phases (pyroxene, olivine, and garnet), a 15% standard deviation for each of the 11 input variables translates through the Monte Carlo model to a ~21% standard deviation in total Li-produced ^3He . Zircon and apatite are more sensitive to uncertainties in grain size and host Li content, and thus have ~25% standard deviations on the total Li-produced ^3He .

An additional source of uncertainty arises from our interpretation of the ^{10}Be concentrations as steady-state erosion rates. This interpretation affects calculated spallation ^3He

production rates in two ways: 1) the size of the $^3\text{He}_{\text{cn}}$ component, and 2) the possibility of ^{10}Be decay over time. To explore the sensitivity of our ^3He production rates to our interpreted erosional history, we consider two end-member alternatives. In the “uneroded surface” case, the surfaces were instantaneously exhumed from > 3 m depth at the time of their apparent ^{10}Be exposure age and remained uneroded. In this case, the $^3\text{He}_{\text{cn}}$ component is 25-40% higher than in the steady-state erosion case, and ^{10}Be decay remains insignificant. In the “uneroded and buried surface” case, surfaces were exposed immediately after eruption for the duration of their ^{10}Be exposure ages and then buried abruptly until being instantly exhumed in the very recent past. In this case, the $^3\text{He}_{\text{cn}}$ components would again be 25-40% higher, and $\sim 25\%$ of the ^{10}Be would have decayed during burial. When production rates are calculated assuming these alternative exhumation models, both models show a negative relationship between production rate and apparent Li (Figure 3.4). This relationship suggests that these non steady-state models result in overcorrection for the Li-produced component. Additionally, when plotted on a diagram of $^{10}\text{Be}/^{21}\text{Ne}$ vs ^{10}Be concentration, both samples fall within error of the steady-state erosion regime (Lal, 1991).

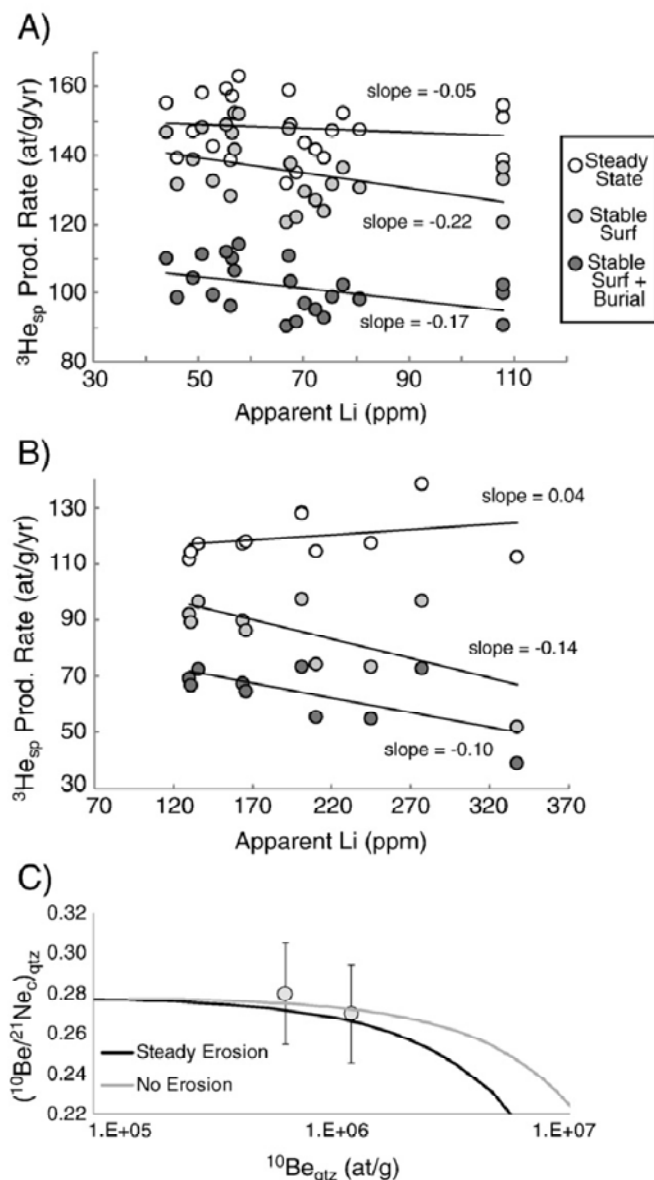


Figure 3.4

Spallation ^3He production rate versus apparent Li for all pyroxene, olivine and garnet analyses (panel A), and for all zircon analyses (panel B). Open symbols were corrected for Li-produced ^3He components assuming a steady-state erosional history as described in the text, and reported in the data tables. Grey circles are calculated assuming an alternative exhumational history in which the surface was exposed at the ^{10}Be exposure age, and remained uneroded until today. Black symbols are calculated assuming a second alternative scenario in which the surface was exposed immediately after eruption for the duration of the ^{10}Be exposure age, then buried for ~ 560 Ka, and abruptly re-exhumed in very recent times causing $\sim 25\%$ of the ^{10}Be to decay. The negative slopes of the two alternative exhumation histories show that these interpretations would lead to over-correction for the Li-produced ^3He component. Panel C shows that our two samples fall within 2σ error of the steady-state erosion island defined by Lal et al. (1991), using SLHL production rates of 4.87 and 17.7 at $\text{g}^{-1} \text{a}^{-1}$ for ^{10}Be and ^{21}Ne respectively, and a scaling factor of 2.75.

3.5.4 Cosmogenic ^3He Production Rates

Subtracting the Li-produced ^3He improves agreement in production rate among all phases, demonstrating that the calculations are reasonable (Tables 3.3 and 3.4). Pyroxene, olivine and garnet give mean $^3\text{He}_{\text{sp}}$ concentrations of ~ 18.4 and ~ 35.5 Mat/g for samples co-5/5x and co-6/6x respectively (Figure 3.1). By taking the $^3\text{He}_{\text{sp}}/^{10}\text{Be}$ ratio and multiplying by an average ^{10}Be production rate of 4.87 at $\text{g}^{-1} \text{a}^{-1}$ (Balco et al., 2008), grand mean production rates of

145 ± 11, 141 ± 16, and 144 ± 30 at g⁻¹ a⁻¹ (2σ) are calculated for pyroxene, olivine, and garnet respectively. Zircon gives mean ³He_{sp} concentrations of 15.4 and 27.7 Mat/g for co-5/5x and co-6/6x respectively, averaged over equivalent radii from 33-78 μm. Apatite gives 19.5 and 36.6 Mat/g respectively for equivalent radii of ~100 μm (Figure 3.2). Repeating the above calculation, the mean apparent production rates for zircon and apatite are 114 ± 8 and 149 ± 28 at g⁻¹ a⁻¹ (2σ).

Errors on production rates are derived from the quadratic propagation of errors on ³He_{sp}, the ¹⁰Be measurement, and the ¹⁰Be production rate. The standard errors on ³He_{sp} for pyroxene, olivine, garnet and apatite were calculated by taking the standard error on replicate measurements of ³He_{cc} for a given phase and propagating it in quadrature with the constant Monte-Carlo error on the Li-³He component for that phase. The 1σ standard error on the ¹⁰Be production rate is taken from Balco et al. (2008) as 4.87 ± 0.26. Because estimates of Li-produced ³He are grain size dependent for zircon, we calculate errors on ³He_{sp} for each analysis individually, take the standard error of all analyses for a given sample, and then propagate this with the ¹⁰Be measurement error and the ¹⁰Be production rate error. The weighted mean of all samples for a given mineral phase is then computed as well as the weighted mean error, and reported above. This analysis ignores systematic errors associated with instrument calibration, as they are thought to be <1% (Min et al., 2003).

3.5.5 Cosmogenic ²¹Ne Production Rates

The amount of cosmogenic ²¹Ne (²¹Ne_c) is calculated by:

$${}^{21}\text{Ne}_c = {}^{21}\text{Ne}_m - {}^{21}\text{Ne}_{\text{air}} - {}^{21}\text{Ne}_{\text{nuc}} \quad (3.2)$$

where ²¹Ne_m is the measured ²¹Ne in the sample, ²¹Ne_{air} is the ²¹Ne derived from trapped air components, and ²¹Ne_{nuc} is the ²¹Ne produced by nucleogenic sources, primarily the reactions ¹⁸O(α,n)²¹Ne and ²⁴Mg(n,α)²¹Ne.

Assuming that all ^{20}Ne is derived from air allows the $^{21}\text{Ne}_{\text{air}}$ component to be calculated by:

$$^{21}\text{Ne}_{\text{air}} = ^{20}\text{Ne}_m \times \left(\frac{^{21}\text{Ne}}{^{20}\text{Ne}} \right)_{\text{air}} \quad (3.3)$$

where $(^{21}\text{Ne}/^{20}\text{Ne})_{\text{air}}$ is the known ratio of 0.002959 in air (Niedermann, 2002).

Because quartz has very little U and Th (the primary sources of α particles), $^{21}\text{Ne}_{\text{nuc}}$ is assumed to be zero. Neon produced by implanted α particles cannot be ruled out although a >300 μm grain diameter and HF leaching should minimize this component (Kohl and Nishiizumi, 1992). However, because pyroxenes can contain moderate amounts of U and Th (Blard and Pik, 2008) and because they are retentive to helium, the amount of radiogenic ^4He can be used to make a rough estimate of $^{21}\text{Ne}_{\text{nuc}}$ based on the relationship:

$$^{21}\text{Ne}_{\text{nuc}}/^4\text{He} = 5.2 \times 10^{-8} \times F_0 \quad (3.4)$$

where F_0 is the mass fraction of oxygen in the mineral (Eikenberg et al., 1993). The mass fraction of oxygen in the pyroxenes is ~ 0.43 , and average ^4He concentrations are 1.7×10^{12} and 3.8×10^{12} at/g, yielding a $^{21}\text{Ne}_{\text{nuc}}$ component of 0.038 and 0.085 Mat/g for co-5x and co-6x respectively, or $\sim 1.2\%$ in both cases. We also consider ^{21}Ne production via the reaction $^{24}\text{Mg}(n,\alpha)^{21}\text{Ne}$, which has a cutoff energy of ~ 3 MeV, and a resonance integral of ~ 0.0054 barns (Nakagawa et al., 2002). An approximate calculation of ^{21}Ne derived from neutron capture by ^{24}Mg can be made by multiplying the radiogenic and cosmogenically derived neutron fluxes (Table 3.8) by the resonance integral and by the atomic density of ^{24}Mg in pyroxene. This calculation yields ~ 0.006 Mat/g of production from radiogenic neutrons, and ~ 0.024 and 0.053 Mat/g of production from cosmogenically derived thermal neutrons in samples co-5 and co-6 respectively.

After subtraction of the small nucleogenic component, production rates of ^{21}Ne are calculated by multiplying the $^{21}\text{Ne}/^{10}\text{Be}$ ratio by the stated ^{10}Be production rate. Averages of all

analyses are 17.7 ± 1.6 and 34.1 ± 3.2 at $\text{g}^{-1} \text{a}^{-1}$ (2σ) in quartz and pyroxene respectively (Table 3.5). The higher value in pyroxene arises from the presence of Mg and Al, which produce more ^{21}Ne than does Si (Leya et al., 1998b). Errors for a given sample are calculated by determining the standard error on replicate estimates of $^{21}\text{Ne}_c$ and propagating this in quadrature with errors on the measured ^{10}Be and the ^{10}Be production rate. The weighted mean of all samples for a given mineral phase is then computed as well as the weighted mean error.

Table 3.8: Selected parameters output from neutron flux calculations

RN stopping rate (n/g*yr*ppm U)	1.92
RN stopping rate (n/g*yr*ppm Th)	0.662
CN stopping rate (n/g*yr)*	950
FMN stopping rate (n/g*yr)*	12.5
SMN stopping rate (n/g*yr)*	167.2
Direct muon produced ^3He ($^3\text{He}/\text{g*yr}$)*	42.7
^3He P.R. from CNs ($^3\text{He}/\text{g*yr*ppm Li}$)*	0.95
^3He P.R. from RNs ($^3\text{He}/\text{g*yr*ppm Li}$)*	0.54
ppm Li in bulk rock	156
Fractional XS of Li	0.1561
Resonance escape probability	0.93
Effective resonance integral (cm^2/g)	0.0029
Macroscopic scattering XS (cm^2/g)	0.1253
Macroscopic absorption XS (cm^2/g)	0.0061

RN=radiogenic slow neutrons, CN=cosmogenic produced slow neutrons

FMN=fast muon produced slow neutrons, SMN=slow muon produced slow neutrons

* Average in upper 4 cm of rock at 1333 m for a 49 Ky exposure age

3.6 Discussion

3.6.1 ^3He Production Rates

Our SLHL production rates of 145 ± 11 and 141 ± 16 at $\text{g}^{-1} \text{a}^{-1}$ (2σ) in pyroxene and olivine are higher than the highest value of 122 ± 14 at $\text{g}^{-1} \text{a}^{-1}$ (1σ) reported by Balco et al. (2008) scaled following Lifton et al. (2005). However, our results are similar to those of Ackert et al. (2003), which were attributed to anomalously low air pressure over the study area. Our values are slightly higher than those of Blard et al. (2006), and are somewhat lower than the average of 159 at $\text{g}^{-1} \text{a}^{-1}$ for olivine and pyroxene calculated from element specific production rates (Kober et al., 2005). Our production rate of 144 ± 30 at $\text{g}^{-1} \text{a}^{-1}$ in garnet is lower than the value of 153 at $\text{g}^{-1} \text{a}^{-1}$ reported by Amidon et al. (2008a) and 154 at $\text{g}^{-1} \text{a}^{-1}$ which they recalculate from the data of

Gayer et al. (2004). This lower value is consistent (although not perfectly) with the apparent overproduction observed at high-elevation in Nepal by both of these studies, and matches the production rate calculated from element-specific production rates of $145 \text{ at g}^{-1} \text{ a}^{-1}$ (Kober et al., 2005).

Our results for pyroxene and olivine thus contribute to the surprisingly wide range of estimated ^3He production rates in these phases. One possible explanation for our higher values relative to those summarized in Balco et al. (2008) is that we compare ^3He directly to ^{10}Be , rather than to a surface exposure age inferred from the crystallization age of a lava flow. We thus avoid the assumption that the sampled flow is uneroded and has never experienced burial, both of which would lower the apparent ^3He production rate in a calibration study. We also avoid the assumption that all ^4He released during fusion of a crushed pyroxene or olivine sample is derived from a mantle component. Studies which follow this procedure, without measuring the U and Th contents of the pyroxene or olivine, may be subject to overcorrection for mantle ^3He (Blard and Farley, 2008; Blard and Pik, 2008). Because these corrections can be as large as 90%, this could lead to a significant underestimate of the amount of cosmogenic ^3He in a sample.

For zircon and apatite, we estimate mean apparent production rates of 114 ± 8 and $149 \pm 28 \text{ at g}^{-1} \text{ a}^{-1}$, for a grain size range of 40-80 μm in zircon, and 100 μm in apatite. Since the first estimates of production rates in these minerals were published by Farley et al. (2006), a ^{10}Be analysis has been obtained on quartz from their sample C3_C4 (3.1). Calculating $^3\text{He}/^{10}\text{Be}$ ratios for sample C3_C4, and multiplying by a ^{10}Be production rate of $4.994 \text{ at g}^{-1} \text{ a}^{-1}$, gives apparent production rates of 114 ± 22 , 144 ± 28 , and $126 \pm 15 \text{ at g}^{-1} \text{ a}^{-1}$ (2σ) for zircon, apatite, and titanite. A subsequent study by Amidon et al. (2008a) proposes an elevation dependent production rate in Nepal, and the lowest elevation sample in their dataset, sample CRN-259 (3215 m), gives apparent production rates of 137 ± 26 and $170 \pm 32 \text{ at g}^{-1} \text{ a}^{-1}$ (2σ) for zircon and apatite respectively. Thus it appears that results from the current study are in good agreement with

results from Bolivia, but somewhat lower than results from Nepal (Amidon et al., 2008a; Farley et al., 2006).

We use the term apparent production rates for zircon and apatite because we have not accounted for redistribution of spalled ^3H and ^3He nuclei among adjacent grains. Because adjacent silicate minerals have higher spallation production rates than in zircon and apatite, a negative correlation between grain-size and $^3\text{He}_{\text{sp}}$ is expected in these phases (Farley et al., 2006). Zircons from sample co-5 show a linear correlation ($r^2=0.98$) between mean equivalent radius (MER) and apparent production rate (APR) described by the linear fit $\text{APR} = -0.55 \cdot \text{MER} + 156$. The apparent production rate in grains with MER of 78 μm is about 20% lower than in grains with MER of 33 μm . A grain size experiment on zircons from Himalayan gneisses also resulted in $\sim 20\%$ lower production rates between mean widths of 38 and 100 μm , whereas results from zircons in a Bolivian ignimbrite showed $\sim 10\%$ decrease in production rate between widths of 50 and 100 μm (Amidon et al., 2008a; Farley et al., 2006). Future datasets may allow calculation of the spalled ^3He and ^3H stopping ranges, and thus of the in-situ ^3He production rate in zircon and apatite. However, the present data suggest that ^3He dating in apatite and zircon can be undertaken using apparent production rates in coarser grain size fractions.

3.6.2 ^{21}Ne Production Rates in Quartz and Pyroxene

The ^{21}Ne production rate of 17.7 ± 1.6 at $\text{g}^{-1} \text{a}^{-1}$ (2σ) we obtain for quartz is within error of all previous calibration studies. This value is 7% less than the value of 19.0 ± 3.7 (2σ) reported by Niedermann, (2000) and similar to a value of 17.7 ± 2.6 at $\text{g}^{-1} \text{a}^{-1}$ that they rescaled from a study of quartz targets exposed for three years at an elevation of 4250 m on Mt. Evans, CO (Graf et al., 1996). Likewise, a recent study that exposed quartz targets over a range of elevation in the Alps for one year found ^{21}Ne production rates of 16.9 ± 1.9 at $\text{g}^{-1} \text{a}^{-1}$ (2σ) (Vermeesch et al., 2008). Our $^3\text{He}_{\text{px}}/^{21}\text{Ne}_{\text{qtz}}$ ratio (~ 8.2) and our $^3\text{He}_{\text{px}}/^{21}\text{Ne}_{\text{qtz}}$ ratio (~ 8.0) are identical to the values reported

from a basaltic andesite in Argentina (Niedermann et al., 2007). The ^{21}Ne production rate of 34.1 ± 3.2 at $\text{g}^{-1} \text{a}^{-1}$ (2σ) we calculate in pyroxene gives a $^{21}\text{Ne}_v/^{3}\text{He}_{\text{sp}}$ ratio of ~ 0.235 , which is similar to the ratio of 0.236 measured in Antarctic pyroxenes (Bruno et al., 1997a; Schafer et al., 1999). This ratio is also similar to ratios of 0.19-0.20 reported from pyroxenes in a Pleistocene lava flow in the western United States (Fenton et al., 2007).

One reason ^{21}Ne production rates may vary between studies is if the neon inventory is not a simple mixture of cosmogenic, nucleogenic and air-derived neon. When our data are plotted on a three-isotope diagram (Figure 3.3), most samples plot near the air-cosmogenic mixing line, suggesting they contain only these three components. However, the hand-picked inclusion-bearing quartz samples, and the two pyroxene samples fused with the laser plot closer to the air-MORB mixing line suggesting that they may also contain a mantle-derived neon component. The fact that pyroxene samples fused with the laser plot near the MORB mixing line, but pyroxene samples heated with the furnace plot near the cosmogenic mixing line suggests that the pyroxenes contain a mantle component which is only released by complete fusion of the crystal (Staudacher and Allegre, 1993). A similar release pattern for mantle-derived neon has been observed in some previous studies (Niedermann, 2002).

3.6.3 An Alternate Method of Calculating Li-Produced ^3He

The labor-intensive approach to calculating the Li-produced ^3He components used in this study (see online appendix) involves point counting of adjacent minerals, Li measurement in all mineral phases, and documentation of average grain size for each sample. A simpler alternative is to measure $^3\text{He}_{\text{nuc}}$ in a shielded sample. At face value, this is of limited use because the shielded minerals do not contain the potentially larger $^3\text{He}_{\text{cn}}$ component produced in the near-surface. However, if the petrology and grain size of the shielded and exposed samples are identical, we can use the shielded ^3He concentration, the (U-Th)/He closure age, the bulk rock

composition, and a neutron production-diffusion model to solve for the grain-size specific apparent Li. Significant time and effort are saved because it is not necessary to measure Li in any mineral phases or to document the distribution of adjacent minerals.

For uneroded surfaces or for surfaces experiencing steady-state erosion, the apparent Li of a mineral determined from the shielded sample can be used to calculate the ${}^3\text{He}_{cn}$ component acquired in the near-surface. Assuming the exposure age or erosion rate of a surface is unknown, the ${}^3\text{He}_{cn}$ concentration is given by:

$${}^3\text{He}_{cn} = ({}^3\text{He}_m - {}^3\text{He}_{muc}) * \frac{{}^3\text{He}_{cn}}{({}^3\text{He}_{cn} + {}^3\text{He}_{sp})} \quad (3.5)$$

where ${}^3\text{He}_m$ is the measured ${}^3\text{He}$ concentration in the surface sample, and ${}^3\text{He}_{sp}$ is the unknown concentration of spallation produced ${}^3\text{He}$. For an uneroded surface, the ratio in the second term in equation 5 is independent of exposure age and is given by:

$$\frac{{}^3\text{He}_{cn}}{({}^3\text{He}_{cn} + {}^3\text{He}_{sp})} = \frac{P_{cn}(0)}{(P_{cn}(0) + P_{sp}(0))} \quad (3.6)$$

Where the spallation production rate $P_{sp}(0)$ is assumed to be known, and the CN production rate $P_{cn}(0)$ can be calculated using the apparent Li and a neutron production-diffusion model (see online appendix). In cases of steady erosion over a time-scale sufficient to have exhumed more than $\sim 800 \text{ g/cm}^2$, the second term in equation 5 is also independent of erosion rate and is given by:

$$\frac{{}^3\text{He}_{cn}}{({}^3\text{He}_{cn} + {}^3\text{He}_{sp})} = \frac{\int P_{cn}(z)dz}{(\int P_{cn}(z)dz + \int P_{sp}(z)dz)} \quad (3.7)$$

where the shape of the $P_{cn}(z)$ profile can also be computed using a neutron-production diffusion model and the apparent Li of the mineral.

3.7 Conclusions

This study calibrates the production rates of cosmogenic ^3He and ^{21}Ne in common minerals against ^{10}Be in quartz from a rhyolite dome in the Coso volcanic field. We show that Li-produced ^3He components can be large, but when subtracted from measured ^3He give results comparable to previous studies. Although our approach is vulnerable to systematic errors associated with modeling neutron production and diffusion, our results appear robust based on comparisons across different samples, mineral phases, and isotope systems. At face value our new production rates of ~ 143 at $\text{g}^{-1} \text{a}^{-1}$ for olivine and pyroxene lie at the high end of previous estimates. This indicates that the complexities of spallogenic ^3He (and ^3H) production remain an open research question.

Zircon and apatite show promise as target phases for ^3He dating due to their ubiquity, relatively low Li contents, and lack of magmatic ^3He components. The Li-produced components in zircon and apatite can be minimized by working with lithologies that have large grain sizes, young U/Th-He closure ages, and low U, Th and Li contents. We also estimate production rates of ^{21}Ne to be 17.7 ± 1.6 and 34.1 ± 3.2 at $\text{g}^{-1} \text{a}^{-1}$ for quartz and pyroxene respectively. These results agree well with previous production rates, and demonstrate that cosmogenic ^{21}Ne dating can be accomplished in rocks high in U and Th, at least if they are relatively young.

Table 3.9: Bulk rock composition and constants used in neutron flux calculations

	Rhyolite Host (ppm)	Andesitic Inclusion (ppm)	Atomic Mass (g/mol)	Avg. Log. Energy Loss per Collision	Scattering Cross Section (cm ² /at)	Absorption Cross Section (cm ² /at)	Resonance Integral (cm ² /at)	Neutron Yield per ppm U (n g ⁻¹ yr ⁻¹ ppm ⁻¹)	Neutron Yield per ppm Th (n g ⁻¹ yr ⁻¹ ppm ⁻¹)
H	2444	942	1.0	1.000	2.05E-23	3.30E-25	0.00E+00	0.00	0.00
Li	156	553	6.9	0.262	9.50E-25	7.10E-23	0.00E+00	24	10
Be	15	0.5	9.0	0.206	6.15E-24	7.60E-27	4.00E-27	265	91
B	4.5	16	10.8	0.174	4.27E-24	7.67E-22	1.72E-21	62	20
C	191	191	12.0	0.158	4.74E-24	3.40E-27	1.60E-27	0.45	0.18
N	0	0	14.0	0.136	1.00E-23	7.50E-26	6.35E-24	0.00	0.00
O	516785	453531	16.0	0.120	3.76E-24	2.00E-28	4.00E-28	0.24	0.08
F	2450	180	19.0	0.102	3.64E-24	9.60E-27	2.10E-26	0.00	0.00
Na	30790	28527	23.0	0.084	3.03E-24	5.30E-25	3.11E-25	12.5	5.9
Mg	301.5	23245	24.3	0.080	3.42E-24	6.30E-26	3.80E-26	5.8	2.5
Al	66812	85235	27.0	0.072	1.41E-24	2.30E-25	1.70E-25	5.1	2.6
Si	348328	253414	28.1	0.070	2.01E-24	1.70E-25	1.27E-25	0.68	0.34
P	22	1714	31.0	0.063	5.00E-24	2.00E-25	0.00E+00	0.86	0.57
S	9	23	32.1	0.061	9.79E-25	5.20E-25	7.00E-23	0.17	0.10
Cl	60	35	35.5	0.055	1.58E-23	3.35E-23	1.37E-23	1.3	0.79
K	38187	20816	39.1	0.050	2.04E-24	2.15E-24	1.00E-24	0.12	0.08
Ca	2859	49410	40.1	0.049	2.53E-24	4.30E-25	2.35E-25	0.04	0.03
Ti	300	12105	47.9	0.041	4.09E-24	6.10E-24	3.10E-24	0.00	0.00
V	0	105	50.9	0.039	4.80E-24	5.08E-24	2.80E-24	0.00	0.00
Cr	20	35	52.0	0.038	3.38E-24	3.07E-24	1.60E-24	0.00	0.00
Mn	248	1065	54.9	0.036	2.20E-24	1.33E-23	1.40E-23	0.00	0.00
Fe	7235	60632	55.8	0.035	1.14E-23	2.56E-24	1.39E-24	0.18	0.20
Co	0.3	26	58.9	0.034	6.00E-24	3.70E-23	5.50E-23	0	0
Ni	0.7	1.8	58.7	0.034	1.78E-23	4.49E-24	1.76E-24	0	0
Cu	1.4	42	63.5	0.031	7.78E-24	3.78E-24	4.10E-24	0	0
Zn	66	83	65.4	0.030	4.08E-24	1.11E-24	2.81E-24	0	0
Rb	425	12	85.5	0.023	6.40E-24	3.80E-25	4.64E-24	0	0
Sr	10	266	87.6	0.023	1.00E-23	1.28E-24	1.10E-23	0	0
Y	74	31	88.9	0.022	7.67E-24	1.28E-24	1.00E-24	0	0
Cd	100	230	112.4	0.018	5.6E-24	-	7E-23	0	0
Zr	0.02	0.09	91.2	0.022	6.40E-24	1.85E-25	9.50E-25	0	0
La	26	29	138.9	0.014	1.01E-23	8.97E-24	1.21E-23	0	0
Ce	48	53	140.1	0.014	-	6.3E-25	3.7E-24	0	0
Pr	6.1	1.5	140.9	0.014	2.54E-24	1.15E-23	1.74E-23	0	0
Nd	22	28	144.2	0.014	1.60E-23	5.05E-23	4.50E-23	0	0
Sm	5.8	5.8	150.4	0.013	3.80E-23	5.82E-21	1.40E-21	0	0
Gd	3.8	4.6	157.3	0.013	1.72E-22	4.90E-20	3.90E-22	0	0
Dy	6.2	4.9	162.5	0.012	1.06E-22	9.40E-22	1.48E-21	0	0
Er	3.9	3.2	167.3	0.012	9.00E-24	1.59E-22	7.30E-22	0	0
Yb	8.7	3.3	173.0	0.012	2.34E-23	3.55E-23	1.55E-22	0	0
Lu	1.2	0.5	175.0	0.011	6.80E-24	7.64E-23	6.22E-22	0	0
Hf	6.8	5.2	178.5	0.011	1.03E-23	1.04E-22	1.99E-21	0	0
Ta	12	2.8	181.0	0.011	6.12E-24	2.05E-23	6.60E-22	0	0
W	1.9	3.9	183.9	0.011	4.77E-24	1.84E-23	3.52E-22	0	0
Pb	37	22	207.2	0.010	1.13E-23	1.71E-25	1.38E-25	0	0
Th	42	7.1	232.0	0.009	1.30E-23	7.37E-24	8.50E-23	0	0
U	14	2	238.0	0.008	9.38E-24	2.68E-24	2.77E-22	0	0

Bold type denotes values that were measured in this study, or taken from Bacon et al. (1981) or Bacon and Metz (1984)

Regular type denotes values taken from Potts et al. (1992)

Chapter 4

COSMOGENIC ^3He PRODUCTION RATES IN APATITE, ZIRCON AND PYROXENE INFERRED FROM BONNEVILLE FLOOD EROSIONAL SURFACES

4.1 Introduction

Cosmogenic nuclide dating of terrestrial surfaces provides a powerful tool with which to study the timing and rate of landscape change. This includes applications as varied as the dating of glacial moraines, establishing slip-rates on faults, measuring the erosion rates of basins, and measuring the rates of soil formation (Bierman and Steig, 1996; Bierman et al., 1995; Brook et al., 1993; Heimsath et al., 1997). Although many important questions have been answered, others remain unanswered, in part due to limitations on the number of samples that can typically be analyzed in studies using ^{10}Be , ^{26}Al , and ^{36}Cl . In contrast, rapid preparation and analysis of samples for cosmogenic ^3He often allows a greater number of samples to be analyzed, but the application of cosmogenic ^3He dating has so far been limited primarily to olivine and pyroxene. Because ^3He is produced in all mineral phases, it can potentially be applied in almost any lithology. This study demonstrates the potential of ^3He dating in zircon and apatite to constrain geomorphic histories in study areas which lack quartz for ^{10}Be , ^{26}Al , or ^{21}Ne dating. In addition, we present a new calibration of ^3He production rates, which agree to within 5% with the revised results from two previous studies.

Part of the reason that cosmogenic ^3He has been relatively under-utilized is that calibration studies, and thus applications, have usually been limited to pyroxene or olivine in young lava flows (Ackert et al., 2003; Blard et al., 2006; Cerling and Craig, 1994; Dunai and Wijbrans, 2000; Licciardi et al., 1999; Licciardi et al., 2006). Because these studies have been performed at a range of elevations and latitudes, the best estimate of the production rate is dependent upon the scaling scheme that is used to convert local measurements to production rates at sea-level high-latitude (SLHL). A compilation of existing calibration studies performed

against ^{14}C or $^{40}\text{Ar}/^{39}\text{Ar}$ ages of uneroded surfaces gives SLHL production rates between ~ 115 and 133 at $\text{g}^{-1} \text{a}^{-1}$ for olivine and pyroxene, with a $\sim 10\%$ standard deviation when a given scaling model is applied (Goehring et al., 2010). More recent studies have focused on inter-isotope calibrations, comparing ^3He in pyroxene, olivine, garnet, zircon, apatite, and titanite against ^{10}Be in quartz (Amidon et al., 2008a; Amidon et al., 2009; Gayer et al., 2004; Niedermann et al., 2009). These studies have yielded ^3He production rates that are systematically higher than those estimated from calibrations against ^{14}C or $^{40}\text{Ar}/^{39}\text{Ar}$. One proposed explanation for this disagreement is that these inter-isotope calibrations have focused on crustal rocks that are high in Li. In such rocks excess ^3He from neutron capture on ^6Li could account for the discrepancy (Dunai et al., 2007) especially in the absence of shielded samples for establishing baseline ^3He level. While this possibility has been refuted, the role of ^6Li is clearly important and is not yet fully understood (Amidon et al., 2008a; Amidon et al., 2009).

The goals of this study are to calibrate ^3He production rates in zircon, apatite and pyroxene independently of ^{10}Be , and to use shielded samples to better document Li-produced ^3He components. We thus present ^3He measurements from zircon, apatite, and pyroxene from shielded and surface exposed samples that have been scoured by the Bonneville outburst flood near Twin Falls, Idaho. This is an ideal calibration site because the timing of the flood is known from numerous ^{14}C ages and has been used in several previous cosmogenic production rate studies (Cerling, 1990; Goehring et al., 2010; Handwerger et al., 1999; Lifton et al., 2009; Lifton et al., 2001). The site also lies within ~ 700 km of many calibration sites in the western US, which reduces scaling-related uncertainties when these studies are compared (Amidon et al., 2009; Cerling and Craig, 1994; Goethals et al., 2009; Licciardi et al., 1999). Our results show that although Li produced ^3He exists in most samples, the use of shielded samples allows subtraction of this component with reasonable precision. This study yields spallation ^3He production rates of 117-139, 123-146, and 96-113 at $\text{g}^{-1} \text{a}^{-1}$ (1σ uncertainties) for pyroxene, apatite, and zircon, depending upon what scaling scheme is adopted (Balco et al., 2008). The

pyroxene result is in agreement with previous production rates obtained by direct dating of geomorphic surfaces. Although the zircon and apatite data are lower than previously published values, this discrepancy is largely reconciled by adopting a revised ^{10}Be production rate of $4.51 \text{ at g}^{-1} \text{ a}^{-1}$.

4.2 Geologic Background and Sampling

The study area is near Twin Falls, Idaho where the Snake River has carved a canyon through which waters of the Bonneville outburst flood passed at $\sim 17.5 \text{ ka}$ (Figure 4.1). Detailed mapping of flood deposits suggests that the floodwaters split into two channels, with $\sim 300,000 \text{ m}^3/\text{sec}$ transported as bank-full flow through the main canyon and $\sim 600,000 \text{ m}^3/\text{sec}$ in the Eden overland channel that exited the canyon near Rupert, Idaho and rejoined just below Perrine bridge (O'Connor, 1993). The confluence of these two channels is coincident with an abrupt widening of the canyon, as well as the occurrence of a large amphitheatre-headed side canyon (the Blue Lakes Alcove) and a massive hydraulically scoured “pot-hole” (Malde, 1968). Although several authors have proposed that these are the result of the Bonneville flood, our results as well as those from recent studies suggest that these features, and similar features nearby, may have formed during earlier flood events (Cerling et al., 1994; Lamb et al., 2008).

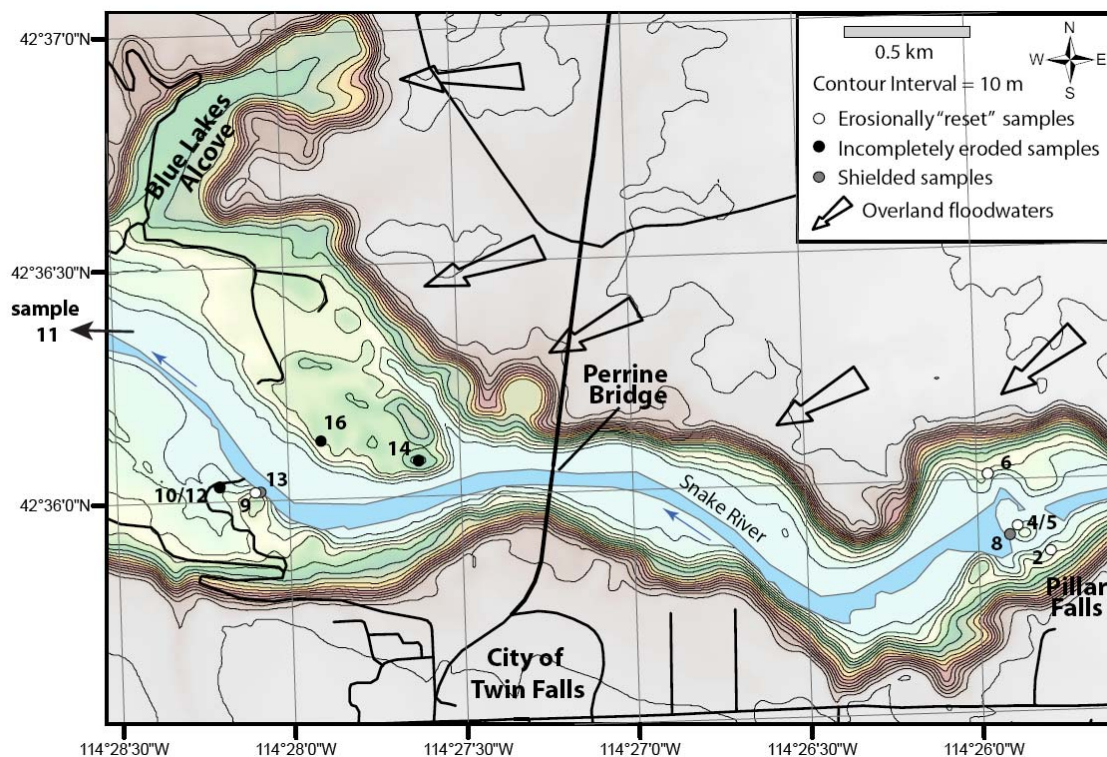


Figure 4.1

Topographic map of the Snake River canyon near Twin Falls, Idaho. Circular symbols represent sampling localities, labeled with sample number and shaded according to their inferred erosional history (see text).

The Bonneville flood was released when the alluvium damming the lake at its overflow was abruptly stripped at ~ 17.5 ka, and the lake level dropped ~ 100 m to the Provo stage. The exact timing is established by comparing the youngest Bonneville stage shoreline ages with the oldest Provo-stage shorelines. Reviews of the Bonneville chronology are given in Godsey et al. (2005) and Oviatt et al. (1992). The two youngest ages from the Bonneville stage are 15.3 and 15.1 ^{14}C ka BP, derived from charcoal and wood respectively (Oviatt et al., 1992; Scott et al., 1983). More recently, three identical ages of 15.1 ^{14}C BP were obtained from three separate mollusk samples from sites just below the Bonneville shoreline (Godsey et al., 2005). The oldest ages associated with the Provo shoreline are both 14.3 ^{14}C ka BP, and are derived from inorganic carbon extracted from tufa and from a mollusk (Light, 1996; Oviatt, 1991). Conversion to calendar years gives 2σ age ranges of 17.5-18.5 ka for the oldest Bonneville ages, and 16.5-

17.5 ka for the youngest Provo age, from which we adopt an age of 17.5 ± 1 ka for the Bonneville flood event (Godsey et al., 2005; Goehring et al., 2010).

At Twin Falls, the Snake River incises the ~ 5.7 Ma Shoshone Falls rhyolite and capping Pliocene basalt flows (Armstrong et al., 1975; Bonnicksen et al., 2008). We divide the Shoshone Falls rhyolite into two units, with the lower unit being a green to gray plagioclase-pyroxene rhyolite. This is overlain by a darker colored rhyolite containing plagioclase, two distinct pyroxenes, and abundant fine grained magnetite. Both units contain abundant zircon and apatite, with zircons tending to be large ($>75 \mu\text{m}$ in cross section) and apatites tending to be very small ($<75 \mu\text{m}$). At Pillar Falls (Figure 4.1) we collected two exposed samples from the upper unit (2 and 6), as well as two exposed samples and one shielded sample from the lower unit (4, 5, and 8). The shielded sample was taken from a deep cave scoured ~ 5 m laterally into the central pillar, and sitting ~ 18 m directly below the surface locations of samples 4 and 5. The latitude, longitude, and elevation of all samples are given in table 4.1.

Table 4.1: Sample locations

Sample	Lat.	Lon.	Elev. (m)
ID1	42.59605	114.39865	1031
ID2	42.59737	114.42984	991
ID3	42.59865	114.43051	959
ID4/5	42.59829	114.43139	980
ID6	42.60018	114.43277	978
ID8	42.59822	114.4319	962
ID9	42.60026	114.46827	1005
ID11	42.62359	114.5143	960
ID12	42.60051	114.47002	975
ID13	42.60028	114.46803	954
ID14	42.60126	114.46031	1021
ID16	42.60205	114.46501	993

Coordinates relative to WGS 84 datum

Rim of canyon at ~ 1100 m elevation

Downstream of Perrine Bridge the widened section of canyon is characterized by well-preserved scour surfaces sitting ~40-60 m above the modern river, and fields of large boulders (“melon gravels”) deposited on lower elevation surfaces, typically 5-15 m above the modern river (Figure 4.1). We sampled three scour surfaces in the upper unit (9, 14, and 16), as well as a shielded sample (13) and two scour surfaces in the lower unit (9 and 10). The shielded sample was situated beneath ~40 m of overburden and ~1.5 m horizontally from a planar vertical cliff face. Sample 11 was collected from the top of a 4 x 2.5 x 3 m flood-deposited boulder of the lower unit lithology, deposited ~2 km downstream from Perrine bridge. Because the upper lithology is composed of a fine grained matrix, all of the samples collected from this lithology (2, 6, 9, 12, 14, and 16) exhibited patina surfaces preserving scour flutes and/or 5-30 cm wide scour pot-holes. In contrast, surfaces from the lower unit (4, 5, and 11) were partially disaggregated with poor preservation of primary scour features. All of the exposed samples were 4-5 cm thick, and were collected from nearly horizontal surfaces with no topographic shielding. We therefore do not apply shielding corrections of any kind.

4.3 Methods

Rocks were crushed, sieved to <300 μm , and rinsed before being separated using standard heavy liquid and magnetic techniques. Resulting apatite and zircon separates were wet-sieved into increments of 30-50, 50-75, 75-125, and >125 μm . However, apatite separates were intact and pure enough only for the 50-75 μm size fraction. Likewise, only pyroxenes from the >190 μm fraction were analyzed. Pyroxene separates were leached in an ultrasonic bath in 10% HF:HNO₃ solution for ~1 hour, whereas zircon was purified in a concentrated HF:HNO₃ solution for 3-4 hours. All samples were visually inspected and picked free of contaminant phases prior to analysis. Mean grain size was determined by photographing the sample prior to loading, and measuring length and width of >150 representative grains per sample. Because the mean grain

sizes computed for given sieve fractions are consistent to within $\sim 2\text{-}3\ \mu\text{m}$ between samples, a constant value is reported for each size fraction and is used in all calculations. Typically 20-40 mg of uncrushed zircon and apatite was loaded into platinum capsules. In some cases, pyroxene was crushed under vacuum in a steel tube following previously published procedures (Patterson et al., 1997). To ensure that all grains were uniformly crushed prior to fusion, all pyroxene samples were ground in a mortar and pestle and sieved through a $<26\ \mu\text{m}$ sieve prior to loading in Al-foil.

Zircon and apatite crystals were degassed by heating platinum packets to $>1100\ ^\circ\text{C}$ for 30 minutes using a 1064 nm Nd:YAG laser similar to previously published procedures (Amidon et al., 2008a; House et al., 2000). Pyroxene powder was degassed for 20 minutes at $1300\ ^\circ\text{C}$ in a double-walled resistance furnace. Re-extracts at the same temperature were performed using both techniques and confirmed complete extraction of He from the samples. He gas was purified over an activated charcoal trap at 77 K and over hot and cold Ti SAES getters before being cryogenically focused at 14 K. Helium was released at 32 K into an MAP 215-50 noble gas mass spectrometer. For low ^4He analyses (apatite and pyroxene), sensitivity was determined by measuring aliquots of both the Caltech “Air” and “MM” standards of similar size to the sample being analyzed (Poreda and Farley, 1992). For high ^4He analyses (zircon) sensitivity was determined by in-run spiking of samples with the “MM” standard, which causes a significant increase in ^3He , while only raising the total He pressure by $<1\ \%$ (Amidon et al., 2008a). ^3He is collected in pulse mode on an electron multiplier whereas ^4He is measured on a Faraday cup. Very high ^4He concentrations in zircon were determined on an aliquot of the sample gas by peak height measurement on a Balzers Prisma quadrupole mass spectrometer. Analytical uncertainty for individual ^3He analyses is dominated by counting statistics on the ^3He signal and is typically $\sim 10\%$ for zircon, $\sim 8\%$ for apatite and $\sim 7\%$ for pyroxene (1σ). We improve on these precision figures by making replicate analyses. Uncertainty on ^4He analyses is dominated by the

standardization of the instrument, and is 1-2%, based on the calibration performed when filling the standard tank.

Lithium measurements were made on an Agilent 7500 series ICP-MS using isotope dilution with a ^6Li spike calibrated with a commercial Li normal solution. Measurements were made on ~1 mg of handpicked material, but not the same aliquots used for ^3He analysis. Most samples were dissolved on a hot plate in a 2:1 HF:HNO₃ cocktail except for zircons, which were Parr bombed in HF, redissolved in HCl, and finally in HNO₃. Reproducibility of Li measurements was established by performing at least two replicate measurements on separately picked aliquots of each sample. Lithium blanks typically total less than 0.1% of measured lithium, with a maximum of ~2%. The sample cleaning procedure, and a 1σ external precision of ~6% are established and discussed by Amidon et al. (2008). In some cases, U and Th concentrations were determined on the same samples as Li by removing an aliquot and spiking it for U and Th analyses. U blanks ranged from 0.1 to 1%, and Th blanks ranged from 1 to 3% of measured concentrations. All U and Th analyses were replicated to better than 5% (1σ).

Bulk rock geochemistry was measured on powdered rock samples (~500 g each) that were subsampled and flux melted into glass disks. Major element concentrations were determined by XRF whereas trace elements and REE's were measured by LA-ICPMS following standard procedures at the Michigan State University laboratory (Vogel et al., 2008). Compositions of individual mineral phases were determined using the JEOL JXA-8200 electron microprobe at Caltech.

4.4 Results

Measured helium concentrations for zircon, apatite, and pyroxene are presented in tables 4.2-4.5. Six of the nine surface exposure samples yield ^3He concentrations in zircon that are

within error of each other, suggesting that they share a common exposure history. The same is true for the apatite analyses from these 6 samples. The remaining surface exposure samples yield significantly higher ^3He concentrations in all phases suggesting that they have retained ^3He from exposure prior to the Bonneville flood. Throughout the remainder of this paper, the six samples with similar concentrations will be referred to as “reset surfaces” and, the 3 samples with high ^3He will be referred to as the “unreset surfaces,” reflecting their incomplete erosional resetting during the flood.

Measured ^3He concentrations in zircons from reset surfaces are ~ 6 Mat/g compared to as much as 28 Mat/g in unreset surfaces (Table 4.2). Concentrations of ^3He in the two shielded samples agree within error at ~ 1.5 Mat/g. Both shielded and exposed zircons show an increase in ^3He concentration with decreasing grain size. For reset samples this typically amounts to about a 30% increase between the >100 μm and <50 μm size fractions (Figure 4.2). Apatites from the 50-75 μm size fraction yielded consistently higher ^3He concentrations than in zircons of the same size, with ~ 9 Mat/g for reset surfaces and up to 29 Mat/g for unreset surfaces (Table 4.3). Shielded apatites contain ~ 3.4 Mat/g of ^3He . Results of two apatite crushing experiments yielded $^3\text{He}/^4\text{He}$ ratios of 0.01 Ra, suggesting no detectable mantle (~ 8 Ra) helium (Table 4.5).

Although both Fe-rich and Fe-Ca pyroxenes were present in most samples (Table 4.7), only pyroxenes with the Fe-Ca composition, $(\text{Mg}_{0.62}\text{Fe}_{0.58}\text{Ca}_{0.74})\text{Si}_2\text{O}_6$, were analyzed for ^3He . Concentrations of ^3He in pyroxene from reset surfaces range from ~ 7 -11 Mat/g and show a strong correlation with Li content (Table 4.4). ^3He concentrations in unreset samples reach 38 Mat/g. The average ^4He concentration is 57 ± 14 Tat/g, giving relatively radiogenic $^3\text{He}/^4\text{He}$ ratios of 0.1-0.5 Ra. Results from crushing experiments show that the trapped helium component is distinctly different between pyroxene from the upper and lower units but is less than 4% of matrix-sited ^3He concentrations in all cases (Table 4.4). Results from

crushing experiments reproduce well, suggesting that complete extraction of magmatic gasses was achieved.

Major element compositions of the upper and lower rhyolite units are nearly identical despite their significant textural variations (Table 4.8). However, bulk rock Li concentrations are significantly different between the two units, with ~15 ppm in the upper unit and ~21 ppm in the lower unit (Table 4.6). The contrast in Li contents between the upper and lower units is magnified in the pyroxenes. Those from the upper unit contain 16-25 ppm of Li, whereas those from the lower unit contain 34-90 ppm. The Li concentrations vary widely across small spatial scales, with three samples collected within ~5 m of each other (4, 5, and 8) giving concentrations of 34, 53, and 90 ppm. Li variations in other mineral phases are less significant, ranging from 1-2 ppm in zircon and from 3-8 ppm in apatite. Bulk rock U and Th concentrations are similar in both units at ~6 and 17 ppm respectively, and are ~250 and ~120 ppm in zircon, and ~0.1 and 0.3 ppm in pyroxene (Table 4.6).

Table 4.2: Zircon ^3He data

	n	$^3\text{He}_m$	1σ	^4He	1σ	$^3\text{He}/^4\text{He}$	MER	$^3\text{He}_{sp+cn}$	$^3\text{He}_{cn}$	$1\sigma_{cn}$	$^3\text{He}_{sp}$	1σ	$^3\text{He PR}$	1σ	
		(Mat/g)	(Mat/g)	(Tat/g)	(Tat/g)	(Ra*1000)	μm	(Mat/g)	(Mat/g)	(Mat/g)	(Mat/g)	(Mat/g)	(at $\text{g}^{-1}\text{a}^{-1}$)	(at $\text{g}^{-1}\text{a}^{-1}$)	
"Reset" surfaces and shielded samples															
< 50 μm															
ID5	2	7.3	0.5	3771	420	1.4	27	5.5	0.6	0.1	4.8	0.6	130	33	
ID6	1	6.3	0.6	3760	380	1.2	27	4.4	0.6	0.1	3.8	0.7	102	38	
ID11	2	6.9	0.5	5286	604	0.9	27	5.1	0.6	0.1	4.4	0.5	120	31	
weighted mean:		6.8	0.4								4.38	0.4	119	25	
ID8 (S)	2	1.5	0.2	4254	835	0.2	27	-	-	-	-	-	-	-	
ID13 (S)	3	2.2	0.2	3004	535	0.4	27	-	-	-	-	-	-	-	
shielded mean:		1.8	0.2												
50<75 μm															
ID2	1	5.5	0.6	3306	356	1.2	38	3.9	0.5	0.1	3.6	0.6	97	33	
ID4	3	6.8	0.4	3732	475	1.3	38	5.2	0.5	0.1	4.9	0.4	134	25	
ID5	4	5.8	0.3	3590	535	1.2	38	4.2	0.5	0.1	3.8	0.3	104	20	
ID6	1	5.6	0.6	3167	339	1.3	38	4.0	0.5	0.1	3.6	0.6	99	33	
ID9	2	5.3	0.4	3172	414	1.2	38	3.7	0.5	0.1	3.4	0.4	92	24	
ID11	2	6.6	0.5	3862	454	1.2	38	4.9	0.5	0.1	4.6	0.5	126	29	
weighted mean:		5.9	0.3								4.0	0.3	109	19	
ID8 (S)	3	1.6	0.1	3454	721	0.3	38	-	-	-	-	-	-	-	
ID13 (S)	5	1.6	0.1	3525	827	0.3	38	-	-	-	-	-	-	-	
shielded mean:		1.6	0.1												
75<100 μm															
ID4	3	5.2	0.3	3543	517	1.1	55	4.0	0.3	0.0	3.8	0.3	102	20	
ID5	2	5.3	0.4	3189	418	1.2	55	4.0	0.3	0.0	3.8	0.4	104	23	
ID6	3	5.3	0.3	3256	471	1.3	55	4.1	0.3	0.0	3.9	0.3	105	20	
ID9	1	5.2	0.5	3204	355	1.2	55	4.0	0.3	0.0	3.8	0.5	102	31	
ID11	1	5.9	0.6	3287	342	1.3	55	4.7	0.3	0.0	4.5	0.6	121	35	
weighted mean:		5.4	0.1								3.9	0.2	105	13	
ID8 (S)	2	1.2	0.1	3506	765	0.2	55	-	-	-	-	-	-	-	
ID13 (S)	5	1.3	0.1	3643	953		55	-	-	-	-	-	-	-	
shielded mean:		1.2	0.1												
>100 μm															
ID4	1	5.1	0.5	3700	415	1.0	105	4.3	0.2	0.0	4.2	0.5	115	31	
ID5	2	4.4	0.3	3683	530	0.9	105	3.6	0.2	0.0	3.5	0.3	95	20	
ID6	2	4.8	0.3	3300	452	1.1	105	4.0	0.2	0.0	4.0	0.4	108	22	
ID9	2	4.9	0.3	3333	453	1.1	105	4.1	0.2	0.0	4.0	0.4	110	22	
ID11	2	4.5	0.3	3566	505	0.9	105	3.7	0.2	0.0	3.7	0.3	100	20	
weighted mean:		4.7	0.1								3.8	0.2	104	11	
ID8 (S)	2	0.7	0.1	3635	1046	0.1	105	-	-	-	-	-	-	-	
ID13 (S)	1	0.9	0.1	3977	850	0.2	105	-	-	-	-	-	-	-	
shielded mean:		0.8	0.1												
Grand Mean (>37 μm):												3.9	0.1	105	9
"Unreset" surfaces															
ID12 (50-75)	1	23.4	1.9	3076	180	5.5	38	21.8	3.2	0.4	19.1	1.9	-	-	
ID12 (75-125)	2	27.5	1.6	3200	205	6.5	55	26.3	2.8	0.4	23.3	1.6	-	-	
ID14 (<75)	1	9.5	0.8	3058	281	2.2	38	7.9	1.2	0.2	7.3	0.8	-	-	
ID14 (75-100)	1	10.7	0.9	3421	296	2.2	55	9.4	1.0	0.1	8.3	0.9	-	-	
ID16 (50-75)	1	23.6	1.9	3438	200	4.9	38	22.0	3.2	0.4	19.0	1.9	-	-	
ID16 (75-100)	3	23.0	1.1	3141	244	5.4	55	21.8	2.3	0.3	19.6	1.1	-	-	
ID16 (>100)	1	22.5	1.8	3881	231	4.2	105	21.7	1.4	0.2	20.4	1.8	-	-	

(S) denotes shielded samples

n = # of replicate analyses; 1σ = standard error, MER = mean equivalent radius; $1\sigma_{cn}$ = Monte Carlo standard deviation on $^3\text{He}_{cn}$ component $^3\text{He}_m$ = measured; $^3\text{He}_{cn}$ = modeled ^3He from ^6Li and cosmogenic neutrons; $^3\text{He}_{sp}$ = net spallation after subtraction of Li-produced componentsProduction rates are determined using a scaling factor of 2.1 and assumed age of 17,500 +/- 500 yrs (1σ) for Bonneville flood event.

Table 4.3: Apatite ^3He data

	n	$^3\text{He}_m$	1σ	^4He	1σ	$^3\text{He}/^4\text{He}$	MER	$^3\text{He}_{sp+cn}$	$^3\text{He}_{cn}$	$1\sigma_{cn}$	$^3\text{He}_{sp}$	1σ	$^3\text{He PR}$	1σ
		(Mat/g)	(Mat/g)	(Tat/g)	(Tat/g)	(Ra*1000)	(μm)	(Mat/g)	(Mat/g)	(Mat/g)	(Mat/g)	(Mat/g)	($\text{at g}^{-1}\text{a}^{-1}$)	($\text{at g}^{-1}\text{a}^{-1}$)
"Reset" surfaces and shielded samples														
ID4	1	9.8	0.8	1207	60	4	36	6.4	0.9	0.1	5.5	0.8	151	74
ID5	2	9.2	0.7	1151	58	6	36	5.9	0.9	0.1	5.0	0.8	136	59
ID6	2	8.9	0.7	1288	64	5	36	5.6	0.7	0.1	4.9	0.7	133	32
ID9	2	9.0	0.7	711	36	10	36	5.6	0.7	0.1	4.9	0.7	135	54
ID11	1	8.7	0.7	889	44	7	36	5.3	0.9	0.1	4.5	0.7	122	35
<i>mean:</i>		9.1	0.2					5.8			4.9	0.3	135	17
Shielded samples														
ID8 (s)	3	3.2	0.3	796	40	3	36	-	-	-	-	-	-	-
ID13 (s)	4	3.5	0.3	609	30	4	36	-	-	-	-	-	-	-
<i>shielded mean:</i>		3.4	0.1											
"Unreset" surfaces														
ID12	1	29.0	2.3	984	49	21	36	25.6	3.8	0.6	21.8	2.4	-	-
ID14	2	14.1	1.1	833	42	13	36	10.7	1.6	0.3	9.1	0.8	-	-
ID16	2	23.3	1.9	1067	53	16	36	19.9	2.5	0.4	17.4	1.4	-	-

n = # of replicate analyses; 1σ = standard error, MER = mean equivalent radius; $1\sigma_{cn}$ = Monte Carlo standard deviation on $^3\text{He}_{cn}$ component
 $^3\text{He}_m$ = measured; $^3\text{He}_{cn}$ = modeled ^3He from ^6Li and cosmogenic neutrons; $^3\text{He}_{sp}$ = net spallation after subtraction of Li-produced components
Production rates are determined using a scaling factor of 2.1 and assumed age of 17,500 +/- 500 yrs (1σ) for Bonneville flood event.

Table 4.4: Pyroxene ^3He data

	n	$^3\text{He}_m$	1σ	^4He	1σ	$^3\text{He}/^4\text{He}$	Li	$^3\text{He}_{nuc}$	$^3\text{He}_{sp+cn}$	$^3\text{He}_{cn}$	$1\sigma_{cn}$	$^3\text{He}_{sp}$	1σ	$^3\text{He PR}$	1σ
		(Mat/g)	(Mat/g)	(Tat/g)	(Tat/g)	(Ra)	(ppm)	(Mat/g)	(Mat/g)	(Mat/g)	(Mat/g)	(Mat/g)	(Mat/g)	($\text{at g}^{-1}\text{yr}^{-1}$)	($\text{at g}^{-1}\text{yr}^{-1}$)
"Reset" Surfaces and Shielded Samples															
ID2	2	6.7	0.3	53	4	0.1	17	1.6	5.1	0.5	0.1	4.7	0.4	127	23
ID4	3	8.5	0.3	52	4	0.1	34	2.8	5.8	0.9	0.1	4.8	0.4	132	24
ID5	4	10.3	0.4	43	3	0.2	53	4.1	6.2	1.5	0.2	4.7	0.4	128	26
ID6	2	6.9	0.3	50	3	0.1	16	1.5	5.4	0.4	0.1	5.0	0.4	136	24
ID9	1	7.8	0.5	40	2	0.2	25	2.1	5.7	0.7	0.1	5.0	0.6	135	34
ID11	3	10.6	0.4	47	3	0.2	62	4.7	5.9	1.7	0.2	4.2	0.5	114	30
										weighted mean:		4.7	0.1	129	10
ID8 (s)	8	6.9	0.2	53	5	0.0	90	7.4	-	-	-	-	-	-	-
ID13 (s)	7	4.3	0.1	72	8	0.0	57	4.6	-	-	-	-	-	-	-
"Unreset" Surfaces															
ID10	2	31.6	1.6	49	2	0.5	17	1.6	30.0	3.3	0.4	26.7	1.6	-	-
ID12	2	37.4	1.9	79	2	0.4	17	1.6	35.9	4.1	0.5	31.7	1.9	-	-
ID14	2	15.8	0.8	57	3	0.2	20	1.8	14.0	1.8	0.2	12.3	0.8	-	-
ID16	1	28.7	2.0	84	2	0.3	20	1.8	27.0	3.8	0.5	23.1	2.1	-	-

n = # of replicate analyses; 1σ = standard error, MER = mean equivalent radius; $1\sigma_{cn}$ = Monte Carlo standard deviation on $^3\text{He}_{cn}$ component
 $^3\text{He}_m$ = measured; $^3\text{He}_{cn}$ = modeled ^3He from ^6Li and cosmogenic neutrons; $^3\text{He}_{sp}$ = net spallation after subtraction of Li-produced components
Production rates are determined using a scaling factor of 2.1 and assumed age of 17,500 +/- 500 yrs (1σ) for Bonneville flood event.

Table 4.5: ^3He crush data

	Mass (g)	^3He (Mat/g)	1σ (Mat/g)	^4He (Tat/g)	1σ (Tat/g)	$^3\text{He}/^4\text{He}$ (Ra)	1σ (Ra)
Pyroxene (Lower Unit)							
ID4	90	0.02	0.05	0.27	0.03	0.06	0.11
ID8	75	0.05	0.07	0.93	0.03	0.04	0.04
ID11	102	0.09	0.05	0.44	0.03	0.14	0.06
Mean		0.05		0.55		0.08	
Pyroxene (Upper Unit)							
ID2	74	0.26	0.08	0.69	0.04	0.27	0.05
ID6	75	0.18	0.07	0.62	0.03	0.20	0.06
ID16	87	0.26	0.07	0.66	0.03	0.28	0.05
Mean		0.23		0.66		0.25	
Apatite							
ID13a*	12	0.19	0.42	6.66	0.22	0.02	0.03
ID13b*	10	0.05	0.46	7.29	0.26	0.01	0.04

*not all grains were completely crushed

Table 4.6: Li, U, and Th data

	<i>Li</i>							<i>U</i>				<i>Th</i>			
	Px	Zr	Ap	G.M.	W.R.	FeO	Plag.	Px	Zr	G.M.	W.R.	Px	Zr	G.M.	W.R.
ID1	-	2	-	-	-	-	-	-	249	-	-	-	-	-	-
ID2	17	2	4	-	-	-	-	-	243	-	-	-	104	-	-
ID4	34	2	7	-	-	-	-	-	205	-	-	0.3	121	-	-
ID5	53	2	-	42	22	33	-	0.1	270	8	-	0.2	169	21	-
ID6	16	1	3	11	-	11	10	0.1	-	-	-	0.3	-	-	-
ID8	90	2	8	8	19	-	30	0.3	459	-	-	1.0	436	-	-
ID9	25	2	-	11	15	-	17	-	200	-	7	-	109	-	17
ID10	-	-	-	-	-	-	-	-	270	-	-	-	109	-	-
ID11	67	2	-	9	22	-	-	0.1	290	8	6	0.4	204	23	14
ID12	17	1	4	4	17	-	-	0.1	236	9	7	0.4	129	23	18
ID13	53	2	6	14	22	-	33	0.1	238	-	-	0.2	137	-	-
ID14	-	-	3	-	-	-	-	-	-	-	-	-	-	-	-
ID16	20	1	-	3	15	-	-	0.1	219	9	7	0.3	120	22	19

G.M. = handpicked groundmass fragments; W.R. = powdered whole rock

Table 4.7: Mineral compositions determined by electron microprobe analysis

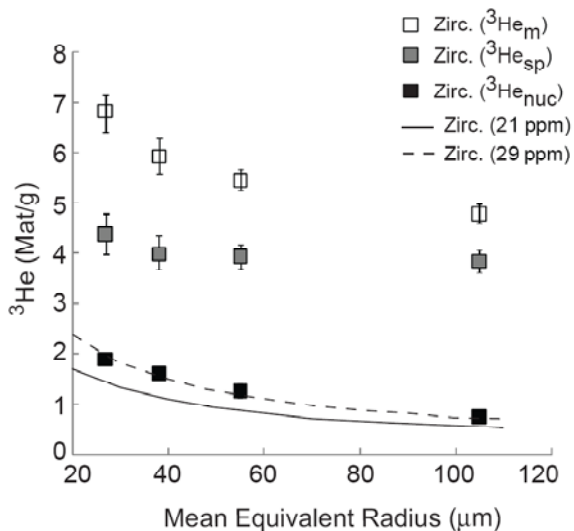
Mineral	n	Na ₂ O	MgO	TiO ₂	Cr ₂ O ₃	K ₂ O	CaO	SiO ₂	Al ₂ O ₃	FeO	MnO	Totals
Sample ID6 (upper unit)												
Fe-Ca-Pyroxene	6	0.3	10.5	0.3	0.0	0.0	17.9	52.0	0.8	18.0	0.6	100.5
	1σ	0.0	0.2	0.0	0.0	0.0	0.2	0.4	0.0	0.3	0.0	0.5
Fe-Pyroxene	3	0.1	13.1	0.1	0.0	0.0	3.7	51.6	0.3	30.7	1.1	100.6
	1σ	0.0	0.1	0.0	0.0	0.0	0.0	0.3	0.0	0.2	0.0	0.3
Groundmass	6	4.2	0.0	0.2	0.0	5.3	0.9	72.8	14.4	0.7	0.0	98.6
	1σ	1.5	0.0	0.1	0.0	0.8	0.4	1.6	2.2	0.6	0.0	1.4
Sample ID8 (lower unit)												
Fe-Ca-Pyroxene	3	0.3	10.7	0.3	0.0	0.0	17.8	51.9	0.9	17.6	0.6	100.1
	1σ	0.0	0.3	0.0	0.0	0.0	0.2	0.1	0.1	0.2	0.0	0.3
Fe-Pyroxene	2	0.1	12.9	0.2	0.0	0.0	3.8	51.3	0.3	30.4	1.1	100.1
Plagioclase	1	6.9	0.0	0.0	0.0	1.2	6.8	60.9	24.1	0.3	0.0	100.3
Groundmass	4	3.0	0.0	0.4	0.0	6.2	0.4	77.7	12.3	1.2	0.0	101.2
	1σ	0.2	0.0	0.3	0.0	0.6	0.1	1.1	0.4	1.5	0.0	0.5

'n' denotes number of separate mineral grains analyzed

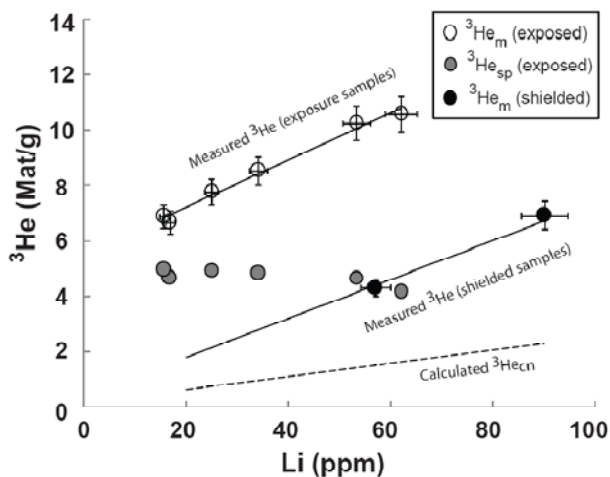
Table 4.8: Bulk rock compositions

sample	ID-2	ID-7	ID-13	Mean
SiO ₂	68.6	68.8	69.3	68.9
TiO ₂	0.6	0.6	0.6	0.6
Al ₂ O ₃	13.1	13.2	13.4	13.3
Fe ₂ O ₃	4.0	4.4	3.8	4.1
MnO	0.1	0.1	0.1	0.1
MgO	0.6	0.7	0.5	0.6
CaO	2.0	2.0	2.2	2.1
Na ₂ O	3.2	3.6	3.5	3.4
K ₂ O	5.0	4.7	4.6	4.8
P ₂ O ₅	0.2	0.2	0.2	0.2
Totals	97.4	98.1	98.2	97.9
LOI (%)	2.3	1.7	1.6	1.9
Ni	BD	BD	BD	BD
Cu	BD	BD	BD	BD
Zn	72	74	72	73
Rb	168	164	164	165
Sr	99	105	119	108
Zr	793	763	790	782
Ba	1111	1114	1238	1154
La	77	80	85	81
Ce	185	189	192	189
Pr	19	19	20	20
Nd	64	66	70	67
Sm	12	13	14	13
Eu	2	2	3	2
Gd	11	12	13	12
Tb	2	2	2	2
Y	68	68	76	71
Dy	11	11	12	11
Ho	2	2	3	2
Er	6	7	7	7
Yb	6	7	7	7
Lu	1	1	1	1
V	59	61	67	62
Cr	12	13	12	12
Nb	96	92	94	94
Hf	15	15	17	16
Ta	5	5	5	5
Pb	51	48	49	49

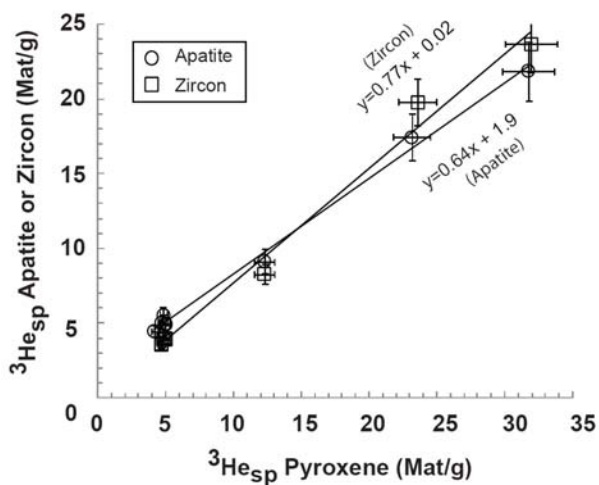
BD: Below detection limit

**Figure 4.2**

Measured ^3He in shielded zircons (black squares), reset surfaces (open squares), and spallation produced ^3He in reset surfaces (gray squares). All are plotted against mean equivalent radius. Solid and dashed lines show model calculation of the nucleogenic ^3He component assuming an average Li content of adjacent phases of 21 and 29 ppm respectively. These values equal the measured bulk rock concentration and the best fit to the data. Error bars denote 1σ standard errors.

**Figure 4.3**

Plot of ^3He vs Li content for pyroxene grains of $> 190 \mu\text{m}$ grain size. Open symbols are measured ^3He in the reset samples. Gray symbols denote spallation produced ^3He in the same samples after subtraction of all Li-produced components. Black circles denote measured nucleogenic ^3He ($^3\text{He}_{nuc}$) in the two shielded samples. Solid lines are linear regressions through data, dashed line shows the calculated $^3\text{He}_{cn}$ component as a function of Li concentration.

**Figure 4.4**

Plot of spallation produced ^3He in pyroxene against both apatite (circles) and zircon (squares). Regression lines and equations are indicated. Note that the zircon regression line pass through the origin, as expected. In contrast the shallow slope and the non-zero intercept for the apatites are unexpected and suggest anomalously low ^3He concentrations in the unreset samples.

4.5 Analysis

4.5.1 The Nucleogenic ^3He Component in Shielded Samples

The presence of matrix-sited ^3He in our shielded samples is due primarily to production via capture of radiogenic neutrons on ^6Li in the reaction $^6\text{Li}(n,\alpha)^3\text{H} \rightarrow ^3\text{He}$. This is evidenced by the correlation between ^3He and Li observed for pyroxenes (Figure 4.3). To understand this ^3He component in relation to other components we use the following equation:

$$^3\text{He}_m = ^3\text{He}_{sp} + ^3\text{He}_{in} + ^3\text{He}_{nuc} + ^3\text{He}_{cn} + ^3\text{He}_{mu} \quad (4.1)$$

where $^3\text{He}_m$ is the total ^3He measured in the sample, $^3\text{He}_{sp}$ is spallation-produced ^3He , $^3\text{He}_{in}$ is inherited from inclusions or prior exposure, $^3\text{He}_{nuc}$ is the Li-produced nucleogenic component produced by capture of radiogenic neutrons, $^3\text{He}_{cn}$ is the Li-produced component produced by capture of cosmogenically derived neutrons, and $^3\text{He}_{mu}$ is the Li-produced component produced by stopping of muons or by capture of muogenic neutrons.

The use of a shielded sample allows the $^3\text{He}_{nuc}$ component to be directly removed from this equation. Because the magmatic $^3\text{He}_{in}$ component has been removed by crushing and because we neglect the muon produced $^3\text{He}_{mu}$ component in these samples (see below), we assume that all of the ^3He measured in the shielded samples is Li produced nucleogenic ^3He , and refer to it as “measured $^3\text{He}_{nuc}$ ”. For pyroxene, we exploit the linear relationship between measured $^3\text{He}_{nuc}$ and Li content in shielded samples to directly subtract the $^3\text{He}_{nuc}$ component from the surface exposure samples, which also span a range of Li contents (Figure 4.3). The sizes of the $^3\text{He}_{nuc}$ components for pyroxene range between ~ 1.5 – 4.7 Mat/g, or ~ 18 – 45 % of the measured surface concentrations (Table 4.4). Because the shielded ^3He components are measured with an equal degree of precision to exposure samples, subtraction of the shielded component does not significantly increase the error. Apparent production rates of ~ 154 at $\text{g}^{-1} \text{a}^{-1}$ are thus obtained for pyroxene, which are higher than previously

obtained values (Goehring et al., 2010) due to the presence of the ${}^3\text{He}_{\text{cn}}$ component (quantified below).

Similar corrections for the apatites and zircons must accommodate the fact that their average grain size is comparable to the stopping range of ${}^6\text{Li}$ -produced ${}^3\text{H}$ in common silicate minerals ($\sim 30 \mu\text{m}$). As a result the redistribution of this component among the rock's constituent phases must be evaluated. Because their Li contents are lower than in the surrounding matrix, the net effect for apatites and zircons is implantation; the smaller the grain size, the more significant the effect (Dunai et al., 2007; Farley et al., 2006). This effect explains, for example, the increase of ${}^3\text{He}_{\text{nuc}}$ from $\sim 0.8 \text{ Mat/g}$ for $\text{MER} = 105 \mu\text{m}$ to $\sim 1.8 \text{ Mat/g}$ for $\text{MER} = 27 \mu\text{m}$ in the shielded zircons (Figure 4.2). For these two phases we thus subtract the mean ${}^3\text{He}_{\text{nuc}}$ measured on shielded samples of a given grain size from all surface samples of that same grain size. This approach does not account for variations in Li concentration between different apatite and zircon samples, or variations in the average Li concentrations of their adjacent minerals. However, it is reasonable to ignore these effects because: 1) the mean concentration of Li in zircon is very low and relatively constant at $\sim 1.5 \pm 0.3 \text{ ppm}$, 2) the concentration of Li in apatite is higher and more variable ($5 \pm 2 \text{ ppm}$) but small grain sizes make internal Li concentration much less important than matrix Li, and 3) we have no independent means with which to evaluate differences in average host Li concentrations. The sample-to-sample consistency of our results at a given grain size validates this simplification. The resultant apparent production rates (${}^3\text{He}_{\text{sp}} + {}^3\text{He}_{\text{cn}}$) are ~ 156 at $\text{g}^{-1} \text{ a}^{-1}$ for apatite, and range from 108-136 at $\text{g}^{-1} \text{ a}^{-1}$ for zircon of different grain sizes. Note that both ${}^3\text{He}_{\text{sp}}$ and ${}^3\text{He}_{\text{cn}}$ are also dependent on grain size as a consequence of redistribution, so this spread in zircon is expected.

4.5.2 Additional ${}^3\text{He}$ Components

In previous work (Amidon et al., 2008a; Amidon et al., 2009), we outlined the model calculations necessary to predict each Li-produced ^3He component. The present dataset allows us to test these calculations by comparison of the ^3He concentrations in surface and shielded samples with measured Li concentrations. More importantly, the model also allows us to compute $^3\text{He}_{\text{cn}}$, so we can isolate the spallation production rate in these phases. The calculation procedures are only briefly discussed below, but are included as an appendix to this paper. For comparison with past and future models, the inputs and resultant neutron flux parameters are tabulated in table 4.9.

Table 4.9: Selected parameters output from neutron flux calculations

Radiogenic neutron stopping rate (n/g*a*ppm U)	1.92
Radiogenic neutron stopping rate (n/g*a*ppm Th)	0.64
Cosmogenic thermal neutron stopping rate (n/g*a)*	624
Cosmogenic epithermal neutron stopping rate (n/g*a)*	1477
Fast muon produced neutron stopping rate (n/g*a)*	11.6
Slow muon produced neutron stopping rate (n/g*a)*	133
^3He P.R. from cosmogenic slow neutrons ($^3\text{He}/\text{g}^*\text{a}^*\text{ppm Li}$) **	1.57
^3He P.R. from radiogenic slow neutrons ($^3\text{He}/\text{g}^*\text{a}^*\text{ppm Li}$) **	0.016
^3He P.R. from slow muons ($^3\text{He}/\text{g}^*\text{a}^*\text{ppm Li}$) **	0.10
^3He P.R. from fast muons ($^3\text{He}/\text{g}^*\text{a}^*\text{ppm Li}$) **	0.01
ppm Li in bulk rock	21.0
Fractional cross section of Li	0.018
Resonance escape probability	0.72
Effective resonance integral (cm^2/g)	0.0044
Macroscopic scattering cross section (cm^2/g)	0.0960
Macroscopic absorption cross section (cm^2/g)	0.0074

* Average in upper 4 cm of rock at 1100 m for a 17.5 ka exposure age

Scaling following Lifton et al. (2005) and Heisinger et al. (2002)

** Only includes production via ^6Li . Not direct production.

Table 4.10: Bulk rock compositions and constants used in neutron flux calculations

	log. energy loss per collision	$\sigma_{\text{scattering}}$ (cm ² /at)	$\sigma_{\text{absorption}}$ (cm ² /at)	resonance integral (cm ² /at)	Conc (ppm)	neutron yield per ppm U (n/g*yr*ppm)	neutron yield per ppm Th (n/g*yr*ppm)	⁴ He stopping power @ 6MeV (MeV*cm ² /g)
H	1.0000	2.05E-23	3.30E-25	0.00E+00	<u>300</u>	0.0	0.0	1081.3
Li	0.2623	9.50E-25	7.10E-23	0.00E+00	<u>22</u>	23.8	10.4	360.1
Be	0.2063	6.15E-24	7.60E-27	4.00E-27	<u>3.2</u>	265.0	91.2	425.6
B	0.1742	4.27E-24	7.67E-22	1.72E-21	<u>15</u>	62.4	19.7	486.8
C	0.1578	4.74E-24	3.40E-27	1.60E-27	191	0.5	0.2	483.9
N	0.1363	1.00E-23	7.50E-26	6.35E-24	59	0.0	0.0	283.3
O	0.1199	3.76E-24	2.00E-28	4.00E-28	487015	0.2	0.1	294.0
F	0.1017	3.64E-24	9.60E-27	2.10E-26	720	0.0	0.0	234.6
Na	0.0845	3.03E-24	5.30E-25	3.11E-25	20110	12.5	5.9	487.3
Mg	0.0801	3.42E-24	6.30E-26	3.80E-26	3437	5.8	2.5	284.9
Al	0.0723	1.41E-24	2.30E-25	1.70E-25	70200	5.1	2.6	204.7
Si	0.0695	2.01E-24	1.70E-25	1.27E-25	322145	0.7	0.3	178.6
P	0.0632	5.00E-24	2.00E-25	0.00E+00	786	0.9	0.6	139.8
S	0.0611	9.79E-25	5.20E-25	7.00E-23	140	0.2	0.1	120.2
Cl	0.0553	1.58E-23	3.35E-23	1.37E-23	40	1.3	0.8	186.9
K	0.0503	2.04E-24	2.15E-24	1.00E-24	26177	0.1	0.1	288.0
Ca	0.0491	2.53E-24	4.30E-25	2.35E-25	14796	0.0	0.0	243.3
Ti	0.0412	4.09E-24	6.10E-24	3.10E-24	3417	0.0	0.0	168.4
V	0.0388	4.80E-24	5.08E-24	2.80E-24	<u>19</u>	0.0	0.0	183.2
Cr	0.0380	3.38E-24	3.07E-24	1.60E-24	<u>10</u>	0.0	0.0	185.3
Mn	0.0360	2.20E-24	1.33E-23	1.40E-23	542	0.0	0.0	158.9
Fe	0.0354	1.14E-23	2.56E-24	1.39E-24	29875	0.2	0.2	144.5
Co	0.0336	6.00E-24	3.70E-23	5.50E-23	<u>4.4</u>	0.0	0.0	124.7
Ni	0.0337	1.78E-23	4.49E-24	1.76E-24	1.0	0.0	0.0	127.2
Cu	0.0311	7.78E-24	3.78E-24	4.10E-24	1.0	0.0	0.0	92.2
Zn	0.0303	4.08E-24	1.11E-24	2.81E-24	73	0.0	0.0	89.8
Rb	0.0232	6.40E-24	3.80E-25	4.64E-24	165	0.0	0.0	176.2
Sr	0.0227	1.00E-23	1.28E-24	1.10E-23	108	0.0	0.0	127.8
Y	0.0223	7.67E-24	1.28E-24	1.00E-24	<u>68</u>	0.0	0.0	172.1
Zr	0.0218	6.40E-24	1.85E-25	9.50E-25	782	0.0	0.0	163.1
Cd	0.0177	5.60E-24	7.00E-23	0.06	0.06	0.0	0.0	65.9
La	0.0143	1.01E-23	8.97E-24	1.21E-23	81	0.0	0.0	149.1
Ce	0.0142		6.30E-25	3.70E-24	189	0.0	0.0	109.6
Pr	0.0141	2.54E-24	1.15E-23	1.74E-23	19.6	0.0	0.0	106.9
Nd	0.0138	1.60E-23	5.05E-23	4.50E-23	66.8	0.0	0.0	101.9
Sm	0.0132	3.80E-23	5.82E-21	1.40E-21	13	0.0	0.0	116.5
Gd	0.0127	1.72E-22	4.90E-20	3.90E-22	12	0.0	0.0	89.2
Dy	0.0123	1.06E-22	9.40E-22	1.48E-21	11.4	0.0	0.0	85.6
Er	0.0119	9.00E-24	1.59E-22	7.30E-22	6.9	0.0	0.0	91.1
Yb	0.0115	2.34E-23	3.55E-23	1.55E-22	6.8	0.0	0.0	69.6
Lu	0.0114	6.80E-24	7.64E-23	6.22E-22	1.0	0.0	0.0	59.9
Hf	0.0112	1.03E-23	1.04E-22	1.99E-21	15.9	0.0	0.0	55.3
Ta	0.0110	6.12E-24	2.05E-23	6.60E-22	5.0	0.0	0.0	61.9
W	0.0108	4.77E-24	1.84E-23	3.52E-22	0.4	0.0	0.0	55.0
Re	0.0107	1.13E-23	8.97E-23	8.31E-22	0.0006	0.0	0.0	43.3
Os	0.0105	1.50E-23	1.60E-23	1.80E-22	0.0001	0.0	0.0	40.8
Pb	0.0096	1.13E-23	1.71E-25	1.38E-25	49.4	0.0	0.0	50.6
Th	0.0086	1.30E-23	7.37E-24	8.50E-23	14	0.0	0.0	43.9
U	0.0084	9.38E-24	2.68E-24	2.77E-22	6	0.0	0.0	41.7

Bold denotes measured values (see online table 1)

Italics denote values taken from Honjo et al. 1992, [Magic Reservoir rhyolite]

Underline denotes values from Bonnichsen et al., (2008) [Bruneau rhyolites]

Regular text denotes values from Potts et al. (1992) for rhyolite

The low energy neutrons that drive ³He production from ⁶Li are derived from three primary sources: 1) radiogenic neutrons produced by decay of U and Th whose alpha

particles are involved in (α,n) reactions on light elements (Andrews and Kay, 1982; Chmiel et al., 2003), 2) ‘tertiary’ cosmogenic neutrons produced by excitation of target nuclei in rock by high-energy atmospheric neutrons (Dunai et al., 2007; Phillips et al., 2001), and 3) muogenic neutrons produced by slowing and stopping of muons by target nuclei in rock (Heisinger et al., 2002a; Heisinger et al., 2002b). Before any neutrons have a high probability of being captured by ${}^6\text{Li}$, they need to be slowed down (thermalized) by elastic collisions with other nuclei in the rock. Because smaller nuclei can absorb more kinetic energy during a collision, the low-energy neutron flux is very sensitive to hydrogen (i.e. water) content in the rock. The low energy neutron flux is also limited by the total ability of nuclei in the rock to absorb (capture) neutrons. Because some elements have very large neutron capture cross sections (Li, B, Gd, etc.), the neutron flux is a sensitive function of the bulk rock concentration of these elements. The compositions and other constants used in our calculations are given in online table 4.10.

For a given low energy neutron flux, ${}^3\text{H}$ production via neutron capture is proportional to Li concentration. Because ${}^3\text{H}$ produced via the ${}^6\text{Li}(n,\alpha){}^3\text{H}$ reaction has a stopping range of $\sim 30\ \mu\text{m}$ in common minerals, significant redistribution can occur between adjacent mineral phases (Farley et al., 2006; Ziegler, 2003). This redistribution is quantitatively modeled by determining the mean equivalent spherical radius of sample grains, and using the equation for implant and export of ions from a sphere (Dunai and Wijbrans, 2000; Farley et al., 2006; Farley et al., 1996).

4.5.2.1 Inherited Component (${}^3\text{He}_{\text{in}}$)

The inherited component can be derived either from trapped magmatic helium or from prior exposure of the sample. Crushing experiments show that the trapped magmatic component amounts to $< 2\%$ of the measured ${}^3\text{He}$ in our samples. This small amount of helium should largely be removed from pyroxene by crushing prior to fusion. Apatite and

zircon were not crushed prior to analysis because they are unlikely to have significant trapped components in their tiny grains and because any magmatic ^3He is included in our corrections based on the shielded samples. Regarding prior exposure, consistent ^3He concentrations in our reset samples suggests that > 3 m of rock was removed during the Bonneville flood and that the samples do not contain a $^3\text{He}_{\text{in}}$ component.

4.5.2.2 Nucleogenic Component ($^3\text{He}_{\text{nuc}}$)

Our fluence calculations described in the appendix are very close to, but slightly overestimate, the measured concentration of ^3He in shielded pyroxene (see $^3\text{He}_{\text{nuc}}$ for samples ID8 and ID13 in Table 4.4). Although the $\sim 6\%$ discrepancy is within error of the calculation inputs, it is worth considering possible explanations such as: 1) an erroneously old crystallization age, 2) underestimates of neutron absorbers or overestimates of U or Th concentrations, or 3) a violation of the assumption that all elements are evenly distributed throughout the rock. The third possibility is likely if the alpha-emitters (U and Th) are isolated in different mineral phases than elements with high (α, n) cross-sections (Na, Al, and Si), thereby preventing (α, n) reactions due to the short (~ 20 μm) range of α particles. The last point has been raised by several previous authors, and is worthy of a brief discussion here (Ballentine and Burnard, 2002; Hu et al., 2009; Martel et al., 1990).

Two simple arguments suggest that the homogeneity assumption is valid in the present case. First, the concentration of U and Th in the ground mass is higher than in the bulk rock by approximately its fractional abundance estimated from point counting, suggesting that virtually all of the U and Th is contained in the groundmass. Second, mineral compositions and point-counting show that almost all of the Na and Al (which account for $\sim 60\%$ of (α, n) reactions) are contained in the groundmass and that Si and O (which account for the rest) are evenly distributed throughout the rock. Because almost all of the U, Th, Na and Al is contained in the groundmass, the homogeneity assumption appears to be valid for these

rhyolites. However in general this may not be true; rocks in which a large fraction of U,Th is housed in trace phases poor in light elements (zircon, monazite, xenotime, etc) will have less nucleogenic ^3He than our model would estimate. Importantly, if U and Th are concentrated in accessory phases, the grain sizes need only be larger than $\sim 25 \mu\text{m}$ to create an inhomogenous distribution of alpha emitters.

Shielded zircon and apatite crystals of a range of (small) grain sizes allow us to estimate the average Li content of adjacent phases. This is useful because the Li content of adjacent phases is required for the calculation of the $^3\text{He}_{\text{cn}}$ component for exposed samples. The plot of $^3\text{He}_{\text{nuc}}$ vs. grain size shows a strong grain size dependence in shielded zircon, implying that the average Li content of adjacent minerals is higher than the internal Li content (Figure 4.2). For both mineral phases, we initially assumed that the average host Li content was equal to the bulk rock Li concentration (~ 21 ppm). As shown by the solid line in figure 4.2, this led to significant underestimates for both zircon and apatite (not shown). This underestimate is consistent with previous studies in which the average host Li concentration (computed by point counting) was higher than the bulk rock due to the presence of high Li phases such as biotite (or groundmass) preferentially in contact with apatite and zircon (Amidon et al., 2009). The best fit (least-squares) agreement between observed and modeled data is achieved with a host Li concentration of 29 ppm for zircon and 46 ppm for apatite.

4.5.2.3 Cosmogenic Neutron and Muogenic Components ($^3\text{He}_{\text{cn}}$ and $^3\text{He}_{\text{mu}}$)

Although muogenic production has been explicitly considered in previous studies, it is thought to produce $\ll 1\%$ of the measured ^3He in all phases and is thus not considered further (Amidon et al., 2009; Lal, 1987). The cosmogenic neutron ($^3\text{He}_{\text{cn}}$) component is produced only when the sample is exposed within ~ 3 meters of the surface. Because it is convolved with the spallogenic component, we have no independent observations (such as shielded samples) with which to assess its magnitude and must therefore rely on calculated values (see appendix for

details). For reset surfaces ${}^3\text{He}_{\text{cn}}$ is determined by multiplying the modeled ${}^3\text{He}_{\text{cn}}$ production rate ($1.57 \text{ at g}^{-1} \text{ a}^{-1} \text{ ppm Li}^{-1}$) by the known exposure age of 17.5 ka (Table 4.9). For unreset surfaces we capitalize on the fact that following subtraction of the nucleogenic component, all remaining ${}^3\text{He}$ can be attributed to the ${}^3\text{He}_{\text{cn}}$ and ${}^3\text{He}_{\text{sp}}$ components (i.e. ${}^3\text{He}_{\text{sp+cn}}$ in tables 4.1-4.3). We then use the newly determined local spallogenic production rate in pyroxene ($270 \text{ at g}^{-1} \text{ a}^{-1}$) to solve for the apparent exposure age (time) and the ${}^3\text{He}_{\text{cn}}$ component using the relationship: $\text{time} = ({}^3\text{He}_{\text{sp}} + {}^3\text{He}_{\text{cn}}) / (p{}^3\text{He}_{\text{sp}} + p{}^3\text{He}_{\text{cn}})$. The exposure ages determined using the pyroxene data are then used to solve for ${}^3\text{He}_{\text{cn}}$ in zircon and apatite. Due to the relatively young exposure ages considered in this study, the ${}^3\text{He}_{\text{cn}}$ components are small; $\sim 0.3 \text{ Mat/g}$ for zircon, $\sim 0.8 \text{ Mat/g}$ for apatite, and $\sim 1 \text{ Mat/g}$ for pyroxene where the variability reflects differences in effective Li concentration. The largest uncertainties in calculating ${}^3\text{He}_{\text{cn}}$ arise from the neutron fluence computation and the average Li content of adjacent minerals (see above).

4.5.3 Uncertainty of ${}^3\text{He}_{\text{sp}}$ Estimates

Several lines of evidence suggest that we have accurately isolated the ${}^3\text{He}_{\text{sp}}$ components listed in Tables 4.2-4.4. First, the slope of the Li vs ${}^3\text{He}_{\text{sp}}$ line for pyroxene is within error of zero, implying no under- or overcorrection for Li-produced components (Figure 4.3). Second, when ${}^3\text{He}_{\text{sp}}$ concentrations in pyroxene are plotted against ${}^3\text{He}_{\text{sp}}$ in zircon (all $>50 \mu\text{m}$ fractions), an excellent linear fit of $[{}^3\text{He}_{\text{sp(zr)}}] = 0.77 * [{}^3\text{He}_{\text{sp(px)}}] + 0.02$ is obtained for units of Mat/g (Figure 4.4). The intercept of this line is within error of zero suggesting that the spallation-induced component has been correctly isolated in both phases. In contrast, a plot of ${}^3\text{He}_{\text{sp}}$ concentrations in apatite against pyroxene yields a linear fit that does not pass through the origin, and has a shallower slope than the zircon-pyroxene plot (Figure 4.4). Based on previous results, apatite should have a steeper slope (i.e. higher production rate) relative to pyroxene than does zircon (Amidon et al., 2008a; Amidon et al., 2009; Farley et al., 2006). Because the reset samples give sensible ${}^3\text{He}$ concentrations and

production rates in relation to zircon and apatite, it appears that this shallow slope and high intercept may be due to leverage on the line exerted by erroneously low ${}^3\text{He}_{\text{sp}}$ concentrations in the three unreset samples (12, 14 and 16). The measured ${}^3\text{He}$ concentrations in apatite from these samples are 20-35% lower than expected based on measurements in zircon and pyroxene, a larger deficit than the entirety of the ${}^3\text{He}_{\text{cn}}$ correction in these samples. Because the apparent deficit is so large, it is difficult to attribute to the incorrect calculation of any of the Li-produced ${}^3\text{He}$ components. We lack a satisfactory explanation for this observation.

The uncertainties on our final ${}^3\text{He}_{\text{sp}}$ concentrations combine analytical errors with the uncertainty on calculation of the Li-produced components (Tables 4.1-4.3). The standard error for each sample (shielded or exposed) is determined by dividing the combined weighted analytical uncertainty by the square root of n replicate analyses. Uncertainties on the Li-produced ${}^3\text{He}_{\text{cn}}$ component were calculated using a Monte Carlo simulation in which 8 variables were allowed to vary over 1000 trials. These variables include internal Li content of the mineral ($1\sigma = 8\%$), average Li content of adjacent minerals ($1\sigma = 15\%$), bulk rock concentrations of the trace elements that strongly modulate neutron production or absorption (H, Li, B, Gd, and Sm) ($1\sigma = 12\%$), and grain radius ($1\sigma = 5\%$). Depending on grain size, these input errors result in 13-18 % standard deviation on the total Li-produced ${}^3\text{He}$.

To determine the 1σ error on the ${}^3\text{He}_{\text{sp}}$ component for a given grain size, we first compute the weighted standard error on ${}^3\text{He}_{\text{sp}}$ for all of the reset surface exposure samples of that grain size. This uncertainty is then added in quadrature with the uncertainties on the ${}^3\text{He}_{\text{nuc}}$ and ${}^3\text{He}_{\text{cn}}$ components, which are taken as the standard deviation of ${}^3\text{He}_{\text{m}}$ for the shielded sample and the Monte-Carlo standard deviation on the calculated ${}^3\text{He}_{\text{cn}}$ component for that grain size. For zircon, because the production rates for the three largest grain size categories are within error of each other, the grand mean ${}^3\text{He}_{\text{sp}}$ is computed as the weighted mean of the three. The standard deviation of the grand mean is then propagated with the 1σ

error on the age of the Bonneville outburst flood (± 0.5 ka) to compute a 1σ uncertainty on the final production rate estimate for each mineral phase.

4.6 Discussion

4.6.1 Production Rates of Spallogenic ^3He

This study provides the fourth calibration of production rates in zircon and apatite (Amidon et al., 2008a; Amidon et al., 2009; Farley et al., 2006). Because the three previous studies have calibrated against ^{10}Be and/or ^{21}Ne , their published production rates are dependent upon the accepted production rates of ^{10}Be and ^{21}Ne in quartz. As a consequence, table 4.11 summarizes published $^3\text{He}/^{10}\text{Be}_{\text{qtz}}$ ratios from previous studies and reports revised production rates relative to a SLHL $^{10}\text{Be}_{\text{qtz}}$ production rate of $4.51 \text{ at } \text{g}^{-1} \text{ a}^{-1}$ (including muogenic production). This revised value for the $^{10}\text{Be}_{\text{qtz}}$ production rate comes from a weighted average of the five production rate scaling schemes presented in Balco et al. (2008), adjusted by a factor of 0.904 to reflect the revised $^{10}\text{Be}/^9\text{Be}$ ratio of the 07KNSTD3110 standard (Balco et al., 2008; Niishizumi et al., 2007). Although there is no statistical basis for averaging production rates derived from different scaling models it is done here to obtain reference production rates that simplify the discussion.

Table 4.11: Summary of results of four ^3He calibration studies for zircon and apatite

	Idaho (This Study)					Coso (Amidon et al., 2009)			Nepal [#] (Amidon et al., 2008)			Bolivia (Farley et al., 2006)			
	St	De	Du	Li	Avg.	$^3\text{He}/^{10}\text{Be}_{\text{qtz}}$	Pub	Rev.	$^3\text{He}/^{10}\text{Be}_{\text{qtz}}^{\#}$	Pub	Rev.	$^3\text{He}/^{21}\text{Ne}_{\text{qtz}}$	$^3\text{He}/^{10}\text{Be}_{\text{qtz}}$	Pub	Rev.
$^{10}\text{Be}_{\text{qtz}}$ P.R.	-	-	-	-	-	-	4.87	4.51	-	4.98	4.51	-	-	4.87	4.51
p^3He Zirc.	96	106	106	113	105	23.3	114	105	30.4	135	137	3.9	22.1	87	100
p^3He Ap.	123	136	136	146	135	30.6	149	138	37.7	168	170	5.0	28.0	112	126
p^3He Px.	117	130	130	139	129	29.7	145	134	-	-	-	-	-	-	-
p^3He Gnt.	-	-	-	-	-	29.7	144	134	34.0	153	153	-	-	-	-
p^3He Tit.	-	-	-	-	-	-	-	-	-	-	-	4.3	24.5	97	110
p^3He Ky.	-	-	-	-	-	-	-	-	39.6	177	179	-	-	-	-

[#]Pub" denotes previously published values; "Rev." denotes values recalculated using average $^{10}\text{Be}_{\text{qtz}}$ production rates from Balco et al. (2008)

"Prop." denotes production rates recalculated using the lower $^{10}\text{Be}_{\text{qtz}}$ production rate proposed in the text

denotes that only the lowest elevation sample (CRN 259) are reported here. ^{10}Be values revised relative to 07KNSTD3110 $^{10}\text{Be}/^9\text{Be}$ ratio

"St", "De", "Du", and "Li" denote different scaling schemes (2.3, 2.08, 2.08, 1.94) following the notation introduced in Balco et al. (2008)

One of the motivations of this study is to produce a set of production rate estimates for zircon and apatite that are independent of the ^{10}Be production rate. We obtain production rates of $\sim 105 \pm 9$ and $\sim 135 \pm 17$ at $\text{g}^{-1} \text{a}^{-1}$ for zircon and apatite averaged over the four scaling models in table 4.11. These rates agree well with the revised rates of ~ 103 and ~ 132 at $\text{g}^{-1} \text{a}^{-1}$ obtained by calibrating ^3He against ^{10}Be in quartz ($p^{10}\text{Be}_{\text{qtz}} = 4.51$ at $\text{g}^{-1} \text{a}^{-1}$) from rhyolite surfaces in Bolivia and California (Amidon et al., 2009). It is important to emphasize that zircon production rates reflect mean values for grain sizes of $\text{MER} \geq 38 \mu\text{m}$, and may not apply to smaller grain sizes due to redistribution of spalled ^3He and ^3H from adjacent mineral phases. In contrast, apatite production rates likely apply to a full range of grain sizes because ^3H and ^3He production rates in adjacent silicate minerals should be comparable to those in apatite (Farley et al., 2006).

For pyroxene, we calculate a production rate of 129 ± 10 at $\text{g}^{-1} \text{a}^{-1}$ averaged over the four scaling models in table 4.11, which also lists scaling factors and production rates calculated using each individual scaling model. These values are within the range of six previous studies, and agree very well with the range of 120-136 at $\text{g}^{-1} \text{a}^{-1}$ recently recalculated against ^{14}C for the nearby Tabernacle Hill site (Goehring et al., 2010). These rates are also in agreement with the revised rate of 134 at $\text{g}^{-1} \text{a}^{-1}$ for pyroxene determined against ^{10}Be in quartz ($p^{10}\text{Be}_{\text{qtz}} = 4.51$ at $\text{g}^{-1} \text{a}^{-1}$) at Coso, California (Amidon et al., 2009).

Based on several recent studies, it seems likely that the ^{10}Be production rate of 4.51 at $\text{g}^{-1} \text{a}^{-1}$ may not be a globally applicable value (Balco et al., 2009; Putnam et al., 2010). We therefore express the zircon and apatite production rates as the arithmetic mean of results from three existing studies, two of which are dependent on the SLHL ^{10}Be production rate in quartz ($p^{10}\text{Be}_{\text{qtz}}$).

$$p(^3\text{He}_{\text{zirc}}) = \frac{(105 + 23.3 * p^{10}\text{Be}_{\text{qtz}} + 22.1 * p^{10}\text{Be}_{\text{qtz}})}{3} \quad (4.2)$$

$$p(^3\text{He}_{\text{ap}}) = \frac{(135 + 30.6 * p^{10}\text{Be}_{\text{qtz}} + 28 * p^{10}\text{Be}_{\text{qtz}})}{3} \quad (4.3)$$

We have not included estimates from the Nepal study of Amidon et al. (2008) in these equations because they are clear outliers from the three other datasets in table 4.11. These samples were measured at elevations of 3200-4600 m near the maximum in rigidity cutoff. Further studies at high elevations and high rigidity cutoff are required to determine if ^3He and/or ^{10}Be production rates are sensitive to changes in the energy spectrum of incident nucleons at these locations. In any case all recent work confirms the peculiarity of ^3He production rate studies in the Himalaya (Amidon et al., 2008a; Gayer et al., 2004) and justifies their exclusion from this computation.

When a value of $4.51 \text{ at g}^{-1} \text{ a}^{-1}$ is used, the standard deviation of the three zircon production rates is reduced from 14 to 3 at $\text{g}^{-1} \text{ a}^{-1}$, and for apatite from 18 down to 6 at $\text{g}^{-1} \text{ a}^{-1}$. The grand mean production rates for spallation produced ^3He are $103 \pm 3 \text{ at g}^{-1} \text{ a}^{-1}$ for zircon (MER $\geq 38 \mu\text{m}$) and $133 \pm 6 \text{ at g}^{-1} \text{ a}^{-1}$ for apatite.

4.6.2 Criteria for ^3He Dating With Zircon and Apatite

The new data presented in this study, and their agreement with revised production rates from previous studies (Table 4.11) strongly suggest that zircon and apatite can be successfully used for cosmogenic ^3He dating, at least under certain circumstances. The most fundamental limitation on the technique is the size of the spallation-produced ^3He component ($^3\text{He}_{\text{sp}}$) relative to the Li-produced ^3He components ($^3\text{He}_{\text{nuc}}$, $^3\text{He}_{\text{cn}}$, $^3\text{He}_{\text{mu}}$). Whereas the size of the $^3\text{He}_{\text{sp}}$ component is entirely a function of location and exposure age, the Li-produced components additionally depend on the Li content, closure age, and to a lesser extent, grain size. Because the Li content of neighboring minerals is typically much higher than in zircon or apatite, the size of the Li-produced component can be reduced by working with large grains (MER $\geq 38 \mu\text{m}$), that are less vulnerable to implantation. A useful metric with which to quantify the vulnerability of a given sample to Li-produced ^3He is the apparent Li

(Li_a). This is calculated using the implant/export equation, which includes the internal Li content (Li_i), the average Li content of adjacent “host” minerals (Li_h), MER (R), and the range of Li-produced ^3H in common silicate minerals (S):

$$Li_a = Li_i \left[1 - 0.75 \left(\frac{S}{R} \right) + 0.0625 \left(\frac{S}{R} \right)^3 \right] + Li_h \left[0.75 \left(\frac{S}{R} \right) - 0.0625 \left(\frac{S}{R} \right)^3 \right] \quad (4.4)$$

For example, a zircon with MER = 50 μm , internal Li = 2 ppm, and host Li = 20 ppm would have an apparent Li of ~ 10 ppm.

For a given apparent Li concentration the ratio of $^3\text{He}_{\text{sp}}/^3\text{He}_{\text{tot}}$ is a function of exposure age and the He closure age of the specific mineral analyzed. The He closure age is identical to the (U-Th)/He age and varies among mineral phases depending upon He diffusion characteristics. Thus, for rocks that have been exhumed from great depths and high temperatures, minerals with higher He diffusivity (e.g., apatite) will have a lower nucleogenic ^3He content than minerals with low diffusivity (e.g., zircon) (Reiners et al., 2002; Wolf et al., 1996). Figure 4.5 shows the evolution of the $^3\text{He}_{\text{sp}}/^3\text{He}_{\text{tot}}$ ratio as a function of exposure age, closure age and apparent Li content. As a practical example of how this figure can be used, limiting the Li-produced ^3He component to $\sim 50\%$ of the total for an apparent Li content of 10 ppm and a ~ 10 My closure age would require a ~ 7 ka exposure at 1000 m elevation. This limitation is relaxed at higher elevations as the spallation production rate increases. Based on our limited survey data (Amidon and Farley, unpublished), zircons and apatites of large grain size in continental igneous rocks have apparent Li concentrations ranging from 5-20 ppm.

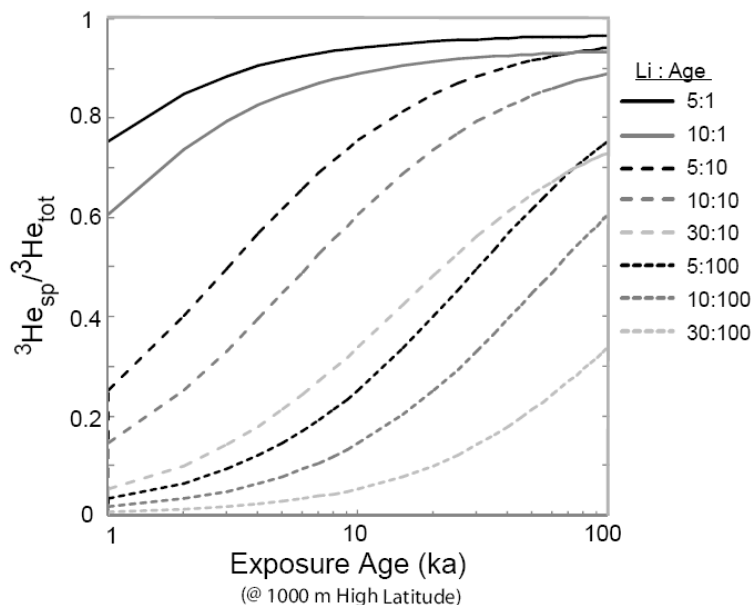


Figure 4.5

Calculations showing the fraction of spallation produced ^3He in apatite as a function of the He closure age, apparent Li content, and exposure age at a 1000 m elevation, high latitude site. Apparent Li is in units of ppm and closure age is in units of Ma. Calculations assume a typical granitic composition with 12 ppm of Th and 4 ppm of U. Spallation produced fractions will increase for higher elevation samples and decrease for lower

If Li produced components are large compared to spallation ^3He , they limit the accuracy with which the surface exposure age can be determined. The three primary sources of error are the analytical errors on the exposed and shielded samples, and the error on the model calculation of the $^3\text{He}_{\text{cn}}$ component. Because analytical errors are directly related to the concentration of ^3He in the sample they become relatively smaller for samples with older exposure ages (or more nucleogenic ^3He in the shielded case). In contrast, because the error on the calculated $^3\text{He}_{\text{cn}}$ component is primarily a function of how well the composition of the rock and the Li content is known, its contribution to the total error increases with Li content.

In many cases, even Li-rich samples can provide relatively precise exposure age estimates. For example, in this study we measure a concentration $\sim 10.3 \pm 0.4$ ($\sim 4\%$) Mat/g of ^3He in an exposed pyroxene sample, and 4.1 ± 0.1 ($\sim 3\%$) in a shielded pyroxene with a similar Li concentration (~ 57 ppm). Because it is determined with reasonable precision, subtracting the $^3\text{He}_{\text{nuc}}$ component gives $\sim 6.2 \pm 0.4$, only moderately increasing the error (to $\sim 7\%$). The relative error on the modeled $^3\text{He}_{\text{cn}}$ component is large at $\sim 1.5 \pm 0.2$ ($\sim 13\%$), but its small absolute value means that it contributes relatively little to the final error of 4.7 ± 0.4

(~9%) on its $^3\text{He}_{\text{sp}}$. Figure 4.6 illustrates approximately how these different sources of error propagate in samples of different exposure age, closure age, and apparent Li content. As an example of its use, we have plotted a hypothetical sample from a ~18 ka Tioga-aged moraine boulder exposed at ~2250 m elevation in the Sierra Nevada mountains of California.

Assuming an apparent Li of 10 ppm and a (U/Th)-He closure age of 50 Ma, the $^3\text{He}_{\text{sp}}$ component in apatite could be determined with a precision of ~7% (circle in figure 4.6). This assumes a single analysis of a 30 mg aliquot of material, and the use of a shielded sample to make the correction for $^3\text{He}_{\text{nuc}}$.

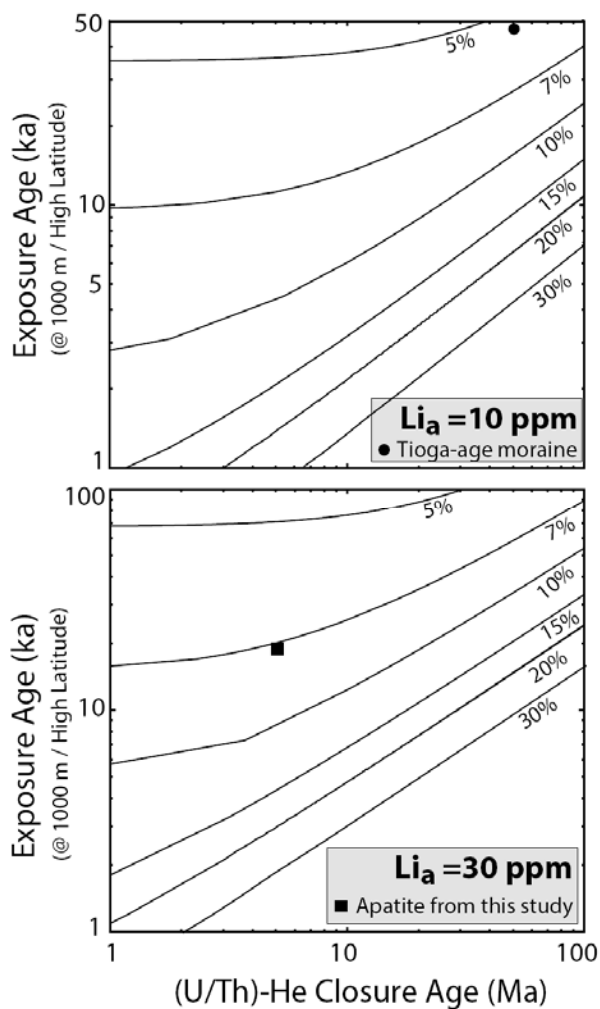


Figure 4.6

Calculations showing the 1σ uncertainties with which the $^3\text{He}_{\text{sp}}$ component can be determined in apatite from a sample collected at a 1000 m elevation, high latitude site. Symbols show typical samples from this study, and from a Tioga-aged moraine composed of a typical Sierra Nevada granodiorite. Although the Tioga age moraine is ~18 ka, it has been plotted at an age of ~50 ka to reflect higher production rates near the occurrence of these moraines at elevations of ~2500 m rather than the 1000 m for which the lines of constant error are plotted. This calculation assumes typical measurement sensitivities obtained at Caltech, and a single analysis of ~30 mg of apatite from the >75 μm size fraction. This quantity of apatite can routinely be obtained from ~1 kg of granitoid rock.

4.6.3 Geomorphic Implications

In addition to providing an opportunity for calibration of ^3He production rates, our data also provide insight into the incision history of the Snake River canyon. The most fundamental observation is that all samples from the upstream site (Pillar Falls) experienced greater than ~3 m of bedrock erosion during the Bonneville flood whereas most samples from the wider part of the canyon below Perrine bridge experienced incomplete erosional resetting. Notably, two of the unreset samples below Perrine bridge (10 and 12) are closer to the modern river level than any of the upstream samples. The apparent contrast between the intensity of erosion at Pillar Falls and further downstream is surprising given that many models of fluvial erosion assume that shear stress on the river bed is proportional to water depth, and thus predict that the wide and narrow parts of the canyon should experience similar erosive forces as long as they are both bank full (Rosgen, 1994).

Based on the observations above, it seems that the depth and width of the canyon below Perrine bridge were not significantly altered by the Bonneville outburst flood. Although our data are insufficient to precisely constrain this earlier history, it seems plausible that much of the existing canyon, including the extensive fluted and potholed bedrock surfaces below Perrine Bridge (samples 14 and 16), may have formed during previous flood events. Such a flood event would have formed much of the surface as it exists today, followed by a minor amount of erosion during the Bonneville flood to create the well-preserved scour features. This idea is intriguing because neither the Eden/Rupert overland channel nor the scoured alcoves have been directly dated to Bonneville age. Additionally, recent work in the Hagerman area has shown that Box canyon, a similar feature to the Blue Lakes alcove, likely formed during pre-Bonneville flood events (Lamb et al., 2008). Finally, the apparent exposure ages of samples 10, 12 and 16 (89, 110, and 89 ka) are similar to the 92 ka average age of three paleo-flood surfaces documented along the Big Lost River, a tributary to the Snake River (Cerling et al., 1994). Future work should focus on dating erosional

features along the Eden overflow channel to directly tie them to the Bonneville flood, or alternatively, tie them to possible earlier flood events.

4.7 Conclusions

New cosmogenic ^3He measurements in zircon, apatite and pyroxene from eight scoured rhyolite surfaces thought to be the product of the Bonneville outburst flood fall into one of two classes. The first class of samples yielded ^3He concentrations that are within error of each other. When corrected for non-spallation ^3He using shielded samples and a model for $^3\text{He}_{\text{en}}$ production, these samples can be used to calibrate the spallation production rate of ^3He against the known ^{14}C age of the Bonneville outburst flood. Synthesizing these new results with previous calibration studies performed by reference to ^{10}Be shows that the ^3He production rates in apatite and zircon agree to within 5% if an averaged ^{10}Be production rate of $4.51 \text{ at g}^{-1} \text{ a}^{-1}$ is adopted (Balco et al., 2008). Making this assumption we obtain a best estimate for the SLHL production rate of $103 \pm 3 \text{ at g}^{-1} \text{ a}^{-1}$ for zircon ($\text{MER} \geq 38 \mu\text{m}$) and $133 \pm 6 \text{ at g}^{-1} \text{ a}^{-1}$ for apatite. The second class of samples contains inherited ^3He from prior exposure, reflecting the complex incision history of the Snake River canyon and suggesting one or more earlier flood events.

These data suggest that uncertainties in production rate are no longer the major source of uncertainty in using spallation ^3He in apatite and zircon for surface exposure dating. Instead the biggest consideration is correction for ^3He produced from the capture of both nucleogenic and cosmogenic neutrons by ^6Li . We demonstrate that although Li-produced components can become large even in fairly young rocks ($> 1 \text{ My}$), in many cases they can be reliably determined using shielded samples. Because zircons contain ~ 10 times less Li than pyroxene and thus much smaller Li-produced components, they can provide more accurate age determinations in some cases.

Chapter 5

MASS SPECTROMETRIC ^3He MEASUREMENT IN ^4He -RICH PHASES: TECHNIQUES AND LIMITATIONS FOR COSMOGENIC ^3He DATING OF ZIRCON, APATITE, AND TITANITE

5.1 Introduction

Cosmogenic dating is a widely used tool for establishing exposure histories of both terrestrial and extra-terrestrial surfaces. Because of its nuclear stability, high production rate from most target elements, and relative ease of measurement, ^3He is a particularly attractive nuclide for these studies. Efforts have been made to develop a diverse family of minerals amenable to cosmogenic ^3He dating; for example, cosmogenic ^3He production rates in apatite, zircon and titanite were recently determined (Amidon et al., 2008a; Amidon et al., 2009; Farley et al., 2006). These particular minerals are ubiquitous on Earth and are therefore appealing dating targets, but they present a unique analytical challenge because they often carry extremely high ^4He concentrations from U and Th decay. For several reasons such high concentrations can reduce the accuracy and precision of ^3He measurements. In this paper we document how high ^4He abundances degrade mass spectrometric ^3He measurements and present approaches by which to minimize these negative consequences. Ultimately the utility of these mineral phases for cosmogenic ^3He dating will hinge on the long term geological history of the sample. Most notably, samples with old (U/Th)-He ages may not be suitable for cosmogenic ^3He dating due to excessively high ^4He contents. Based on these considerations we present constraints on the range of geological settings in which cosmogenic ^3He dating of apatite, zircon and titanite is likely to be successful.

The presence of spallation produced cosmogenic ^3He in terrestrial samples was first recognized by researchers who had been focusing on measuring the trapped magmatic He component in olivine and pyroxene (Craig and Poreda, 1986; Kurz, 1986a; Lal, 1987). As a

result, early applications of cosmogenic ^3He dating focused on olivine and pyroxene, and only recently has attention extended to more diverse mineral phases such as zircon, apatite, titanite, garnet, and Fe-Ti oxides (Amidon et al., 2008a; Farley et al., 2006; Gayer et al., 2004; Kober et al., 2005). Of these, the production rates in zircon and apatite are the best calibrated (against both ^{10}Be and ^{14}C), giving production rates of ~ 103 and 133 at $\text{g}^{-1} \text{a}^{-1}$ respectively (Amidon and Farley, 2010). However, most of these calibration studies were performed on samples with (U/Th)-He ages of < 6 Ma, which accordingly have relatively low concentrations of radiogenic ^4He . As the technique is applied more widely, the range of (U/Th)-He ages (a proxy for radiogenic ^4He), and exposure ages (a proxy for ^3He) that combine to give routinely measurable $^3\text{He}/^4\text{He}$ ratios must be defined.

To place constraints on the geologic conditions in which cosmogenic ^3He dating in zircon, apatite, and titanite is likely to succeed, we must first understand the analytical limitations associated with measurement of small amounts of ^3He in the presence of large amounts of ^4He . We thus investigate the performance of the Caltech MAP 215-50 noble gas mass spectrometer when operated under high ^4He pressures and discuss how these performance characteristics place a lower limit on the measurable $^3\text{He}/^4\text{He}$ ratio. The three analytical issues discussed in this paper are: 1) instrument sensitivity at ^4He pressures well above, and $^3\text{He}/^4\text{He}$ ratios well below, what can be achieved by external standards, 2) the abundance sensitivity of the instrument, i.e., the $^3\text{He}/^4\text{He}$ ratio at which tailing of ^4He onto the ^3He beam becomes significant, and 3) the effects of large amounts of ^4He on the accuracy of the regression used to convert the time evolution of the ^3He beam into a ^3He abundance. We show that ^3He sensitivity at high ^4He pressures can be reliably determined by isotope dilution via the introduction of a spike of high $^3\text{He}/^4\text{He}$ ratio standard midway through the analysis. To establish the abundance sensitivity, we use a sample of cosmic-ray shielded thorianite (ThO_2) to generate large amounts of helium gas with an extremely low $^3\text{He}/^4\text{He}$ ratio ($\sim 0.54 \times 10^{-10}$). We also document a decrease in the ^3He precision that can be

obtained for very low $^3\text{He}/^4\text{He}$ ratio samples due to an increase in the slope of the ^3He vs. time evolution with increasing amounts of ^4He .

5.2 Helium Extraction and Mass Spectrometry

Helium extraction is performed by thermal degassing in a double-walled resistance furnace or by Nd-YAG laser heating of sample loaded in a platinum packet. In the resistance furnace, samples are heated to 1500°C for 20 minutes following standard procedures (Patterson and Farley, 1998). However in many cases a variant of the laser method developed for (U/Th)-He dating is preferred because grains can be recovered after He outgassing for additional analyses or to demonstrate sample purity (House et al., 2000). For cosmogenic dating, large (6 x 3 mm) platinum tubes are used, which can typically accommodate up to 35 mg of zircon or 25 mg of apatite. Previously degassed capsules are loaded with sample and placed into wells in a copper planchet. To minimize thermal conduction to the copper, the capsules are placed on top of small lengths of tungsten wire. The capsules are heated to about 1200°C by rastering the laser beam across the surface of the capsule. Although the exact temperature achieved by each sample is not monitored, complete degassing is verified by re-extraction steps at the same temperature.

Following extraction, the evolved gas is exposed to a hot SAES getter and expanded into a ~1.5 L expansion volume. A ~1 % aliquot is then analyzed in a Pfeiffer Prisma quadrupole mass spectrometer to obtain a ^4He measurement (Wolf et al., 1996). The remainder of the He is cryogenically focused and released into a MAP 215-50 magnetic sector mass spectrometer. This instrument uses a Nier-type electron impact ion source, and measures the resulting ion signal by peak jumping between a Channeltron electron multiplier operated in pulse counting mode for ^3He and a Faraday cup with $10^{11} \Omega$ resistor for ^4He . Most of the ~45 minute sample collection time is devoted to counting ^3He ions using 30 second integrations and 600 second blocks. Measurements

of the ^4He peak, as well as off-peak masses 2.7 and 3.2 are made for 30 seconds each between ^3He collection cycles.

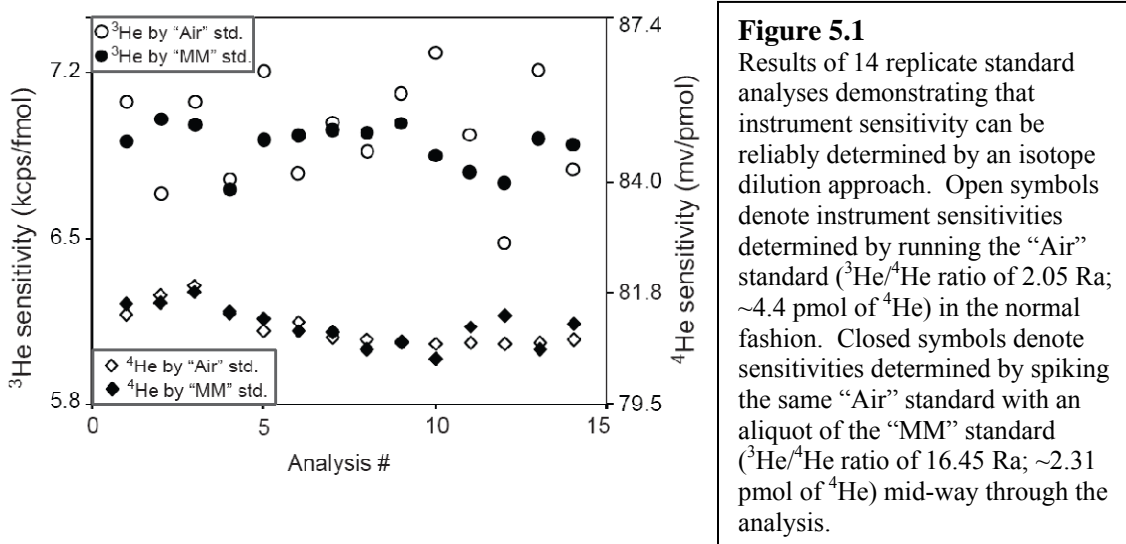
Simultaneous with this analysis, an aliquot of the “Murdering Mudpot” (MM) standard (16.45 Ra; ~ 2.31 pmol of ^4He) is prepared in the extraction line for use as an isotope dilution spike. After ~ 45 minutes of data acquisition on the sample this spike is introduced into the mass spectrometer. This results in a large increase in the ^3He signal without a significant change in the amount of ^4He or in sensitivity. This step allows the in-run ^3He sensitivity to be determined by fitting one regression line to the pre-spike ^3He data, and another to the post-spike data. The linear fit applied to the pre-spike data is used to estimate the ^3He signal derived from the sample at time zero, and also to make a forward prediction of the signal generated by the sample at the time of the spike inlet. A second line is then fit to the post-spike data, and is used to predict the combined signal from the sample and spike immediately after spike introduction. The difference between these two values is the net signal resulting from the ^3He in the spike, and is divided by the known amount of ^3He in the spike to estimate the ^3He sensitivity for each individual analysis.

Upon completion of the measurement, the mass spectrometer inlet valve is opened and the helium gas back-pumped to a turbomolecular pump. This step prevents exposure of the mass spectrometer ion pump to large amounts of ^4He , which we observed to become a source of ^4He following repeated exposure.

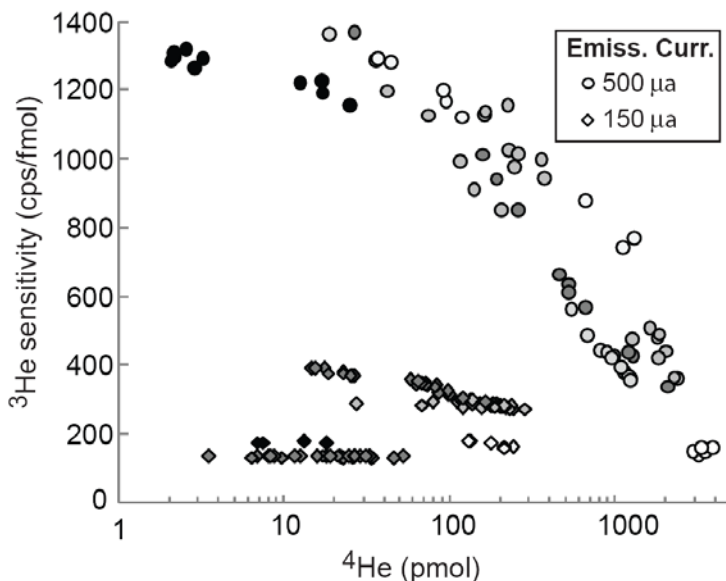
5.3 Determining Instrument Sensitivity

The accuracy of the spiking technique was demonstrated by analyzing a series of 14 aliquots of the Caltech “Air” standard ($^3\text{He}/^4\text{He}$ ratio of 2.05 Ra, ~ 4.4 pmol of ^4He) using this method. As shown in figure 5.1, the mean sensitivity calculated directly from the Air standard and from the subsequent MM spike agreed within 2%, within error of their known concentrations. The sensitivities calculated from the 14 replicate MM spikes have a standard deviation of 1.3%, lower

than the 3.5% for the replicate Air standards because the larger ^3He signal derived from the MM standard reduces the counting statistics error.



It is necessary to spike our analyses because large amounts of ^4He result in space charge effects that lead to decreases in the sensitivity of the mass spectrometer. Figure 5.2 shows a compilation of ^3He sensitivities obtained for various amounts of ^4He under various tuning conditions over a several year period that unambiguously document this effect. Although sensitivities up to ~ 13.5 kcps/fmol ^3He can be obtained by setting the trap current to $500 \mu\text{a}$, the maximum ^3He sensitivity decreases rapidly with increasing ^4He amount. In contrast, when operated at a trap current of $150 \mu\text{a}$, the sensitivity decreases much more slowly with increasing ^4He . It has been shown previously that the highest sensitivity is typically achieved near the ^4He pressure at which the mass spectrometer is tuned (Burnard and Farley, 2000). Our data agree with this result, and it is thus possible that higher sensitivities can be obtained for high- ^4He analyses at $500 \mu\text{a}$ by tuning the instrument at higher ^4He pressures.

**Figure 5.2**

Instrument sensitivities determined during actual sample analyses at emission currents of either 500 μa (circles) or 150 μa (diamonds) for a variety of tuning conditions. Different tuning conditions are denoted by different symbol fill colors. Note that the sensitivity decreases much more rapidly as function of ^4He pressure when running at 500 μa .

5.4 Determining Abundance Sensitivity

The feasibility of accurately measuring cosmogenic ^3He in high- ^4He phases depends on the $^3\text{He}/^4\text{He}$ ratio of the mineral. For minerals with extremely low $^3\text{He}/^4\text{He}$ ratios ($< \sim 10^{-9}$), generating a measurable ^3He signal often requires introduction of very large amounts of ^4He that may cause electrical arcing between the high voltage plates of the ion source or cause measurable tailing of the ^4He peak (or the HD peak) onto the ^3He peak.

A firm lower limit on the measurable $^3\text{He}/^4\text{He}$ ratio can be obtained by combining estimates of the effective detection limit for ^3He with the ^4He pressure at which arcing is expected. Assuming a plate spacing of about 5 mm and a voltage difference of ~ 4 kv in the ion source, the Paschen equation (Hartmann et al., 2000) indicates electrical discharge will occur at about 4 mbar He pressure. Given a volume of about 1 liter in the MAP flight tube, this pressure corresponds to about ~ 0.2 μmol ($\sim 10^{17}$ atoms) of ^4He . Assuming a detection limit of 1 cps of ^3He and a sensitivity of 2.3 kcps/fmol ^3He (Figure 5.2), the absolute detection limit for ^3He at high ^4He pressure is ~ 3.7 fmol ($\sim 1 \times 10^5$ atoms). Combining these two figures gives the lowest $^3\text{He}/^4\text{He}$ ratio at which ^3He can be accurately detected: about 1×10^{-12} . Attempts to measure ^3He in gas with

a lower $^3\text{He}/^4\text{He}$ ratio would either yield a ^3He beam too small to accurately quantify, or amounts of ^4He so large that arcing would occur.

Above this hard limit, the lowest measurable $^3\text{He}/^4\text{He}$ ratio is governed by the abundance sensitivity of the mass spectrometer as a function of the ^4He amount. To document this characteristic for the MAP 215-50, we used a sample of cosmic-ray shielded thorianite (ThO_2) from the Great Bear Lake mine (NWT, Canada) as a source of nearly pure ^4He . Thorianite was selected for its high ^4He production rate relative to other nuclear reactions (e.g., $^6\text{Li}(n,\alpha)^3\text{H}$) and because, unlike ^{238}U , ^{232}Th does not produce ^3He from fission. We first established the $^3\text{He}/^4\text{He}$ ratio of the thorianite by running incrementally larger aliquots of He until a measurable ^3He signal was obtained. To insure that no ^4He ions or HD ions were tailing onto mass 3 during these experiments, the ion count rate at mass 3.2 was monitored during the analysis and mass scans were performed immediately following the analysis (Figure 5.3). Because ^3He measurements were very close to blank level the measured $^3\text{He}/^4\text{He}$ ratios have large errors. Nonetheless, four replicate analyses suggest the thorianite has a $^3\text{He}/^4\text{He}$ ratio of $0.54 \times 10^{-10} \pm 0.17 \times 10^{-10}$ (1σ).

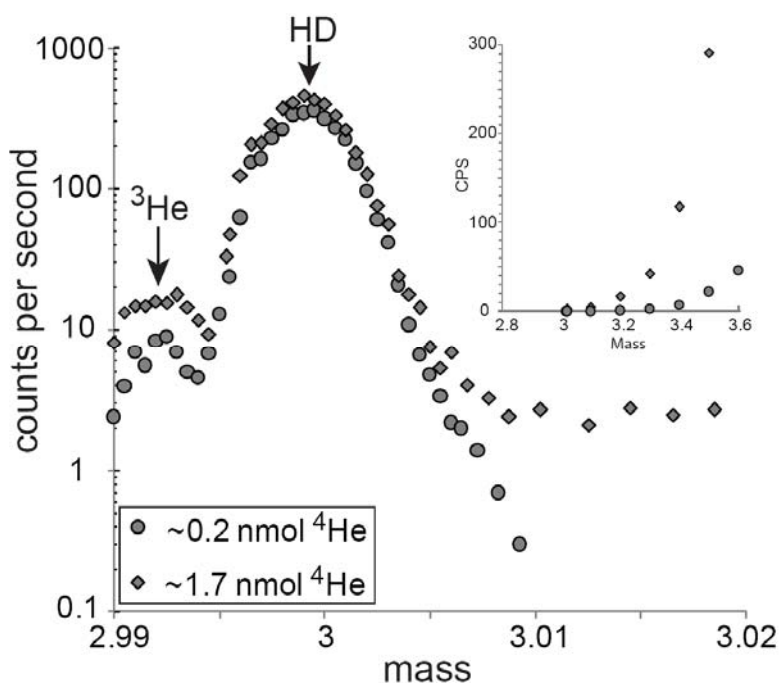


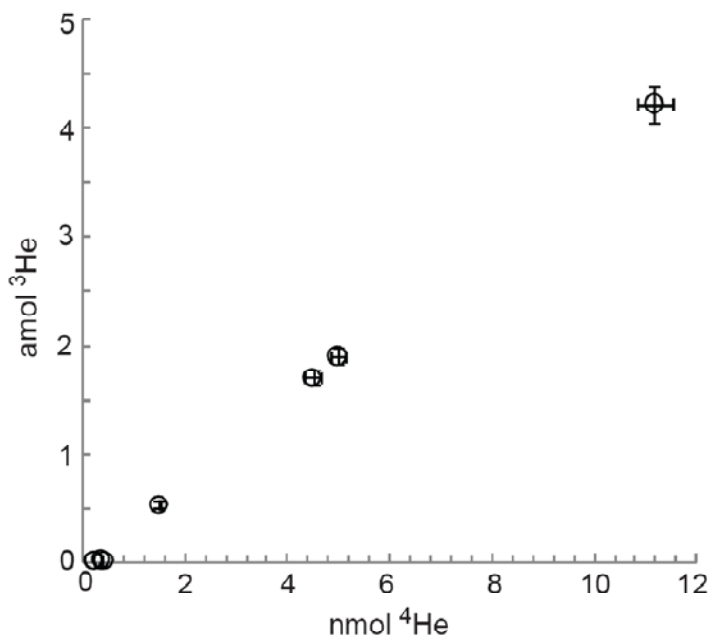
Figure 5.3

Mass scans performed on helium gas derived from shielded thorianite samples. Samples with ~ 0.2 nmol of ^4He do not show tailing of ^4He ions onto mass 3, whereas samples with ~ 1.7 nmol of ^4He show significant tailing. The size and shape of the HD peak is unchanged between the two analyses suggesting that tailing of HD onto ^3He is not a problem at high ^4He pressures. The inset panel shows results of the same mass scans over a larger mass range.

Next, we determined the abundance sensitivity by analyzing successively larger aliquots of the thorianite-derived gas. The onset of significant tailing was first detected at ~1.16 nmol of ^4He ($\sim 7 \times 10^{14}$ atoms), as indicated by the presence of ions at mass 3.2. Mass scans up to 3.6 AMU demonstrate conclusively that the measured signal at mass 3.2 is due to tailing of the ^4He peak (Figure 5.3). Successive analyses at ^4He amounts above 1.16 nmol allow calculation of the abundance sensitivity (Figure 5.4). This is done by first multiplying the measured ^4He by the established $^3\text{He}/^4\text{He}$ ratio of the thorianite gas to determine the number of ions measured at mass 3 that can be attributed to ^3He in the thorianite gas. This is then subtracted from the measured mass 3 signal, with the remainder attributed to tailing of ^4He ions onto mass 3, as described by:

$${}^4\text{He}_{M3} = M3_{meas} - ({}^3\text{He}/{}^4\text{He})_{thorianite} * {}^4\text{He}_{meas} \quad (5.1)$$

where ${}^4\text{He}_{M3}$ denotes the number of ^4He atoms counted at mass 3, $M3_{meas}$ denotes the combined number of ^3He and ^4He atoms counted at mass 3, $({}^3\text{He}/{}^4\text{He})_{thorianite}$ is the previously determined $^3\text{He}/^4\text{He}$ ratio of thorianite, and ${}^4\text{He}_{meas}$ denotes the total number of ^4He atoms counted at mass 4. The resulting abundance sensitivity is $\sim 3.1 \times 10^{-10}$ over the ^4He range from ~1 to 12 nmol (Table 5.1).

**Figure 5.4**

Results of helium analyses on cosmic-ray shielded thorianite samples from a mine. The ^3He is derived primarily from tailing of ^4He ions onto the mass 3 peak, and the slope of the ^4He vs. ^3He relationship approximately defines the abundance sensitivity ($\sim 3.1 \times 10^{-10}$) between ~ 1 - 12 nmol of ^4He .

Table 5.1: Thorianite measurements

	mass 3 (amol)	1σ	mass 4 (nmol)	1σ	$^3\text{He}/^4\text{He}$ ($\times 10^{-10}$)	1σ	mass 3.2 (cps)
No tailing of ^4He onto mass 3							
TH1	0.010	0.002	0.22	0.01	0.47	0.11	0.0
TH2	0.015	0.004	0.22	0.01	0.72	0.22	0.0
TH3	0.023	0.006	0.36	0.01	0.64	0.14	0.0
TH4	0.013	0.005	0.41	0.01	0.33	0.10	0.0
			Mean:		0.54	0.10	
Observed tailing of ^4He onto mass 3							
TH5	0.530	0.036	1.5	0.04	3.6	0.4	0.5
TH6	1.700	0.072	4.5	0.13	3.8	0.4	5.0
TH7	1.898	0.081	5.0	0.15	3.8	0.4	5.0
TH8	4.219	0.180	11.2	0.34	3.8	0.4	20.0

5.5 Precision of ^3He Measurements

A major factor controlling the precision of the ^3He concentration is the need to make a series of time-resolved ^3He measurements that document ion consumption and/or liberation of ^3He from surfaces within the mass spectrometer. These factors are eliminated by regressing the temporal evolution of the ^3He peak height to the time of inlet. The ^3He count rate typically decreases with

time at very low ^4He amounts due to the consumption of ions. At high ^4He amounts, ^3He count rates typically increase with time due to scrubbing of ^3He atoms from the surfaces of the ionization chamber and detector by collisions with ^4He atoms. In almost all cases we find that ^3He count rate is a linear function of time justifying our use of linear regression techniques. Our experimental data show that the rise rate of the ^3He signal correlates with the amount of ^4He in the mass spectrometer (Figure 5.5).

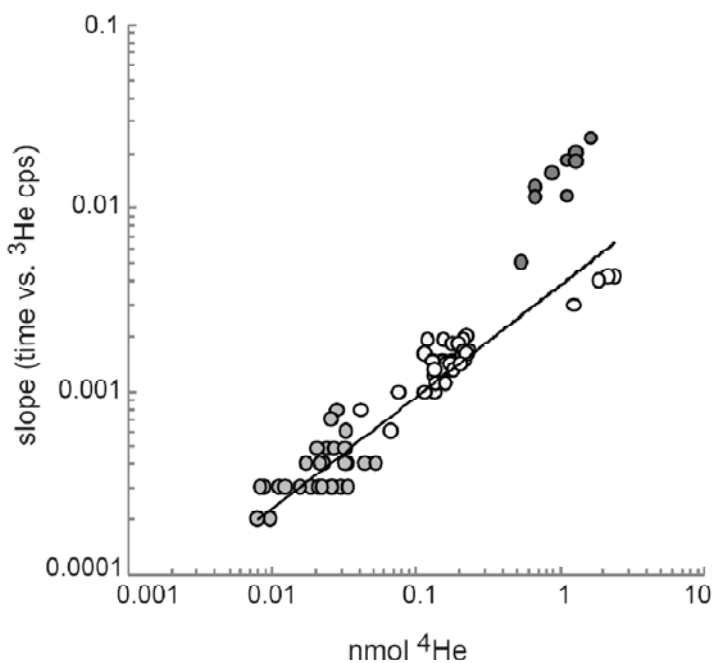


Figure 5.5

Slope of the time vs. ^3He signal (counts per second) array for analyses run at a variety of ^4He pressures. Symbol fill color denotes analyses performed at different times and under different tuning conditions. The line reflects a linear fit to all of the data points except for the group of dark grey symbols with the highest slopes.

The uncertainty on the intercept of the ^3He evolution array increases as the slope of the line becomes steeper. Because the amount of ^4He exerts the strongest control on the slope of the array, the precision with which low ^3He signals can be determined depends on the amount of ^4He present. However, because the positive slope results from ^3He ions from previous samples implanted into the mass spectrometer, this effect may be lower in instruments with limited exposure to ^3He . In our experiments the major recent source of ^3He in the instrument was the MM spike introduced to quantify sensitivity.

To illustrate the approximate tradeoffs between slope and ^3He precision, we performed a Monte Carlo simulation in which a series of synthetic datasets were produced for a range of ^3He signals from 0.5 to 3 cps. The first step was to determine the standard deviation of 18 actual datasets with negligible temporal evolution in ^3He . These standard deviations are plotted against cps in figure 5.6 and agree well with the standard deviations predicted from counting statistics. Synthetic datasets (time vs. ^3He cps) with zero slope were then randomly created for 0.5, 1, 2, and 3 cps, each with a standard deviation predicted by counting statistics. Slopes of 0.001 to 0.01 were then applied to each synthetic dataset and the uncertainty of the intercept determined for each slope. This process was repeated 500 times, and the mean uncertainty for each combination of signal intensity and slope was computed. The results (Figure 5.6) show that the error on the intercept is most sensitive to slope when the ^3He signal is $<\sim 1$ cps.

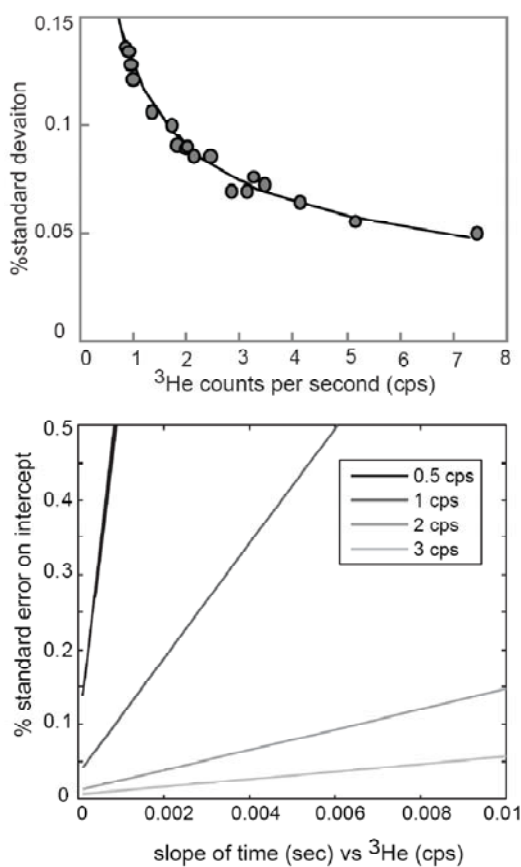


Figure 5.6

Top panel shows the standard deviation of 18 analyses which exhibited a negligible time vs. ^3He slope. Calculated standard deviations from the data (circles) match well with the standard deviations predicted by counting statistics (solid line). These errors form the basis for the Monte Carlo calculations shown in the bottom panel and described in section 5 of the text.

5.7 Discussion

The considerations described above define a minimum $^3\text{He}/^4\text{He}$ ratio above which ^3He in a sample can be reliably measured. The onset of severe tailing of the ^4He peak onto the ^3He peak occurs at ~ 1.16 nmol of ^4He ($\sim 7 \times 10^{14}$ atoms), at which point the highest achievable ^3He sensitivity is near 2.3 kcps/fmol. At this sensitivity ~ 5.02 fmol ($\sim 135,000$ atoms) of ^3He are required to generate a measurable signal of 0.5 cps, corresponding to a minimum measurable $^3\text{He}/^4\text{He}$ ratio of $\sim 2 \times 10^{-10}$. Under typical operating conditions, a single analysis of a sample with a $^3\text{He}/^4\text{He}$ ratio of $\sim 2 \times 10^{-10}$ would be subject to an uncertainty of about 75%. However, because counting statistics scale as the square root of the counts, this uncertainty decreases rapidly as the $^3\text{He}/^4\text{He}$ ratio increases.

The lowest achievable uncertainty for a given $^3\text{He}/^4\text{He}$ ratio is determined by the ^3He count rate and the slope of the time vs. ^3He array. As described above, these variables are determined by the sample size (i.e. the amount of ^4He released from the sample) and the instrument sensitivity. An inherent tradeoff exists when considering the sample size (i.e. ^4He signal) that yields the best precision for a given $^3\text{He}/^4\text{He}$ ratio. On the one hand, larger samples yield a larger ^3He signal that can be measured more precisely (Figure 5.6 top panel). However, this improved precision is offset by the loss of precision inflicted by the steeper slopes associated with high ^4He in larger samples (Figure 5.6 bottom panel). If it is assumed that sensitivity is roughly constant between ~ 0.9 and 1.16 nmol of ^4He (a reasonable approximation for the 150 ua conditions in figure 5.2), a simple set of calculations can be made to determine the ideal sample size that should be run to yield the maximum precision.

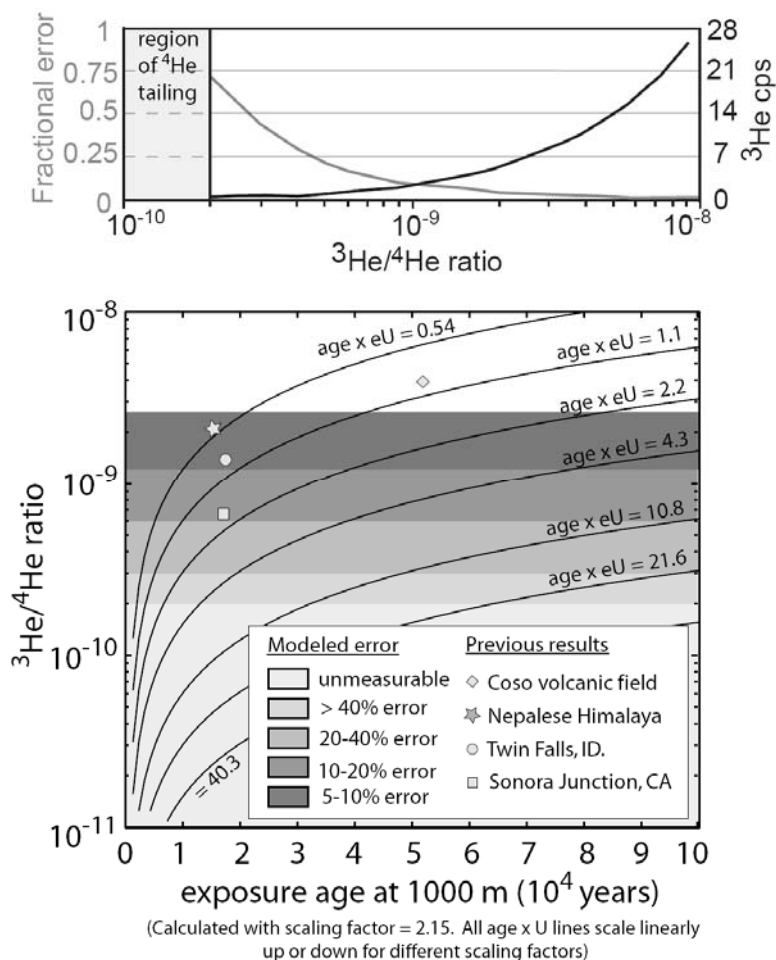
The calculations are performed by assuming a ^3He sensitivity of 2.24 kcps/fmol for all analyses. The slope of the ^3He vs. time relationship for a given ^4He amount is taken from the fit to observed data shown by the line in figure 5.5. The uncertainty as a function of slope and ^3He signal intensity is taken from the Monte Carlo calculations shown in figure 5.6. For each $^3\text{He}/^4\text{He}$ ratio, an iterative search is then performed for the ^4He amount (a proxy for sample mass), that

gives the lowest uncertainty for that ${}^3\text{He}/{}^4\text{He}$ ratio while also giving at least 0.5 cps of ${}^3\text{He}$ signal and less than 1.16 nmol of ${}^4\text{He}$. Results in figure 5.7 show that uncertainties of <20% (on a single analysis) can be routinely achieved for samples with ${}^3\text{He}/{}^4\text{He}$ ratios above $\sim 5 \times 10^{-10}$. For all measurable ${}^3\text{He}/{}^4\text{He}$ ratios, the lowest error is always achieved by running the largest sample possible. In other words, the reduction in counting statistics error associated with running a larger sample always outweighs the added uncertainty introduced by steeper slopes of the ${}^3\text{He}$ vs time array. However, for any sample with a ${}^3\text{He}/{}^4\text{He}$ ratio $> 8 \times 10^{-9}$ running the maximum sample size (i.e. approaching the threshold for ${}^4\text{He}$ tailing) yields a precision of less than 1%. Thus, as the ${}^3\text{He}/{}^4\text{He}$ increases above a value of $\sim 8 \times 10^{-9}$, proportionally smaller samples can be analyzed while still obtaining a 1% analytical precision.

The minimum ${}^3\text{He}/{}^4\text{He}$ ratio that can be routinely measured ($\sim 2 \times 10^{-10}$) places fundamental limitations on the geological contexts within which cosmogenic ${}^3\text{He}$ dating is possible in apatite, titanite and zircon. Because ${}^4\text{He}$ is produced primarily from radioactive decay of U and Th, the ${}^4\text{He}$ concentration in a mineral is a function of U and Th concentration and He closure age. The latter depends on both sample cooling history and on the mineral's He diffusivity. The closure temperatures of the accessory phases considered here are $\sim 70^\circ\text{C}$ for apatite and about $\sim 180^\circ\text{C}$ for both zircon and titanite. ${}^3\text{He}$ is produced via two distinct pathways: 1) cosmic ray neutron-induced spallation in the near surface, and 2) low-energy neutron capture on ${}^6\text{Li}$ in both the near and deep sub-surface (Amidon et al., 2008a; Farley et al., 2006). For the purpose of this discussion, we will assume that production via Li can be ignored noting that the details of production from ${}^6\text{Li}$ have been discussed elsewhere (Amidon et al., 2008a; Dunai et al., 2007; Farley et al., 2006). The amount of ${}^3\text{He}$ present in a sample is then a function of the local spallation production rate and the exposure age. For any given mineral, spallation production rates increase exponentially with increasing elevation and can decrease by as much as 50% from the poles to the equator (Lal and Peters, 1967). As a consequence of these factors, high ${}^3\text{He}/{}^4\text{He}$ ratios are expected in samples with young He closure ages exposed at high elevations

(e.g. a 100 ka ignimbrite erupted at 5000 m in Bolivia) for long time periods, whereas low $^3\text{He}/^4\text{He}$ ratios are expected from samples with old He closure ages exposed at lower elevations for shorter periods (e.g. a Holocene landslide deposit in coastal Australia).

The trade-offs between exposure age and (U-Th)/He closure age on the precision of the ^3He determination are illustrated in figure 5.7, which shows the expected $^3\text{He}/^4\text{He}$ ratio for apatite as a function of its cosmogenic exposure age, closure age and effective U (eU) content (defined as: $[\text{eU}] = [\text{U}] + 0.235[\text{Th}]$). This figure allows the user to make a rough calculation of the expected $^3\text{He}/^4\text{He}$ ratio in minerals from a variety of geologic contexts. Each curved line represents the evolution of the $^3\text{He}/^4\text{He}$ ratio for a unique multiple of the closure age (Ga) and eU content (ppm). Overlain on the lines of constant eU*age are shaded bands that correspond to the approximate precision with which a single analysis of the given $^3\text{He}/^4\text{He}$ ratio can be performed. For comparison, we have plotted samples from the following geologic contexts: Tioga-aged (~18 ka) moraines from the Sierra Nevada (unpublished), meta-sedimentary rocks from moraines in the Nepal Himalaya (Amidon et al., 2008a), rhyolite surfaces from Coso, California (Amidon et al., 2009) and Twin Falls, Idaho (Amidon and Farley, 2010). It is important to note that the lines of constant eU*age in figure 7 are generated using a sea-level high-latitude production rate of $133 \text{ at g}^{-1} \text{ a}^{-1}$ and a scaling factor 2.15. For minerals with different production rates or different scaling factors, these lines will scale linearly up or down in $^3\text{He}/^4\text{He}$ space. Likewise, the analysis of multiple aliquots of the same sample can greatly improve the precision of the ^3He measurement for a given sample.

**Figure 5.7**

The top panel shows the lowest analytical precision that can be achieved for a given $^3\text{He}/^4\text{He}$ ratio (black line) and the corresponding ^3He signal (grey line). The bottom panel shows the evolution of $^3\text{He}/^4\text{He}$ ratios as a function of sample exposure age for a unique combination of (U-Th)/He closure age and effective U (eU) content. Shaded bands represent the approximate uncertainty with which ^3He can be determined on a single analysis of a sample with the given $^3\text{He}/^4\text{He}$ ratio. Samples with $^3\text{He}/^4\text{He}$ ratios below $\sim 2 \times 10^{-10}$ do not yield reliably measurable quantities of ^3He without exceeding the ^4He threshold (~ 1.16 nmol) where tailing of the ^4He peak onto mass 3 become severe.

Based on the above considerations, it is useful to consider which mineral phases are best suited for cosmogenic ^3He dating in different geologic contexts. For example, because apatite has a lower He closure temperature, lower eU content, and higher cosmogenic ^3He production rate, it often contains $^3\text{He}/^4\text{He}$ ratios that are 5-50 times higher than zircons from the same rock (Amidon et al., 2008a; Amidon et al., 2009). This means that apatite is the preferred mineral to work with in geological terranes with (U-Th)/He ages $\gg 50$ Ma. However, purifying large quantities of zircon or titanite is typically easier than purifying apatite because of their higher abundance and because strong acids can be used during purification. Large samples are a great benefit because more large unbroken grains are available, and because replicate samples can be run to improve

the precision. Additionally, zircon tends to survive much better in fluvial and marine environments, making it an obvious choice for detrital studies.

6 Conclusions

Recent calibration studies have shown that apatite, zircon and titanite are suitable phases for cosmogenic ^3He dating. However, the precision and accuracy with which ^3He can be measured in these phases may be limited by the potentially large amount of ^4He from the decay of U and Th over geologic time. Based on the characteristics of a typical MAP 215-50 noble gas mass spectrometer, we conclude that the lowest $^3\text{He}/^4\text{He}$ ratio that can be routinely measured is $\sim 2 \times 10^{-10}$. Ratios higher than $\sim 5 \times 10^{-10}$ are required to achieve a precision of better than 20% on a single analysis. These constraints arise from the need to generate a ^3He signal of $> \sim 1$ count per second, while not exceeding a threshold ^4He concentration of ~ 1.16 nmol of ^4He at which point tailing of the ^4He peak begins to compromise the ^3He measurement. While a broad range of (U-Th)/He closure ages and exposure histories will produce mineral phases with $^3\text{He}/^4\text{He}$ ratios $> \sim 5 \times 10^{-10}$, there are limitations to applications of cosmogenic ^3He dating in apatite, zircon, or titanite in geological terranes with (U-Th)/He closure ages $> \sim 50$ Ma, exposure ages of < 5 ka, or at sites very close to sea-level.

Chapter 6

CONCLUSIONS AND FUTURE APPLICATIONS

6.1 Summary of Findings

The primary goal of this thesis has been to calibrate the production rates of ^3He in accessory mineral phases. Although the results from individual calibration studies seemed disparate early in this work (i.e. the Himalaya and Coso studies), the revision of the ^{10}Be half life (Niishizumi et al., 2007), and the subsequent lowering of the ^{10}Be production rate (Balco et al., 2008), greatly improved the agreement between the different calibration studies. Following equations 4.2 and 4.3, our best estimates of the production rates are 103 ± 3 , 110 ± 11 , 133 ± 6 , and 134 ± 13 for zircon, titanite, apatite and spessartine garnet respectively. Although the exact production rates will undoubtedly change with future refinement of the ^{10}Be production rate, the small relative uncertainties on our existing estimates suggests that zircon, apatite, titanite and garnet are suitable phases for precise cosmogenic ^3He dating.

The primary challenge in establishing production rates of spallation produced ^3He has been quantifying and removing ^3He produced by capture of both low energy radiogenic and cosmogenic neutrons on ^6Li . Although the fundamental approach to calculating various Li-produced components was introduced in our first calibration study (Nepal; chapter 2), the young exposure ages and (U/Th)-He closure ages of the rocks made the Li produced components quite small in samples from that study. Subsequently, the Coso study (chapter 3) showed that in young rocks (0.6 Ma) with old exposure ages (~60-100 ka), Li-produced ^3He from cosmogenically derived neutrons dominates the Li-produced ^3He budget. In contrast, the geologically old (~5.7 Ma), but recently exposed (~18 ka) samples from the Idaho study showed that Li-produced ^3He from capture of radiogenic neutrons can also dominate the Li-produced ^3He budget. Although the uncertainty associated with Li-produced ^3He will always be a challenge for cosmogenic ^3He

dating, this uncertainty can be greatly reduced by making corrections based on samples that have been shielded from cosmic rays. As shown in chapter 4, the use of a shielded sample allows direct measurement of the nucleogenic ^3He component and subtraction from exposed samples. Furthermore, shielded samples provide a means to directly compute the “apparent Li” content of a sample, which improves the accuracy with which the cosmogenic Li-produced component can be calculated.

Another unique aspect of cosmogenic ^3He dating in zircon and apatite is their small grain size makes them vulnerable to redistribution of both spallation and Li-produced ^3He and ^3H . This issue was explored through experiments in which zircons were carefully sieved into grain size fractions that were analyzed separately. Because zircon tends to have lower Li-capture and spallation ^3He production rates than its neighboring minerals, redistribution of ^3He is always expected to result in a negative relationship between grain size and ^3He concentration. Strong negative relationships are observed in both the Coso and Idaho studies, which are largely eliminated after subtraction of the Li-produced ^3He components, demonstrating that redistribution of Li-produced ^3H is significant. The redistribution of spallation produced ^3He has been more difficult to quantify. For example, in the Coso and Nepal studies, the concentration of spallation produced ^3He (after subtraction of Li-produced components) are within error for all zircon grain size fractions. In contrast, the smallest zircons from the Idaho study ($<50\ \mu\text{m}$) do show a substantially higher ^3He concentration than all larger grain sizes, suggesting implantation of spallation produced ^3He could be significant for $<50\ \mu\text{m}$ grains (figure 4.2). While the details of grain-size dependent production rates remain an open question (see below), it appears that this is not a significant issue for zircons larger than $50\ \mu\text{m}$, or for mineral phases with spallation production rates similar to that of the average rock.

Another challenge of cosmogenic ^3He dating in zircon and apatite, is the analytical problems associated with measuring small amounts of cosmogenic ^3He in the presence of large

amounts of radiogenic ^4He , often with limited sample material. As described in chapter 5, some of these challenges were addressed by developing an isotope dilution methodology relying on the ^3He rich “Murdering Mudpot” spike to determine the instrument sensitivity. Chapter 5 shows that this approach allows measurement of samples with $^3\text{He}/^4\text{He}$ ratios as low as 2×10^{-10} , although often with less than desirable precision. The practical implications of the low precision for low $^3\text{He}/^4\text{He}$ samples is that cosmogenic dating with apatite and zircon becomes challenging in geological contexts that have some combination of young exposure ages (<10 ka), low elevation (<500 m), or old (U/Th)-He closure ages (>50 Ma). Although none of our calibration studies approached the region of very low precision, future applications will undoubtedly push these limitations. Another unique challenge is obtaining large enough quantities of zircon and apatite to make reliable measurements. Although this is not discussed in the thesis chapters, it is a very practical limitation of the technique. For example, the purification of 25-50 mg of large apatite or zircon crystals can be a challenge in many rock types. For this reason, cosmogenic ^3He dating in zircon or apatite will be most successfully applied to felsic igneous rocks and some high grade meta-sedimentary rocks.

6.2 Open Questions and Potential Applications

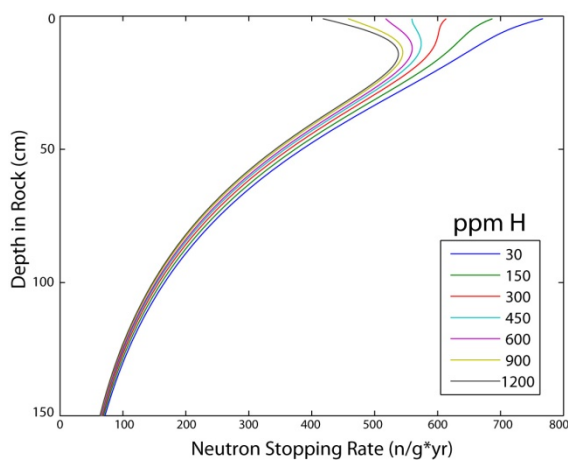
The calibration studies presented in this thesis present several questions for further research, some of which may lead to new applications for cosmogenic ^3He dating. One of the most interesting questions is whether the production rate of ^3He has a different energy dependence than other cosmogenic isotopes such as ^{21}Ne or ^{10}Be . If such differences exist, it would imply that the production rates of ^3He and ^{21}Ne respond differently to changes in the nucleon energy spectrum as a function of elevation and latitude on Earth (Gayer et al., 2004; Lei et al., 2004; Sato and Niita, 2006). As proposed in chapter 2, if changes in the energy spectrum

with elevation lead to a change in the $^3\text{He}/^{21}\text{Ne}$ ratio, this could provide the basis for a new form of paleo-altimetry. The most obvious way to test this hypothesis is to analyze $^3\text{He}/^{21}\text{Ne}$ ratios in a single mineral phase from a single lithology over a vertical profile spanning 3-4 km of elevation. Alternatively, arrays of target mineral phases can be deployed at a range of elevations for 5-10 years, and subsequently recovered for analysis (Vermeesch et al., 2009). Such experiments are ideally performed at high rigidity cutoffs, where altitude dependent changes in the energy spectrum are most pronounced. For example, at equatorial latitudes (90°E , 0°N) the median nucleon energy changes from ~ 90 to 126 MeV over an altitudinal range 0-5000 m, whereas it only changes from ~ 88 to 100 MeV over the same altitudinal range at high latitude sites. As more complete neutron cross sections become available, it should also be possible to make quantitative predictions of these effects.

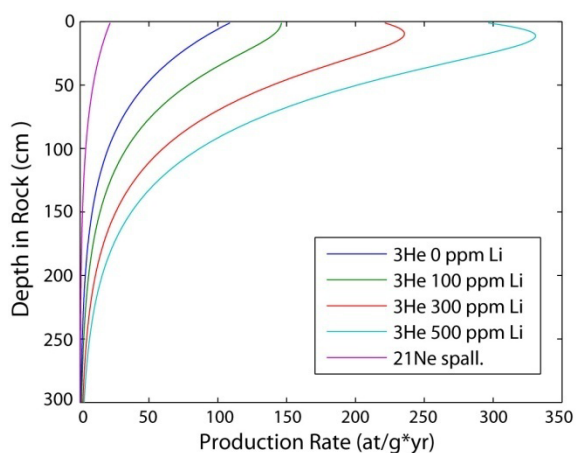
A difference in the energy dependence of ^3He production relative to other isotopes could also lead to changes in the $^3\text{He}/^{21}\text{Ne}$ production ratio with depth in rock. It is widely thought that the energy spectrum of the nuclear cascade changes abruptly near the air-rock interface, where the cascade goes from being sustained by the secondary nucleons produced from nitrogen, to nucleons produced primarily from O, Si, and Al (Masarik et al., 2007). In addition, the neutron moderating properties of rock are quite different than those of air, immediately changing the energy spectrum of the existing cascade. For example, theoretical calculations show that at the air-aluminum interface the flux of 14 MeV neutrons deviates from that predicted from the exponential developed deeper in the solid by $\sim 40\%$ (Masarik et al., 2007). Based on the excitation functions presented in chapter 2, such medium energy neutrons may be able to drive significant ^3He production without inducing production of heavier isotopes, leading to different depth-dependent production rates. Such effects have been well documented in studies simulating the irradiation of meteorites with high energy galactic protons. The transition from a nuclear cascade dominated by high energy protons to a neutron-dominated cascade within rock leads to deviations from an exponential production profile for ^{21}Ne and other isotopes (Leya et al., 2004).

On Earth, changes in production rate with depth in rock can be studied by measuring multiple nuclides from minerals in the same depth profile, or by embedding synthetic minerals into rock at high elevation and measuring the in-grown isotopes after an appropriate amount of time. As described below, energy-dependent production rate profiles could ultimately be used to extract detailed information about the history of erosion or burial of surfaces in the landscape.

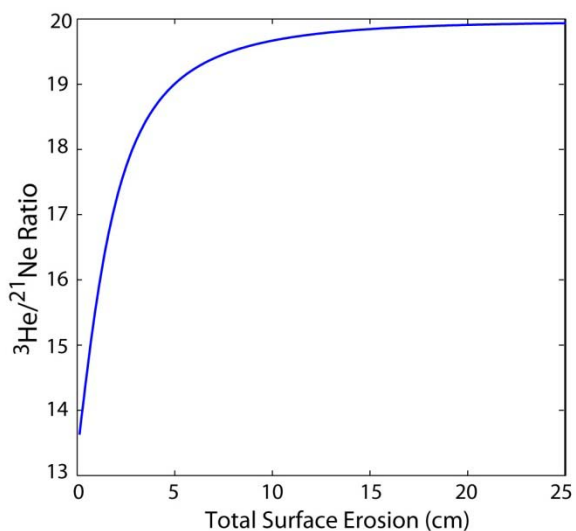
Unlike high energy neutrons, the flux of cosmogenically derived slow neutrons (<1 keV) does not decay exponentially with depth below the air-rock interface. Because rocks tend to moderate neutrons more effectively than air, the low energy flux shows a peak near 20 g/cm^2 , decreasing upwards due to diffusion of low energy neutrons from the air-rock interface (Figure 6.1). Thus, for minerals in which ^3He production by neutron capture on ^6Li is significant (e.g. 100 ppm Li hornblende), the combined production rate of spallation and Li produced ^3He will deviate from a simple exponential profile (Figure 6.2). Assuming that ^{21}Ne in quartz retains a nearly exponential spallation-production profile, then the $^3\text{He}_{\text{hbl}}/^{21}\text{Ne}_{\text{qtz}}$ ratio would be extremely sensitive to small amounts of erosion or burial. Figure 6.3 shows how the $^3\text{He}_{\text{hbl}}/^{21}\text{Ne}_{\text{qtz}}$ ratio evolves with time for an initially uneroded surface in a granite with 1200 ppm of H. The initial $^3\text{He}_{\text{hbl}}/^{21}\text{Ne}_{\text{qtz}}$ ratio in the uneroded surface is uniquely low in the sample's history due to the reduced low-energy neutron flux in the near surface. Once erosion commences, the ratio at the surface begins to rise as material is brought to the surface from a deeper part of the profile where ^3He and ^{21}Ne have accumulated at a higher ratio. If steady erosion continues, the $^3\text{He}_{\text{hbl}}/^{21}\text{Ne}_{\text{qtz}}$ ratio rises monotonically until it achieves a steady-state value. Thus information about the erosion history is contained in not only the cosmogenic concentration, but in the ratio of the two nuclides. This plot suggests that the $^3\text{He}/^{21}\text{Ne}$ ratio in a surface sample can be used to detect very small amounts of erosion or burial of nominally uneroded surfaces.

**Figure 6.1**

Modeled stopping rates of cosmogenic thermal (and epithermal) neutrons as a function of depth in a granite for various H contents. Computed after Phillips et al., (2001).

**Figure 6.2**

Cosmogenic ^3He production rate (including spallation and Li-produced ^3He) profiles at SLHL in minerals of varying Li content residing in a granite with 1200 ppm H. This was modeled as described by Amidon et al. (2008, 2009).

**Figure 6.3**

Cosmogenic $^3\text{He}/^{21}\text{Ne}$ evolution for a surface experiencing continuous erosion, computed for the 300 ppm Li case in Figure 6.2. Note how sensitive the $^3\text{He}/^{21}\text{Ne}$ ratio is to total erosion, reflecting the different depth profiles of cosmogenic production for $^3\text{He}_{\text{Li}}$ and ^{21}Ne . Calculated as in Figure 6, and assuming a spallation production ratio of 6 for $^3\text{He}/^{21}\text{Ne}$.

As described above, results from grain size analyses in the Idaho calibration study suggest that some redistribution of spallation produced ^3He and/or ^3H takes place between fine grained mineral phases. Efforts to calculate the magnitude of such effects are hampered by limited data on the energy distribution of ^3He and ^3H produced by direct neutron reactions. Some observational datasets are available for the energy spectrum of spalled ^3H and ^3He in air, but are restricted to very high elevations where the nucleon energy spectrum is skewed towards higher energies (Powell et al., 1959). The available laboratory data for ^3H and ^3He is limited to high energy proton reactions on ^{12}C , ^{26}Al , ^{40}Ca , and ^{56}Fe (<http://www.nndc.bnl.gov/exfor/endlf00.jsp>). Recognizing the severely limited data availability, figure 6.4 presents likely energy distributions for ^3He and ^3H produced from common rock forming elements by 100 MeV incident neutrons. These energy distributions are derived from a weighted average of the ^{12}C and ^{56}Fe spectra for a granitic rock with a mean atomic mass of 22 AMU. Figure 6.4 shows that the energy distribution of ^3H and ^3He produced from light elements (16-28 AMU), is probably peaked in the energy range 20-50 MeV. Converting these energies into ranges in common silicate minerals, figure 6.5 shows that virtually all of the spallation produced ^3H is redistributed between grains of $<300\ \mu\text{m}$ in cross section, whereas the redistribution of ^3He only becomes significant below $\sim 50\ \mu\text{m}$. The implication of this figure is that for most accessory mineral phases virtually all ^3H produced inside of the crystal is expelled, whereas most of the ^3He is retained. The loss of ^3H and ^3He by ejection from the crystal is balanced by implantation from neighboring minerals, with the exact balance governed by the grain size and relative production rates between adjacent phases. The most fundamental implication of the near-complete redistribution of spallation produced ^3H is that the production rate in any mineral phase will be a function of bulk rock composition as well

as mineral composition. Additional research will be required to document the exact production ratio of ${}^3\text{He}/{}^3\text{H}$, as well as their energy distributions for major elements.

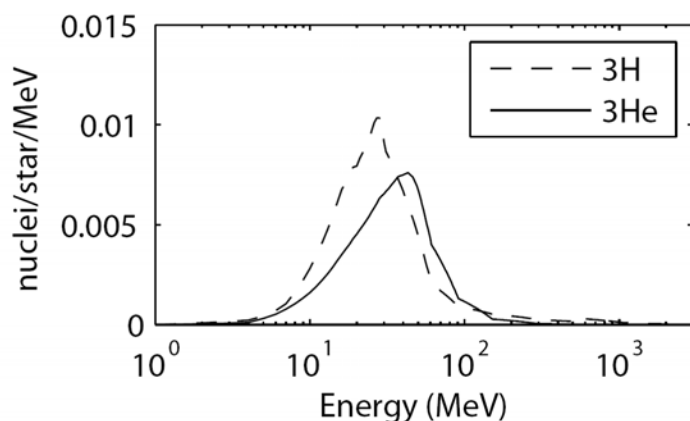


Figure 6.4

Mean energy distribution of ${}^3\text{H}$ and ${}^3\text{He}$ produced by a 100 MeV neutron in a rock whose composition is approximated by a mean atomic mass of 22 AMU.

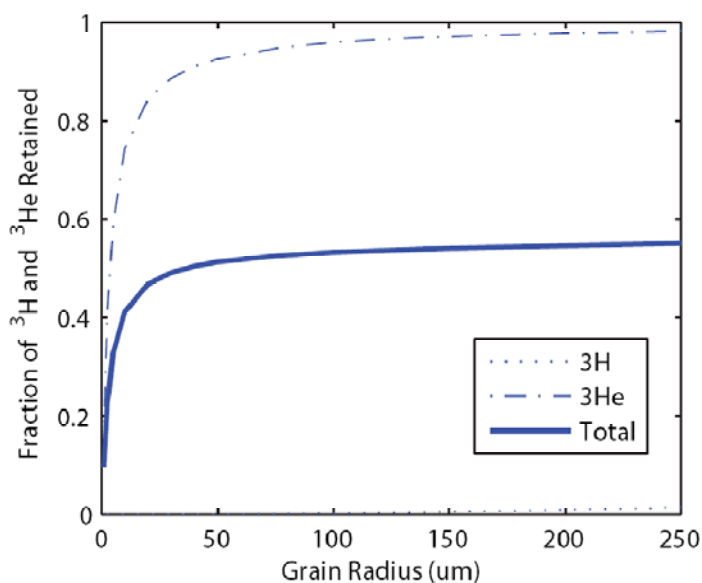


Figure 6.5

Plot of spherical grain radius against the fraction of ${}^3\text{H}$ and ${}^3\text{He}$ produced inside of the mineral that is retained and deposited inside of the mineral. Depending upon the production rate in adjacent rock and air, the fraction that is implanted from the crystal can be either larger or smaller than what is lost by ejection. The ${}^3\text{H}/{}^3\text{He}$ production rate is assumed to be 1.

Cosmogenic ${}^3\text{He}$ dating in zircon and apatite has several potentially interesting applications. One promising application is the analysis of paleo-cosmogenic ${}^3\text{He}$ in detrital sediments. Geologists often study the erosion of mountain belts over time by comparing modern erosion rates (10^{-10} to 10^{-4} years) with thermochronologic “cooling ages” (10^5 – 10^7 year timescales) [Burbank *et al.*, 2003; Willett *et al.*, 2003]. One limitation of this approach is that rates are often extrapolated linearly through time, without any information about how changes in climate driven erosion on 10^4 year timescales affect long term rates of exhumation (Zhang *et al.*, 2001). Such

information can be obtained by measuring cosmogenic isotope concentrations in foreland sediments that record the integrated erosion rate throughout the sediment source area and comparing them with (U/Th)-He cooling ages from detrital apatites in the same sediment. Cosmogenic ^3He in zircon and apatite is an ideal isotope system for such an application because it is a stable isotope that can be measured in the same samples used for cooling ages. Several first order questions can be addressed by developing a paired stratigraphy of cosmogenic ^3He and apatite (U/Th)-He cooling ages. For example, do erosion rates actually correspond to climatic forcing inferred from the marine isotope record? Do rapid glacial-interglacial transitions enhance or limit long term erosion and exhumation rates?

Despite their obvious relevance, the application of cosmogenic isotopes to understanding rates of soil formation and chemical weathering has lagged behind other applications. In addition to providing a low cost alternative for all types of soil studies, ^3He in zircon may play a unique role in soil studies that use Zr enrichment as a proxy for chemical weathering. The basic approach is to measure Zr in deeply weathered soil profiles (including the saprolite and bedrock), assume Zr is completely immobile, and use the ratio of $[\text{Zr}]_{\text{soil}}/[\text{Zr}]_{\text{bedrock}}$ as a proxy for the total amount of mass that has been removed by chemical weathering (Riebe et al., 2003). Several authors have noted that in granitic rocks almost all of the Zr is likely contained in zircon (Nesbitt et al., 1996; Riebe et al., 2001a). If the amount of cosmogenic ^3He in zircon is used to solve directly for the total residence time of zircon in the upper 3-5 meters of soil and saprolite, the rate of chemical weathering can also be obtained. This approach was first introduced by Riebe et al., (2003) using ^{10}Be in quartz to determine the steady-state denudation rate of soils. Because quartz is extremely stable, its residence time in physically eroding soils should be nearly the same as zircon, implying that measurements of cosmogenic ^3He and ^{10}Be (or ^{21}Ne) in quartz should yield the same denudation rate and subsequent chemical weathering rates. However, in soils that experience only chemical weathering, the difference between the cosmogenic inventories in zircon (no dissolution) and quartz (some dissolution) can be used to solve for the

rate of quartz dissolution, a parameter that has been difficult to study due to its very slow rate (Brady and Walther, 1990; Schulz and White, 1999). Similar studies could be made of deeply weathered paleo-soils from Paleocene-Eocene thermal maximum, perhaps placing constraints on the degree of elevated soil acidity, and chemical weathering rates during those times. Zircon may also play a unique role in understanding processes in soils that are experiencing some degree of physical erosion. For example, because zircon grains are often considerably smaller than quartz grains, they are likely to be selectively removed by physical process at a higher rate than larger quartz grains. In this case, the difference in exposure duration between zircon and quartz, or of different zircon grain sizes, could be used to study the grain size dependence of physical weathering processes in soils.

Bibliography

Ackert, R.P., Singer, B.S., Guillou, H., Kaplan, M.R., Kurz, M.D., 2003. Long-term cosmogenic ^3He production rates from $^{40}\text{Ar}/^{39}\text{Ar}$ and K-Ar dated Patagonian lava flows at 47 degrees S. *Earth and Planetary Science Letters* 210, 119-136.

Ahmad, A., Irfan, M., Zafar, M., Khan, A.R., Aziz, T., Shafi, M., 1979. Role of pick-up process in the production of fast tritons and ^3He nuclei. *Indian Journal of Pure & Applied Physics* 17, 308-312.

Amidon, W., Farley, K.A., Burbank, D.W., Pratt-Sitaula, B., 2008a. Anomalous cosmogenic ^3He production and elevation scaling in the high Himalaya. *Earth and Planetary Science Letters* 265, 287-301.

Amidon, W.H., Farley, K.A., 2010. Cosmogenic ^3He dating of apatite, zircon and pyroxene from Bonneville flood erosional surfaces. *Quaternary Geochronology In Review*.

Amidon, W.H., Farley, K.A., Hynek, S.A., 2008b. A field test of cosmogenic ^3He dating in calcite. *Abstracts with Programs - Geological Society of America*, 40.

Amidon, W.H., Rood, D.H., Farley, K.A., 2009. Cosmogenic ^3He and ^{21}Ne production rates calibrated against ^{10}Be in minerals from the Coso volcanic field. *Earth and Planetary Science Letters* 280, 194-204.

Andrews, J.N., Kay, R.L.F., 1982. Natural production of tritium in permeable rocks. *Nature* 298, 361-363.

Armstrong, R.L., Leeman, W.P., Malde, H.E., 1975. K-Ar dating, Quaternary and Neogene volcanic-rocks of Snake River Plain, Idaho. *American Journal of Science* 275, 225-251.

Armstrong, T.W., Chandler, K.C., Barish, J., 1973. Calculations of neutron-flux spectra induced in Earth's atmosphere by galactic cosmic-rays. *Journal of Geophysical Research* 78, 2715-2726.

Bacon, C.R., Duffield, W.A., Nakamura, K., 1980. Distribution of Quaternary rhyolite domes of the Coso Range, California - Implications for extent of the geothermal anomaly. *Journal of Geophysical Research* 85, 2425-2433.

Bacon, C.R., Macdonald, R., Smith, R.L., Baedeker, P.A., 1981. Pleistocene high-silica rhyolites of the Coso volcanic field, Inyo County, California. *Journal of Geophysical Research* 86, 223-241.

Bacon, C.R., Metz, J., 1984. Magmatic inclusions in rhyolites, contaminated basalts, and compositional zonation beneath the Coso volcanic field, California. *Contributions to Mineralogy and Petrology* 85, 346-365.

Balco, G., Briner, J., Finkel, R.C., Rayburn, J.A., Ridge, J.C., Schaefer, J.M., 2009. Regional ^{10}Be production rate calibration for late-glacial northeastern North America. *Quaternary Geochronology* 4, 93-107.

Balco, G., Shuster, D.L., 2009. ^{26}Al - ^{10}Be - ^{21}Ne burial dating. *Earth and Planetary Science Letters* 286, 570-575.

Balco, G., Stone, J.O., Lifton, N.A., Dunai, T.J., 2008. A simple, internally consistent, and easily accessible means of calculating surface exposure ages or erosion rates from ^{10}Be and ^{26}Al measurements. *Quaternary Geochronology* 3, 174-195.

Balco, G., Stone, J.O.H., Jennings, C., 2005a. Dating plio-pleistocene glacial sediments using the cosmic-ray-produced radionuclides ^{10}Be and ^{26}Al . *American Journal of Science* 305, 1-41.

Balco, G., Stone, J.O.H., Mason, J.A., 2005b. Numerical ages for Plio-Pleistocene glacial sediment sequences by $^{26}\text{Al}/^{10}\text{Be}$ dating of quartz in buried paleosols. *Earth and Planetary Science Letters* 232, 179-191.

Ballentine, C.J., Burnard, P.G., 2002. Production, release and transport of noble gases in the continental crust, In: Porcelli, D., Ballentine, C.J., Wieler, R. (Editors), *Noble Gases in Geochemistry and Cosmochemistry*, pp. 481-538.

Barbey, P., Brouand, M., Le Fort, P., Pecher, A., 1996. Granite-migmatite genetic link: the example of the Manaslu granite and Tibetan Slab migmatites in central Nepal. *Lithos* 38, 63-79.

Bierman, P., Steig, E.J., 1996. Estimating rates of denudation using cosmogenic isotope abundances in sediment. *Earth Surface Processes and Landforms* 21, 125-139.

Bierman, P.R., 1994. Using in-situ produced cosmogenic isotopes to estimate rates of landscape evolution- a review from the geomorphic perspective. *Journal of Geophysical Research-Solid Earth* 99, 13885-13896.

Bierman, P.R., Caffee, M., 2002. Cosmogenic exposure and erosion history of Australian bedrock landforms. *Geological Society of America Bulletin* 114, 787-803.

Bierman, P.R., Gillespie, A.R., Caffee, M.W., 1995. Cosmogenic ages for earthquake recurrence intervals and debris flow fan deposition, Owens-Valley, California. *Science* 270, 447-450.

- Blard, P.H., Farley, K.A., 2008. The influence of radiogenic ^4He on cosmogenic ^3He determinations in volcanic olivine and pyroxene. *Earth and Planetary Science Letters* 226, 20-29.
- Blard, P.H., Pik, R., 2008. An alternative isochron method for measuring cosmogenic ^3He in lava flows. *Chemical Geology* 251, 20-32.
- Blard, P.H., Pik, R., Lave, J., Bourles, D., Burnard, P.G., Yokochi, R., Marty, B., Trusdell, F., 2006. Cosmogenic ^3He production rates revisited from evidence of grain size dependent release of matrix-sited helium. *Earth and Planetary Science Letters* 247, 222-234.
- Bodemann, R., Lange, H.J., Leya, I., Michel, R., Schiekkel, T., Rosel, R., Herpers, U., Hofmann, H.J., Dittrich, B., Suter, M., Wolfli, W., Holmqvist, B., Conde, H., Malmborg, P., 1993. Production of residual nuclei by proton-induced reactions on C, N, O, Mg, Al, and Si Nuclear Instruments & Methods in Physics Research Section B-Beam Interactions with Materials and Atoms 82, 9-31.
- Bonnichsen, B., Leeman, W.P., Honjo, N., McIntosh, W.C., Godchaux, M.M., 2008. Miocene silicic volcanism in southwestern Idaho: geochronology, geochemistry, and evolution of the central Snake River Plain. *Bulletin of Volcanology* 70, 315-342.
- Brady, P.V., Walther, J.V., 1990. Kinetics of Quartz Dissolution at Low-Temperatures. *Chemical Geology* 82, 253-264.
- Brook, E.J., Kurz, M.D., Ackert, R.P., Denton, G.H., Brown, E.T., Raisbeck, G.M., Yiou, F., 1993. Chronology of Taylor Glacier Advances in Arena Valley, Antarctica, Using Insitu Cosmogenic ^3He and ^{10}Be . *Quaternary Research* 39, 11-23.
- Brouand, M., Banzet, G., Barbey, P., 1990. Zircon behavior during crustal anatexis. Evidence from the Tibetan Slab migmatites (Nepal). *Journal of Volcanology and Geothermal Research* 44, 143-161.
- Brown, E.T., Edmond, J.M., Raisbeck, G.M., Yiou, F., Kurz, M.D., Brook, E.J., 1991. Examination of Surface Exposure Ages of Antarctic Moraines Using Insitu Produced Be-10 and Al-26. *Geochimica Et Cosmochimica Acta* 55, 2269-2283.
- Brown, E.T., Molnar, P., Bourles, D.L., 2005. Comment on "Slip-rate measurements on the Karakorum Fault may imply secular variations in fault motion". *Science* 309.
- Bruno, L.A., Baur, H., Graf, T., Schluchter, C., Signer, P., Wieler, R., 1997a. Dating of Sirius Group tillites in the Antarctic Dry Valleys with cosmogenic ^3He and ^{21}Ne . *Earth and Planetary Science Letters* 147, 37-54.

Bruno, L.A., Baur, H., Graf, T., Schluchter, C., Signer, P., Wieler, R., 1997b. Dating of Sirius Group tillites in the Antarctic Dry Valleys with cosmogenic He-3 and Ne-21. *Earth and Planetary Science Letters* 147, 37-54.

Brunstein, K.A., 1964. Measurement of Low-Energy Cosmic-Ray Protons. *Physical Review B* 133, 1520-&.

Bryce, J.G., Farley, K.A., 2002. ³He exposure dating of magnetite. *Geochimica et Cosmochimica Acta* 66, A108-A108.

Burbank, D.W., Blythe, A.E., Putkonen, J., Pratt-Sitaula, B., Gabet, E., Oskin, M., Barros, A., Ojha, T.P., 2003. Decoupling of erosion and precipitation in the Himalayas. *Nature* 426, 652-655.

Burke, B.C., Heimsath, A.M., Dixon, J.L., Chappell, J., Yoo, K., 2009. Weathering the escarpment: chemical and physical rates and processes, south-eastern Australia. *Earth Surface Processes and Landforms* 34, 768-785.

Burnard, P.G., Farley, K.A., 2000. Calibration of pressure-dependent sensitivity and discrimination in Nier-type noble gas ion sources. *Geochemistry Geophysics Geosystems* 1.

Carmichael, H., Bercovitz, M., Shea, M.A., Magidin, M., Peterson, R.W., 1968. Attenuation of Neutron Monitor Radiation in Atmosphere. *Canadian Journal of Physics* 46, 1006-&.

Carretier, S., Regard, V., Soual, C., 2009. Theoretical cosmogenic nuclide concentration in river bed load clasts: Does it depend on clast size? *Quaternary Geochronology* 4, 108-123.

Cerling, T., 1990. Dating geomorphic surfaces using cosmogenic ³He. *Quaternary Research* 33, 148-156.

Cerling, T., Craig, H., 1994. Cosmogenic ³He production rates from 39N to 46N latitude, western USA and France. *Geochimica et Cosmochimica Acta* 58, 249-255.

Cerling, T.E., Poreda, R.J., Rathburn, S.L., 1994. Cosmogenic ³He and ²¹Ne Age of the Big Lost River Flood, Snake River Plain, Idaho. *Geology* 22, 227-230.

Chadwick, M.B., Oblozinsky, P., Herman, M., Greene, N.M., McKnight, R.D., Smith, D.L., Young, P.G., MacFarlane, R.E., Hale, G.M., Frankle, S.C., Kahler, A.C., Kawano, T., Little, R.C., Madland, D.G., Moller, P., Mosteller, R.D., Page, P.R., Talou, P., Trelue, H., White, M.C., Wilson, W.B., Arcilla, R., Dunford, C.L., Mughabghab, S.F., Pritychenko, B., Rochman, D., Sonzogni, A.A., Lubitz, C.R., Trumbull, T.H., Weinman, J.P., Brown, D.A., Cullen, D.E., Heinrichs, D.P., McNabb, D.P., Derrien, H., Dunn, M.E., Larson, N.M., Leal, L.C., Carlson, A.D., Block, R.C., Briggs, J.B., Cheng, E.T.,

Huria, H.C., Zerkle, M.L., Koziar, K.S., Courcelle, A., Pronyaev, V., van der Marck, S.C., 2006. ENDF/B-VII.0: Next generation evaluated nuclear data library for nuclear science and technology. Nuclear Data Sheets 107, 2931-3059.

Chevalier, M.L., Ryerson, F.J., Tapponnier, P., Finkel, R.C., Van Der Woerd, J., Li, H.B., Liu, Q., 2005a. Response to comment on "Slip-rate measurements on the Karakorum Fault may imply secular variations in fault motion". Science 309.

Chevalier, M.L., Ryerson, F.J., Tapponnier, P., Finkel, R.C., Van der Woerd, J., Li, H.B., Liu, Q., 2005b. Slip-rate measurements on the Karakorum Fault may imply secular variations in fault motion. Science 307, 411-414.

Chmiel, G., Fritz, S., Elmore, D., 2003. Control of ^{36}Cl production in carbonaceous shales by phosphate minerals. Geochimica et Cosmochimica Acta 13, 2377-2395.

Cocconi, G., 1947. Extensive Air Showers and the Cascade Theory. Physical Review 72, 964-966.

Cocconi, G., Tongiorgi, V.C., Widgoff, M., 1950. Cascades of Nuclear Disintegrations Induced by the Cosmic Radiation. Physical Review 79, 768-780.

Cockburn, H.A.P., Seidl, M.A., Summerfield, M.A., 1999. Quantifying denudation rates on inselbergs in the central Namib Desert using in situ-produced cosmogenic ^{10}Be and ^{26}Al . Geology 27, 399-402.

Colchen, M., Le Fort, P., Pecher, A., 1986. Geological reserach in the Nepal Himalaya, Annapurna-Manaslu-Ganesh Himal; notice of the geological map 1:200,000. Centre Nationale de la Recherche Scientifique, Paris.

Copeland, P., Watson, E.B., Urizar, S.C., Patterson, D., Lapen, T.J., 2007. Alpha thermochronology of carbonates. Geochimica et Cosmochimica Acta 71, 4488-4511.

Craig, H., Poreda, R., 1986. Cosmogenic ^3He in terrestrial rocks: the summit lavas of Maui. Proceedings of the National Academy of Sciences 83, 1970-1974.

Dahanayake, C., Francois, P.E., Fujimoto, Y., Iredale, P., Waddington, C.J., Yasin, M., 1955. On Heavy Unstable Particles Produced in High Energy Nuclear Disintegrations. Nuovo Cimento 1, 888-903.

Deniel, C., Vidal, P., Fernandez, A., Le Fort, P., Peucat, J., 1987. Isotopic study of the Manaslu granite (Himalaya, Nepal)- Inferences on the age and source of Himalayan leucogranites. Contributions to Mineralogy and Petrology 96, 78-92.

Dixon, J.L., Heimsath, A.M., Kaste, J., Amundson, R., 2009. Climate-driven processes of hillslope weathering. Geology 37, 975-978.

- Dunai, T., Stuart, F.M., Pik, R., Burnard, P.G., Gayer, E., 2007. Production of ^3He in crustal rocks by cosmogenic thermal neutrons. *Earth and Planetary Science Letters* 258, 228-236.
- Dunai, T., Wijbrans, J., 2000. Long-term cosmogenic ^3He production rates (152 ka-1.35 Ma) from $^{40}\text{Ar}/^{39}\text{Ar}$ dated basalt flows at 29 N latitude. *Earth and Planetary Science Letters* 176, 147-156.
- Dunai, T.J., Roselieb, K., 1996. Sorption and diffusion of helium in garnet: Implications for volatile tracing and dating. *Earth and Planetary Science Letters* 139, 411-421.
- Eikenberg, J., Signer, P., Wieler, R., 1993. U-Xe, U-Kr and U-Pb systematics for dating U minerals and investigations of the production of nucleogenic Ne and Ar. *Geochimica et Cosmochimica Acta* 57, 1053-1069.
- Farley, K.A., 2000. Helium diffusion from apatite: General behavior as illustrated by Durango fluorapatite. *Journal of Geophysical Research-Solid Earth* 105, 2903-2914.
- Farley, K.A., 2002. (U-Th)/He dating: Techniques, calibrations, and applications, *Noble Gases in Geochemistry and Cosmochemistry*. Mineralogical Soc America, Washington, pp. 819-844.
- Farley, K.A., Libarkin, J., Mukhopadhyay, S., Amidon, W.H., 2006. Cosmogenic and nucleogenic ^3He in apatite, titanite, and zircon. *Earth and Planetary Science Letters* 248, 451-461.
- Farley, K.A., Wolf, R.A., Silver, L.T., 1996. The effects of long alpha-stopping distances on (U-Th)/He ages. *Geochimica Et Cosmochimica Acta* 60, 4223-4229.
- Fenton, C.R., Niedermann, S., Goethals, M., Schneider, B., 2007. Cosmogenic $^{21}\text{Ne}/^3\text{He}$ in olivines and pyroxenes from a pleistocene basalt flow, Western Grand Canyon National Park, Arizona, USA. *Geochimica Et Cosmochimica Acta* 71, A272-A272.
- Friedlander, G., Kennedy, J.W., Macias, E.S., Miller, J.M., 1981. *Nuclear and Radiochemistry*, John Wiley & Sons, New York.
- Garzanti, E., Gorza, M., Martenelli, L., Nicora, A., 1994a. Transition from diagenesis to metamorphism in the Paleozoic to Mesozoic succession of the Dolpo-Manang synclinorium and Thakkhola Graben (Nepal Tethys Himalaya). *Eclogae geol. Helv.* 87, 613-632.
- Garzanti, E., Nicora, A., Tintori, A., Sciunnach, D., Angiolini, L., 1994b. Late Paleozoic stratigraphy and petrography of the Thini Chu group (Manang, central Nepal): sedimentary record of Gondwana glaciation and rifting of Neotethys. *Riv. It. Paleont. Strat.* 100, 155-194.

- Gayer, E., Lavé, J., Pik, R., France-Lanord, C., 2006. Monsoonal forcing of Holocene glacier fluctuations in Ganesh Himal (Central Nepal) constrained by cosmogenic ^3He exposure ages of garnets. *Earth and Planetary Science Letters* 252, 275-288.
- Gayer, E., Pik, R., Lave, J., France-Lanord, C., Bourles, D., Marty, B., 2004. Cosmogenic ^3He in Himalayan garnets indicating an altitude dependence of the $^3\text{He}/^{10}\text{Be}$ production ratio. *Earth and Planetary Science Letters* 229, 91-101.
- Gehrels, G.E., DeCelles, P.G., Martin, A., Ojha, T.P., Pinhassi, G., Upreti, B.N., 2003. Initiation of the Himalayan Orogen as an early Paleozoic thin-skinned thrust belt. *GSA Today* 13, 4-9.
- Godsey, H.S., Currey, D.R., Chan, M.A., 2005. New evidence for an extended occupation of the Provo shoreline and implications for regional climate change, Pleistocene Lake Bonneville, Utah, USA. *Quaternary Research* 63, 212-223.
- Goehring, B., Kurz, M., Balco, G., Schaefer, J., Licciardi, J., Lifton, N., 2010. A reevaluation of in situ cosmogenic ^3He production rates. *Quaternary Geochronology* in press.
- Goethals, M.M., Hetzel, R., Niedermann, S., Wittmann, H., Fenton, C.R., Kubik, P.W., Christl, M., von Blanckenburg, F., 2009. An improved experimental determination of cosmogenic $^{10}\text{Be}/^{21}\text{Ne}$ and $^{26}\text{Al}/^{21}\text{Ne}$ production ratios in quartz. *Earth and Planetary Science Letters* 284, 187-198.
- Goldhagen, P., Reginatto, M., Kniss, T., Wilson, J.W., Singleterry, R.C., Jones, I.W., Van Steveninck, W., 2002. Measurement of the energy spectrum of cosmic-ray induced neutrons aboard an ER-2 high-altitude airplane. *Nuclear Instruments & Methods in Physics Research Section A* 476, 42-51.
- Gosse, J., Phillips, F., 2001. Terrestrial in situ cosmogenic nuclides: theory and application. *Quaternary Science Reviews* 20, 1475-1560.
- Graf, T., Marti, K., Wiens, R.C., 1996. The ^{21}Ne production rate in a Si target at mountain latitudes. *Radiocarbon* 38, 155-156.
- Granger, D.E., Kirchner, J.W., Finkel, R., 1996. Spatially averaged long-term erosion rates measured from in situ-produced cosmogenic nuclides in alluvial sediment. *Journal of Geology* 104, 249-257.
- Guillot, S., Le Fort, P., 1995. Geochemical constraints on the bimodal origin of High Himalayan leucogranites. *Lithos* 35, 221-234.
- Handwerger, D.A., Cerling, T.E., Bruhn, R.L., 1999. Cosmogenic ^{14}C in carbonate rocks. *Geomorphology* 27, 13-24.

- Hartmann, P., Donko, Z., Bano, G., Szalai, L., Rozsa, R., 2000. Effect of different elementary processes on the breakdown in low-pressure helium gas. *Plasma Sources Science and Technology* 9, 183–190.
- Heimsath, A.M., Chappell, J., Spooner, N.A., Questiaux, D.G., 2002. Creeping soil. *Geology* 30, 111-114.
- Heimsath, A.M., Dietrich, W.E., Nishiizumi, K., Finkel, R.C., 1997. The soil production function and landscape equilibrium. *Nature* 388, 358-361.
- Heimsath, A.M., Dietrich, W.E., Nishiizumi, K., Finkel, R.C., 1999. Cosmogenic nuclides, topography, and the spatial variation of soil depth. *Geomorphology* 27, 151-172.
- Heisinger, B., Lal, D., Jull, A.J.T., Kubik, P.W., Ivy-Ochs, S., Knie, K., Nolte, E., 2002a. Production of selected cosmogenic radionuclides by muons: 2. Capture of negative muons. *Earth and Planetary Science Letters* 200, 357-369.
- Heisinger, B., Lal, D., Jull, A.J.T., Kubik, P.W., Ivy-Ochs, S., Neumaier, S., Knie, K., Lazarev, V., Nolte, E., 2002b. Production of selected cosmogenic radionuclides by muons: 1. fast muons. *Earth and Planetary Science Letters* 200, 345-355.
- Hendrick, L.D., Edge, R.D., 1966. Cosmic-ray neutrons near the earth. *Physical Review* 145, 1023-1025.
- Hetzl, R., Niedermann, S., Tao, M., Kubik, P.W., Ivy-Ochs, S., Gao, B., Strecker, M.R., 2002. Low slip rates and long-term preservation of geomorphic features in Central Asia. *Nature* 417, 428-432.
- House, M.A., Farley, K.A., Stockli, D., 2000. Helium chronometry of apatite and titanite using Nd-YAG laser heating. *Earth and Planetary Science Letters* 183, 365-368.
- Hu, R.Z., Burnard, P.G., Bi, X.W., Zhou, M.F., Peng, J.T., Su, W.C., Zhao, J.H., 2009. Mantle-derived gaseous components in ore-forming fluids of the Xiangshan uranium deposit, Jiangxi province, China: Evidence from He, Ar and C isotopes. *Chemical Geology* 266, 86-95.
- IvyOchs, S., Schluchter, C., Kubik, P.W., Synal, H.A., Beer, J., Kerschner, H., 1996. The exposure age of an Egesen moraine at Julier Pass, Switzerland measured with the cosmogenic radionuclides ^{10}Be , ^{26}Al and ^{36}Cl . *Eclogae Geologicae Helvetiae* 89, 1049-1063.
- Kirchner, J.W., Finkel, R.C., Riebe, C.S., Granger, D.E., Clayton, J.L., King, J.G., Megahan, W.F., 2001. Mountain erosion over 10 yr, 10 k.y., and 10 m.y. time scales. *Geology* 29, 591-594.

- Klinger, Y., Avouac, J.P., Abou Karaki, N., Dorbath, L., Bourles, D., Reyss, J.L., 2000. Slip rate on the Dead Sea transform fault in northern Araba valley (Jordan). *Geophysical Journal International* 142, 755-768.
- Kober, F., Ivy-Ochs, S., Leya, I., Baur, H., Magna, T., Wieler, R., Kubik, P.W., 2005. In situ cosmogenic ^{10}Be and ^{21}Ne in sanidine and in situ cosmogenic ^3He in Fe-Ti-oxide minerals. *Earth and Planetary Science Letters* 236, 404-418.
- Kohl, C.P., Nishiizumi, K., 1992. Chemical isolation of quartz for measurement of in situ produced cosmogenic nuclides. *Geochimica et Cosmochimica Acta* 56, 3583-3587.
- Kurz, M.D., 1986a. Cosmogenic helium in a terrestrial igneous rock. *Nature* 320, 435-439.
- Kurz, M.D., 1986b. In-situ production of terrestrial cosmogenic helium and some applications to geochronology *Geochimica et Cosmochimica Acta* 50, 2855-2862.
- Kurz, M.D., Colodner, D., Trull, T.W., Moore, R.B., O'Brien, K., 1990. Cosmic-ray exposure dating with in-situ produced cosmogenic ^3He : results from young Hawaiian lava flows *Earth and Planetary Science Letters* 97, 177-189.
- Lal, D., 1987. Production of ^3He in terrestrial rocks. *Chemical Geology* 66, 89-98.
- Lal, D., 1991. Cosmic ray labeling of erosion surfaces: In situ production rates and erosion models. *Earth and Planetary Science Letters* 104, 424-439.
- Lal, D., Peters, B., 1967. Cosmic ray produced radioactivity in the earth, *Handbuch der Physik*. Springer-Verlag, pp. 551-612.
- Lamb, M.P., Dietrich, W.E., Aciego, S.M., DePaolo, D.J., Manga, M., 2008. Formation of Box Canyon, Idaho, by megaflood: Implications for seepage erosion on Earth and Mars. *Science* 320, 1067-1070.
- Le Fort, P., 1981. Manaslu leucogranite: A collision signature of the Himalaya a model for its genesis and emplacement. *Journal of geophysical research* 86, 10545-10568.
- Lei, F., Clucas, S., Dyer, C., Truscott, P., 2004. An atmospheric radiation model based on response matrices generated by detailed Monte Carlo simulations of cosmic ray interactions. *IEEE Transactions on Nuclear Science* 51, 10.1109/TNS.2004.839131.
- Leya, I., Baur, H., Busemann, H., Wieler, R., Gloris, M., Neumann, S., Michel, R., Herpers, U., 1998a. Measurement of cross sections for the proton-induced production of helium and neon isotopes from magnesium, aluminum, and silicon. *Meteoritics & Planetary Science* 33, A94-A94.

- Leya, I., Begemann, F., Weber, H.W., Wieler, R., Michel, R., 2004. Simulation of the interaction of galactic cosmic ray protons with meteoroids: On the production of ^3H and light noble gas isotopes in isotropically irradiated thick gabbro and iron targets. *Meteoritics & Planetary Science* 39, 367-386.
- Leya, I., Busemann, H., Baur, H., Wieler, R., Gloris, M., Neumann, S., Michel, R., Sudbrock, F., Herpers, U., 1998b. Cross sections for the proton-induced production of He and Ne isotopes from magnesium, aluminum, and silicon. *Nuclear Instruments & Methods in Physics Research Section B-Beam Interactions with Materials and Atoms* 145, 449-458.
- Leya, I., Lange, H.J., Lupke, M., Neupert, U., Daunke, R., Fanenbruck, O., Michel, R., Rosel, R., Meltzow, B., Schiekkel, T., Sudbrock, F., Herpers, U., Filges, D., Bonani, G., Dittrich-Hannen, B., Suter, M., Kubik, P.W., Synal, H.A., 2000a. Simulation of the interaction of galactic cosmic-ray protons with meteoroids: On the production of radionuclides in thick gabbro and iron targets irradiated isotropically with 1.6 GeV protons. *Meteoritics & Planetary Science* 35, 287-318.
- Leya, I., Lange, H.J., Neumann, S., Wieler, R., Michel, R., 2000b. The production of cosmogenic nuclides in stony meteoroids by galactic cosmic-ray particles. *Meteoritics & Planetary Science* 35, 259-286.
- Licciardi, J., Kurz, M.D., Clark, P., Brook, E., 1999. Calibration of cosmogenic ^3He production rates from Holocene lava flows in Oregon, USA, and effects of the Earth's magnetic field. *Earth and Planetary Science Letters* 172, 261-271.
- Licciardi, J.M., Kurz, M.D., Curtice, J.M., 2006. Cosmogenic ^3He production rates from Holocene lava flows in Iceland. *Earth and Planetary Science Letters* 246, 251-264.
- Lifton, N., Bieber, J., Clem, J., Duldig, M., Evenson, P., Humble, J., Pyle, R., 2005. Addressing solar modulation and long-term uncertainties in scaling secondary cosmic rays for in situ cosmogenic nuclide applications. *Earth and Planetary Science Letters* 239, 140-161.
- Lifton, N., Caffee, M., Finkel, R., Schaefer, J., Stone, J., Goehring, B., Phillips, D., Oviatt, C.G., Rood, D., 2009. A new estimate of the spallogenic production rate of in situ cosmogenic ^{10}Be from lake Bonneville shoreline features, Promontory Point, Utah. *Geological Society of America Abstracts* 41, 229.
- Lifton, N., Smart, D.F., Shea, M.A., 2008. Scaling time-integrated in situ cosmogenic nuclide production rates using a continuous geomagnetic model. *Earth and Planetary Science Letters* 268, 190-201.
- Lifton, N.A., Jull, A.J.T., Quade, J., 2001. A new extraction technique and production rate estimate for in situ cosmogenic ^{14}C in quartz. *Geochimica Et Cosmochimica Acta* 65, 1953-1969.

- Light, A., 1996. Amino acid paleotemperature reconstruction and radiocarbon shoreline chronology of the Lake Bonneville Basin, USA, PhD Thesis, University of Colorado.
- Malde, H.E., 1968. The catastrophic late Pleistocene Bonneville Flood in the Snake River plain, Idaho. Geological Society of America Professional Paper 596, 52.
- Mamyrin, B.A., Tolstikhin, I.N., 1984. Helium Isotopes in Nature, Elsevier, Amsterdam.
- Manley, C.R., Bacon, C.R., 2000. Rhyolite thermobarometry and the shallowing of the magma reservoir, Coso volcanic field, California. *Journal of Petrology* 41, 149-174.
- Martel, D.J., Onions, R.K., Hilton, D.R., Oxburgh, E.R., 1990. The role of element distribution in production and release of radiogenic helium - the Carnmenellis granite, southwest England. *Chemical Geology* 88, 207-221.
- Masarik, J., 2002. Numerical simulation of in-situ production of cosmogenic nuclides. *Geochimica et Cosmochimica Acta* 66, 491.
- Masarik, J., 2008. Calculation of cosmogenic nuclide production rates in the Earth atmosphere and in terrestrial surface. *Geochimica Et Cosmochimica Acta* 72, A600-A600.
- Masarik, J., Beer, J., 2009. An updated simulation of particle fluxes and cosmogenic nuclide production in the Earth's atmosphere. *Journal of Geophysical Research- Atmospheres* 114.
- Masarik, J., Kyeong, K., Reedy, R.C., 2007. Numerical simulations of in situ production of terrestrial cosmogenic nuclides. *Nuclear Instruments and Methods in Physics Research B* B259, 642-645.
- Masarik, J., Reedy, R.C., 1995. Terrestrial cosmogenic-nuclide production systematics calculated from numerical simulations. *Earth and Planetary Science Letters* 136, 381-395.
- Matmon, A., Schwartz, D.P., Finkel, R., Clemmens, S., Hanks, T., 2005. Dating offset fans along the Mojave section of the San Andreas fault using cosmogenic ^{26}Al and ^{10}Be . *Geological Society of America Bulletin* 117, 795-807.
- Michel, R., Bodemann, R., Busemann, H., Daunke, R., Gloris, M., Lange, H.J., Klug, B., Krins, A., Leya, I., Lupke, M., Neumann, S., Reinhardt, H., SchnatzButtgen, M., Herpers, U., Schiekel, T., Sudbrock, F., Holmqvist, B., Conde, H., Malmborg, P., Suter, M., DittrichHannen, B., Kubik, P.W., Synal, H.A., Filges, D., 1997. Cross sections for the production of residual nuclides by low- and medium-energy protons from the target elements C, N, O, Mg, Al, Si, Ca, Ti, V, Mn, Fe, Co, Ni, Cu, Sr, Y, Zr, Nb, Ba and Au. *Nuclear Instruments & Methods in Physics Research Section B-Beam Interactions with Materials and Atoms* 129, 153-193.

Michel, R., Gloris, M., Lange, H.J., Leya, I., Lupke, M., Herpers, U., Dittrichhannen, B., Rosel, R., Schiek, T., Filges, D., Dragovitsch, P., Suter, M., Hofmann, H.J., Wolfli, W., Kubik, P.W., Baur, H., Wieler, R., 1995. Nuclide production by proton-induced reactions on elements ($6 < Z < 29$) in the energy-range from 800 to 2600 MeV Nuclear Instruments & Methods in Physics Research Section B-Beam Interactions with Materials and Atoms 103, 183-222.

Miller, J.S., Wooden, J.L., 2004. Residence, resorption and recycling of zircons in Devils Kitchen rhyolite, Coso Volcanic field, California. *Journal of Petrology* 45, 2155-2170.

Min, K.W., Farley, K.A., Renne, P.R., Marti, K., 2003. Single grain (U-Th)/He ages from phosphates in Acapulco meteorite and implications for thermal history. *Earth and Planetary Science Letters* 209, 323-336.

Nakagawa, T., Kawasaki, H., Shibata, K., 2002. Curves and tables of neutron cross sections in JENDL-3.3, Japan Atomic Energy Research Institute, Tokyo.

Nesbitt, H.W., Young, G.M., McLennan, S.M., Keays, R.R., 1996. Effects of chemical weathering and sorting on the petrogenesis of siliciclastic sediments, with implications for provenance studies. *Journal of Geology* 104, 525-542.

Niedermann, S., 2002. Cosmic-ray-produced noble gases in terrestrial rocks: Dating tools for surface processes, In: Porcelli, D., Ballentine, C.J., Wieler, R. (Editors), *Noble Gases in Geochemistry and Cosmochemistry: Reviews in Mineralogy and Geochemistry* 47. Mineralogical Society of America, Washington D.C., pp. 731-784.

Niedermann, S., Goethals, M.M., Pilz, P., 2009. Evidence for a high ^3He or low ^{10}Be production rate from cosmogenic nuclide cross-calibration. *Geochimica et Cosmochimica Acta* 73, A940.

Niedermann, S., Graf, T., Marti, K., 1993. Mass spectrometric identification of cosmic-ray produced ^{21}Ne in terrestrial quartz: the neon inventory of Sierra Nevada quartz separates. *Earth and Planetary Science Letters* 118, 65-73.

Niedermann, S., Pilz, P., Goethals, M., 2007. Assessing the relative production rates of cosmogenic ^3He and ^{21}Ne in olivine, pyroxene and quartz. *Geochimica Et Cosmochimica Acta* 71, A717-A717.

Niishizumi, K., Imamura, M., Caffee, M., Southon, J.R., Finkel, R.C., McAninch, J., 2007. Absolute calibration of ^{10}Be AMS standards. *Nuclear Instruments and Methods in Physics Research B* 258, 403-413.

Nir, A., Kruger, S.T., Lingenfeller, E.J., 1966. Natural Tritium. *Reviews of Geophysics* 4, 441-&.

- O'Connor, J.E., 1993. Hydrology, hydraulics, and geomorphology of the Bonneville flood. Geological Society of America Special Paper 274, 83.
- Oviatt, C.G., 1991. Quaternary geology of the Black Rock Desert, Millard County, Utah, Utah Geological and Mineralogical Survey, Salt Lake City.
- Oviatt, C.G., Currey, D.R., Sack, D., 1992. Radiocarbon Chronology of Lake Bonneville, Eastern Great-Basin, USA. *Palaeogeography Palaeoclimatology Palaeoecology* 99, 225-241.
- Owen, L.A., Finkel, R.C., Barnard, P.L., Ma, H., Asahi, K., Caffee, M.W., Derbyshire, E., 2005. Climatic and topographic controls on the style and timing of late Quaternary glaciation throughout Tibet and the Himalaya defined by ^{10}Be cosmogenic radionuclide surface exposure dating *Quaternary Science Reviews* 24, 1391-1411.
- Patterson, D.B., Farley, K.A., 1998. Extraterrestrial ^3He in seafloor sediments: Evidence for correlated 100 kyr periodicity in the accretion rate of interplanetary dust, orbital parameters, and Quaternary climate. *Geochimica et Cosmochimica Acta* 62, 3669-3682.
- Patterson, D.B., Farley, K.A., McInnes, B., 1997. Helium isotopic composition of the Tabar-Lihir-Tanga-Feni island arc, Papua New Guinea *Geochimica et Cosmochimica Acta* 61, 2485-2496.
- Phillips, F., Plummer, M.A., 1996. A program for reinterpreting in-situ cosmogenic nuclide data for surface exposure dating and erosion studies. *Radiocarbon* 38, 98-99.
- Phillips, F., Stone, W.D., Fabryka-Martin, J.T., 2001. An improved approach to calculating low-energy cosmic ray neutron fluxes near the land/atmosphere interface. *Chemical Geology* 175, 689-701.
- Pigati, J.S., Lifton, N.A., 2004. Geomagnetic effects on time-integrated cosmogenic nuclide production with emphasis on in situ ^{14}C and ^{10}Be . *Earth and Planetary Science Letters* 226, 193-205.
- Poreda, R.J., Farley, K.A., 1992. Rare-gases in Samoan xenoliths. *Earth and Planetary Science Letters* 113, 129-144.
- Potts, P.J., Tindle, A.G., Webb, P.C., 1992. *Geochemical reference material compositions*, CRC Press, Ann Arbor.
- Powell, C.F., Fowler, P.H., Perkins, D.H., 1959. *The study of elementary particles by the photographic method*, Pergamon Press, New York.
- Pratt-Sitaula, B., 2004. *Glaciers, climate, and topography in the Nepalese Himalaya*, UC Santa Barbara, Santa Barbara, 152 pp.

- Putkonen, J., Swanson, T., 2003. Accuracy of cosmogenic ages for moraines. *Quaternary Research* 59, 255-261.
- Putnam, A.E., Schaefer, J., Barrell, D.J.A., Vendergoes, M., Denton, G.H., Kaplan, M.R., Finkel, R.C., Schwartz, R., Goehring, B., Kelley, S.E., 2010. In situ cosmogenic ^{10}Be production-rate calibration from the Southern Alps, New Zealand. *Quaternary Geochronology* In Press.
- Reiners, P.W., Farley, K.A., 1999. Helium diffusion and (U-Th)/He thermochronometry of titanite. *Geochimica Et Cosmochimica Acta* 63, 3845-3859.
- Reiners, P.W., Farley, K.A., Hicke, H.J., 2002. He diffusion and (U-Th)/He thermochronometry of zircon: initial results from Fish Canyon Tuff and Gold Butte. *Tectonophysics* 349, 297-308.
- Riebe, C.S., Kirchner, J.W., Finkel, R.C., 2003. Long-term rates of chemical weathering and physical erosion from cosmogenic nuclides and geochemical mass balance. *Geochimica Et Cosmochimica Acta* 67, 4411-4427.
- Riebe, C.S., Kirchner, J.W., Granger, D.E., 2001a. Quantifying quartz enrichment and its consequences for cosmogenic measurements of erosion rates from alluvial sediment and regolith. *Geomorphology* 40, 15-19.
- Riebe, C.S., Kirchner, J.W., Granger, D.E., Finkel, R.C., 2001b. Strong tectonic and weak climatic control of long-term chemical weathering rates. *Geology* 29, 511-514.
- Rosgen, D.L., 1994. A Classification of Natural Rivers. *Catena* 22, 169-199.
- Sato, T., Niita, K., 2006. Analytical functions to predict cosmic-ray neutron spectra in the atmosphere. *Radiation Research* 166, 544-555.
- Schaefer, J.M., Ivy-Ochs, S., Wieler, R., Leya, J., Baur, H., Denton, G.H., Schluchter, C., 1999. Cosmogenic noble gas studies in the oldest landscape on earth: surface exposure ages of the Dry Valleys, Antarctica. *Earth and Planetary Science Letters* 167, 215-226.
- Schaller, M., von Blanckenburg, F., Hovius, N., Kubik, P.W., 2001. Large-scale erosion rates from in situ-produced cosmogenic nuclides in European river sediments. *Earth and Planetary Science Letters* 188, 441-458.
- Schaller, M., von Blanckenburg, F., Hovius, N., Veldkamp, A., van den Berg, M.W., Kubik, P.W., 2004. Pale erosion rates from cosmogenic ^{10}Be in a 1.3 Ma terrace sequence: Response of the river meuse to changes in climate and rock uplift. *Journal of Geology* 112, 127-144.
- Schiekel, T., Sudbrock, F., Herpers, U., Gloris, M., Lange, H.J., Leya, I., Michel, R., Dittrich, B., Hannen, B., Synal, H.A., Suter, M., Kubik, P.W., Blann, M., Filges, D., 1996.

- Nuclide production by proton-induced reactions on elements ($6 < Z < 29$) in the energy range from 200 MeV to 400 MeV. *Nuclear Instruments & Methods in Physics Research Section B-Beam Interactions with Materials and Atoms* 114, 91-119.
- Schneider, C., Masch, L., 1993. The metamorphism of the Tibetan Series from the Manang area, Marsyandi Valley, Central Nepal, In: Treloar, P.J., Searle, M.P. (Editors), *Himalayan Tectonics*. Geological Society of London, London, pp. 357-374.
- Schulz, M.S., White, A.F., 1999. Chemical weathering in a tropical watershed, Luquillo mountains, Puerto Rico III: Quartz dissolution rates. *Geochimica Et Cosmochimica Acta* 63, 337-350.
- Scott, W.E., McCoy, W.D., Chroba, R.R., Rubin, M., 1983. Reinterpretation of the exposed record of the last two cycles of Lake Bonneville, Western United States. *Quaternary Research* 20, 261-285.
- Searle, M.P., Godin, L., 2003. The South Tibetan Detachment and the Manaslu Leucogranite: A structural reinterpretation and restoration of the Annapurna-Manaslu Himalaya, Nepal. *Journal of Geology* 111, 505-523.
- Shuster, D.L., Farley, K.A., 2005. Diffusion kinetics of proton-induced ^{21}Ne , ^3He , and ^4He in quartz. *Geochimica et Cosmochimica Acta* 69, 2349-2359.
- Siame, L.L., Bourles, D.L., Sebrier, M., Bellier, O., Castano, J.C., Araujo, M., Perez, M., Raisbeck, G.M., Yiou, F., 1997. Cosmogenic dating ranging from 20 to 700 ka of a series of alluvial fan surfaces affected by the El Tigre fault, Argentina. *Geology* 25, 975-978.
- Simon, J., Vazquez, J.A., Renne, P.R., Schmitt, A.K., Bacon, C.R., Reid, M.R., 2008. Accessory mineral U-Th-Pb ages and $^{40}\text{Ar}/^{39}\text{Ar}$ eruption chronology, and their bearing on rhyolitic magma evolution in the Pleistocene Coso volcanic field, California. *Contributions to Mineralogy and Petrology* in review.
- Simpson, J.A., 1951. Neutrons produced in the atmosphere by the cosmic radiations. *Physical Review* 83, 1175-1188.
- Simpson, J.A., Fonger, W., Treiman, S.B., 1953. Cosmic Radiation Intensity-Time Variations and Their Origin .1. Neutron Intensity Variation Method and Meteorological Factors. *Physical Review* 90, 934-950.
- Simpson, J.A., Uretz, R.B., 1953. Cosmic ray neutron production in elements as a function of latitude and altitude. *Physical Review* 90, 44-50.
- Staudacher, T., Allegre, C.J., 1993. The cosmic ray produced $^3\text{He}/^{21}\text{Ne}$ ratio in ultramafic rocks. *Geophysical Research Letters* 20, 1075-1078.

- Vermeesch, P., Baur, H., Heber, V.S., Kober, F., Oberholzer, P., Schaefer, J.M., Schluchter, C., Strasky, S., Wieler, R., 2009. Altitudinal scaling of cosmogenic ^3He and ^{21}Ne in artificial quartz targets. *Geochimica et Cosmochimica Acta* 73, A1379-A1379.
- Vermeesch, P., Heber, V., Strasky, S., Kober, F., Schaefer, J., Baur, J., Schluchter, C., Wieler, R., 2008. Cosmogenic ^3He and ^{21}Ne measured in artificial quartz targets after one year of exposure in the Swiss Alps. *Geophysical Research Abstracts* 10, EGU2008-A-08431.
- Vogel, T.A., Hidalgo, P.J., Patino, L.C., Tefend, K.S., Ehrlich, R., 2008. Evaluation of magma mixing and fractional crystallization using whole-rock chemical analyses: Polytopic vector analyses. *Geochemistry, Geophysics, Geosystems - G3* 9, doi:10.1029/2007GC001790.
- Webber, W.R., Higbie, P.R., McCracken, K.G., 2007. Production of the cosmogenic isotopes ^3H , ^7Be , ^{10}Be , and ^{36}Cl in the Earth's atmosphere by solar and galactic cosmic rays. *Journal of Geophysical Research-Space Physics* 112.
- Wolf, R.A., Farley, K.A., Silver, L.T., 1996. Helium diffusion and low-temperature thermochronometry of apatite. *Geochimica et Cosmochimica Acta* 60, 4231-4240.
- Yamashita, M., Stephens, L.D., Patterson, H.W., 1966. Cosmic-Ray-Produced Neutrons at Ground Level - Neutron Production Rate and Flux Distribution. *Journal of Geophysical Research* 71, 3817-3828.
- Yasin, M., 1964. Emission of fast helium nuclei and tritons from high-energy nuclear disintegrations. *Nuovo Cimento* 34, 1145-1155.
- Young, E., Myers, A., Munson, E., Conklin, N., 1969. Mineralogy and geochemistry of fluorapatite from Cerro de Mercado, Durango, Mexico. U.S. Geological Survey Professional Paper 650-D, 84-93.
- Zatzick, M.R., Maxson, D.R., 1963. Angular distributions of (N,D) pickup reactions in ^{14}N , ^{31}P , and ^{32}S at 14 Mev. *Physical Review* 129, 1728-1748.
- Zhang, P.Z., Molnar, P., Downs, W.R., 2001. Increased sedimentation rates and grain sizes 2-4 Myr ago due to the influence of climate change on erosion rates. *Nature* 410, 891-897.
- Ziegler, J.F., 2003. Stopping and Range of Ions in Matter (SRIM), <http://www.srim.org/>.
- Zreda, M.G., Phillips, F.M., 1995. Insights into alpine moraine development from cosmogenic ^{36}Cl buildup dating. *Geomorphology* 14, 149-156.

Appendix A

Matlab scripts for computation of ^3He production

Introduction:

This is a series of matlab scripts that are designed to calculate the amount of Li-produced ^3He in a given mineral sample(s). This is done by first entering in relevant information about the sample(s), such as the equivalent grain radius, helium closure age (U-Th/He age), exposure age (or erosion rate), elevation, bulk rock composition, and Li-content of the mineral and its host.

The code begins with the "master" script called "**li_3he.m**" which allows you to specify a lot of information at the top of the code, and then calls five lower-level scripts to make the relevant calculations. It is IMPORTANT to note that each of the underlying scripts can be used as stand-alones, which users may find useful for a variety of cosmogenic problems, that are not related to Li and ^3He . For example, the scripts allow you to calculate elevation scaling, and neutron fluxes produced by radiogenic, cosmogenic, and muogenic sources.

Getting Started:

Place the .zip file in a new folder, named whatever you prefer. Unzip the file, so that all the sub files ARE IN THE SAME FOLDER. Open the matlab program, and set your working directory to the same folder where you just put all of the files. This can be done using the "current directory" toolbar window at the top of the screen, or the file folder menu on the left hand side of the screen. Next, select file--> open-->**li_3he.m**. This will open the main "**li_3he.m**" script in the editor screen. Check to make sure you are happy with all of the user inputs before starting. Once you are ready to run, go to the main matlab window, and at the prompt ">>" type "**li_3he.m**" (no quotes).

The "li_3he" script

The code begins by opening and loading several data files. One of these files is called "**granite_data.txt**." this is text file which contains the concentration of each element in the bulk rock, as well as some basic nuclear properties of each element, such as its absorption cross-section, scattering cross-section, resonance integral, and alpha stopping power. To see the full dataset, you should open "granite data.xls" which has headers for each row and column, the .txt version only has the values, and is intended only for reading by matlab. Note that if you make changes to the .xls file, you must manually copy them over to the .txt file before they can be read by matlab. Always save the text file as tab delimited. To make changes to the bulk concentration, update the "ppm" column, but then make sure to cut and paste the recalculated "at/g" column into the text file, because that is what matlab uses in the calculation.

Another data file is called "**min_data_example.txt**", this is the file which contains relevant information about all of the samples you would like to make calculations for. IMPORTANTLY, the number of rows in this file will determine how many samples the code processes. Having only a single row will mean the "**li_3he.m**" script only loops once, and only makes one set of calculations. Again, you can see the column headers by opening "**min_data_example.xls**", but must cut and paste into the text file when changes are made. Always save the text file as tab delimited. The categories are self-explanatory, and NOT ALL OF THEM ARE USED in the calculation, some are just for reference. So, don't worry if you don't know the ^{10}Be concentration, for example.

Details of the script are very well annotated (view in matlab editor). However, at the beginning, you are asked to choose whether you want to **simulate erosion**. Choosing yes, will activate a section of the script (near the bottom), that simulates erosion by calculating the production rate at each depth increment, and then simulating a parcel of rock being exhumed through this profile at the specified erosion rate. If you choose no, then the code assumes a simple exposure history, and averages the nuclide content in the upper 4 cm of rock.

There is also a section at the bottom that generates an **output text file**. This can be

opened in excel or any word processing program to view the results of the calculation for each mineral. In the output file, each row corresponds to a different sample, and each column corresponds to a different variable. Additional output variables can be added, or existing output variables changed by modifying the code.

The "conv_elev" script

This script converts elevation (in meters) to atmospheric depth in (g/cm^2). It follows Stone et al., (2000), and assumes a standard atmosphere. It does not make location-specific calculations considering local air pressure, as described in Stone et al. (2000).

The "lifton_scaling" script

This script calculates elevation and latitude scaling factors following Lifton et al. (2005) exactly. Right now it is set up so that it only returns scaling factors for spallation, fast muons, and slow muons, and rigidity cutoff. However, all of the relevant variables can be found in the script, and can be accessed by running the script as a stand-alone. Note that this script calls the "lifton_err_calc.m" script which must be in the same folder for this to run properly. It also calls three text files "lifton_ages.txt", "polar_wander.txt", "moment.txt", and "solar_scaling.txt" which all must be present for the script to run properly. These files are the exact same data that can be found in the lifton spreadsheet. I have included the spreadsheet in the .zip file for comparison with the results of the matlab script.

The "phillips_th_neut_flux" script

This script calculates the flux and stopping rate of cosmogenically derived thermal neutrons in a depth-profile of rock following Phillips et al., (2001). This does not include radiogenic or muon produced neutrons, it only includes 1) evaporation neutrons and 2) thermalized atmospheric "secondary" neutrons. This is a similar calculation to what is done by

CHLOE, but is based verbatim on Phillips' 2001 paper. These calculations are most heavily dependent on three things; 1) bulk rock composition, 2) elevation, and 3) the value chosen for SLHL neutron flux at the rock-air interface. Phillips et al. (2001) use a value of ~ 626 n/g*yr, however, higher values have been reported in Bierman et al. (1995) and elsewhere. This value scales with the fast neutron flux, (i.e. the S_{sp} variable produced in the scaling script).

Note also that two mistakes were found in the Phillips et al. (2001) equations, which have been verified with Fred Phillips. In particular, the denominator of eq. 13 should be a "+" instead of a "-", and the first subscript in equation 24 should be an "i" instead of a "j".

I have included an optional dataset "**Phillips_data.txt**" (and the .xls version), which contains data from the Liu et al. (1994) concrete block experiment, and can be used to reproduce the results in that paper, as well as the Phillips et al. (2001) paper.

The "heis_muon" script

This script calculates a profile of neutron stopping rate produced by stopping of fast and slow muons. It also calculates direct production of ^3He by fast muon stopping. The muon stopping profiles are calculated following Heisinger et al. (2001), and the neutron and ^3He production is calculated following Lal, (1987). Note that the muon calculations are fairly well established, but the resultant neutron/ ^3He production are basically rough estimates given by Lal, (1987). More accurate values may or may not exist in more recent literature (I looked, and didn't find them). This script has been verified against the plots in the Heisinger et al. (2001) papers.

The "rad_neut_flux" script

This script calculates the neutron flux generated by radiogenic processes following Chmiel et al. (2003). These come from two sources 1) (n, α) reactions on light elements, and 2) fission of U and Th. This script calculates a number of useful parameters, including the resonance escape probability, macroscopic absorption cross section, the thermal and epithermal

neutron fluxes, which are both passed back to the main script. These calculations have been checked against Andrews (1987), and Andrews (2001), and give comparable results.

"Li_3He.m"

```

%This script is specifically designed to take information about a suite
of samples
%and calculate the amount of 3He produced via 6Li.  Calculations of Li
%produced 3He follow Farley et al. 2006 and Amidon et al. 2008

%External Files:
%contained in "cosmo_scripts_v1.0.zip"

%External Scripts:
%"conv_elev.m" (after Stone, 2000)
%"lifton_scaling.m" (Lifton et al., 2005)
%"phillips_th_neut_flux.m" (Phillips et al., 2001)
%"heis_muon.m" (Heisinger et al., 2000)
%"rad_neut_flux.m" (Chmiel et al., 2003)

%%%%%%%%%%%%%%%%%%%%%%%%%%%%%%%%%%%%%%%%%%%%%%%%%%%%%%%%%%%%%%%%%%%%%%%%
%%%
clf
clear all

rawdata=dlmread('granite_data.txt','\t');
data=rawdata;
mindata=dlmread('min_data_example.txt','\t');

style=input('Do you want to simulate erosion case? (yes=1,no=0)')
isotope=input('which isotope? (14C=0; 10Be=1; 26Al=2; stable=3)')
%isotope=3;

for p=1:size(mindata,1) %Loop over all samples in the input file

%%%%%%%%%%%%%%%%%%%%%%%%%%%%%%%%%%%%%%%%%%%%%%%%%%%%%%%%%%%%%%%%%%%%%%%%
%%%You need to manually enter values for these
variables%%%%%%%%%%%%%%%%%%%%%%%%%%%%%%%%%%%%%%%%%%%%%%%%%%%%%%%%%%%%%%%%%%%%%%%%
Ts=288.15; %Mean temperature at sea level (K)
Ps=1013.25; %Mean pressure at sea level (hPa)
range3He=30; %Stopping range of li produced 3He nuclei
(microns) (!! This changes !!)
watper=0; % Weight percent of water in air (leave as
zero to replicate Phillips, 2001 calculations)
Pf_0_slhl=626; % SLHL Neutron flux (all energies) at the
rock-air interface. Scales with fast neutrons. (key parameter for
Phillips, 2001 calculation)
Afn=160; % Atmospheric attenuation length for fast
neutrons (g/cm^2)
depth_inc=420; %Number of increments that depth profiles
should be broken into (i.e. size of output vectors)
depth=4200; %depth of the profile below rock surface
(cm)
hedepth=300000; % He closure depth (cm)
erate=mindata(p,14); %erosion rate (cm/yr)
time=mindata(p,2)*10^6; %Elapsed amount of time for erosion
simulation (years)

```

```

%%This section extracts some key values from the input tables%%
%data=rawdata;
ppm_li_min=mindata(p,3);      %ppm of li in the mineral of interest
ppm_li_rock=data(2,8);       %ppm of li in the bulk rock
ppm_li_host=mindata(p,9);    %ppm of li in the host mineral
gr=mindata(p,4);             %equivalent spherical radius of grains (in
microns)
cl_age=mindata(p,2);         %He closure age of mineral (my)
elev=mindata(p,6);          %Sample elevation (m)
exp_age=mindata(p,5);        %exposure age of the sample (years)
meas3he=mindata(p,8);       %measured "cosmogenic" 3he in the sample
(Mat/g)
lon=mindata(p,11);          %longitude (decimal degrees, negative
values for western and southern hemispheres)
lat=mindata(p,10);          %latitude (decimal degrees, negative values
for western and southern hemispheres)
density=mindata(p,12);      % Density of rock (g/cm^3)

ppm_u_rock=30;              %Only if you are interested in xenon
calculation
ppm_u_min=1000;

%%These variables get calculated from the above inputs%%%%%%%%%%%%%%%%%%%%%%%%%%%%%%%%
timesteps=time*erate;      %Number of time steps the
erosion model will iterate through
time_inc=(1/erate)*(depth/depth_inc); %years per model time step
depthstep=(depth/depth_inc)*density; %The thickness of each model
depth increment (g/cm^2)
StoR=range3He/gr;          %ratio of stopping range to grain radius
li_fract=data(2,4).*data(2,6)/sum(data(:,4).*data(:,6)); %fraction of
neutrons stopped on Li (unitless)
u_fract=data(49,4).*data(49,6)/sum(data(:,4).*data(:,6));

%%%%%%%%%%%%%%%%%%%%%%%%%%%%%%%%%%%%%%%%%call on external
scripts%%%%%%%%%%%%%%%%%%%%%%%%%%%%%%%%%%%%%%%%%

%convert elevation in m to atmospheric depth in g/cm^2 (after Stone,
2000)
[att_depth,ad_err]=conv_elev(elev,Ts,Ps);

%calculates scaling following Lifton et al., 2005
[SP_scale,FM_scale,SM_scale,RC_loc]=lifton_scaling(lat,lon,att_depth,ad
_err,exp_age,isotope);

% Calculates thermal neutrons from fast neutrons (Phillips, 2001)
[ethsr_c,thsr_c,thflux,ethflux,p_ss]=phillips_th_neut_flux(depthstep,de
pth_inc,density,att_depth,Pf_0_slhl,SP_scale,Afn,watper,p);

%Calculates Muon-produced neutrons following Heisinger (2002)
[thsr_sm,thsr_fm,fastmuon_3he,depths]=heis_muon(depthstep,depth_inc,den
sity,att_depth,SP_scale,SM_scale,Pf_0_slhl,Afn,p_ss);

%calculates radiogenic neutron flux following (Chmiel et al., 2003)

```

```
[rad_n_flux,rad_n_prod,p_e,rad_n_sr,Ieff_pr,scat,therm]=rad_neut_flux(d
epth_inc,time_inc,depthstep,density,p);
```

```
%%%%%%%%%%%%%%%%%%%%%%%%%%%%%%%%%%%%%%%%%%%%%%%%%%%%%%%%%%%%%%%%%%%%%%%%
%%
```

```
%%%Combine the thermal and epithermal CTN stopping rates from Phillips
et al. (2001)
th_sr_c=thsr_c+ethsr_c;
```

```
%Now sum all of the neutron stopping rate profiles, for total stopping
rate
tot_n_sr=rad_n_sr+th_sr_c+thsr_sm+thsr_fm;  %(n/g*yr)
```

```
%%%Now calculate the fraction of lithium that is in the mineral of
%%%interest, and in the host mineral
fr_li_min=(ppm_li_min/ppm_li_rock); % (unitless)
fr_li_host=(ppm_li_host/ppm_li_rock);% (unitless)
fr_u_min=(ppm_u_min/ppm_u_rock);
```

```
%%%The actual effective mass of each mineral for stopping, multiplied
by the neutron flux with depth:
```

```
min_sr_c=((li_fract*fr_li_min)*th_sr_c);      % Stopping rate of CTN's
on Li in mineral (n/yr*g)
host_sr_c=((li_fract*fr_li_host)*th_sr_c);  % Stopping rate of CTN's on
Li in host (n/yr*g)
```

```
min_sr_r=((li_fract*fr_li_min)*rad_n_sr);    % Stopping rate of RN's
on Li in mineral (n/yr*g)
host_sr_r=((li_fract*fr_li_host)*rad_n_sr);  % Stopping rate of RN's
on Li in host (n/yr*g)
```

```
min_sr_sm=((li_fract*fr_li_min)*thsr_sm);    % Stopping rate of slow
muon produced neutrons (SMN) on Li in mineral (n/yr*g)
host_sr_sm=((li_fract*fr_li_host)*thsr_sm);  % Stopping rate of slow
muon produced neutrons on Li in host (n/yr*g)
```

```
min_sr_fm=((li_fract*fr_li_min)*thsr_fm);    % Stopping rate of fast
muon produced neutrons (FMN) on Li in mineral (n/yr*g)
host_sr_fm=((li_fract*fr_li_host)*thsr_fm);  % Stopping rate of fast
muon produced neutrons on Li in host(n/yr*g)
```

```
%%Here we calculate the apparent 3He production rate for the mineral of
%%interest separately for thermal neutrons produced by radiogenic (r),
cosmogenic (c), slow muon (sm) and fast muon
%%reactions (fm). Implant/eject calculations follow Farley, 2006.
```

```
pr_min_c=min_sr_c.*(1-
.75*(StoR)+.0625*((StoR)^3))+host_sr_c.*(0.75*(StoR)-.0625*((StoR)^3));
%Apparent 3He production rate in mineral from CTN's on Li (at/g*yr)
pr_min_r=min_sr_r.*(1-
.75*(StoR)+.0625*((StoR)^3))+host_sr_r*(.75*(StoR)-.0625*((StoR)^3));
%Apparent 3He production rate in mineral from RN's on Li (at/g*yr)
```

```

pr_min_sm=min_sr_sm*(1-
.75*(StoR)+.0625*((StoR)^3))+host_sr_sm*(.75*(StoR)-.0625*((StoR)^3));
%Apparent 3He production rate in mineral from SMN's on Li (at/g*yr)
pr_min_fm=min_sr_fm*(1-
.75*(StoR)+.0625*((StoR)^3))+host_sr_fm*(.75*(StoR)-.0625*((StoR)^3));
%Apparent 3He production rate in mineral from FMN's on Li (at/g*yr)

%%%%%%%%%%%%%%%%%%%%%%%%%%%%%%%%%%%%%%%%%%%%%%%%%%%%%%%%%%%%%%%%%%%%%%%%%This section calculates some basic output
values%%%%%%%%%%%%%%%%%%%%%%%%%%%%%%%%%%%%%%%%%%%%%%%%%%%%%%%%%%%%%%%%%%%%%%%%%
top=ceil(4/(depth/depth_inc)); %This calculates the number of vector
entries
rad3he=pr_min_r*cl_age*10^6; %total 3He produced from radiogenic
neutrons on Li (at/g)
ctn3he=exp_age*mean(pr_min_c(1:top)); %total 3He produced from
cosmogenic thermal neutrons in upper 4 cm (at/g)(not including sm and
fm component)
fm3he=mean(pr_min_fm(1:top))*exp_age; %total 3He produced from fm
derived thermal neutrons (at/g)
sm3he=mean(pr_min_sm(1:top))*exp_age; %total 3He produced from sm
derived thermal neutrons (at/g)

%%% A xenon section%%%%%%%%%%%%%%%%%%%%%%%%%%%%%%%%%%%%%%%%%%%%%%%%%%%%%%%%%%%%%%%%%%%%%%%%%
min_usr_r=((u_fract*fr_u_min)*rad_n_sr); %Extra xenon
feature... ignore this!
min_usr_c=((u_fract*fr_u_min)*tot_n_sr);
%%%%%%%%%%%%%%%%%%%%%%%%%%%%%%%%%%%%%%%%%%%%%%%%%%%%%%%%%%%%%%%%%%%%%%%%%

%%%This section simulates erosion by creating a depth column below
thesurface, calculating the produced 3He in each time step, and adding
it
%%%to the cell above. Depending on rate and duration of the simulate
erosion, the profile may or may not reach steady state.
if style==1
fm_3he=zeros(1,length(tot_n_sr));sm_3he=zeros(1,length(tot_n_sr));ctn_3
he=zeros(1,length(tot_n_sr));xenon=zeros(1,length(tot_n_sr));

for i=1:timesteps%this is the number of incremental time steps
    for j=1:length(ctn_3he) %this is the whole vertical profile
        if j==length(ctn_3he) %sets the base conc equal to zero with
each step
            %fm_3he(j)=0;
            %sm_3he(j)=0;
            ctn_3he(j)=0;
            xenon(j)=0;
        else
            ctn_3he(j)=ctn_3he(j+1)+(pr_min_c(j)*time_inc);
            %fm_3he(j)=fm_3he(j+1)+(pr_min_fm(j)*time_inc); %Adds the 3He
in the increment below, to the next increment above, simulating erosion
            sm_3he(j)=sm_3he(j+1)+(pr_min_sm(j)*time_inc); %Adds the 3He
in the increment below, to the next increment above, simulating erosion
            xenon(j)=xenon(j+1)+(min_usr_c(j)*time_inc);
        end
    end
end
end
end

```

```

ctn3he=mean(ctn_3he(1:top)); %Total CTN/Li produced 3He in the upper
4 cm of rock after erosion is finished (at/g)(does not include
radiogenic)
fm3he=mean(fm_3he(1:top)); %Total FMN/Li produced 3He in the upper 4
cm of rock after erosion is finished (at/g)(does not include
radiogenic)
sm3he=mean(sm_3he(1:top)); %Total SMN/Li produced 3He in the upper 4
cm of rock after erosion is finished (at/g)(does not include
radiogenic)
surf_xenon=mean(xenon(1:top));
end

%total 3He produced from Li assuming given closure age and specified
erosional history
tot3he=rad3he+ctn3he+fm3he+sm3he; %(at/g)
rad_xenon=min_usr_r*cl_age*10^6;

%%This section saves some variables into a tab delimited text file
titled "output"%%
%%Each row will correspond to a specific sample, each column to a
different calculated output for that sample%%
output(p,1)=mindata(p,1); %col 1: Sample ID numbers
output(p,2)=meas3he; %col 2: Measured 3He in sample
output(p,3)=exp_age; %col 3: Apparent exposure age of surface
in Ky, known a priori (i.e. an input)
output(p,4)=cl_age; %col 4: Closure age of mineral in sample
in My (known a priori)
output(p,5)=ppm_li_min; %col 5: Li concentration in mineral
output(p,6)=ppm_li_host; %col 6: Li concentration in host mineral
output(p,7)=tot3he/10^6; %col 7: Total 3He produced from
6Li (Radiogenic and Cosmogenic thermal neutrons)
output(p,8)=rad3he/10^6; %col 8: 3He produced from 6Li via
radiogenic thermal neutrons
output(p,9)=ctn3he/10^6; %col 9: 3He produced from 6Li via
cosmogenic thermal neutrons
output(p,10)=fm3he/10^6; %col 10: 3He produced from 6Li via
fast muon produced neutrons
output(p,11)=sm3he/10^6; %col 11: 3He produced from 6Li via
slow muon produced neutro
end
save output output -ascii -tabs

%%Optional plotting script%%
plot((depths/density)/100,thsr_c)
hold on
plot((depths/density)/100,ethsr_c)
plot((depths/density)/100,thsr_sm)
plot((depths/density)/100,rad_n_sr)
xlim([0 3])
xlabel('Depth (m)')
ylabel('stopping rate (n/g*yr)')
title('stopping rate profiles')

```

"conv_elev.m"

```

Function [att_depth,ad_err]=conv_elev(elev,Ts,Ps);

%%%%This converts elevation in m to an atmospheric height in g/cm^2.
%NOTE: This assume the standard atmospheric pressure at sea level.
%According to Stone, 2000 this varies by as much as +/- 4.4 hPa,
although
%the difference is not large for most moderate latitude continental
sites.
%A higher precision value could be obtained by getting the sea level
%pressure data as a function of lat/long and incorporating that into
this
%model... presumably a big data matrix, which could be called on.

%start with the eq 1 for standard atmospheric pressure given by Stone,
2000

%%%%%%%%Inputs for use as a stand alone
script%%%%%%%%%%%%%%
%elev=0
%Ps=1013.25; % sea level pressure in hPa (1hPa=1 millibar=.01456
lb/in^2)
%Ts=288.15; %sea level temp in K
%%%%%%%%%%%%%%
%%
mmw=28.9644353;% Mean molecular weight of atmosphere (g/mol)
g=9.80665; % Gravitational constant (m/s^2)
R=8.31451; %Gas constant [(N m)/(mol K)]
alr=.0065; %adiabatic lapse rate in K/m
gmr=.03417; %constant equal to gM/R; g=grav constant, M=molar weight
of air, R=gas constant

pres=Ps*exp((-gmr/alr)*(log(Ts)-log(Ts-alr*elev))); %air pressure in
hPa

att_depth=pres*.01456/6.4516*453.59237; %This is just a units
conversion from, hPa to g/cm^2
ad_err=(Ts*alr/(Ts+alr*elev)^2)*(10*Ps/g)*(g*mmw/(1000*R*alr))*(Ts/(Ts+
alr*elev))^((g*mmw/(1000*R*alr))-1)*elev;

```

"rad_neut_flux.m"

Function

```
[rad_n_flux,rad_n_prod,p_e,rad_n_sr,Ieff_pr,scat,therm]=rad_neut_flux(d
epth_inc,time_inc,depthstep,density,p);
```

```
%%This script calculate the flux of neutrons from radiogenic sources,
%%following Chmiel, 2003. Assuming homogenous distribution of all
elements
%%in rock. Note that this script exports the TOTAL radiogenic neutron
flux
%%(not just thermal neutron flux)for use in calculations in li_3he.m
```

```
%%%%%%%%%%%%%%%%%%%%%%%%%%%%%%%%%%%%%%%%%%%%%%%%%%%%%%%%%%%%%%%%%%%%%%%%Inputs Section
```

```
%%%%%%%%%%%%%%%%%%%%%%%%%%%%%%%%%%%%%%%%%%%%%%%%%%%%%%%%%%%%%%%%%%%%%%%%
```

```
rawdata=dlmread('granite_data.txt');
```

```
data=rawdata;
```

```
mindata=dlmread('min_data_example.txt','\t');
```

```
%%%Variables for use of script as stand alone%%%%%%%%%%%%%%%%%%%%%%%%%%%%%%%%%%%%%%%%%%%%%%%%%%%%%%%%%%%%%%%%%
```

```
%clear all
```

```
%clf
```

```
%ppm_li_g=0;
```

```
%ppm_li_ss=0;
```

```
%data(2,8)=ppm_li_g;
```

```
%data(2,6)=ppm_li_g*(10^-6)*(1/6.94)*6.02e23
```

```
%data1(2,8)=ppm_li_ss;
```

```
%data1(2,6)=ppm_li_ss*(10^-6)*(1/6.94)*6.02e23
```

```
%depth=10000; %Depth in rock in cm
```

```
%depth_inc=250; %Number of increments in depth profile (in
rock)
```

```
%density=2.7; %Density of rock
```

```
%depthstep=(depth/depth_inc)*density; %actual value of each depth
increment (g/cm^2)
```

```
%time_inc=(1/erate)*(depth/depth_inc); %this is in units of yrs per
increment
```

```
%%%%%%%%%%%%%%%%%%%%%%%%%%%%%%%%%%%%%%%%%%%%%%%%%%%%%%%%%%%%%%%%%%%%%%%%
```

```
%%%%%%%%%%%%%%%%%%%%%%%%%%%%%%%%%%%%%%%%%%%%%%%%%%%%%%%%%%%%%%%%%
```

```
%The average mass stopping power is assumed to be 6 MeV
```

```
f_ab=data(:,8)./1000000; %convert ppm element into ug in a gram of
rock
```

```
% Calculate the production rate in n/g*yr
```

```
a=sum(f_ab.*data(:,12).*data(:,10))/sum(f_ab.*data(:,12)); %Eq. A3
```

```
b=sum(f_ab.*data(:,12).*data(:,11))/sum(f_ab.*data(:,12)); %Eq. A4
```

```
rad_n_prod=.470*data(49,8)+a*data(49,8)+b*data(48,8); %Total
yield of radiogenic neutrons (n/g/yr) Eq. A2
```

```
%Calculate the effective resonance integral, the macro scattering x-s,
the
```

```
%macro thermal x-s, and the average energy loss per collision
```

```
Ieff=0;Ieff_pr=0; scat=0;therm=0;sigp=0;
```

```

for i=1:length(data)
    if data(i,8)>0
        Ieff=Ieff+data(i,5);    %effective resonance integral Eq. A7
        Ieff_pr=Ieff_pr+data(i,5)*data(i,6);    %Eq. A8
        scat=scat+data(i,6)*data(i,3);    %Macro. scattering XS,
Eq. A11
        therm=therm+data(i,6)*data(i,4);    %Macro. absorbtion XS,
Eq. A12
        sigp=sigp+data(i,6)*data(i,3)*data(i,2);
    end
end
p_e=exp(-(Ieff_pr/sigp));    %%resonance escape probability (unitless)
Eq. A13

phi_n_g=p_e*(rad_n_prod/therm)+(1-p_e)*(rad_n_prod/Ieff_pr);    %Eq. A6
Total neutron flux in n/cm^2*yr, including thermal and epi components
rad_n_flux=phi_n_g;
rad_n_sr=(phi_n_g*therm);    %Divide flux by macro. absorbt. XS to get
stopping rate in n/g/yr

```

"heis_muon.m"

```

function
[thsr_sm,thsr_fm,fastmuon_3he,depths]=heis_muon(depthstep,depth_inc,den
sity,att_depth,SP_scale,SM_scale,Pf_0_slhl,Afn,p_ss);

%This calculates neutron production via slow and fast muons from
%The heisenberg, 2000 papers. NOTE: It calculates total neutrons
%produced, and does not scale them down
%for the resonance escape probability!!! Not clear what the energy
%distribution of muon produced neutrons is.

%%%Inputs fo use as a stand alone script%%%%%%%%%%%%%%%%%%%%%%%%%%%%%%%%%
%clear all
%clf
%depth=42000;           %Depth of rock profile in cm
%depth_inc=10000;      %Number of increments in depth profile
%(in rock)
%density=2.7;          %Density of rock
%depthstep=(depth/depth_inc)*density; %actual value of each depth
increment (g/cm^2)
%att_depth=1033.2;     %Atmospheric depth (g/cm^2)
%Ssp=1;                %Spallation scaling factor for elevation
and latitude combined
%Ssm=1;                %Slow muon scaling factor for elevation
and latitude combined
%I_ss=.75;            % resonance escape probability (unitless)
%Pf_0_slhl=950;       %Rate of epithermal neutron production
from fast neutrons, SLHL
%Afn=160;             %Fast neutron attenuation in rock
%%%%%%%%%%%%%%%%%%%%%%%%%%%%%%%%%%%%%%%%%%%%%%%%%%%%%%%%%%%%%
%%%%%%%%%%%%%%%%%%%%%%%%%%%%%%%%%%%%%%%%%%%%%%%%%%%%%%%%%%%%%

%%%%%%%%%%%%%%%%%%%%%%%%%%%%%%%%%%%%%%%%%%%%%%%%%%%%%%%%%%%%%
%Some variables relative to muon production%%%%%%%%%%%%%%%%%%%%%%%%%%%%%%%%%
L_sm_at=13.50; %Slow muon attenuation length in the atmosphere
(g/cm^2)
L_sm_rock=15.10; %Fast muon attenuation length in the atmosphere
(g/cm^2)
L_fm=43.20; %Fast muon attenuation length (g/cm^2) (Heisinger, p. 352)
(Braucher, 2003 suggests 5300)
alpha=.75; % Constant from p. 351 of Heisinger (2002)
pos_att_dep=1033.2-att_depth;

%%This loop generates a vector with depths below rock surface in
hg/cm^2
count=0;
for i=1:depth_inc
count=count+1;
depths(i)=(depthstep*count)/100; %units of g/cm^2
end

%%%%%%%%%%%%%%%%%%%%%%%%%%%%%%%%%%%%%%%%%%%%%%%%%%%%%%%%%%%%%
SLOW MUONS (Heisinger, part 2)%%%%%%%%%%%%%%%%%%%%%%%%%%%%%%%%%%%%%%%%%%%%%%%%%%%%%%%%%%%%%

%2) now calculate the muogenic stopping rate versus depth by following
Hesinger, 2002 (part 2: slow muons), and using an

```

```

%average value of 1.24 neutrons per stopped muon (fast and slow
averaged?) (from Charlambus,
%1971),(lal predicts 0.8 neutrons per slow muon capture, and 2 muons
per
%stopped fast muon)
%and a ratio of positive to negative muons (Ku=1.25) (from heisinger,
2002

f_neg=1/(1+1.268);          %fraction of negative muons (heisinger, Eq. 4)
for i=1:depth_inc
n_of_h(i)=3.21-.297*log(depths(i)+42)+(1.21*10^-3)*(depths(i));
%(Eq. 5)
if (depths(i))<2000

phi_v(i)=(258.5/(((depths(i))+210)*(((abs(depths(i))+10)^1.66)+75)))*ex
p(-(5.5*10^-4)*(depths(i)));  %(Eq. 3) Vertical muon flux in rock <
2000 hg/cm^2, at SLHL
else
phi_v(i)=((1.82*10^-6)*((1211/(depths(i))))^2)*exp(-
(depths(i))/1211)+2.84*10^-13);          %(Eq. 2) vertical muon flux in
rock > 2000 hg/cm^2, at SLHL, FROM PART 1 fast muon paper
end
R(i)=((2*pi)/(n_of_h(i)+1))*phi_v(i)*exp((pos_att_dep/100)/L_sm_at);
%(scaled Eq. 6) (mu/g*s) heisinger, 2002, adjusts vertical flux for
full sky angle, and scales for lat/elev.
end

for i=1:depth_inc-1
    deriv(i)=-((R(i+1)-R(i))/(depths(i+1)-depths(i)));    %Takes
derivative of the flux with depth, as part of eq 13
end

phi_heis=f_neg.*deriv.*.01.*60.*60.*24.*365;    %(Eq. 13) this is the
actual depth profile at the specified elevation, high latitude,
assuming a rock L of 15.1 at/g
phi_heis(depth_inc)=phi_heis(depth_inc-1);

%NOTE: This is a calc of negative muon stopping vs. depth, according
to eq
%10, and allows explicit inclusion of an attenuation length in rock,
results
%diverge at depth.
phi_heis_eq10=phi_heis(1).*exp(-(depths./L_sm_rock));

%%%%%%%%FAST MUONS (heisinger PART
1)%%%%%%%%
%IMPORTANTLY: This calculation may only be valid at sea level,
because
%the average energy spectrum (E) and the beta term (beta) are written
in
%simplified forms that are not necessarily applicable across a range
of
%elevations.
phiH=(2*pi./(n_of_h+1)).*phi_v*exp((pos_att_dep/100)/L_fm); %%This is
Eq. 5, from pt. 1, with the vertical muon flux scaled for elevation

```

```

for i=1:depth_inc
    E(i)=7.6+321.78*(1-exp((-8.059*10^-4)*depths(i)))+50.7*(1-exp((-
5.05*10^-5)*depths(i)));    %%Eq. 11,from pt. 1, depth dependence of
mean energy
beta(i)=.846-.015*log(depths(i)+1)+.003139*(log(depths(i)+1)^2);    %Eq.
16 from pt. 1, this is the beta term as a function of depth
end
phi_fm=beta.*phiH.*(E.^alpha)*60.*60.*24.*365;    %Eq 17.5, the
coefficient to calc either neutron, or nuclide production
p_fm=(phi_fm*4.8*10^-6);    %Eq. 21 This is the neutron production from
fast muons.
phi_heis_fm=(1-f_neg).*deriv.*.01.*60.*60.*24.*365;
phi_heis_fm(depth_inc)=phi_heis_fm(depth_inc-1);
for i=1:depth_inc
    phi_heis_fmeq10(i)=phi_heis_fm(1)*exp(-depths(i)/L_fm);
end
fastmuon_3he=phi_heis_fmeq10*.16; % This is the 3he and 3H production
rate from stopped fast muons using 16% from lal, 1987

%%%This takes the slow muon stopping rate profile calculated by
Heisinger, and multiplies by
%%%0.8 neutrons per stop (lal, 1987). Neutron production from fast
muons
%%%is calculated directly from eq. 21 of Heisinger (part 1).

thsr_sm=phi_heis_eq10*.8;    % neutrons produced from slow muon capture
(n/g/yr)
thsr_fm=p_fm;    % neutrons produced from fast muon capture (n/g/yr)

%loglog(depths,phi_heis_eq10)
%axis([1 10^3 10^-3 10^3])

depths=depths*100;

```

"Lifton_scaling.m"

```

function
[SP_scale,FM_scale,SM_scale,RC_loc]=scaling(lat,lon,att_depth,ad_err,exp_age,isotope);

%%this script follows Lifton et al. (2005) spreadsheet exactly.
%%Relevant data tables from the original appendix have been copied
directly from their spreadsheet and
%%are used in exactly the same way.

%%This script can be called by Li_3He.m, or act as a stand alone if you
use the dat values below

%%%Specify these inputs if operating this script as stand-
alone%%%%%%%%%%
%clear all
%isotope=input('which isotope? (14C=0; 10Be=1; 26Al=2; stable=3)')
%lat=37; %Latitude in decimal degrees (negative for S.
Hem.)
%lon=-117; %Longitude in decimal degrees (negative for W.
Hem.)
%att_depth=881.1089; %Atmospheric depth (g/cm^2)
%ad_err=0.5344; %Error on atmospheric depth
%exp_age=92500; %exposure age (years)
%%%%%%%%%%%%%%%%%%%%%%%%%%%%%%%%%%%%%%%%%%%%%%%%%%%%%%%%%%%%%%%%%%%%%%%%%%
%%%%%%%%%%

%%%%%%%%%%Fixed Inputs (don't change
these)%%%%%%%%%%
ages=dlmread('lifton_ages.txt','\t');
pw=dlmread('polar_wander.txt','\t');
moment=dlmread('moment.txt','\t');
solardata=dlmread('solar_scaling.txt','\t');
deg2rad=0.0174532925199433;rad2deg=57.2957795130823;

%%%Change these if you want, but don't comment them out%%%%%%%%%%
pr_slhl(1)=1; %SLHL production rate for mineral (at/g/yr)
pr_slhl(2)=pr_slhl(1)*.054; %Absolute 1s error on SLHL production
rate (at/g/yr)
latrad=lat*deg2rad;lonrad=lon*deg2rad; % **don't change** radians
conversion

%%%This parts sets the parameters differently depending upon
isotope%%%%%%%%%%
if isotope==1 %10Be
decay_const=4.59037867920494e-7;
fspall(1)=0.963877; %Fraction of production from spallation
(following Lifton, 2005)
fspall(2)=0.003630; %1s Percent Error on Fraction of
production from spallation (following Lifton, 2005)
ffmuon(1)=.016881; %Fraction of production from fast muons
(following Lifton, 2005)

```

```

ffmuon(2)=.002360;           %1s Percent Error on Fraction of production
from fast muons (following Lifton, 2005)
fsmuon(1)=.019241;           %Fraction of production from slow muons
(following Lifton, 2005)
fsmuon(2)=.001271;           %1s Percent Error on Fraction of production
from slow muons (following Lifton, 2005)
elseif isotope==3 %stable
    decay_const=6.93147180560e-
17;fspall(1)=1;fspall(2)=0;ffmuon(1)=0;ffmuon(2)=0;fsmuon(1)=0;fsmuon(2
)=0;
elseif isotope==2 %26Al
    decay_const==9.68082654413331e-
7;fspall(1)=.954382;fspall(2)=.004772;ffmuon(1)=.0214;ffmuon(2)=.002581
;fsmuon(1)=.02416;fsmuon(2)=.002191;
else %14C

decay_const==0.000120968094338559;fspall(1)=.829576;fspall(2)=.023445;f
fmuon(1)=.019838;ffmuon(2)=.011271;fsmuon(1)=.150586;fsmuon(2)=.012173;
end

%%%%%%%%Define a whole bunch of constants for later
on%%%%%%%%
c1=1.8399;c2=-1.1854e2;c3=-4.942e-2;c4=8.0139e-1;c5=1.2708e-
4;c6=9.4647e-1;
c7=-3.2208e-2;c8=1.2688;SDres=.046254;c1se=1.0353E-
02;c2se=2.6567E+00;c3se=1.7512E-03;
c4se=4.2170E-03;c5se=4.3896E-05;c6se=3.1630E-02;c7se=4.6392E-
03;c8se=4.0327E-02;
a1=2.4424E+00;a2=-2.8717E-03;a3=4.7441E-07;a4=4.3045E-05;a5=-3.7891E-
02;a6=-7.6795E-04;
b1=5.1132E+00;b2=-8.8225E-03;b3=3.7346E-06;b4=7.9712E-05;b5=-7.5605E-
02;b6=-1.3203E-03;
psperr=sqrt((fspall(1)*pr_slhl(2))^2+(pr_slhl(1)*fspall(2))^2);
pfmerr=sqrt((ffmuon(1)*pr_slhl(2))^2+(pr_slhl(1)*ffmuon(2))^2);
psmerr=sqrt((fsmuon(1)*pr_slhl(2))^2+(pr_slhl(1)*fsmuon(2))^2);
%%%%%%%%
%%

%%%%%%%%Determine the number of age steps (z) will need to be
calculated%%%%%%%%
if exp_age < 50000
    zmax=(exp_age/100)+1;
else
    zmax=ceil(501+((exp_age-50000)/1000));
end
M_Mo=[0,0];ITpr=[0,0]; %Initialize some variables

%%%%%%%%Start looping over the age steps, calculating
params%%%%%%%%
for z=1:zmax

%%%%%%%%calculate magnetic latitude (columns D and E)%%%%%%%%
age=1+(ages(z)/100);
if age<102

```

```

mag_lat(z,1)=90-
rad2deg*(acos(sin(latrad)*sin(pw(age,3))+cos(pw(age,3))*cos(latrad)*cos
(pw(age,7)-lonrad)));
dplat(z)=rad2deg*((acos(cos(latrad)*cos(pw(age,3))*cos(lonrad)*cos(pw(a
ge,7))+cos(latrad)*cos(pw(age,3))*sin(lonrad)*sin(pw(age,7))+sin(latrad
)*sin(pw(age,3)))*tan(cos(latrad)*cos(pw(age,3))*cos(lonrad)*cos(pw(age
,7))+cos(latrad)*cos(pw(age,3))*sin(lonrad)*sin(pw(age,7))+sin(latrad)*
sin(pw(age,3)))*(cos(latrad)*-
sin(pw(age,3))*cos(lonrad)*cos(pw(age,7))+cos(latrad)*-
sin(pw(age,3))*sin(lonrad)*sin(pw(age,7))+sin(latrad)*cos(pw(age,3)))*p
w(age,5));
dplon(z)=rad2deg*((acos(cos(latrad)*cos(pw(age,3))*cos(lonrad)*cos(pw(
age,7))+cos(latrad)*cos(pw(age,3))*sin(lonrad)*sin(pw(age,7))+sin(latra
d)*sin(pw(age,3)))*tan(cos(latrad)*cos(pw(age,3))*cos(lonrad)*cos(pw(ag
e,7))+cos(latrad)*cos(pw(age,3))*sin(lonrad)*sin(pw(age,7))+sin(latrad)
*sin(pw(age,3)))*(cos(latrad)*cos(pw(age,3))*cos(lonrad)*-
sin(pw(age,7))+cos(latrad)*cos(pw(age,3))*sin(lonrad)*cos(pw(age,7))+si
n(latrad)*cos(pw(age,3)))*pw(age,9));
mag_lat(z,2)=sqrt((dplat(z)^2)+(dplon(z)^2));      %The error
else
mag_lat(z,1)=lat;
mag_lat(z,2)=0;
end

%%%%calculate the magnetic intensity scaling (column B and
C)%%%%%%%%%%%%%%%%%%%%%%%%%%%%%%%%%
for i=1:(length(moment)-1)
    if moment(i,1)==ages(z)
        M_Mo(z,1)=moment(i,2);      %The value
        M_Mo(z,2)=moment(i,3);      %the 1s error
    elseif moment(i,1)< ages(z) && ages(z) < moment(i+1,1)
        M_Mo(z,1)=moment(i,2)+(((moment(i+1,2)-
moment(i,2))/(moment(i+1,1)-moment(i,1)))*(ages(z)-moment(i,1)));
        M_Mo(z,2)=sqrt(((1-((ages(z)-moment(i,1))/(moment(i+1,1)-
moment(i,1))))*moment(i,3))^2+(((ages(z)-moment(i,1))/(moment(i+1,1)-
moment(i,1)))*moment(i+1,3))^2);
    end
end

%%%%%Calculate the solar intensity scaling (columns H and
I)%%%%%%%%%%%%%%%%%%%%%%%%%%%%%%%%%
if ages(z)>=11300
    s(z,1)=.9497;      %The value
    s(z,2)=.0003;      %The 1s error
else
for i=1:(length(solardata)-1)
    if (solardata(i,1)-60)<ages(z) && ages(z)<(solardata(i+1,1)-60)
%subtract 70 from age for years before 1950
        s(z,1)=solardata(i,2);
        s(z,2)=solardata(i,3);
    end
end
end

%%%%%%%%%This section calculates the rigidity cutoffs%%%%%%%%%
d1=1.5765e1;d2=3.7995;d1se=9.3293E-02;d2se=5.5357E-02;

```

```

if
(M_Mo(z,1)*d1*(cos(deg2rad*(mag_lat(z,1))))^d2)<(d1*(cos(deg2rad*(55))))
^d2);
    RC(z,1)=d1*(cos(deg2rad*(55)))^d2;

RC(z,2)=sqrt((RC(z,1)*.075520694)^2+(RC(z,1)*M_Mo(z,2))^2+(M_Mo(z,1)*sq
rt(((cos(deg2rad*(mag_lat(z,1))))^d2)*dlse)^2+((d1*cos(deg2rad*(mag_lat(
z,1))))^d2)...
    *log(cos(deg2rad*(mag_lat(z,1))))*d2se)^2+((-
d1*d2*cos(deg2rad*(mag_lat(z,1))))^(d2-
1))*sin(deg2rad*(mag_lat(z,1))*deg2rad*(mag_lat(z,2))^2))^2);
else
    RC(z,1)=M_Mo(z,1)*d1*(cos(deg2rad*(mag_lat(z,1))))^d2;

RC(z,2)=sqrt((RC(z,1)*.075520694)^2+(RC(z,1)*M_Mo(z,2))^2+(M_Mo(z,1)*sq
rt(((cos(deg2rad*(mag_lat(z,1))))^d2)*dlse)^2+((d1*cos(deg2rad*(mag_lat(
z,1))))^d2)...
    *log(cos(deg2rad*(mag_lat(z,1))))*d2se)^2+((-
d1*d2*cos(deg2rad*(mag_lat(z,1))))^(d2-
1))*sin(deg2rad*(mag_lat(z,1))*deg2rad*(mag_lat(z,2))^2))^2);
end

%%%calculate scaling factors for spallation (Ssp), fast muons (Sfm) and
slow muons (Ssm)%%%%%%%%%%
Ssp(z)=exp(c1*log(att_depth*s(z,1))-
s(z,1)*exp(c2*s(z,1)/((RC(z,1)+5*s(z,1))^(2*s(z,1))))+c3*att_depth^c4+c
5*(att_depth*(RC(z,1)+4*s(z,1)))^c6+c7*(RC(z,1)+4*s(z,1))^c8);
if RC(z,1)<4
Sfm(z,1)=exp(a1+a2*att_depth+a3*att_depth^2+(a4*att_depth*4)+(a5*4)+(a6
*4^2));
Ssm(z,1)=exp(b1+b2*att_depth+b3*att_depth^2+(b4*att_depth*4)+(b5*4)+(b6
*4^2));
else
Sfm(z,1)=exp(a1+a2*att_depth+a3*att_depth^2+(a4*att_depth*RC(z,1))+(a5*
RC(z,1))+(a6*RC(z,1)^2));
Ssm(z,1)=exp(b1+b2*att_depth+b3*att_depth^2+(b4*att_depth*RC(z,1))+(b5*
RC(z,1))+(b6*RC(z,1)^2));
end

%%%call the external script "lifton_err_calc.m" to calculate
errors%%%%%%%%%%
[spcov(z),Ssp_err(z),fmcov(z),Sfm_err(z),smcov(z),Ssm_err(z),log_sp_err
(z)]=lifton_err_calc(att_depth,ad_err,RC,z,s,Ssp,Sfm,Ssm);

%%%Calculates the modern "instantaneous" production rates and
errors%%%%%%%%%
Spr(z,1)=pr_slhl(1)*Ssp(z)*fspall(1);           %Modern spallation PR
(at/g/yr) Column AB
Spr(z,2)=sqrt((pr_slhl(1)*fspall(1)*Ssp_err(z))^2+(Ssp(z)*psperr)^2);
%Column AC
FMpr(z,1)=(pr_slhl(1)*Sfm(z)*ffmuon(1));       %Modern fast muon
production rate (at/g/yr) Column AD
FMpr(z,2)=sqrt((pr_slhl(1)*ffmuon(1)*Sfm_err(z))^2+(Sfm(z)*pfmerr)^2);
%Column AE

```

```

SMpr(z,1)=(pr_slhl(1)*Ssm(z)*fsmuon(1));      %%Modern slow muon
production rate (at/g/yr)  Column AF
SMpr(z,2)=sqrt((pr_slhl(1)*fsmuon(1)*Ssm_err(z))^2+(Ssm(z)*psmerr)^2);
%Column AG
Tpr(z,1)=Spr(z,1)+FMpr(z,1)+SMpr(z,1);  %total modern production rate
(at/g/yr)  Column AH
Tpr(z,2)=sqrt(Spr(z,2)^2+FMpr(z,2)^2+SMpr(z,2)^2);  %Error on total
modern production rate (at/g/yr)  Column AI

%Calculate weighting vectors and time integrated prod. rate%%%%%%%%%
weighting(z,1)=(exp(-decay_const*ages(z)))/((Tpr(z,2)/Tpr(z,1))^2);
%Column AT
Pxwt(z,1)=(Tpr(z,1)*weighting(z));      %Column AU
P2xwt(z,1)=((Tpr(z,1)^2)*weighting(z));  %Column AV

end %This finishes looping over all the age values

%%%%%%%%new loop to calculate integrated production rates (column
AL)%%%%%%%%%
for z=1:zmax
ITpr(z,1)=sum(Pxwt(z:zmax))/sum(weighting(z:zmax)); %Total time
integrated production rate for Spall, FM and SM (at/g/yr)
end

%%%%%%%%Final loop to calculate errors on integrated PR (Columns AW and
AX)%%%%%%%%%
for z=1:zmax
inv_s_sq(z,1)=ITpr(z)*sqrt(1/sum(weighting(z:zmax))); %Column AW
if (((sum(P2xwt(z:zmax))/sum(weighting(z:zmax)))-(ITpr(z,1)^2))/(zmax-
z))>0
    scatter(z,1)=sqrt(((sum(P2xwt(z:zmax))/sum(weighting(z:zmax)))-
(ITpr(z,1)^2))/(zmax-z)); %column AX
else
    scatter(z,1)=0;
end

ITpr(z,2)=max(scatter(z),inv_s_sq(z)); % Column AM 1s % error on
integrated PR for Spall, FM, and SM
end

TPr=ITpr(1);
SP_scale=Ssp(zmax);
FM_scale=Sfm(zmax);
SM_scale=Ssm(zmax);
RC_loc=RC(zmax,1);

```

"Lifton_err_calc.m"

function

```
[spcov, Ssp_err, fmcov, Sfm_err, smcov, Ssm_err, log_sp_err]=lifton_err_calc(
att_depth, ad_err, RC, z, s, Ssp, Sfm, Ssm);
```

```
%%%%%%%%Calculate errors for spallation
```

```
scaling%%%%%%%%%
```

```
a1=2.4424E+00;a2=-2.8717E-03;a3=4.7441E-07;a4=4.3045E-05;a5=-3.7891E-
02;a6=-7.6795E-04;
```

```
alse=1.1848E-01;a2se=2.7678E-04;a3se=1.5923E-07;a4se=3.2362E-
06;a5se=3.9933E-03;a6se=1.4728E-04;SDresFM=.0175;smod_err=.05;
```

```
c1=1.8399;c2=-1.1854e2;c3=-4.942e-2;c4=8.0139e-1;c5=1.2708e-
4;c6=9.4647e-1;
```

```
c7=-3.2208e-2;c8=1.2688;SDres=.046254;c1se=1.0353E-
02;c2se=2.6567;c3se=1.7512E-03;
```

```
c4se=4.2170E-03;c5se=4.3896E-05;c6se=3.1630E-02;c7se=4.6392E-
03;c8se=4.0327E-02;
```

```
spcov=2*((log(s(z,1)*att_depth))*(-exp(c2*(RC(z,1)+5*s(z,1))^(-
2*s(z,1)))*(s(z,1)^2)*(RC(z,1)+5*s(z,1))^(-2*s(z,1)))*0.0040593
+(log(s(z,1)*att_depth))*(att_depth^c4)...
*_
```

```
0.000017527+(log(s(z,1)*att_depth))*(c3*att_depth^c4*log(att_depth))*-
0.000041586
+(log(s(z,1)*att_depth))*((att_depth*(RC(z,1)+4*s(z,1)))^c6)*3.6466E-07
+(log(s(z,1)*att_depth))...
```

```
*((c5*(att_depth*(RC(z,1)+4*s(z,1)))^c6)*log(att_depth*(RC(z,1)+4*s(z,1)
)))*-0.00026256 +(log(s(z,1)*att_depth))*((RC(z,1)+4*s(z,1))^c8)*-
0.00003218 +(log(s(z,1)*att_depth))*log(RC(z,1)+4*s(z,1))...
```

```
*c7*(RC(z,1)+4*s(z,1))^c8*-0.00026678 +(-
exp(c2*(RC(z,1)+5*s(z,1))^(-2*s(z,1)))*(s(z,1)^2)*(RC(z,1)+5*s(z,1))^(-
2*s(z,1)))*(att_depth^c4)*-0.0013492 +(-exp(c2*(RC(z,1)+5*s(z,1))^(-
2*s(z,1)))*(s(z,1)^2)...
*(RC(z,1)+5*s(z,1))^(-2*s(z,1)))*(c3*att_depth^c4*log(att_depth))*-
```

```
0.0032908 +(-exp(c2*(RC(z,1)+5*s(z,1))^(-
2*s(z,1)))*(s(z,1)^2)*(RC(z,1)+5*s(z,1))^(-
2*s(z,1)))*((att_depth*(RC(z,1)+4*s(z,1)))^c6)...
*0.000022665 +(-exp(c2*(RC(z,1)+5*s(z,1))^(-
2*s(z,1)))*(s(z,1)^2)*(RC(z,1)+5*s(z,1))^(-
2*s(z,1)))*((c5*(att_depth*(RC(z,1)+4*s(z,1)))^c6)*log(att_depth*(RC(z,
```

```
1)+4*s(z,1))))*-0.01604 +...
(-exp(c2*(RC(z,1)+5*s(z,1))^(-
2*s(z,1)))*(s(z,1)^2)*(RC(z,1)+5*s(z,1))^(-
2*s(z,1)))*((RC(z,1)+4*s(z,1))^c8)*0.0049605 +(-
exp(c2*(RC(z,1)+5*s(z,1))^(-2*s(z,1)))*(s(z,1)^2)*(RC(z,1)+5*s(z,1))^(-
2*s(z,1)))...
*(log(RC(z,1)+4*s(z,1))*c7*(RC(z,1)+4*s(z,1))^c8)*0.048868
```

```
+(att_depth^c4)*(c3*att_depth^c4*log(att_depth))*7.3717E-06
+(att_depth^c4)*((att_depth*(RC(z,1)+4*s(z,1)))^c6)*-5.4318E-08
+(att_depth^c4)...
```

```

*((c5*(att_depth*(RC(z,1)+4*s(z,1)))^c6)*log(att_depth*(RC(z,1)+4*s(z,1)
))) *3.9184E-05 +(att_depth^c4)*(RC(z,1)+4*s(z,1))^c8 *3.8385E-06
+(att_depth^c4)*(log(RC(z,1)+4*s(z,1))*c7*(RC(z,1)+4*s(z,1))^c8)...
    *3.0982E-05
+(c3*att_depth^c4*log(att_depth))*(att_depth*(RC(z,1)+4*s(z,1)))^c6*-
1.2320E-07
+(c3*att_depth^c4*log(att_depth))*(c5*(att_depth*(RC(z,1)+4*s(z,1)))^c
6)...
    *log(att_depth*(RC(z,1)+4*s(z,1))) *8.8938E-05
+(c3*att_depth^c4*log(att_depth))*(RC(z,1)+4*s(z,1))^c8 *8.4228E-06
+(c3*att_depth^c4*log(att_depth))*(log(RC(z,1)+4*s(z,1))*c7*(RC(z,1)+4*
s(z,1))^c8)...
    *6.7768E-05
+((att_depth*(RC(z,1)+4*s(z,1)))^c6)*((c5*(att_depth*(RC(z,1)+4*s(z,1)
))^c6)*log(att_depth*(RC(z,1)+4*s(z,1))))*-1.3881E-06
+((att_depth*(RC(z,1)+4*s(z,1)))^c6)*((RC(z,1)+4*s(z,1))^c8)*-1.6036E-
07 ...

+((att_depth*(RC(z,1)+4*s(z,1)))^c6)*(log(RC(z,1)+4*s(z,1))*c7*(RC(z,1)
+4*s(z,1))^c8)*-1.3199E-06
+((c5*(att_depth*(RC(z,1)+4*s(z,1)))^c6)*log(att_depth*(RC(z,1)+4*s(z,1)
))) *((RC(z,1)+4*s(z,1))^c8)*1.1559E-04 ...

+((c5*(att_depth*(RC(z,1)+4*s(z,1)))^c6)*log(att_depth*(RC(z,1)+4*s(z,1)
))) *((log(RC(z,1)+4*s(z,1))*c7*(RC(z,1)+4*s(z,1))^c8)*9.5263E-04
+((RC(z,1)+4*s(z,1))^c8)*((log(RC(z,1)+4*s(z,1))*c7*(RC(z,1)+4*s(z,1))^c
8)*1.8651E-04 );

% Ssp_err=sqrt((Ssp(z)*(sqrt(abs((sqrt((log(s(z,1)*att_depth)*c1se))^2+((
exp(c2*(RC(z,1)+5*s(z,1))^-2*s(z,1)))*(s(z,1)^2)*(RC(z,1)+5*s(z,1))^(-
2*s(z,1)))*c2se)^2+(att_depth^c4)*c3se)^2...
%
+((c3*att_depth^c4*log(att_depth))*c4se)^2+(((att_depth*(RC(z,1)+4*s(z,
1)))^c6)*c5se)^2+(((c5*(att_depth*(RC(z,1)+4*s(z,1)))^c6)*log(att_depth
*(RC(z,1)+4*s(z,1))))*c6se)^2+(((RC(z,1)+4*s(z,1))^c8)...
%
*c7se)^2+((log(RC(z,1)+4*s(z,1))*c7*(RC(z,1)+4*s(z,1))^c8)*c8se)^2+((-
exp(c2*s(z,1))*((RC(z,1)+5*s(z,1))^-
2*s(z,1))))+c1/s(z,1)+4*c7*c8*(RC(z,1)+4*s(z,1))^(c8-
1))+4*c5*c6*att_depth....
%
*((att_depth*(RC(z,1)+4*s(z,1)))^(c6-1))-
exp(c2*s(z,1))*((RC(z,1)+5*s(z,1))^-
2*s(z,1)))*s(z,1)*(c2*(RC(z,1)+5*s(z,1))^-
2*s(z,1))+c2*s(z,1)*(RC(z,1)+5*s(z,1))^-
2*s(z,1))*((10*s(z,1)/(RC(z,1)+5*s(z,1)))...
%
-
2*log(RC(z,1)+5*s(z,1)))*s(z,2))^2+((c7*c8*(RC(z,1)+4*s(z,1))^c8-
1))+2*c2*exp(c2*s(z,1))*((RC(z,1)+5*s(z,1))^-
2*s(z,1)))*s(z,1)^3*(RC(z,1)+5*s(z,1))^-2*s(z,1)-
1))+c5*c6*att_depth...
%
*((att_depth*(RC(z,1)+4*s(z,1)))^(c6-
1))*RC(z,2))^2+((c1/att_depth+c3*c4*(att_depth^(c4-
1))+c5*c6*(RC(z,1)+4*s(z,1))*((att_depth*(RC(z,1)+4*s(z,1)))^(c6-
1))*ad_err)^2))^2+(spcov))))^2+(Ssp(z)*SDres)^2);

```

```

dc1=log(att_depth*s(z,1));
dc2=-exp(c2*(RC(z,1)+5*s(z,1))^(
2*s(z,1)))*(s(z,1)^2)*(RC(z,1)+5*s(z,1))^(
-2*s(z,1));
dc3=att_depth^c4;
dc4=c3*att_depth^c4*log(att_depth);
dc5=(att_depth*(RC(z,1)+4*s(z,1)))^c6;
dc6=(c5*(att_depth*(RC(z,1)+4*s(z,1)))^c6)*log(att_depth*(RC(z,1)+4*s(z
,1)));
dc7=(RC(z,1)+4*s(z,1))^c8;
dc8=log(RC(z,1)+4*s(z,1))*c7*(RC(z,1)+4*s(z,1))^c8;
dS=-exp(c2*s(z,1))*((RC(z,1)+5*s(z,1))^(
2*s(z,1)))+c1/s(z,1)+4*c7*c8*((RC(z,1)+4*s(z,1))^(c8-
1))+4*c5*c6*att_depth*((att_depth*(RC(z,1)+4*s(z,1)))^(c6-1))-
exp(c2*s(z,1))*((RC(z,1)+5*s(z,1))^(
2*s(z,1)))*s(z,1)*(c2*((RC(z,1)+5*s(z,1))^(
-2*s(z,1)))+c2*s(z,1)*((RC(z,1)+5*s(z,1))^(
-2*s(z,1)))*((10*s(z,1)/(RC(z,1)+5*s(z,1)))-2*log(RC(z,1)+5*s(z,1))));
drc=c7*c8*((RC(z,1)+4*s(z,1))^(c8-
1))+2*c2*exp(c2*s(z,1))*((RC(z,1)+5*s(z,1))^(
-2*s(z,1)))*s(z,1)^3*((RC(z,1)+5*s(z,1))^(
-2*s(z,1)))+c5*c6*att_depth*((att_depth*(RC(z,1)+4*s(z,1)))^(c6-1));
dx=c1/att_depth+c3*c4*(att_depth^(c4-
1))+c5*c6*(RC(z,1)+4*s(z,1))*((att_depth*(RC(z,1)+4*s(z,1)))^(c6-1));

log_sp_err=((dc1*c1se)^2)+((dc2*c2se)^2)+((dc3*c3se)^2)+((dc4*c4se)^2)
+((dc5*c5se)^2)+((dc6*c6se)^2)+((dc7*c7se)^2)+((dc8*c8se)^2)+((dS*s(z,2
))^2)+((drc*RC(z,2))^2)+((dx*ad_err)^2))^(1/2);

Ssp_err=sqrt((Ssp(z)*(sqrt(abs(log_sp_err^2+spcov))))^2+(Ssp(z)*SDres)^
2);%
%%%%%%%%Calculate errors for fast and slow muon
%%%%%%%%scaling%%%%%%%%
%%%%%%%%These are just constants
abFast=-3.25396E-05;acFast=1.84549E-08;adFast=9.83221E-08;aeFast=-
0.000108343;afFast=1.59601E-06;bcFast=-4.3898E-11;bdFast=-1.51103E-10;
beFast=1.33561E-07;bfFast=-6.59584E-10;cdFast=4.99682E-14;ceFast=-
3.31486E-11;cfFast=-3.10052E-13;deFast=-1.07713E-08;dfFast=1.04729E-
10;efFast=-4.1842E-07;

b1=5.1132E+00;b2=-8.8225E-03;b3=3.7346E-06;b4=7.9712E-05;b5=-7.5605E-
02;b6=-1.3203E-03;
blse=1.1694E-01;b2se=3.8936E-04;b3se=2.8414E-07;b4se=8.5686E-
06;b5se=1.0862E-02;b6se=3.8470E-04;smod_err_sm=.06;SDresSM=.0628;
abslow=-4.1658E-05;acSlow=2.8138E-08;adSlow=4.3200E-07;aeSlow=-7.1754E-
04;afSlow=1.8451E-05;
bcSlow=-1.0935E-10;bdSlow=-3.9882E-10;beSlow=1.0478E-06;bfSlow=-
4.3257E-08;cdSlow=-2.8143E-14;ceSlow=-4.1970E-10;
cfSlow=2.9585E-11;deSlow=-7.7146E-08;dfSlow=3.1508E-10;efSlow=-2.6040E-
06;

if RC(z,1)< 4
%%log_fm_err is column Q from Lifton, 2005%%%%%%%%
log_fm_err=sqrt(abs(alse^2+((att_depth)*a2se)^2+((att_depth^2)*a3se)^2+
(att_depth^4*a4se)^2+(4*a5se)^2+(a6se*4^2)^2+((a2+a4*4+2*a3*att_depth)*
ad_err)^2+((a5+a4*att_depth+2*a6*4)*RC(z,2))^2));

```

```

fmcov=2*(abFast*att_depth+acFast*att_depth^2+adFast*att_depth*4+aeFast*
4+afFast*(4^2)+bcFast*(att_depth^3)+bdFast*(att_depth^2)*4+beFast*att_d
epth*4+bfFast*att_depth*(4^2)+cdFast*(att_depth^3)*(4)+ceFast*(att_dept
h^2)*(4)+cfFast*(4^2)*(att_depth^2)+deFast*(4^2)*att_depth+dfFast*(4^3)
*att_depth+efFast*4^3);
%%%log_sm_err is column W from Lifton, 2005%%%%%%%%%%
log_sm_err=sqrt(abs(blse^2+((att_depth)*b2se)^2+((att_depth^2)*b3se)^2+
(att_depth*4*b4se)^2+(4*b5se)^2+(b6se*4^2)^2+((b2+b4*4+2*b3*att_depth)*
ad_err)^2+((b5+b4*att_depth+2*b6*4)*RC(z,2))^2));
smcov=2*(abslow*att_depth+acSlow*att_depth^2+adSlow*att_depth*4+aeSlow*
4+afSlow*(4^2)+bcSlow*(att_depth^3)+bdSlow*(att_depth^2)*4+beSlow*att_d
epth*4+bfSlow*att_depth*(4^2)+cdSlow*(att_depth^3)*(4)+ceSlow*(att_dept
h^2)*(4)+cfSlow*(4^2)*(att_depth^2)+deSlow*(4^2)*att_depth+dfSlow*(4^3)
*att_depth+efSlow*4^3);
else
log_fm_err=sqrt(abs(alse^2+((att_depth)*a2se)^2+((att_depth^2)*a3se)^2+
(att_depth*RC(z,1)*a4se)^2+(RC(z,1)*a5se)^2+(a6se*RC(z,1)^2)^2+((a2+a4*
RC(z,1)+2*a3*att_depth)*ad_err)^2+((a5+a4*att_depth+2*a6*RC(z,1))*RC(z,
2))^2));
fmcov=2*(abFast*att_depth+acFast*att_depth^2+adFast*att_depth*RC(z,1)+a
eFast*RC(z,1)+afFast*(RC(z,1)^2)+bcFast*(att_depth^3)+bdFast*(att_depth
^2)*RC(z,1)+beFast*att_depth*RC(z,1)...
+bfFast*att_depth*(RC(z,1)^2)+cdFast*(att_depth^3)*(RC(z,1))+ceFast*(at
t_depth^2)*(RC(z,1))+cfFast*(RC(z,1)^2)*(att_depth^2)+deFast*(RC(z,1)^2)
*att_depth+dfFast*(RC(z,1)^3)*att_depth+efFast*RC(z,1)^3);
log_sm_err=sqrt(abs(blse^2+((att_depth)*b2se)^2+((att_depth^2)*b3se)^2+
(att_depth*RC(z,1)*b4se)^2+(RC(z,1)*b5se)^2+(b6se*RC(z,1)^2)^2+((b2+b4*
RC(z,1)+2*b3*att_depth)*ad_err)^2+((b5+b4*att_depth+2*b6*RC(z,1))*RC(z,
2))^2));
smcov=2*(abslow*att_depth+acSlow*att_depth^2+adSlow*att_depth*RC(z,1)+a
eSlow*RC(z,1)+afSlow*(RC(z,1)^2)+bcSlow*(att_depth^3)+bdSlow*(att_depth
^2)*RC(z,1)+beSlow*att_depth*RC(z,1)...
+bfSlow*att_depth*(RC(z,1)^2)+cdSlow*(att_depth^3)*(RC(z,1))+ceSlow*(at
t_depth^2)*(RC(z,1))+cfSlow*(RC(z,1)^2)*(att_depth^2)+deSlow*(RC(z,1)^2)
*att_depth+dfSlow*(RC(z,1)^3)*att_depth+efSlow*RC(z,1)^3);

end

Sfm_err=sqrt((Sfm(z)*(sqrt(abs(log_fm_err^2+fmcov))))^2+(Sfm(z)*smod_er
r)^2+(Sfm(z)*SDresFM)^2);
Ssm_err=sqrt((Ssm(z)*(sqrt(abs(log_sm_err^2+smcov))))^2+(Ssm(z)*smod_er
r_sm)^2+(Ssm(z)*SDresSM)^2);

```

"phillips_th_neut_flux.m"

```

function
[ethsr_c,thsr_c,thflux,ethflux,p_ss]=phillips_th_neut_flux(depthstep,de
pth_inc,density,att_depth,Pf_0_slhl,Ssp,Afn,watper,p);
%This function descirbes the flux of thermal neutrons with depth
%as solved for in Phillips et. al., 2001 (chemical geology)

Pf_0=Pf_0_slhl*Ssp;
rawdata=dlmread('granite_data.txt');
data=rawdata;
mindata=dlmread('min_data_example.txt','\t');

%%%%%%%%input parameters for use as standalone script%%%%%%%%
%clear all
%clf
%data=dlmread('coso_composition.txt');
%Afn=160;      %fast neutron attenuation length (g/cm^2)
%Ssp=5;       %spallation scaling factor
%watper=0;    %water in air
%get scaling from P+L, otherwise enter these manually.
%depthstep=.1;
%density=2.7;
%depth_inc=4000; % number of depth increments (size of vector)
%depth=1000;     %depth in cm
%depthstep=(depth/depth_inc)*density%   % Depth step in g/cm^2
%Pf_0=626*Ssp % SLHL production rate of epithermal neutrons from fast
neutrons at the land/atmosphere interface (n/g/yr).
%Taken from Bierman, 1995, who took it from Lal, 1991?? Ssp is lat+alt
%apallation scaling factor. THIS CAN VARY BETWEEN 600 AND 950 CHECK
%LITTERATURE
%%%%%%%%%%%%%%%%%%%%%%%%%%%%%%%%%%%%%%%%%%%%%%%%%%%%%%%%%%

%%%%%%%%This section Calculates water in the air
data(1,9)=data(1,9)*watper;data(51,9)=data(51,9)*watper;data(5:7,9)=dat
a(5:7,9).*(1-watper);data(50,9)=data(50,9)*(1-watper); %adjust for h20
content
data(:,7)=data(:,9).*(1./data(:,1)).*(6.02*10^23);

%%%%%%%%%%%%%%%%%%%%%%%%%%%%%%%%%%%%%%%%CALCULATED PARAMETERS for Epithermal flux (SEC.
3)%%%%%%%%%%%%%%%%%%%%%%%%%%%%%%%%%%%%%%%%
Abar_a=(sum(data(:,1).*data(:,7)))/sum(data(:,7));
%Average atomic weight of air
%Abar_a=14.5
%average atomic wiehgt of air used by Phillips g/mol
Abar_ss=sum((data(:,8)/1000000).*data(:,1)); %Average atomic weight of
rock g/mol
sum_a=sum(data(:,3).*data(:,7)); %Macroscopic neutron
sctatering x-section for air (cm^2/g)
sum_ss=sum(data(:,3).*data(:,6)); %Macroscopic neutron
sctatering x-section for rock (cm^2/g)
Deth_a=1/(3*sum_a*(1-2*(1/(3*Abar_a))))); %epithermal neutron
diffusion coefficient for air (g/cm^2)--the term "2" has units of
g/mol

```

```

Deth_ss=1/(3*sum_ss*(1-2*(1/(3*Abar_ss))));           %epithermal neutron
diffusion coefficient for rock (g/cm^2)--the term "2" has units of
g/mol
eps_a=sum(data(:,2).*data(:,3).*data(:,7))/sum(data(:,3).*data(:,7));
%air- macroscopic log decrement energy loss per neutron collision
(unitless)
eps_ss=sum(data(:,2).*data(:,3).*data(:,6))/sum(data(:,3).*data(:,6));
%rock- macroscopic log decrement energy loss per neutron collision
(unitless)
I_a=sum(data(:,5).*data(:,7));                       %effective
resonance integral for absorption of epithermal neutrons by air
(cm^2/g)
I_ss=sum(data(:,5).*data(:,6));                       %effective
resonance integral for absorption of epithermal neutrons by air
(cm^2/g)
Aeth_a=1/(eps_a*I_a+eps_a*sum_a);                     %effective
epithermal neutron attenuation length for air (g/cm^2)
Aeth_ss=1/(eps_ss*I_ss+eps_ss*sum_ss);                %effective
epithermal neutron attenuation length for rock (g/cm^2)
Reth_a=1;                                             %normalization
factor for neutron production rate in air (unitless) NOTE: diff than
defined in Liu et al. 1994
Reth_ss=sqrt((Abar_ss/Abar_a));                       %normalization factor
for neutron production rate in rock (unitless) NOTE: diff than
defined in Liu et al. 1994
Leth_a=sqrt(Deth_a/(1/Aeth_a));                       %epithermal
neutron diffusion length in air (g/cm^2)????
Leth_ss=sqrt(Deth_ss/(1/Aeth_ss));                   %epithermal
neutron diffusion length in rock (g/cm^2)????

phi_star_a=Pf_0*(Reth_a/((1/Aeth_a)-Deth_a/(Afn^2))); % Eq. 12
(n/cm^2*yr) theoretical epithermal neuatron flux in air
phi_star_ss=Pf_0*(Reth_ss/((1/Aeth_ss)-Deth_ss/(Afn^2))); %Eq. 12
(n/cm^2*yr) theoretical epithermal neuatron flux in rock at surface,
if air had the same properties
Dphi_star_ss=phi_star_a-phi_star_ss;                 %Eq. 14a
(n/cm^2*yr) difference between flux in rock and air
Dphi_star_a=phi_star_ss-phi_star_a;                  %%Eq. 14a
(n/cm^2*yr) difference between flux in air and rock
Dphi_2star=Dphi_star_ss-((Deth_a/Deth_ss)*Dphi_star_a); %Eq. 14b
(n/cm^2*yr) difference, with the flux in air adjusted for ratio of
diff. coefficients

FDphi_eth_a=((Deth_ss/Leth_ss)*Dphi_star_a)-
((Deth_ss/Afn)*Dphi_2star)/((Deth_a/Leth_a)+(Deth_ss/Leth_ss)); %Eq.
13 (n/cm^2*yr)
FDphi_eth_ss=((Deth_a/Leth_a)*Dphi_star_ss)-
((Deth_ss/Afn)*Dphi_2star)/((Deth_a/Leth_a)+(Deth_ss/Leth_ss)); %Eq.
13 (n/cm^2*yr)
%%%%%%%%%%%%%%%%%%%%%%%%%%%%%%%%%%%%%%%%%%%%%%%%%%%%%%%%%%%%%%%%%%%%%%%%
%%%%%%%%%%%%%%%%%%%%%%%%%%%%%%%%%%%%%%%%%%%%%%%%%%%%%%%%%%%%%%%%%%%%%%%%

%%%%%%%%%%%%%%%%%%%%%%%%%%%%%%%%%%%%%%%%%%%%%%%%%%%%%%%%%%%%%%%%%%%%%%%%CALCULATED PARAMETERS FOR THERMAL NEUTRON FLUX
(SEC.4)%%%%%%%%

```

```

p_a=exp(-I_a/sum(data(:,3).*data(:,7).*data(:,2)));      %Eq. 16
(unitless) resonance escape probability of air, following Chimel and
Liu,
p_ss=exp(-I_ss/sum(data(:,3).*data(:,6).*data(:,2)));    %Eq. 16
(unitless) resonance escape probability of air, following Chimel and
Liu,
Rth_a=1;                                                  %Eq. 17 (unitless)
ratio of thermalized epithermal neutrons in air to itself
Rth_ss=p_ss/p_a;                                         %Eq. 17 (unitless)
same in rock NOTE: Disagrees with Liu 1994, they use a "total" R
which multiplies Rth and Reth
%Rth_ss=(p_ss/p_a)*sqrt(Abar_ss/Abar_a)
Ath_a=1/sum(data(:,4).*data(:,7));                       %Eq. 18 (g/cm^2) mean
free path for thermal neutrons in air
Ath_ss=1/sum(data(:,4).*data(:,6));                     %%Eq 18 (g/cm^2)
mean free path for thermal neutrons in rock
Dth_a=Deth_a;                                           %Eq. 19 Diffuion
coefficient for thermal neuatrons in air
Dth_ss=Deth_ss;                                         %Eq. 19 Diffuion
coefficient for thermal neuatrons in air
Lth_a=sqrt(Dth_a/(1/Ath_a));                             %thermal neutron
diffusion length in air (g/cm^2)
Lth_ss=sqrt(Dth_ss/(1/Ath_ss));                         %thermal neutron
diffusion length in rock (g/cm^2)

phi_star_th_a=(p_a*Rth_a*phi_star_a)/(Aeth_a*((1/Ath_a)-
(Dth_a/(Afn^2))));                                     %Eq. 21 (n/cm^2*yr) thermal neuatron
flux in air
phi_star_th_ss=(p_a*Rth_ss*phi_star_ss)/(Aeth_ss*((1/Ath_ss)-
(Dth_ss/(Afn^2))));                                   %Eq. 21 (n/cm^2*yr) thermal neuatron flux
in rock at surface, theoretical
suiq_eth_a=(p_a*Rth_a*FDphi_eth_a)/(Aeth_a*((1/Ath_a)-
(Dth_a/(Leth_a^2))));                                 %Eq. 22 (n/cm^2*yr)
suiq_eth_ss=(p_a*Rth_ss*FDphi_eth_ss)/(Aeth_ss*((1/Ath_ss)-
(Dth_ss/(Leth_ss^2))));                               %Eq. 22 (n/cm^2*yr)
Dsuiq_eth_a=suiq_eth_ss-suiq_eth_a;
%Eq. 25 (n/cm^2*yr)
Dsuiq_eth_ss=suiq_eth_a-suiq_eth_ss;
%Eq. 25 (n/cm^2*yr)
Dphistar_th_a=phi_star_th_ss-phi_star_th_a;
%Eq. 24 (n/cm^2*yr) (modified to follow Gosse +Phillips; i.e.
subscript on left term is i not j)
Dphistar_th_ss=phi_star_th_a-phi_star_th_ss;
%Eq. 24 (n/cm^2*yr) (modified to follow Gosse +Phillips; i.e.
subscript on left term is i not j)

suiq_th_a=(Dth_a*(phi_star_th_a*(1/Afn)-suiq_eth_a*(1/Leth_a))...
-Dth_ss*(phi_star_th_ss*(1/Ath_ss)+suiq_eth_ss*(1/Leth_ss))...
+(Dth_ss/Lth_ss)*(Dphistar_th_a+Dsuiq_eth_a))*(1/((Dth_ss/Lth_ss)+(Dth
_a/Lth_a)));     %Eq. 23 (n/cm^2*yr)

suiq_th_ss=(Dth_a*(phi_star_th_a*(1/Afn)-suiq_eth_a*(1/Leth_a))...
-Dth_ss*(phi_star_th_ss*(1/Ath_ss)+suiq_eth_ss*(1/Leth_ss))...

```

```

+(Dth_a/Lth_a)*(Dphistar_th_ss+Dsquiq_eth_ss))*(1/((Dth_ss/Lth_ss)+(Dth
_a/Lth_a)));      %Eq. 23 (n/cm^2*yr)

%This section calculates the thermal and epithermal neutron fluxes
(Eqs. 11 and 20) at each depth increment.
count=0
for i=1:depth_inc
thflux(i)=phi_star_th_ss*exp((-depthstep*count)/Afn)+squiq_eth_ss*exp(-
abs(depthstep*count)/Leth_ss)+squiq_th_ss*exp(-
abs(depthstep*count)/Lth_ss);
ethflux(i)=phi_star_ss*exp((-depthstep*count)/Afn)-FDphi_eth_ss*exp(-
abs(depthstep*count)/Leth_ss);
count=count+1;
depths(i)=(depthstep*count);
end
thsr_c=thflux/Ath_ss;    %This goes from flux in n/cm^2*yr to stopping
rate in n/g*yr
ethsr_c=ethflux/Ath_ss; %NOTE: This should really be divided by
Aeth_ss, but that gives unreasonable results....

%%%%%%%%%%%%%%%%%%%%%%%%%%%%%%%%%%%%%%%%%%%%%%%%%%%%%%%%%%%%%%%%%%%%%%%%Plotting section%%%%%%%%%%%%%%%%%%%%%%%%%%%%%%%%%%%%%%%%%%%%%%%%%%%%%%%%%%%%%%%%%%%%%%%%
%figure(1)
%clf
%plot(depths,thflux)
%hold on
%plot(depths,ethflux,'b:')
%xlabel('Depth (g/cm^2)')
%ylabel('n/cm^2/yr')
%title('Neutron Fluxes Following Phillips et al., 2001')
%legend('thermal neutrons','epithermal neutrons')

```

Appendix B
Matlab scripts for computation of analytical uncertainties

"ID_plot_errors.m"

```

%%Script used to generate figure 4.6, which shows error contours for
%%specific combinations of Exposure age and U/Th-He closure age.

%External files called:  None

%External scripts called: None

%%%%%%%%%%%%%%%%%%%%%%%%%%%%%%%%%%%%%%%%%%%%%%%%%%%%%%%%%%%%%%%%%%%%%%%%
%
clear all
clf

%Define the range of exposure ages and U/Th-He ages
expages=[0.0001:0.0001:0.1];  nucages=[0.1:0.1:150];

%Assume a nucleogenic production rate of 0.012 at.g.yr.ppmLi
nucconc_1=nucages*0.012;  nucconc_10=nucages*0.12;
nucconc_30=nucages*0.36;

%assume 15% error on 3hectn calculation
moderr=0.15;  PR=115; SF=2.275;  he_sp=expages.*PR*SF;

%Assume a 3hesp/3hectn ratio and compute 3Hectn for each Li case
he_ctn_1=he_sp.*0.005;  he_ctn_10=he_sp.*0.05; he_ctn_30=he_sp.*0.15;

%%Loop through and compute total 3He, then compute errors based on the
%%fitted error function from excel spreadsheet for the 10 ppm case
for i=1:length(expages)
    for j=1:length(nucconc_1)
        he_m_10(i,j)=he_sp(i)+he_ctn_10(i)+nucconc_10(j);
        he_m_1(i,j)=he_sp(i)+he_ctn_1(i)+nucconc_1(j);
        he_m_30(i,j)=he_sp(i)+he_ctn_30(i)+nucconc_30(j);

        if (8.485*he_m_10(i,j)^-0.26)>2
            m_err_10(i,j)=((8.485*he_m_10(i,j)^-0.26)./100).*he_m_10(i,j);
        else
            m_err_10(i,j)=0.02.*he_m_10(i,j);
        end

        if (8.485*he_m_1(i,j)^-0.26)>2
            m_err_1(i,j)=((8.485*he_m_1(i,j)^-0.26)./100).*he_m_1(i,j);
        else
            m_err_1(i,j)=0.02.*he_m_1(i,j);
        end

        if (8.485*he_m_30(i,j)^-0.26)>2
            m_err_30(i,j)=((8.485*he_m_30(i,j)^-0.26)./100).*he_m_30(i,j);
        end
    end
end

```

```

        else
            m_err_30(i,j)=0.02.*he_m_30(i,j);
        end

    end

end

%%repeat the loop for the 30 ppm case
for i=1:length(nuconc_10)
    if (8.485*nuconc_10(i)^-0.26)>2
        nuc_err_10(i)=((8.485*nuconc_10(i)^-
0.26)./100).*nuconc_10(i);
    else
        nuc_err_10(i)=0.02.*nuconc_10(i);
    end

    if (8.485*nuconc_1(i)^-0.26)>2
        nuc_err_1(i)=((8.485*nuconc_1(i)^-0.26)./100).*nuconc_1(i);
    else
        nuc_err_1(i)=0.02.*nuconc_1(i);
    end

    if (8.485*nuconc_30(i)^-0.26)>2
        nuc_err_30(i)=((8.485*nuconc_30(i)^-
0.26)./100).*nuconc_30(i);
    else
        nuc_err_30(i)=0.02.*nuconc_30(i);
    end
end

%%Compute the absolute errors on the CTN components by multiplying the
%%fractional model error by the magnitude of the CTN component for the
1, 10,
%% and 30 ppm cases.
ctn_err_30=he_ctn_30.*moderr;  ctn_err_10=he_ctn_10.*moderr;
ctn_err_1=he_ctn_1.*moderr;

%Loop through and calculate the total error on the 3Hesp component
(quadratic)
for i=1:length(expages)
    for j=1:length(nuconc_10)
        spall_matrix(i,j)=he_sp(i);
        errone(i,j)=sqrt(m_err_1(i)^2+ctn_err_1(i)^2+nuc_err_1(j)^2);

errten(i,j)=sqrt(m_err_10(i)^2+ctn_err_10(i)^2+nuc_err_10(j)^2);
err30(i,j)=sqrt(m_err_30(i)^2+ctn_err_30(i)^2+nuc_err_30(j)^2);
    end
end

%Compute the fractional error on the 3Hesp component
fracterr_1=errone./spall_matrix;  fracterr_10=errten./spall_matrix;
fracterr_30=err30./spall_matrix;

% Clean up our of range entries in the fractional error
for i=1:size(fracterr_1,1)

```

```

for j=1:size(fracterr_1,2)
    if fracterr_1(i,j)<0
        fracterr_1(i,j)=1000;
    elseif fracterr_1(i,j)>1
        fracterr_1(i,j)=1;
    end
    if fracterr_10(i,j)<0
        fracterr_10(i,j)=1000;
    elseif fracterr_10(i,j)>1
        fracterr_10(i,j)=1;
    end
    if fracterr_30(i,j)<0
        fracterr_30(i,j)=1000;
    elseif fracterr_30(i,j)>1
        fracterr_30(i,j)=1;
    end
end
end

%%Plot option 1: Make contour plots of the fractional errors
clf
figure(1)
v2=[0.05 0.1 0.15 0.2 0.25 0.3 0.35 0.4 0.45 0.5]
subplot(2,1,1)
[C2,h2]=contour(nucages,expages,fracterr_10,v2)
xlabel('U/Th-He Closure Age (my)');ylabel('Exposure Age (ky)');view([0,0,1]);
xlim([0 100]);ylim([0 0.05])

v3=[0.05 0.1 0.15 0.2 0.25 0.3 0.35 0.4 0.45 0.5]
subplot(2,1,2)
[C3,h3]=contour(nucages,expages,fracterr_30,v3)
xlabel('U/Th-He Closure Age (my)');ylabel('Exposure Age (ky)');view([0,0,1]);
xlim([0 100]);ylim([0 0.1])

break

%%Plot option 2: extract the fractional error contours
%%as vector arrays, and then plots them as individual lines. This is
the
%%section used to make the figure.

clear coord5 coord7 coord10 coord15 coord20 coord30
count=0;count1=0;count2=0;count3=0;count4=0;count5=0;
for i=1:1000%size(fracterr_30,1)
    for j=1:1000%size(fracterr_30,2)
        if ((fracterr_30(i,j) < 0.05001) & (fracterr_30(i,j) >
0.04999))
            count=count+1;
            coord5(1,count)=i/10;coord5(2,count)=j/10;
        end
        if ((fracterr_30(i,j) < 0.07001) & (fracterr_30(i,j) >
0.06999))
            count5=count5+1;
            coord7(1,count5)=i/10;coord7(2,count5)=j/10;
        end
    end
end

```

```

end
    if ((fracterr_30(i,j) < 0.10001) & (fracterr_30(i,j) >
0.09999))
        count1=count1+1;
        coord10(1,count1)=i/10;coord10(2,count1)=j/10;
    end
    if ((fracterr_30(i,j) < 0.1501) & (fracterr_30(i,j) > 0.1499))
        count2=count2+1;
        coord15(1,count2)=i/10;coord15(2,count2)=j/10;
    end
    if ((fracterr_30(i,j) < 0.201) & (fracterr_30(i,j) > 0.199))
        count3=count3+1;
        coord20(1,count3)=i/10;coord20(2,count3)=j/10;
    end
    if ((fracterr_30(i,j) < 0.31) & (fracterr_30(i,j) > 0.29))
        count4=count4+1;
        coord30(1,count4)=i/10;coord30(2,count4)=j/10;
    end
end

end

clf
loglog(coord5(2,:),coord5(1,:));
hold on
loglog(coord10(2,:),coord10(1,:));hold
on;loglog(coord15(2,:),coord15(1,:));
loglog(coord20(2,:),coord20(1,:));loglog(coord30(2,:),coord30(1,:));log
log(coord7(2,:),coord7(1,:));
xlim([1 100]); ylim([1 100])

%%Save the extracted contour lines for optional plotting in excel
output=[nucages'; expages']
save D:\Willy\Idaho\Paper\Figures\contourfig\agelists output -ascii -
tabs
save D:\Willy\Idaho\Paper\Figures\contourfig\fracterr_10 fracterr_10 -
ascii -tabs
save D:\Willy\Idaho\Paper\Figures\contourfig\fracterr_30 fracterr_30 -
ascii -tabs

```

"Slope_errors.m"

```

%%This script is used to generate the lower panel in figure 5.6,
%%it creates synthetic datasets, imposes a slope and determines what
%%the error on the linear fit is.

%External files: none

%Exteral scripts: none

%%%%%%%%%%%%%%%%%%%%%%%%%%%%%%%%%%%%%%%%%%%%%%%%%%%%%%%%%%%%%%%%%%%%%%%%
%%
clear all
clf

%%%%%%%%%%%%%%%%%%%%%%%%%%%%%%%%%%%%%%%%%%%%%%%%%%%%%%%%%%%%%%%%%%%%%%%%
%%Inputs%%%%%%%%%%%%%%%%%%%%%%%%%%%%%%%%%%%%%%%%%%%%%%%%%%%%%%%%%%%%%%%%%%%%%%%%
mu=[0.5 1 2 3]; % mean 3He signal intensities (cps)
sigma=[0.18 0.13 0.09 0.075]; %Uncertainties associated with each 3He
value,
%taken from observed data in top panel of figure 5.6
t=[170:60:3890]; %Time steps in each synthetic data array
slopes=[0.0001 0.0002 0.003 0.0004 0.0006 0.0008 0.001 0.002 0.003
0.004 0.006 0.008 0.01]
%%%%%%%%%%%%%%%%%%%%%%%%%%%%%%%%%%%%%%%%%%%%%%%%%%%%%%%%%%%%%%%%%%%%%%%%
for e=1:length(sigma) %Loop over the specified errors

for k=1:300 %Loop over the number of synthetic datasets
cps=mu(e)+sigma(e)*randn(1,187); %generate the kth data array

for i=1:length(slopes)
clear cps_s
for j=1:length(t)
cps_s(j)=cps(j)*((slopes(i)*t(j)+mu(e))/mu(e)); %Apply slope to
data
end
[B dev stats]=glmfit(t,cps_s); %record intercept and error
ints(k,1,i)=B(1);ints(k,2,i)=stats.se(1);
end
end

mean_ints(:,(2*e-1):2*e)=squeeze(mean(ints,1))'
%clear ints
end
%%Loop through results matrix and and compute fractional errors
cnt=0;
for i=2:2:size(mean_ints,2)
cnt=cnt+1;
fracterr(:,cnt)=mean_ints(:,i)./mean_ints(:,i-1);
end

%%Plot up fractional errors versus slope for each 3He cps value
clf
plot(slopes,fracterr(:,1:4),'linewidth',2)
ylim([0 0.5])
xlabel('Slope of time (sec) vs 3He (cps)')

```

```
ylabel('% Standard Error on intercept')  
legend('0.5 cps', '1 cps', '2 cps', '3 cps')
```

"Ratio_Plotter.m"

```

%%%This script is used to generate the lower panel in figure 5.7,
%%it calculates 3He from exposure age and 4He from closure age

%External files: none

%External scripts: none

%%%%%%%%%%%%%%%%%%%%%%%%%%%%%%%%%%%%%%%%%%%%%%%%%%%%%%%%%%%%%%%%%%%%%%%%
%%
clear all
clf

%Specify scaling factor and production rate
SF=2.15; PR=133;

%%Specify devcay constants
dc238=log(2)/4.47e9; dc235=log(2)/7.04e8; dc232=log(2)/1.4e10;

%Compute 3Hesp for an array of exposure ages
for i=1:100
    expages(i)=i*1000;
    he3(i)=i*1000*SF*PR;
end

%Compute U and Th concentrations
uvals=[50 100 200 400]
for j=1:4
    th(j)=uvals(j)/3;
    u235(j)=(((uvals(j)*(1/137.88))*(10^-6))/235)*6.022e23;
    u238(j)=((uvals(j)*(10^-6))/238)*6.022e23;
    th232(j)=((th(j)*(10^-6))/232)*6.022e23;
end

%Compute 4He concentrations
ages=[10^7 10^8]
cnt=0;
for j=1:4
    for a=1:2
        cnt=cnt+1;
        he(cnt)=8*u238(j)*(exp(dc238*ages(a))-
1)+7*u235(j)*(exp(dc235*ages(a))-1)+6*th232(j)*(exp(dc232*ages(a))-1);
    end
end

%%Compute 3He/4He ratios
for i=1:100
    for j=1:8
        ratio(i,j)=he3(i)/he(j);
    end
end

%%Plot the exposure ages vs the 3He/4He ratios
semilogy(expages,ratio)
ylim([10^-12 10^-8])

```

"Compute_errors2.m"

```

%%%This script is used to generate the top panel in figure 4.7
%%%It determines the lowest achievable error for a 3He analysis at a
given
%%%3He/4He ratio

%External files: None

%External Scripts: "slope_errors_auto.m"

%%%%%%%%%%%%%%%%%%%%%%%%%%%%%%%%%%%%%%%%%%%%%%%%%%%%%%%%%%%%%%%%%%%%%%%%
clear all

sens=100; %hold sensitivity fixed in this case.
max4=(7*10^14)*(10^-12); %4He threshold at which tailing is observed
to begin
mincps=0.5; % Minimum 3He signal (in cps) required
for analysis
min3=((mincps/sens)*(10^-12))/22400)*6.022e23; %Number of atoms
required to give minimum cps

cnt=0;
values=[2*10^-9:2*10^-9:10^-8]% 8*10^-10 10^-9 4*10^-9 8*10^-9 10^-
8]
for k=1:length(values) %iterate through the 3He/4He ratios
    i=values(k);
    cnt=cnt+1
    ratio34(cnt)=i; %record 3He/4He ratios
    min4(cnt)=(min3/i)*(10^-12); %define minimum 4He to get
target cps (Tatoms)
    cnt2=0;
    lowesterr(cnt)=1;bestmu(cnt)=0; %Initialize variables
    clear slope mu fracterr at3
    for j=round(min4(cnt)):1:round(max4) %iterate from the minimum
4He to the maximum where scattering occurs
        cnt2=cnt2+1;
        at3(cnt2)=(j*i)*10^12; %atoms of 3He for the given
4He
        mu(cnt2)=(((at3(cnt2)*sens)*(10^12))*22400)/6.022e23; %cps of
3He for the given 4He
        slopes(cnt2)=0.00007807*j^0.60711864; %Slope for
the given 4He

[fracterr(cnt2),mean_int(cnt2,:)] = slope_errors_auto(mu(cnt2),slopes(cnt
2)); %Run the montecarlo script to get the error.

        if fracterr(cnt2)<lowesterr(cnt)
            lowesterr(cnt)=fracterr(cnt2); % record the lowest error
            best4(cnt)=j; %record the 4He value
that gave the lowest error
            bestmu(cnt)=mu(cnt2); %record the mean cps value
that gave the lowest error
            bestslope(cnt)=slopes(cnt2); %record the slopethat gave
the lowest error
        end

```

```
end
end

%%Output results for plotting in Excel
output=[ratio34' bestmu' lowesterr' bestslope' best4']
save errorcalc_cps1_sens100_max4_7 output -ascii -tabs
```

"slope_errors_auto.m"

```

%% This script is called by "compute_errors2.m" and does a monte
carlo
%% calculation to determine the average uncertainty on the intercept
for
%% a data array of given 3He cps (mu) and slope (slopes)

%external files: none

%external scripts: none

%%%%%%%%%%%%%%%%%%%%%%%%%%%%%%%%%%%%%%%%%%%%%%%%%%%%%%%%%%%%%%%%%%%%%%%%
%%
function [fracterr,mean_int]=slope_errors_auto(mu,slopes)

sigma=0.116*(mu^-0.43); %extract the % S.D. from fit to observed
errors
sigma2=sigma*mu; % Compute the absolute standard deviation
t=[170:60:3890]; %set time range

for k=1:70 %loop over a bunch of monte carlo
iterations
cps=mu+sigma2*randn(1,187); %Generate an array of random numbers
around the mean CPS
%%with the specified standard deviation
clear cps_s
for j=1:length(t)
cps_s(j)=cps(j)*((slopes*t(j)+mu)/mu); % Add the slope to a
given dataset
end
[B dev stats]=glmfit(t,cps_s); %Output the intercept and standard
error
ints(k,1)=B(1);ints(k,2)=stats.se(1);

end % Record intercept and error
mean_int=mean(ints,1)';
fracterr=mean_int(2)/mean_int(1); %Compute fractional error.

```